THE UNIVERSITY OF
WARWICK

Library Declaration and Deposit Agreement

1. STUDENT DETAILS

Please complete the following:

Full name: **RHYS GARETH JONES**

University ID number: **0421387**

2. THESIS DEPOSIT

2.1. I understand that under my registration at the University, I am required to deposit my thesis with the University in BOTH hard copy and in digital format. The digital version should normally be saved as a single pdf file.

2.2. The hard copy will be housed in the University Library. The digital version will be deposited in the University's Institutional Repository (WRAP). Unless otherwise indicated (see 2.3 below) this will be made openly accessible on the Internet and will be supplied to the British Library to be made available online via its Electronic Theses Online Service (EThOS) service.

[At present, theses submitted for a Master's degree by Research (MA, MSc, LLM, MS or MMedSci) are not being deposited in WRAP and not being made available via EthOS. This may change in future.]

2.3. In exceptional circumstances, the Chair of the Board of Graduate Studies may grant permission for an embargo to be placed on public access to the hard copy thesis for a limited period. It is also possible to apply separately for an embargo on the digital version. (Further information is available in the Guide to Examinations for Higher Degrees by Research.)

2.4. If you are depositing a thesis for a Master's degree by Research, please complete section (a) below. For all other research degrees, please complete both sections (a) and (b) below:

(a) Hard Copy

I hereby deposit a hard copy of my thesis in the University Library to be made publicly available to readers **after an embargo period of 2 years** as agreed by the Chair of the Board of Graduate Studies.

I agree that my thesis may be photocopied. **YES**

(b) Digital Copy

I hereby deposit a digital copy of my thesis to be held in WRAP and made available via EThOS.

Please choose one of the following options:

EITHER My thesis can be made publicly available online. **NO**

OR My thesis can be made publicly available only after **21st July 2014 (YES)**

OR My full thesis cannot be made publicly available online but I am submitting a separately identified additional, abridged version that can be made available online. **NO**

OR My thesis cannot be made publicly available online. **NO**

3. GRANTING OF NON-EXCLUSIVE RIGHTS

Whether I deposit my Work personally or through an assistant or other agent, I agree to the following:

Rights granted to the University of Warwick and the British Library and the user of the thesis through this agreement are non-exclusive. I retain all rights in the thesis in its present version or future versions. I agree that the institutional repository administrators and the British Library or their agents may, without changing content, digitise and migrate the thesis to any medium or format for the purpose of future preservation and accessibility.

4. DECLARATIONS

(a) I DECLARE THAT:

- I am the author and owner of the copyright in the thesis and/or I have the authority of the authors and owners of the copyright in the thesis to make this agreement. Reproduction of any part of this thesis for teaching or in academic or other forms of publication is subject to the normal limitations on the use of copyrighted materials and to the proper and full acknowledgement of its source.

- The digital version of the thesis I am supplying is the same version as the final, hard-bound copy submitted in completion of my degree, once any minor corrections have been completed.

- I have exercised reasonable care to ensure that the thesis is original, and does not to the best of my knowledge break any UK law or other Intellectual Property Right, or contain any confidential material.

- I understand that, through the medium of the Internet, files will be available to automated agents, and may be searched and copied by, for example, text mining and plagiarism detection software.

(b) IF I HAVE AGREED (in Section 2 above) TO MAKE MY THESIS PUBLICLY AVAILABLE DIGITALLY, I ALSO DECLARE THAT:

- I grant the University of Warwick and the British Library a licence to make available on the Internet the thesis in digitised format through the Institutional Repository and through the British Library via the EThOS service.

- If my thesis does include any substantial subsidiary material owned by third-party copyright holders, I have sought and obtained permission to include it in any version of my thesis available in digital format and that this permission encompasses the rights that I have granted to the University of Warwick and to the British Library.

5. LEGAL INFRINGEMENTS

I understand that neither the University of Warwick nor the British Library have any obligation to take legal action on behalf of myself, or other rights holders, in the event of infringement of intellectual property rights, breach of contract or of any other right, in the thesis.

Please sign this agreement and return it to the Graduate School Office when you submit your thesis.

Student's signature: ..... Date: **17th July 2012**

Publications and Awards

- Jones, Rhys; Mao, Ken; Phang, Albert; Allen, Brian; Effects of linear and angular misalignment on a spur gear pair, 8th International Conference on Condition Monitoring and Machinery Failure Prevention Technologies 2011, Cardiff, United Kingdom, 20-22 June 2011, Volume 2, pp. 711-722.

- Jones, Rhys; Mao, Ken; Phang, Albert; Allen, Brian; Effects of linear and angular misalignment on a spur gear pair, Insight - Non-Destructive Testing and Condition Monitoring, Volume 53, Number 8, August 2011 , pp. 420-425.

- British Institute of Non-Destructive Testing, The Len Gelman Award for the best paper published in the Proceedings of the Institute's Condition Monitoring Conference CM 2011/MFPT 2011 by a person in the early stages of their career.

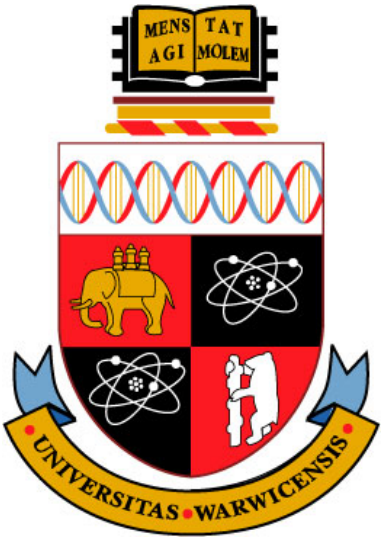

The Mathematical Modelling of Gearbox Vibration under Applied Lateral Misalignment

by

Rhys Gareth Jones

Thesis

Submitted to the University of Warwick

in partial fulfilment of the requirements

for admission to the degree of

Doctor of Philosophy

School of Engineering

July 2012

THE UNIVERSITY OF WARWICK

Contents

List of Tables

List of Figures

Acknowledgments

I would like to take this opportunity to thank all the people who have helped me along this journey, culminating in the production of this thesis. Firstly I would like to thank everybody at the University of Warwick, for their help and support, and give a special mention to my supervisor Ken Mao, to whom I owe this opportunity.

I offer my thanks to Duncan Shepherd, for his dedication to the project and for allowing me to be a part of it, Brian Allen and Albert Phang at QinetiQ for their valued input and guidance, and to Andrew Starr at Cranfield University for his endless enthusiasm behind the project. I would also like to thank my various colleagues on this project for their help and friendship.

I would like to thank the EPSRC and the MoD for the funding in these tight financial time, which has allowed me to undertake this project and gain so much.

I am indebted to my family for their love and support, which extends beyond this PhD into everything I do, and to my friends, that without their continual harassment about me still being a student, I might never have finished. And no, no matter how much you nag, I will not name you here.

Finally I cannot thank enough my fiancé, Vikki, for her unquestionable love and caring. I hope I can offer you 10% of the support you have given me over the last 5 years. Sorry for talking about gears so much.

Thesis Notes

Due to the large number of results in this thesis an additional CD is supplied, which contains all of the figures presented in the thesis along with additional results that have been omitted for the sake of space. Figures on this CD are usually stored as PNG files; however where applicable MATLAB figures are also supplied, which contain the raw results, and can be modified.

The CD is often referred to as the Digital Appendix in the main body of the thesis.

Abstract

In the mathematical modelling of gear vibrations it is found that there is a gap between the transient models developed in academia and the steady state models frequently used in industry. It is seen that the academic models are adept at modelling the nonlinear phenomena seen during gear contact for system with only a few degrees-of-freedom, whereas the industrial models are capable of solving the linear steady state response of more complex transmission systems.

The work presented in this thesis attempts to bridge the gap between the two models, through the development of a transient nonlinear model of a gear pair with increased degrees-of-freedom. An understanding of the gear contact is achieved through the use of advanced static finite element analysis with nonlinear gear contact. Through FEA the effects of gear misalignment on these contact conditions is also investigated.

The findings from the FEA are then used in a mathematical model of a single stage spur gear transmission, which is developed as part of the thesis, to determine the system accelerations. The mathematical model includes the time varying mesh stiffness and the time varying and nonlinear bearing stiffness's and frictional forces. The effects of lateral misalignment seen in the FEA results are also included into the model to investigate their effects.

The model parameters are then varied to determine their effects and the simulated accelerations are compared against experimental results. It is found from this comparison that although some similarities between the simulated and experimental results are achieved for the aligned case, insufficient corroboration is found for the axially and radially misaligned results to confirm the validity of the mathematical model for modelling misalignment.

From this, further experimental results were requested to gain a better confidence in the effects of lateral misalignment.

Chapter 1

Introduction

In the transmission system of helicopters, the gearbox is classed as a safety critical component; the failure of which can lead to accidents and possibly fatalities. In fact Learmount [1] stated that in 1999, of the 192 turbine helicopter accidents which occurred worldwide, 28 were due to mechanical failures with the most common being the drive train. As a means to detect and classify faults within the transmission system, and within various other components, monitoring systems are regularly installed on commercial and military helicopters. These are given the generalized term HUMS (Health and Usage Monitoring Systems), and take the form of various sensors distributed about the helicopter. These sensors relay information to a control unit, where algorithms are used to determine a set of condition indicators (CI's), which summarise the complex and extensive raw data into a set of numbers which can be easily assessed. In some cases these can be used to give CAUTION or ALARM readings to the health of specific components.

Within the transmission system the three main sources of information come from vibration monitoring, oil debris analysis and oil temperature analysis [2], however acoustic monitoring has also started to receive attention. Although common, oil debris analysis is unable to determine failures where little or no debris is produced, for example cracking of the gear tooth; which are also the most likely causes of catastrophic failure. Oil temperature analysis is often also only used as a secondary indicator as noticeable increases in temperature are only present late in the compo-

nent degeneration [2]. Therefore the most attractive monitoring method available is the use of vibration data; however this is not without its limitations.

Although claimed by many that algorithms for condition monitoring of components is sufficiently mature [2], the UK Civil Aviation Authority (CAA) claim that HUMS has a 70% detection rate, a figure highlighted by the Eurocopter AS332 L2 Super Puma crash over the north sea on 1st April 2009. This has since been attributed to a failure of the main rotor gearbox that went undetected by the installed HUMS [3]. This lead to the Air Accident Investigation Branch (AAIB) issuing a recommendation in the initial report (Safety Recommendation 2009-050) to improve the gearbox monitoring and warning systems on the helicopter to provide adequate alerts.

A problem encountered through the application of HUMS is the need to set thresholds, such that maintenance and inspection can be carried out when a CI exceeds this limit. A fine balance must be sought, requiring enough sensitivity of the system to detect faults early but also not produce unnecessary alarms, which require investigation, maintenance and downtime of equipment. Three cases are often highlighted.

- FALSE-POSITIVE: this occurs when the threshold is exceeded when the condition of a component is tolerable.
- FALSE-NEGATIVE: occurs when HUMS does not detect a fault in the system.
- CORRECT-DECISION: HUMS detects that there is/is not a fault in the system.

There is often a compromise between the number of FALSE-POSITIVES and FALSE-NEGATIVES, when setting thresholds; however a better understanding behind the fundamentals of vibration applied to HUMS can be used to reduce this compromise and allow for better threshold setting.

One such fundamental phenomenon that is not widely studied in the literature is the effects of misalignment at the gear contact, and this is where this thesis

looks to contribute to the field of vibration monitoring of gearboxes.

There are two methods through which a better understanding can be achieved, either through continued experimental work applied to test rigs or on operational aircraft, or through mathematical modelling. This thesis is part of a wider project looking to undertake both approaches in a unified manner to validate the less costly, with respect to time and money, mathematical model; and within this thesis the mathematical modelling approach is detailed.

Many reviews have been performed into the mathematical modelling of gearbox vibrations [4–6], and most state the primary source of excitation as the transmission error (TE) [6, 7]. This can be classified as the difference between the actual rotational position of the driven gear and the position it would take if the gears were unmodified, rigid and perfectly aligned.

This flexibility of contact can be determined by a number of means, however with the increase in available computational power and the improvements in computational methods, the Finite Element Method (FEM) has grown in popularity as the tool of choice in determining the TE.

Due to the still considerable computational expense of performing dynamic simulations of complex 3 dimensional nonlinear models using the FEM, the TE is often calculated in the static mode to determine a simplified contact stiffness, referred to as the mesh stiffness. This stiffness is then used in simplified dynamic models to connect gears and increase computational efficiency.

Another output from the static FE analysis (FEA) that is often used in the determination of frictional forces in the dynamic model is the Load Sharing Ratio (LSR). This is the portion of the total transmitted load applied to individual teeth at a given rotational contact position. This project calculates the LSR for a number of aligned and misaligned cases and shows the variation in LSR during meshing; these results are also compared against theoretical models of LSR which depend on analytically derived geometric contact positions.

The final output of the FEA is unique to this study and helps to understand the effects of misalignments on the static response of a gear pair. This is the reaction

forces on the gear centre. In previous studies of misalignments using the FEM the areas of concern are generally the stresses on the tooth face or at the tooth root. These have found uses in determining the strength of gears under misalignment but tell little of the dynamic response of the gears. When gears are moved out of alignment, forces are generated which cannot be solely described by the mesh stiffness. The reaction forces and moments (RFi, RMi) at the gear centres give an insight into the development of these forces and allow theoretical and functional relationships between the misalignments, applied forces and the generated reaction forces to be tested.

As mentioned, the static parameters determined in the FEA are used to define and simplify the calculation of the dynamic response of the gearbox system. The mesh stiffness acts as a spring element coupling together the gears, and because of this, only transmits load in one direction, which is known as the Line-Of-Action (LOA). Further forces are generated perpendicular to the LOA by friction; however these are commonly the only mesh forces considered. When misalignment is introduced forces develop in directions that are not described by the simple Spring-Friction mesh stiffness model; these are termed here as Off-Line-Of-Action (OLOA) forces, and can introduce other modes of vibration into the model.

Another limitation of the majority of academic models of gearbox vibration is that the transmission path from the gear contact point to the points of interest within the transmission system is described by a much reduced system of equation. The descriptions of transmission components such as the shafts and bearings are also heavily simplified to linear independent springs; this means that there is no interconnection between the various modes of vibration. The mesh stiffness is however usually time-varying and nonlinear to describe the variations in the number of teeth in contact. In industrial models it is common to increase the detail of the surrounding structure through the use of FE models; however to reduce computational costs the gear contact is taken as a linear value so that eigenvalue extraction and steady state analysis can be performed. This work increases the complexity of the academic model to introduce coupling of the various modes of vibration but

also allows for transient responses of the system due to the nonlinear time-varying nature of the gear contact representation.

1.1 Objectives

The main objective of this project is to add to the fundamental knowledge base in the field of gearbox vibration through the use of mathematical modelling applied to misaligned gear pairs. The following work is undertaken in this thesis to reach this objective.

Development of gear CAD program

As a tool for the research project a program is developed capable of producing two-dimensional and three-dimensional gears directly in the FE package ABAQUS. This will reduce the data loss experienced when transferring geometry models between Computer Aided Design (CAD) packages and the FE package, where the geometry is meshed. This will subsequently improve the accuracy of the gear involute profile and obtained results.

Finite Element Analysis

Full 3D FEA of gear contact is performed, using a highly refined mesh in the contact zone to capture the local Hertzian deformation, with outputs including TE/mesh stiffness, LSR and reaction forces at the gear centre, which till this point have not readily been investigated.

A major contribution of this work to the understanding of gear vibrations is the investigation into the static effects of misalignment on gear contact, including a detailed study on the effects of four misalignment types under various loading cases. Until now the FE investigation of misalignments has received limited attention and when present has focused mainly on the determination of gear strength. This project aims to investigate its effect on the dynamic response of the gears through the use of the static FEM coupled to a simplified numerical model.

Development of a Finite Element based dynamic gearbox model

In the majority of dynamic gearbox models previously presented, many simplifications are made for the various gearbox components. Mainly the supporting structure, bearings and shafts are represented as a set of linear springs operating in a single direction alone. This project aims to develop a new dynamic model based on finite element representations of many of the system components, which includes non-linearity of the bearings and Model-Order-Reduction (MOR) techniques applied to the supporting structure. This allows interconnection between the various modes of vibration, and a more complex representation of the transmission path.

Inclusion of friction to the FE based dynamic model

A method for the inclusion of the time-varying nonlinear frictional forces and moments developed during the dynamic response is given. This is the first time that the inclusion of friction to a model of this type has been presented.

The friction model is also expanded to include the effects of axial sliding and hence the effects of axial friction, which till this point has not been seen in any published work.

Inclusion of misalignment forces to the FE based dynamic model

A major contribution of this thesis in the field of gearbox dynamics is the investigation of the dynamic effects of lateral misalignments, such as axial misalignment and centre distance variation. Misalignments are incorporated into the dynamic model through theoretical relationship corroborated with the FEM.

Comparison between simulated and experimental results

No experimental results have been found in the literature with regard to the dynamic response of a gear pair system under controlled misalignment. This project is the first to present this information and compare it against theoretical results.

1.2 Thesis Structure

Chapter 1 - Introduction

Chapter 2 - Literature Review

In Chapter 2 a review of the available literature is undertaken; this is used to give the reader a brief overview of the work performed in the modelling of gear vibrations, touching on both the various dynamic models and the FEA of gear contact. Examples of more in depth reviews are provided for further reading.

Where appropriate the focus of the literature review is aimed at work performed with respect to gear misalignment. In subsequent chapters describing the formulation of the dynamic vibration model, aspects of the literature review are reiterated to validate the modelling assumptions.

Chapter 3 - Finite Element Analysis: Modelling Procedure

In Chapter 3 the process of finite element analysis (FEA) is described; this begins with the formulation of a program capable of producing the complex involute gear tooth profile, which can be directly imported into the FEA package ABAQUS. Next the modelling approach used in determining the gear contact parameters in 3D is described, including material property definitions, boundary conditions, contact formulation and the calculation of the output parameters.

Chapter 4 - Finite Element Analysis: Results

In Chapter 4 results are presented from the simulations of Chapter 3, describing the Transmission Error (TE), Load Sharing Ratio (LSR) and reaction forces and moments (RFi, RMi) under perfect alignment and various loading conditions.

The final section of Chapter 4 investigates the effects of misalignments on the TE, LSR and RFi/RMi. Results are analysed under various misalignment values and loads and compared to theoretical approximations where applicable.

Chapter 5 - Cranfield Test Rig

Before the development of the mathematical model of the experimental gear rig, a description of the physical rig is given. This comprises of a brief overview of the main components along with the instrumentation installed and the outputs generated. No results are given in this section, as these a reserved for comparison with theoretical results in subsequent chapters. The development and design procedure for the rig are also omitted as they were not performed by the author.

Chapter 6 - Development of a Hybrid Dynamic Model

Chapter 6 looks to break down the modelling approach into the component parts of the physical system. Initially a FE representation of the shaft as a Timoshenko beam is presented, and from here the ancillary rig components described in Chapter 5 are included as FE simplifications. Some FE work is presented in this chapter to describe the calculation of the stiffness' of the in-house built components through a technique known as Component Mode Synthesis (CMS) or Model Order Reduction (MOR).

Also described in the latter parts of the chapter is the inclusion of the gear contact excitations, such as the normal tooth contact, friction and lateral gear misalignments.

Chapter 7 - Results: Parametric Study

Results in Chapter 7 are exclusively devoted to the outputs of the dynamic model developed in Chapter 6, where at various stages of model development the system parameters are varied to determine their effects.

Initially the model is constrained to allow only rotation of the shaft, and throughout the chapter the model becomes increasingly more complex with the addition of lateral motion, normal sliding friction, axial friction and misalignment.

Chapter 8 - Results: Experimental

In Chapter 8 simulated time and frequency domain results are compared against experimental results to determine appropriate system parameters and to corroborate phenomena seen in the simulated results. Trends in the system responses as a result of lateral misalignment are also investigated and compared against the trends seen in the latter parts of Chapter 7.

Chapter 9 - Conclusions.

This chapter describes the conclusions gained from the research and indicates further research required in the field to increase the knowledge base of vibration under misalignment.

Chapter 2

Literature Review

Scientific concern about gears and the loads they could transmit was a topic of much interest in the early part of the 20th century, with work on gear dynamics really beginning in the 1920's and early 1930's. Much of the early work was interested in the phenomena of the dynamic effect, where loads on the gear teeth increased with rising speed [8]. This was observed as a reduction in the life of the gears under high speed operating conditions. Research into the modelling of gears is ongoing and has found interest in sectors such as automotive and aerospace, where high power-to-weight-ratio gearboxes are highly desirable. There is extra concern in the aerospace industry, where the modelling of gears has focused on the health of the gear train, since these are safety critical components.

2.1 Reviews in Gear Dynamics

One of the most notable reviews in the field of gear vibration modelling was performed by Özgüven and Houser [4] and, although published in 1988, is still used as the starting point for investigation into the dynamics of gears by many authors. Reviewing the numerous gear models developed in the three decades prior to publishing, the paper divides the models into the five categories given below, although it is also stated that some models can be placed within a number of these categories.

1. Simple Dynamic Factor Models: Used to determine gear root stress formulae via empirical, semi-empirical methods and dynamic models for determination of the dynamic factor, which is a factor applied to the static load to determine the strength and life of gears under operating loads.

2. Models with Flexible Teeth: Flexibility of gear body, shafts, bearings are neglected and the tooth stiffness is considered as the only energy store, which usually reduces to a Single Degree of Freedom (SDOF) mass-spring model. These models can be further developed to determine the dynamic factor.

3. Models for Gear Dynamics: These include other stiffness elements, such as the shafts. In particular the torsional flexibility of shafts is found to be important along with the transverse flexibility of the bearings. Traditionally tooth compliance contribution is introduced through the time varying mesh stiffness.

4. Models for Gear Rotor Dynamics: Transverse shaft vibrations are specified in two perpendicular directions, which allows the shaft to whirl (shaft centre circulates within the bearing at half rotation speed [9]). Torsional vibration is usually considered and, as with gear dynamic models, include vibrations due to teeth flexibility through time varying mesh stiffness's.

5. Models for Torsional Vibrations: Flexibility of the gear teeth is neglected and the torsional model is obtained through the use of flexible shafts connected to rigid gears.

Many models within this review, and other literature, which appear to be vastly different from each other, are said to be in agreement with experimental data. Özgüven and Houser [4] claim the reason for this is due to the determination of the experimental set up. For example, short shafts can be assumed transversely stiff, whereas the same cannot be said for long, slender shafts. Furthermore the results are also dependent on the desired outcome of the modelling, for example the tooth stresses, might only require the lower modes of vibration, whereas noise analysis may

also require higher order modes. Therefore the model is specific to the experimental situation and the required outcome.

In a later report by Kahraman and Singh [10] a broader categorisation was proposed which split the models into four categories, which were:

1. Linear Time Invariant (LTI) - These models do not account for nonlinearities such as friction or clearance type nonlinearity, and the mesh stiffness is approximated as the average stiffness over the mesh cycle.

2. Linear Time Varying (LTV) - Like LTI models LTV models do not account for nonlinearities; however the mesh stiffness varies through mesh cycle due to changing numbers of teeth in mesh.

3. Non-Linear Time Invariant (NLTI) - In NLTI models the mesh stiffness is assumed constant, however one or more nonlinearities may be introduced.

4. Non-Linear Time Varying (NLTV) - NLTV models include the combined effects of varying system stiffness's, due to changes in the number of teeth in contact, with nonlinearities associated with friction or backlash/clearance.

The models included in the report by Özgüven and Houser [4] generally fall into the first two categories; it is only within the last decade or two that the non-linear problems have started to be solved, which is largely attributable to the availability of computers capable of fast numerical mathematics.

A review of the work undertaken in the field of non-linear gear dynamic modelling was undertaken by Wang *et al* [5] in 2003. This is the most up-to-date and comprehensive review of gear dynamics found and covers work performed on the time-varying stiffness parameters for single-mesh gears, where the effects of tooth profile modification, involute contact ratio (ICR) and tooth friction on the dynamics of the gear pair are considered. Furthermore, this paper reviews work performed on multi-mesh systems, systems with backlash and vibro-impact, and gear systems with multiple nonlinearities, such as time-varying stiffness and backlash. This review concludes that further work is required on the modelling of systems with multiple

clearances, multiple nonlinearities (friction and backlash), high speeds and improved design characteristics through the understanding and inclusion of nonlinearities. This paper however neglects to indicate the relationship between nonlinearities and defects in gears, an area which is only sparsely covered in the literature and is of great interest in many industries.

2.2 Analytical Gear Model

To gain a perspective of the issues behind the mathematical modelling of gear dynamics a simple SDOF model is described, based on the model developed by Kahraman and Singh [10], which is found in many of the available literature [11–13] and is shown below in Figure 2.1.

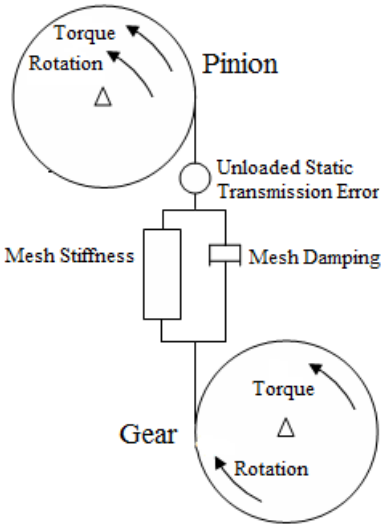

Figure 2.1: SDOF non-linear model of spur gear pair developed by Kahraman and Singh [10]

Figure 2.1 consists of two rigid disks fixed at their centres representing the gear bodies and their inertias, which are constrained to allow only rotational motion. Presently the two rotational DOF of the gears are coupled via the mesh stiffness acting along the line of action (LOA), resulting in a SDOF system. As the gear moves through a single contact cycle the number of teeth in contact changes and the mesh stiffness value becomes a function of time, which parametrically excites the system. This can also be said for the mesh damping; however, it has been shown

by Kahraman and Singh [10] that the influence on the system response by the time-varying damping is much less than that of the time-varying stiffness and because of this the majority of papers incorporate the mean component of mesh damping. The final parameter acting along the LOA is the unloaded Static Transmission Error (uSTE), which is modelled as a time-varying linear displacement excitation to include the effects of profile modifications/errors and certain wear schemes (scuffing, pitting and spalling) that cause a deviation from conjugate action.

This simple SDOF model has been used in many investigations to model the effects of various contact phenomena such as the inclusion of backlash through clearance type nonlinearity [14–18]. This is achieved by applying a clearance function to the mesh stiffness causing it to be positive, negative or zero depending on the clearance state of the gear teeth. These three values relate to normal contact, contact on the reverse gear faces and no tooth contact respectively. It has been found that the inclusion of clearance type nonlinearities evokes a number of response phenomena including jump discontinuities in the forced response curves and possible chaotic motions [17]; however, contact loss of this kind is usually only experienced in lightly loaded gears running near their resonant frequencies or resting on highly flexible supports, where large motions of the gears are found.

Vaishya and Singh [19–21] have also used this simple dynamic model to investigate the modeling techniques and effects of friction on the rotational response of the system, where the frictional force acts in a direction perpendicular to the LOA and generates moments based on the position of the contact point along the LOA. In these papers it was concluded that even in a torsional (SDOF) system friction, along with the methodologies used to incorporate it, has a significant effect on the dynamic response, and that increased work was required to generate a more complete friction formulation based on the complex load sharing characteristic between teeth and the inclusion of backlash. The final recommendation for further work was to include the effects of friction into a higher DOF model to study the effects of friction on the lateral vibrations; further discussion on the use of friction in dynamic models will be given later.

Faggionin *et al* [22] used the SDOF model with backlash nonlinearity in the optimisation of a spur gear pair through modification of the tooth tip and root profile shape, where the mesh stiffness and profile deviations shown in Figure 2.1 are obtained through a constantly updated finite element model of the gear pair. From this investigation it was concluded that the optimization technique coupled with the SDOF model gave reasonable results with respect to the Root Mean Squared transmission error obtained through experimental testing.

Tamminana *et al* [13] used the SDOF model with backlash to define a relationship between the dynamic gear deformation and dynamic factors, whilst verifying the development of a new hybrid finite element model of the gear contact, which divides the gear into two regions, the near-field region and the far-field region. The near-field region models the contact deformations using a semi analytical approach, removing the need for a highly refined mesh in the contact zone and reducing the required computational cost of modelling contact; whereas the far-field region uses traditional finite elements to model the deformation of the gears since a much coarser FE mesh is required to accurately model these areas. The results show that the semi-finite element model is more capable of representing the RMS dynamic transmission error when compared to experimental results. This is most likely due to removing the assumption that the mesh stiffness in Figure 2.1 is based on quasi-static simulations.

Finally the SDOF model has also found use in determining the torsional response of a geared system under faults in the contact stiffness due to gear breakage [23], where to account for a tooth breakage the mesh stiffness is set to zero, representing a complete tooth loss. Litak and Friswell [23] also included a nonlinear stiffness function to account for backlash, and found that one broken tooth had little influence on the dynamic response of the system; however the crude nature of the inclusion of tooth defects and the simple model suggest caution should be taken over the results.

One of the major problems with the SDOF model is that it is unable to transmit lateral forces as a result of gear contact and therefore the effects of lateral

gear motion can not be studied. Kahraman and Singh [24] addressed this by increasing the system DOF to 4 by attaching springs to the gear centres aligned with the LOA, which accounted for the flexibilities in the bearings and shaft and allowed the study of the lateral gear deflection and dynamic response of the system. The gear support spring is aligned along the LOA since the only force emanating from the gear contact is along the LOA, however if the line of action is allowed to move or other forces exist that do not act along the LOA, further compliances must be included into the model. Figures 2.2(a) and 2.2(b) show the 4 DOF model proposed by Kahraman and Singh [24] and a 6 DOF model, which allows forces to be generated within the gear contact that are not aligned with the LOA. Figure 2.2(b) also allows the modelling of shaft whirl, where the shafts and gears move in the plane of the gears.

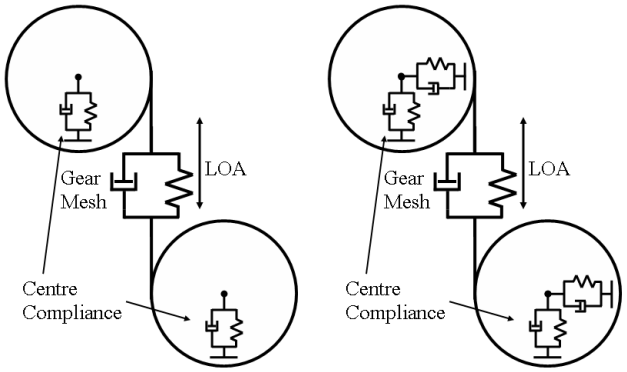

(a) 4 DOF model (b) 6 DOF model

Figure 2.2: Mathematical gear models with centre movement

Skrickij and Bogdevičius [25] used a 6 DOF model to investigate various analytical methods of determining the mesh stiffness and the effects of instantaneous variations in the centre distance on the gear dynamics. These phenomena were also investigated by Kim *et al* [26] using a similar 6 DOF model to allow lateral motion of the gear centres, which caused variation in the pressure/contact angle and contact ratio of the gear pair. However while Skrickij and Bogdevičius [25] included clearance nonlinearities within the gear mesh, Kim *et al* [26] did not, which was deemed acceptable from the conclusions of Skrickij and Bogdevičius, who stated that

under steady conditions the effects of backlash were negligible. Both investigations concluded that the effects of centre distance variation on the mesh stiffness and dynamic response of the system were non-negligible, however they were dependent on the stiffness of the supporting structures and consequently the degree of gear motion.

The effects of dynamic backlash and their effects on gear dynamics have been tackled by Siyu *et al* [27], who used the 6 DOF model to combine the effects of friction and backlash. In this model the normal tooth forces and backlash act in the vertical direction while friction acts along the horizontal direction; however although gear motion is seen in both these directions the effects of centre distance on the pressure angle, contact ratio and mesh stiffness are not included in the analysis and the normal tooth forces remain aligned with the vertical bearing stiffness throughout simulation. This means that regardless of the movement of the gears the normal forces always act vertically and frictional forces act horizontally.

With friction acting perpendicularly to the normal tooth forces it is necessary when considering the lateral gear motions to use a model, which is capable of deformation in both forcing directions. Along with the work performed by Siyu *et al* [27], investigations into the effects of friction on the dynamic response of a geared system have been carried out by He *et al* [28, 29] and Liu and Parker [30]. He *et al* [28] investigated the combined effects of time varying mesh stiffness and friction, concluding that sliding friction increased the magnitude of the second harmonic of the gear contact and was a large source of vibration during contact. In this model He *et al* used a square wave approximation of the coefficient of friction based on the sliding direction of the teeth surfaces, while in a later paper He *et al* [29] investigated other possible friction formulations. In this investigation it was found that the sharp variation in the friction coefficient as a result of the changing sliding direction at the pitch point, under the square wave approximation, did not compare well with experimental results where there was a softening at the pitch point.

Although these increased DOF models are able to model the coupled lateral-torsional vibration that occurs during gear contact, they are unable to accurately

model the transmission of the vibration throughout the structure, since the structural compliances are lumped at the gear centre. In many practical gearing applications it is undesirable or impossible to position vibration sensors at the gear centres and therefore the vibratory response of these simplified systems are unable to successfully model the vibration path to virtual accelerometers placed in more appropriate positions on the gearbox structure. To achieve a more realistic expression of the transmission path the individual component compliances can be split [31–34].

In a paper by Howard *et al* [31] a 16 DOF model was developed, as shown in Figure 2.3, which included the rotational motions of the motor, load and the two gears, and the vertical and horizontal motions of the bearings and gears. Due to the alignment of the gears the vertical motions are completely described by the normal tooth loads, while the horizontal motions are attributed to the frictional forces; where this alignment is specified to simplify the system equations of motion. The paper used the model to investigate the combined effects of friction and gear cracking using the condition indicator kurtosis and concluded that friction had a negligible effect on the kurtosis value in most cases.

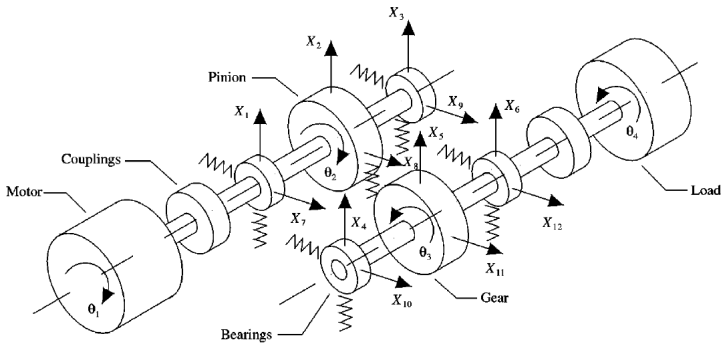

Figure 2.3: 16 DOF gearbox model proposed by Howard *et al* [31]

This model was expanded by the same researchers to determine the response of two meshing gear pairs in a 26 DOF model based on the same assumptions of Figure 2.3 [32]. In the original investigation of the 16 DOF model it was noted that previous investigations by other researchers had shown that the dynamic response of

the system can be dominated by profile errors. This was investigated further in the 26 DOF model and concluded that for the gear pair studied, pitch and profile errors of 10 microns had a great effect on the system response, which caused difficulties in detecting a tooth crack of 5 mm.

The 16 DOF model was also used by Sawalhi and Randall [33, 34] to model the interaction between the vibrations emanating from gear contact and those from the bearings. In this investigation the model was expanded to 34 DOF, where the majority of the additional 18 DOF came from a new 5 DOF bearing model (12 DOF) and the rotational motion of the bearings (4 DOF) and optical encoders positioned at the free ends of the shafts (2 DOF). The complex bearing model, which accounts for slippage, Hertzian contact between the bearing internals and the time varying stiffness through the number of internal elements in contact, was used to introduce faults in the various bearing components, where the dynamic response of the system was found to compare well with experimental studies.

In all the above lumped parameter models the system components are described by stiffnesses and point masses acting along the LOA and perpendicular to it, and with the exception of the bearing model proposed by Sawalhi and Randall [33, 34] these motions are completely uncoupled, where usually the LOA motions are due to normal tooth contact and the horizontal motions are due to friction. The gear mesh forces represented by the lumped parameter models act in only three directions. This was challenged by Blankenship and Singh [35], who stated that these models were inadequate when modelling forces and motions due to system misalignments and changes to the instantaneous contact plane, where additional forces were generated. In their paper Blankenship and Singh develop a true gear mesh interface for internal and external spur and helical gears based on their instantaneous positions, where the load distribution and forces generated in the gear mesh are achieved by discretizing the facewidth into a number of stiffness elements and balancing the external and internal forces. The resulting models only included the gears and paid little attention to the system components shown in Figure 2.3 and the application of the model under various conditions.

A similar model was devised by Velex and Maatar [36], which was expanded to include the lateral and angular motions of the gear centres for the purpose of studying the effects of mounting error and tooth profile errors. In this model the compliance of the supporting structure was modelled as a set of 6 uncoupled linear stiffnesses at the gear centre, meaning the various coupled forces in the gear mesh were uncoupled in the motions of the gear centres. This was later addressed to some extent in a paper by Velex and Cahouet [37] studying the effects of friction on the system dynamics, where the shaft was modelled as a finite element beam with coupled compliances; however the bearings were still treated as linear independent spring stiffnesses. Conclusions from this work are that friction can generate significant time varying excitations due to the reversal of the sliding direction at the pitch point, however the effects of sliding friction diminish with increased rotational speed.

A similar mesh interface technique has been employed by Eritenel and Parker [38], where the model was expanded to include the compliance of the shaft and bearings to study the effects of partial contact loss across the facewidth. Through discretization of the tooth face the compliance of the teeth can be assumed through two spring stiffnesses, one representing the translational motions and one the tilting motions, which are nonlinear depending on the contacting conditions at the tooth face. They concluded that when the centre of contact is not aligned with the centre of the tooth width the tilting motion of the gears introduces a new mode of vibration, which is not incorporated in the simple single spring models illustrated in Figures 2.1, 2.2(a) and 2.2(b).

2.3 Transmission Error and Mesh Stiffness

In the majority of the models proposed above, the system is internally and externally excited to obtain a dynamic response that can be analysed. Within these models it is widely accepted that Transmission Error (TE) is a primary source of internal excitation within gears, with TE described as the difference between the position that the output shaft of a gear drive would have if the gearbox were perfectly

formed and perfectly rigid; and the actual position of the output shaft [12, 39, 40]. More concisely, Sweeney and Randall [39] state that:

> *Transmission Error is the deviation of the relative angular position of two gear shafts from the position determined by the gear ratio and perfectly conjugate mesh action.*

One of the biggest steps in gear modelling was taken by Harris in 1958 [41] who illustrated the importance of TE in the dynamic response of geared systems. In his modelling he included excitation from tooth profile modifications, variation in tooth stiffness and the non-linearity in the stiffness from loss of contact. One of the everlasting contributions of Harris work was the conclusion that the behaviour of gears at low speed can be depicted as a set of Static TE curves; later to be called Harris maps. An illustration of a standard Harris map is given below in Figure 2.4.

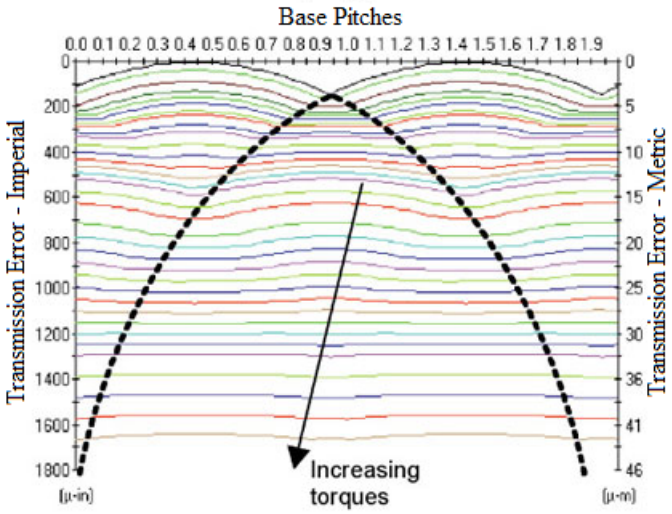

Figure 2.4: Harris map - taken from http://www.gearsolutions.com [accessed 13/09/2010]

In Figure 2.4 each curve represents the STE at a specific load, with variations of the STE indicating the point at which double tooth contact occurs. This curve also shows the usefulness of the Harris map in the design of gears with the intent of reducing gear noise and vibration. By minimizing the STE at the design load the gear vibration can be minimized, this is achieved through ensuring a constant

contact ratio, and therefore mesh stiffness, at that load through profile modification.

Many papers have developed algorithms with the intent of reducing gear noise through the reduction of STE, one such paper is that by Tavakoli and Houser [42], who were able to use an optimization algorithm to reduce the Fourier spectrum of the STE through tip and root relief. It was shown however, that deviations from the design torque result in a sharp increase in the transmission error.

Transmission error can occur from a variety of sources, where Shigley and Mischke [8] list a number of these including, inaccuracies in the profile shape, tooth stiffness variation, dynamic unbalance of rotating members, wear of contacting areas, misalignment and deflection of shaft, and tooth friction. The majority of these factors will be discussed at a later point, however it is observed in a number of papers that gear deflection is a major contributing factor to TE and thus it is discussed here.

Gear flexibility is often determined as the sum of the flexibilities from three sources [12, 40, 43], which are gear tooth bending as a cantilever beam, local Hertzian deformation and gear body flexibility. It is also noticed that as a gear pair moves through a meshing cycle the mesh stiffness changes due to the number of teeth in contact [13], which results in a change in the tooth deflection and in the angular position of the driven gear (TE). As shown in Figure 2.1 the transmission error is often incorporated into the model through two sources, the time varying mesh stiffness and a linear displacement along the LOA. The mesh stiffness alters the system in two approaches; firstly the natural frequency of the system can be altered and secondly the mesh is parametrically excited through changes in deflections due to variations in the stiffness value. The uSTE affects the system via a linear displacement through the mesh, and includes the contribution of profile errors which are load independent.

2.3.1 Transmission Error Calculation

TE is an important consideration in the modelling and can be found through a number of methods such as energy methods, flexibility matrices, linear finite ele-

ment methods and nonlinear finite elements. These calculations of TE can be split into two categories; the first is by analytical means, such as energy methods and through component flexibilities, and the second is through numerical techniques such as the finite element method.

Analytical Methods

Many analytical methods for determining the TE have been developed and the majority of the earlier methods have already been extensively reviewed by Özgüven and Houser [4]. It can be seen that the analytical models are based around the aforementioned assumption that the flexibility of a pair of gears in contact comprises the gear body flexibility, the tooth bending as a beam and the local contact deformation. This is illustrated by Conry and Seireg [44] who modelled the total elastic deformations as the combination of the local tooth deformation as two infinitely long contacting cylinders and tooth bending as a cantilever beam. This method assumed that the gear bodies behaved as simply supported solid cylinders for the purpose of calculating the deformation at the gear tooth root, and from this the deformations along the line of action were calculated. The total deflection/separation was then calculated as the sum of the tooth bending for both gears and the local deformation which applies to both. This resulted in an illustrated TE that was close to sinusoidal, however the formulation appeared to only consist of a single gear tooth in contact and when multiple teeth were in mesh the deflection was altered through influence coefficients.

In 1985 a method of determining TE from was proposed by Yang and Sun [45] who approximated the single tooth flexibility exclusively as the unit width Hertzian deflection. This omitted an important source of deflection in the tooth bending, which was tackled by Yang and Lin [46] in 1987 through the potential energy stored in the meshing gear system. In this method the contacting force was decomposed into two perpendicular components to represent tooth bending and the axial compression. This resulted in stiffness equations for the components $1/k_{bendg1}$, $1/k_{bendg2}$, $1/k_{axialg1}$ and $1/k_{axialg2}$, which are given in ref [46].

This was later expanded by Tian [47] to include the effects of shear energy. From this method the individual TE components were found and combined in series to determine the TE for a single tooth in contact. For double tooth contact the TE was found by doubling the single tooth TE, as performed by Yang and Sun [45].

An alternate method for the determination of the unit width tooth bending deflection was given by Kuang and Yang [48] for a single tooth in contact. This was given as a function of the radial loading position and involved many coefficients, which were determined through a curve fitting procedure as a cubic polynomial function of the number of teeth.

This technique was referenced in the 2003 review by Parey and Tandon [11] and used in 2006 by Parey *et al* [12] to investigate defective gears and different signal processing techniques.

Tavakoli and Houser [42] determined the TE from the compliances due to beam deflection (from transverse load, shear and moments), Hertzian contact and rigid body tooth rotation at the base. Formulations were given in both plane strain and stress, and TE calculations were performed in conjunction with tooth contact analysis at predefined rotation positions to determine the load conditions for the stiffness to be measured. This method was also used by Kahraman and Singh [10] in 1991 while investigating the effect of backlash type non-linearities on the system response.

It was stated by Shigley and Mischke [8] that another contributing factor to TE was friction and in the previous analytical models determining TE this has been ignored. This was tackled in 2009 by Liu and Parker [30] who investigated the effect of friction on tooth bending and found that the inclusion of the friction bending effect (caused by the friction moment) altered the deflection by 25-30% compared to the frictionless case. Liu and Parker stated that through experimental work [37, 49, 50] there is no need for separate static and dynamic terms and hence a single term for friction can be used; commonly taken between 0.03-0.1. Although it is established that 0.1 is often too high for well lubricated systems [30] many papers continue to use this value, which is also the case with Liu and Parker and hence this

could give figures for the effect of friction which are overestimated.

Rather than modelling TE through mesh stiffness Özgüven and Houser [51] deduce the loaded static transmission error (LSTE) from the equations of motion neglecting the dynamic terms. This linear displacement along the line of contact is then used as the parametric forcing of the equations of motion with time invariant average mesh stiffness. In comparing the dynamic factors calculated through this model with a time varying system, experimental data and other analytical models, they concluded that the displacement excitation from variable mesh stiffness was more important than the change in the systems natural frequency due to varying mesh stiffness. It can be argued, as it is in Özgüven and Houser [4], that although single degree of freedom models may be sufficient for determining tooth loads and root stresses, as used in determining the dynamic factor, they may be insufficient in modelling the system vibrations, and it is not clear whether this conclusion will hold true when investigating the vibration at the bearings.

This technique appears to be a simpler approach to the time varying mesh stiffness problem; however it was stated that it may not work, and could be dependent on the system parameters [10], such that Özgüven recommended further investigation on the subject [52]. This however has not stopped the LSTE technique being used in many recent publications [53, 54] with Kubur *et al* [55] stating that using the LSTE with an average mesh stiffness was an acceptable method of modelling internal excitations in helical gear systems. It is not believed that this is necessarily true since LSTE is usually determined under quasi-static conditions and hence by ignoring the differences between the gear deflections under instantaneous loads and those under quasi-static conditions, with varying stiffness', the linear excitations produced through the LSTE will not truly define these variations in responses.

Numerical Techniques

The next set of methods looks at the work performed in numerical simulation of the mesh stiffness, mainly through the Finite Element Analysis of gears in contact. This has recently evolved in the field of gear dynamics due to the increase

in computational power available to researchers. In the past the accurate analysis of the contact area could not be modelled due to the fine mesh and subsequent number of calculations required, which prohibited the use of this powerful method. In 1982 Coy and Chao[56] investigated Hertzian contact in gears using 8-node quadrilateral plane strain elements and point loads, and found that Hertzian deflection accounted for around 25% of the total deformation. A similar method using 8-node quadrilateral plane stress elements and point loads was conducted by Muthukumar and Raghavan [57] on a single tooth model with loading at the tip, pitch point and mid point. In the finite element model the deflection was taken from the loaded node and was in agreement with experimental studies on the loading. Later this approach was also applied by Du *et al* [43] and Bettaïeb *et al* [58], where deflections were taken from the centre of the gear tooth to omit deflection due to Hertzian contact. Finally Chaari *et al* [59] used the linear finite element method to determine the transmission error and mesh stiffness of a spur gear tooth including a crack to coroborate analytical mesh stiffness calculations based on deflections of the tooth as a beam with flexible foundations and contact deformation. However due to the lack of load sharing between adjacent teeth the stiffness computed did not capture the complex effects of tooth cracking on the stiffness.

Although the above investigations approximate contact in a linear sense, through applying point loads to contact points to investigate the transmission error, it is more common to utilize this method to study the stress distributions in gear teeth for the purpose of gear strength calculation [60–63]. The problem with this methodology is the need for the calculation of the contact points before simulation, and still this assumes that the load applied is small and the contact positions are based solely on the kinematics of gear contact and not the deflections of the gear tooth.

A advancement of the linear finite element method has been to introduce non-linearity at the gear contact through the use of contact, or gap, elements. This technique involves inserting a nonlinear spring between nodes on contacting surfaces, such that the spring stiffness is zero until the clearance between the two nodes is

zero; at which point the spring is able to transfer loads between the two bodies.

This technique has been used by many authors including Du *et al* [43] and Wang and Howard [64, 65]; who used it to compute quasi-static TE, along with the load sharing ratio (LSR) and tooth stresses, by computing the difference in angular position of a point on the driven gear to its theoretical ideal position, which was then used in Equation 2.1 to calculate the rotational mesh stiffness.

$$k_m(t) = T/TE(t) \tag{2.1}$$

Where $k_m(t)$ is the time varying mesh stiffness, T is the applied torque and $TE(t)$ is the calculated transmission error.

Wang and Howard also used this method to calculate the inherent TE and stress errors in 2D analyses compared to 3D analysis for a number of different facewidths [66]. They found that errors are inherently present in 2D analyses; however when considering gears with small facewidths a plane stress (zero through thickness stress) approach is more appropriate, and likewise plain strain (zero through thickness strain) is more suited to wide face gears.

Mao [67–69] dismissed the use of contact elements due to the need for assumed contact positions prior to analysis and the inability for them to model the substantial sliding present in gear contact. Instead Mao used a pure master-slave contact algorithm, which requires no prior knowledge of the contact positions and allows contact points to move arbitrarily during contact; this was applied by Mao to model the transmission error of helical gears with various profile modification [68], the contact pressures on teeth under micro geometry modification [67] and the von Mises stresses of polymer gears for the purpose of wear predictions [69].

In many papers this contact algorithm, or variants of it, have been used to model the stresses generated in gears at the contact points or at the root of the gear tooth either through two [70] or three-dimensional analysis [71–75]. Pedrero *et al* [76] also utilized the master-slave contact procedure to analyse the load sharing properties of external involute gears and compared the results to theoretical LSR

based on the inverse of the elastic potential energy of a pair of unit width involute teeth under unit load.

Apart from the work by Mao [68], this contact approach has found little use in the calculation of the transmission error and mesh stiffness. Tharmakulasingam *et al* [77] modelled 2D gears using plane strain conditions to optimize gear design through the reduction of the static transmission error using FEA. Wei [78] also used this method to model the bending stresses of two and three-dimensional gears and the transmission error of the complete gear using 4751 2D elements.

In many investigations performed at the Ohio State University [13, 28, 79–81] the TE is calculated from a hybrid deformable body model consisting of two regions; in the region far from the contact zone FE's were used to determine the deflections, whereas in the area around the contact zone a semi-analytical deformation model, based on the Bousinesq and Cerruti solutions, was used. This produced a more computationally efficient solution, since an extremely refined mesh was not required in the contact area. The Finite Element/Contact Mechanics (FE/CM) model was able to output LSTE, tooth forces and tooth deflections and from these outputs three methodologies were presented in the above literature for determining the mesh stiffness. He *et al* [28] used the tooth force and deflection outputs to determine the mesh stiffness in a similar fashion to the analytical approaches; Parker *et al* [80], and Ambarisha and Parker [81] computed the STE and determined the mesh stiffness through a linear form of Equation 2.1, while Tamminana *et al* [13] modified this equation by removing the effect of unloaded STE in the form

$$k_m(t) = \frac{T}{r_{b1}}\left[\frac{1}{(\mathrm{LSTE} - e)}\right] \tag{2.2}$$

Where k_m is now the lateral stiffness, r_{b1} is the base radius of gear 1 and e is the unloaded Static Transmission Error (uSTE).

In Equation (2.2), e is determined through the calculation of STE under the no load condition, which removes the effect of profile modifications from the determination of the mesh stiffness; an often overlooked factor in the numerical

calculation of mesh stiffness. The effect of profile modification is still included in the analytical model as a parametric excitation along the pressure line as shown in Figure 2.1.

Finally Li [82–84] developed a method of loaded tooth contact analysis (LTCA) through finite element analysis combined with a geometric face contact model to determine possible contact pairs. Through this method Li investigated the effects of profile modification, machining errors and misalignments on the contact and bending stresses in spur gears [82] along with their effects on the transmission error and LSR [83], and the effects of the addendum length on these parameters [84]. In the analysis of the TE and LSR under misalignment only the rotational misalignments of the contacting planes are considered where it is concluded that misalignments have little effect on the LSR and only the rotation that causes non-parallel contact of the contacting planes has any effect on the transmission error. These effects are limited to the magnitude of the TE and cause no variation in the phase of contact.

The two broad methodologies for determining the time-varying excitation parameter of mesh stiffness (analytical and numerical) have been discussed, and apart from a few papers that determine the transmission error purely from a geometric stand point [85–87], these two methodologies account for the majority of published literature.

Due to the vast number of DOF in the numerical approach it is clear that the analytical methodology has an advantage in the computational efficiency of the solution, however the accuracy of the analytical solution is determined by the need for accurate knowledge of the contact points and this in itself is a long process.

2.4 Friction

As gear teeth move through mesh there are two primary motions which occur; these are rolling and sliding of the teeth. With sliding of the contact point and normal force acting on the teeth friction will exist, and since the direction of sliding changes as the teeth move past the pitch point so will the friction force

direction. From the above statements two initial predictions can be made which are corroborated in the literature; these are that the effect of friction is primarily in a direction perpendicular to the pressure line, often called off-line-of-action (OLOA) force [20], and secondly that in the frequency domain friction has an effect on the second gear mesh harmonic of the gear dynamics [29].

A review of different friction formulations has been performed by Vaisyha and Singh [21] and He *et al* [29] with Vaishya and Singh stating that friction can be modelled in several different manners. These include, as an excitation, a time varying parameter, a nonlinear coupling agent or as a source of energy dissipation.

2.4.1 Normal Meshing Force

The two most common methods for determining the mesh force result from either the averaged quasi-static mesh force determined before the dynamic analysis [11, 19], or the dynamic force which can be derived from the dynamic TE [21, 28, 29]. These methodologies for determining the mesh force were investigated in a paper by Vaishya and Singh [19] in 2001 where the formulations for both methods were given as:

$$\text{Quasi-Static Friction: } F_f(t) = \mu_i N(t) \tag{2.3a}$$

$$\text{Dynamic Friction: } F_f(t) = \mu_i \left(k_m(t)\,\delta(t) + c\dot{\delta}(t) \right) \tag{2.3b}$$

Where F_f is the frictional force, μ is the coefficient of friction, N is the normal tooth load, δ is the dynamic transmission error and c is the damping coefficient.
In the quasi-static formulation the time varying mesh force was calculated from the square wave load sharing ratio, whereas in the dynamic formulation the dynamic TE terms can be expanded to include the translational and rotational gear displacements [29], and the unloaded STE (e) [28] in the form:

$$\delta(t) = [r_{b1}\theta_1(t) - r_{b2}\theta_2(t) + x_1(t) - x_2(t) - e(t)] \tag{2.3c}$$

$$\dot{\delta}(t) = \left[r_{b1}\dot{\theta}_1(t) - r_{b2}\dot{\theta}_2(t) + \dot{x}_1(t) - \dot{x}_2(t) - \dot{e}(t) \right] \tag{2.3d}$$

Where r_b are the gear base radii, θ are the rotational positions of the gears and x are the gear displacements along the line-of-action. In the above equation $\dot{}$ represents differentiation with respect to time.

While including the friction force into the governing equations it is of interest to see that the dynamic friction formulation causes the friction coefficient to appear in the homogeneous portion of the equation. This therefore causes the friction force to be modelled as a time-varying parameter, whereas the quasi-static friction formulation only appears in the forcing term and hence it is simply modelled as an external load.

2.4.2 Friction Coefficient Variation

Due to the complex lubricating problem which is present in gearing there are a number of formulations for the friction coefficient. This alteration in coefficient value is due to the two different lubrication regimes, elastohydrodynamic (EHD) and boundary layer lubrication, which are present when a gear is operated near its maximum load capacity and which may cause partial breakdown of the lubricant [21]. With EHD lubrication the friction coefficient is determined from many factors such as, surface velocity (V), normal load (N), rolling velocity (VR), dynamic viscosity (η_0), surface curvature (ρ) and fluid inlet temperature $Temp_L$ [21]. The simplest modelling approach is the Coulomb friction method where the friction coefficient is constant between the point of initial contact and the pitch point where it changes sign. This gives a periodic friction coefficient function in the shape of a square wave, and can be expressed as:

$$\mu\left(t\right) = \mu_0 \mathrm{sgn}\left(V_s\right) \tag{2.4a}$$

Where V_s is the sliding velocity and

$$\mathrm{sgn}\left(V_s\right) = \begin{cases} +1, & V_s > 0 \\ 0, & V_s = 0 \\ -1, & V_s < 0 \end{cases} \tag{2.4b}$$

In a paper by He *et al* [29] the effect of five different coefficient formulations

on the gear dynamics were investigated. Model I was taken as the simple Coulomb model while a second popular model, the Benedict and Kelley model [88], was taken as Model II; a model developed by Xu *et al* [89] was used as Model III, a smoothed Coulomb model was used as Model IV and a composite model was used as Model V. The different variations in the friction coefficient with time are shown below in Figure 2.5 for each model.

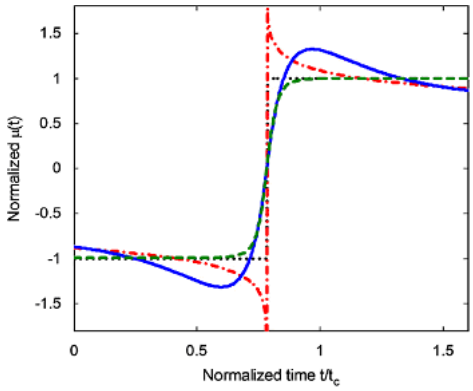

Figure 2.5: Friction Coefficients vs. time, '–' Model I, '–' Model II, '–' Model III, '–' Model IV. [29]

From Figure 2.5 it can be seen that Models I and II have a distinct discontinuity at the pitch point where there is an instantaneous change in direction of the friction force. In experiments [90] it was shown that there was actually smoothing in this region as shown in Models III and IV, especially under boundary layer lubrication conditions.

Model IV is taken as an alteration of the Coulomb model through the equation:

$$\mu\left(t\right) = \frac{2}{\pi}\mu_0 \tan^{-1}\left(\frac{V_s}{V_0}\right) \tag{2.5}$$

To arrive at Model IV, where V_0 is a reference velocity to normalize the sliding velocity and control the degree of nonlinearity at the pitch point; with lower values increasing the slope.

Model V, which is not shown, employs a system where, depending on the operational and tribological conditions, any of the Models (I-IV) can be used to determine the friction coefficient.

Another formulation for the friction coefficient given in the literature [20, 21] is developed from a model by Kelley and Lemanski [91] and is given below:

$$\mu = C_1 \frac{1}{1 - C_2 R_q} \log_{10} \left[\frac{C_3 w}{\eta_0 V_s V_R^2 \left(\rho_{g1} + \rho_{g2}\right)^2} \right] \tag{2.6}$$

Where C_1, C_2 and C_3 are empirical coefficients, w is the distributed load per unit length, R_q is the compound surface roughness, ρ is the surface curvature, η is the dynamic viscosity and V_R is the rolling velocity. This is similar when compared with the Benedict and Kelley equation given below as a function of roll angle (α).

$$\mu\left(\alpha\right) = 0.0127 C_R \log_{10} \left(\frac{3.17 \times 10^8 \mathrm{LSR}\left(\alpha\right) w}{\eta_0 V_s\left(\alpha\right) V_e^2\left(\alpha\right)} \right), \qquad C_R = \frac{44.5}{44.5 - R_q} \tag{2.7}$$

Where V_e is the entraining velocity, which is the addition of tangential velocities along the LOA.

In the models by Kelley and Lemanski [91], Benedict and Kelley [88], and Xu *et al* [89] coefficients exist that must be derived empirically. In the Coulomb models, once an average coefficient value is found the computation is relatively straight forward, however this is at the cost of some accuracy. In research referenced by Vaishya and Singh [20] its is shown that during a meshing cycle the variations in the magnitude of the friction coefficient have less effect than the change in sign when the tooth moves through the pitch point. This gives backing to Models I and IV however it may be seen that when the sliding velocity increases and boundary lubrication breaks down this may not be applicable.

2.4.3 Sliding Velocity

During the formulation of the friction coefficient the sliding velocity plays an important role in determining its sign and in some cases its magnitude. When the friction coefficient is an explicit function of time the analysis is inherently linear, however when dealing with instantaneous velocities to determine the friction coefficient it exhibits an implicit nonlinearity. In the formulation of friction coefficients from the Coulomb models, the friction coefficient can be determined explicitly

through the use of geometrically determined sliding velocities for varying gear angles or times; this will however ignore the instantaneous velocities associated with vibration. These can be included in the simple Coulomb model [20] as follows:

$$\mu\left(t,\dot{\theta}_{g1},\dot{\theta}_{g2}\right)=\operatorname{sgn}\left[\xi_{g2}\left(t\right)\left(\Omega_{g2}+\dot{\theta}_{g2}\left(t\right)\right)+\xi_{g1}\left(t\right)\left(\Omega_{g1}+\dot{\theta}_{g1}\left(t\right)\right)\right] \tag{2.8}$$

Where ξ is the position along the pressure line, Ω is the mean angular speed component of the gear and θ is the time varying angular rotation component.

2.4.4 Friction Damping

Vaishya and Singh [20] state that friction dissipates energy from the system and therefore can be included into the governing equations as a damping term. This is briefly mentioned in another paper by Vaishya and Singh [21] and is present in the papers by Velex and Cahouet [37] and Ambarisha and Parker [81]; however it appears that this is not explicitly mentioned in many papers.

2.5 Misalignments

One of the main aims of this research is to study the effects of instantaneous misalignment on the vibration in geared systems; however little literature has been found on the subject of tooth contact under misalignment and where it has been observed, the potential contact points have been determined from unloaded Tooth Contact Analysis (TCA). In some papers this has been the final output such as the work by Li and Chiou [86] who investigated gear tooth surface modification along the facewidth, changing the contact condition from a line load to a point load by varying the facewidth surface curvature. By changing to a point load it is suggested that misalignment errors will be reduced as there will be a reduction in edge contact. TE was determined using four main assumptions; these are that the gears are rigid, profile error is small (neglected), temperature and dynamic effects are ignored, assembly errors can be measured. Due to these assumptions the numerical analysis showed that under perfect alignment there was zero TE and there was no change in results when the centre distance was changed to incorporate error, or

when the vertical separation was increased. These results were not validated with experimental data and other experimental data has shown that with deformation the transmission error even in geometrically perfect gears with no assembly errors would not be zero. Also it is intuitive to see that by increasing the centre distance the contact ratio would be decreased and this would have an effect on TE if deformation of the gear was included. This is quoted in the paper by Davis *et al* [92] and shown in the paper by Du *et al* [43]. TE is seen when assembly errors are introduced in the z-direction and when rotated around the x and y axis. The results from this paper are interesting from a profile construction point of view but the TCA performed is over simplified and the results do not coincide well with reality.

A similar approach was used by Simon [87, 93–96] when investigated a number of different gear forms, where the main advancement of these papers was the ability to determine these points of contact under loading through determination of the line of minimum separation. These investigations concluded that misalignments worsen conjugate action, which results in higher contact pressures and increase the TE.

Velex and Maatar [36] combined the global phenomena of misalignments and eccentricities with the local errors of shape deviations into a single function for the calculation of the path of contact. The numerical solution method employed to determine the TE involved the iterative calculation of the path of contact and from this the mesh stiffness was calculated and the dynamic characteristics were found.

The only studies performed using the finite element method to investigate the effects of misalignment on gear contact parameters have been performed by Li [82, 83], which have been discussed previously, Ameen [62], who used distributed point loads to describe the non-uniform load distribution encountered under misalignment to determine the stresses in the contact zone and tooth root, and Mao [68], who used the master-slave contact algorithm to study the effects of micro-geometry and profile modification on the stress distribution in the contact zone. Of these three studies only one paper by Li [83] has studied the effects of misalignment on the contact parameters usually used in dynamic models of gear vibration, such as the TE and

LSR, where other papers have focused on the stresses on the loaded teeth, which are used for determining the load carrying capacity and lifing of the gears.

At present very little work has been performed on the static effects of misalignments using the finite element analysis and even less has been performed with regard to its effect on the transmission error, load sharing ratio and reaction forces generated under contact, which could be used in approximating contact in a dynamic gearbox model. Even though Blankenship and Singh were able to develop a gear mesh interface model based on the instantaneous positions of the gears in 1995 [35] and separate models were also subsequently developed by Velex and Maatar [36], Velex and Cahouet [37] and Eritenel and Parker [38] the dynamic effects of misalignments are also scarcely studied. The effects of linear misalignment on the instantaneous contact conditions through the mesh stiffness, frictional forces and backlash have only recently been studied in papers by Siyu *et al* [27], Kim *et al* [26] and Skrickij and Bogdevičius [25], which have been discussed previously and where the dynamic models contain only a few DOF and employ simplifications in the ancillary components.

From the available literature it is found that more work is required on the understanding of the effects of misalignment on the static contact between teeth, through the use of finite element analysis, with emphasis on the traditional components used to approximate contact in dynamic models, such as the mesh stiffness or transmission error and load sharing ratio. It is also evident that interest in the effects of the instantaneous misalignments on the dynamic response of the system is increasing; however as yet the dynamic models are extremely simple and only model the lateral motions of the gear bodies rather than the transmission of the vibration through the gearing structure, which is a possible area of further investigation.

Chapter 3

Finite Element Analysis: Modelling Procedure

In geared systems, a major source of vibration emanates from the gear contact, either through varying deflection of the teeth, friction from sliding surfaces, tooth contact loss, or from other forces occurring as a result of misalignment. To study the various phenomena which occur at the gear contact, a highly accurate contact model is simulated using the Finite Element Method (FEM) to generate simplifications of the complex contact conditions.

This chapter introduces the static FEM applied to gear contact, which includes the development of the gear geometry, the assignment of material and contact properties, the loads and boundary conditions, and the method of applying misalignments to the gear pair.

3.1 Gear Geometry Generation

A major requirement for geared systems is that for a constant input speed, the output rotational velocity remains relatively constant, which is known as conjugate action. Conjugate action can be achieved through many tooth shape combinations, however the involute tooth profile has become widely adopted due to the relative simplicity of its manufacture and because both gear teeth use the same tooth profile shape.

For the analysis of gear pairs using the finite element method, accurate representation of the involute profile is required. This is achieved through the mathematical representation of the gear cutting process, where a straight rack is used to cut into a cylinder, to generate Cartesian coordinates as a function of the gear rotation angle. The representation can be split into 3 distinct regions: the tooth profile (involute), the fillet, and the bottom land, as shown in Figure 3.1. This section splits the generation of the gear profile into these three regions, and once complete combines them into a single tooth and radially copies them to form a complete gear, where the modification of the gear profile across the facewidth to include crowning is investigated.

The equations presented in this chapter have been combined with material and BC information into a simple to use GUI to allow the fast generation of Finite Element models in ABAQUS through its interpreted higher level python scripting capabilities, where example python scripts for crowned and uncrowned gears are given in Appendix A.

3.1.1 Mathematical equations of gear cutting

As previously mentioned an unmodified gear tooth comprises of 3 distinct regions: the involute profile, the root fillet and the bottom land. These distinct regions are obtained from equations given by Hefeng *et al* [97] and Salamoun and Suchy [98], which describe the gear cutting action, and hence the coordinates that follow the section form.

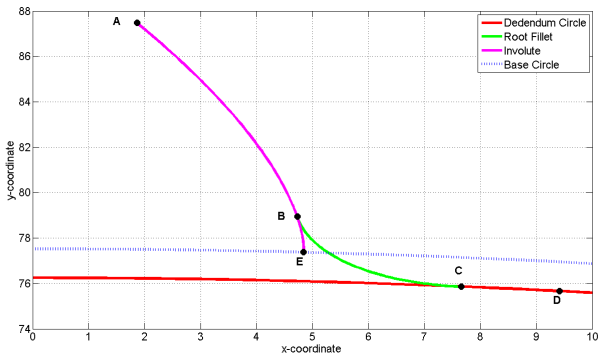

Figure 3.1: Construction of gear tooth from 3 distinct regions

Through these three portions a complete tooth flank can be generated, to which profile modifications, such as tip relief, can be added and a full gear created.

Bottom Land

The bottom land has a simple circular shape corresponding to the dedendum radius of the gear, and is formed through the flat portion of the gear cutter, such that the coordinates of a point lying on the bottom land can be determined from the gear angle (θ), as shown below.

$$x = (r - l_d\,(xi * m))\cos\theta \tag{3.1a}$$

$$y = (r - l_d\,(xi * m))\sin\theta \tag{3.1b}$$

Where r is the pitch radius, l_d is the gear dedendum length, xi is the addendum modification coefficient and m is the gear module.

Knowledge of the limits on θ, which correspond to the point of transition with the root fillet, shown as Point C in Figure 3.1, and the midpoint on the bottom land (Point D) are required to generate this portion of the tooth flank. Point C is found using the local fillet angle (ψ) discussed later, by stating that the local fillet angle is 90°; Point D is found through subtracting the angle associated with an arc of half the bottom land length from the angle at Point C, where the bottom land length (δ) is given by:

$$\delta = \frac{p_c}{2} - 2a_c\tan\phi - 2r_c\cos\phi \tag{3.2}$$

and where the half arc angle (θ_δ) is:

$$\theta_\delta = \frac{\delta}{2r} \tag{3.3}$$

Where p_c is the circular pitch of the gear, r_c is the cutter tip radius, ϕ is the pressure angle and a_c is the cutter addendum length, which can be calculated through the equation:

$$a_c = l_d - r_c\,(1 - \sin\phi) \tag{3.4}$$

Two maxima on the cutter form, which in turn dictates the gear tooth form, can be calculate. These relate to situations where there is no bottom land (full fillet root) and where the cutter tip radius is zero (pointed rack tooth), which are maxima on the tip radius and the gear dedendum respectively and can be calculated through Equations (3.5).

$$d_{max} = \frac{p_c}{(4\tan\phi)} = \frac{\pi}{4P_d\tan\phi} \tag{3.5a}$$

$$(r_c)_{max} = \frac{\frac{p_c}{4} - l_d\tan\phi}{(\sin\phi - 1)\tan\phi + \cos\phi} \tag{3.5b}$$

where P_d is the diametral pitch.

Using the above equations and selecting standard manufacturers gear and rack properties, the bottom land can be generated from Point D to Point C, where the tooth fillet begins.

Tooth Root Fillet

The tooth fillet is the portion of the tooth profile that connects the involute portion of the flank to the circular portion of the bottom land. Its shape is determined by the profile of the cutter and the parameters used for the bottom land, where its coordinates are calculated in a local coordinate system centered at:

$$x_{lc} = \frac{1}{4}\pi m + l_d\tan\phi + r_c\tan\frac{1}{2}\left(90^\circ - \phi\right) \tag{3.6a}$$

$$y_{lc} = -\left(l_d - x_i m - r_c\right) \tag{3.6b}$$

where Figure 3.2, taken from Salamoun and Suchy [98], illustrates the location of the fillet and its centre (S_{no}).

Using the coordinates calculated in Equation (3.6) any point on the fillet can be calculated in the local coordinate system as a function of the rotational angle (ψ_n) about the local coordinate system centre.

$$x_l = x_{lc} - r_c\cos\psi_n \tag{3.7a}$$

$$y_l = y_{lc} - r_c\sin\psi_n \tag{3.7b}$$

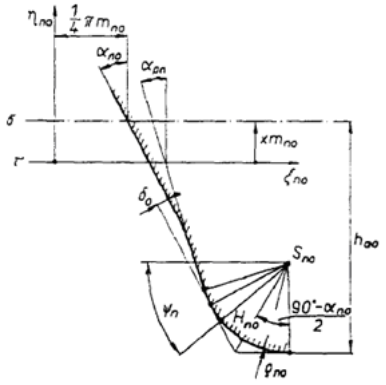

Figure 3.2: Fillet coordinate system: taken from Salamoun and Suchy [98]

The rotation in the local coordinate system (ψ_n) can be related to the overall rotation of the gear through the equation:

$$\theta = \frac{1}{r_p}\left(x_l - \frac{y_l}{\tan\psi_n}\right) \tag{3.8}$$

Such that using Equation (3.8) to link the two rotations, ψ_n and θ, and transforming the local coordinates into the global coordinate system yields complete functions for the fillet coordinates, given the gear rotation angle in the form:

$$x = r_p \sin\theta + \frac{y_l}{\sin\psi_n}\cos\left(\psi_n - \theta\right) \tag{3.9a}$$

$$y = r_p \cos\theta + \frac{y_l}{\sin\psi_n}\sin\left(\psi_n - \theta\right) \tag{3.9b}$$

Unlike the bottom land the fillet transition points can be easily determine from Equation (3.8) using local rotation limits of $\psi_n = 90°$ (Point C) and $\psi = \phi$ (Point D) to calculate appropriate gear rotation angles.

Involute

Unlike the fillet the involute coordinates can be described in the general coordinate system using the equations below, however the determination of the final gear angle corresponding to the required addendum length is more challenging.

$$x = r\sin\theta - \left(r\theta - \frac{s}{2}\right)\cos\phi\cos\left(\theta - \phi\right) \tag{3.10a}$$

$$y = r\cos\theta + \left(r\theta - \frac{s}{2}\right)\cos\phi\sin\left(\theta - \phi\right) \tag{3.10b}$$

where in the above equations s is the tooth thickness at the pitch circle calculated through:

$$s = m\left(\frac{\pi}{2} + 2x_i\tan\phi\right) \tag{3.11}$$

As mentioned in the previous section the first limit applied to the rotation angle is the point at which $\psi_n = \phi$ (Point B) and the total rotation required to completely describe the involute profile from the base circle (Point E) to the addendum limit (Point A) is given by:

$$\theta_{total} = \tan\left(\cos^{-1}\frac{r_b}{r_a}\right) \tag{3.12}$$

Where r_b and r_a are the gear base and addendum radii respectively. In the complete profile the involute begins from the transition coordinates of the fillet curve (Point B) and not the base circle (Point E) and therefore an alternate final angle is required, such that when the involute is drawn from the base circle the initial gear roll angle (θ_b) is given by:

$$\theta_b = \tan\phi + \frac{s}{2r} \tag{3.13}$$

and the difference between the start angles is given as:

$$\theta_{diff} = \theta_b - \theta\left(\psi_n = \phi\right) \tag{3.14}$$

where $\theta\left(\psi_n = \phi\right)$ is the global gear angle related to the a local fillet angle when it is equal to the pressure angle, as given in Equation (3.8). The total gear rotation describing the generation of the involute profile is then calculated by subtracting the difference in start angle from the total required rotation, such that:

$$\theta_{total} = \tan\left(\cos^{-1}\frac{r_b}{r_a}\right) - \theta_{diff} \tag{3.15}$$

where the limits of rotation are given as $\theta\left(\psi_n = \phi\right)$ and $\theta\left(\psi_n = \phi\right) - \theta_{total}$.

3.1.2 Gear Generation

2D and unmodified 3D gears

By using the above equations a single gear tooth flank can be generated and complete gear teeth can then be obtained by mirroring the coordinates about the line x = 0 (y-axis) and connecting the addendum limit coordinates. Complete 2D or straight cut 3D gears can then be generated by creating a radial pattern of the single gear tooth about the origin. Mathematically this can be performed via the rotational transfer matrix where the centre of each gear tooth is separated by the pitch angle ($\theta_P = 2\pi/N$), where N is the number of gear teeth, with the coordinate transfer matrix given below.

$$\begin{Bmatrix} x' \\ y' \end{Bmatrix} = \begin{bmatrix} \cos\theta_P & \sin\theta_P \\ -\sin\theta_P & \cos\theta_P \end{bmatrix} \begin{Bmatrix} x \\ y \end{Bmatrix} \tag{3.16}$$

A 3D gear is obtained by extruding the complete gear coordinates in the z-direction, while 2D gears are generated as a planar surface from these coordinates, however in many gear applications facewidth modification, such as crowning, is required to accommodate various running conditions and therefore the ability to model 3D crowned teeth is desirable.

3D crowned gear generation

When dealing with gear teeth that are modified along the facewidth, simple radial patterning and extrusion of the gear geometry will not suffice. A CAD methodology has been derived to allow the generation of modified gear tooth geometry, which will be given below. In the following example the modification is performed manually in a CAD package however the generation of crowned gear teeth has been automated within the user GUI to allow fast generation.

In the first step the coordinates for the gear tooth flank are imported into the CAD/CAE pre-processor package, and the involute profile is generated as a spline, as shown in Figure 3.3(a), then enclosed as shown in Figures 3.3(b) – 3.3(d). In Figure 3.3(b) a line is drawn up to the y-axis from the highest point on the involute

curve representing the top land of the gear; while in Figure 3.3(c) an arc, centred at the origin, is used to extend the bottom land along the dedendum circle, which eliminates gaps during the crowning process. Finally in Figure 3.3(d) the shape is fully enclosed by drawing straight lines between the free ends and the origin.

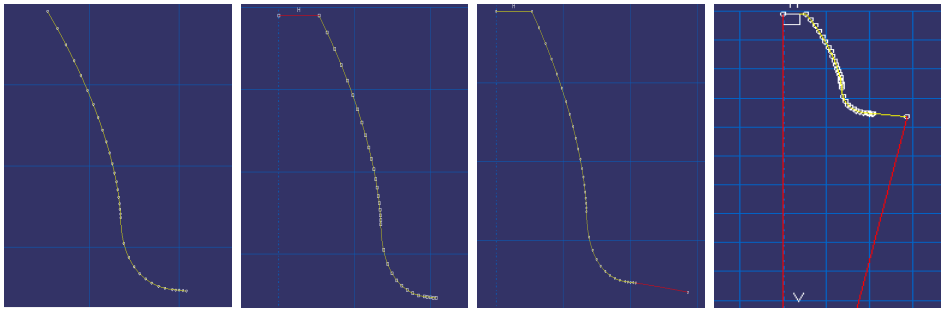

(a) Involute import (b) Top Land (c) Bottom Land (d) Profile enclosed

Figure 3.3: Data import and profile encapsulation

The section shown in Figure 3.3(d) is then swept along a path in a perpendicular plane to the sketch plane, which represents the crowning curvature. The determination of the path geometry can be set through the amount of crowning and the half facewidth, as illustrated in Figure 3.4.

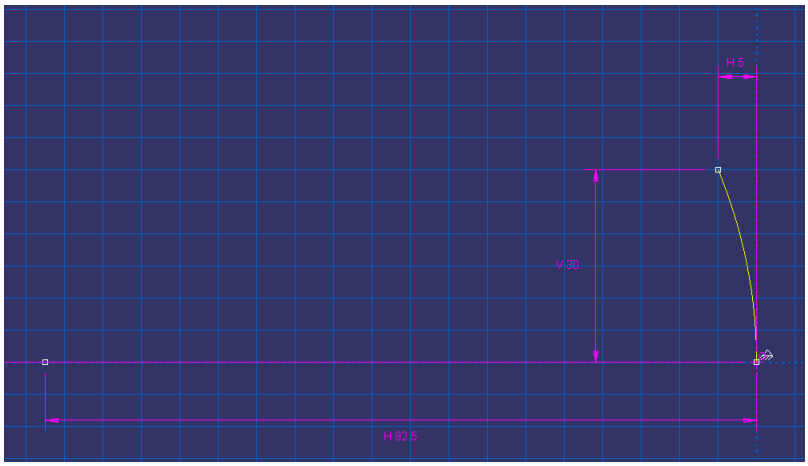

Figure 3.4: Gear crowning path

Once the sketch has been swept along the path the resultant shape shown in Figures 3.5(a) and 3.5(b) is produced, which can be referred to as an "unrefined" tooth quarter, due to the imprecise geometry caused by the sweeping of the enclosed tooth profile along the crowning path. This is clearly seen in Figure 3.5(b) where

there are portions of the gear which lie on the negative side of the vertical line (space occupied by the other flank), and the two gear sides, which are located on the top and bottom of the tooth in Figure 3.5(b), are also not parallel. To rectify this, the tooth is "trimmed" along the two lines shown in Figure 3.5(b), with the resultant portion shown in Figures 3.5(c) and 3.5(d).

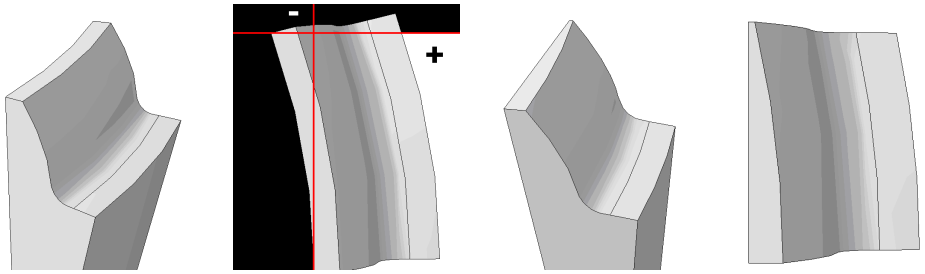

(a) unrefined (b) unrefined (c) refined (d) refined

Figure 3.5: Trimming of "unrefined" tooth quarter

To generate a complete tooth this portion is mirrored about the x-y plane and the subsequent portions are mirrored about the y-z plane as shown in Figure 3.6.

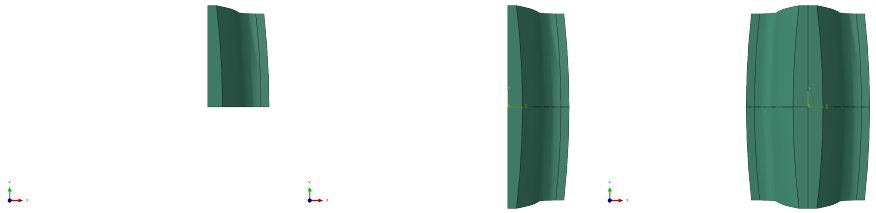

(a) Tooth quarter (b) Tooth half (c) Whole tooth

Figure 3.6: Tooth generation

This tooth can then be patterned radially about the origin, in the same way as the straight cut spur gears, and the pieces combined to generate a complete gear as shown in Figure 3.7, which has also been modified to include the gear rim and a shaft hole. This can then be meshed, boundary conditions, and loads can be applied, and eventually it can be solve for the particular problem of interest.

As mentioned the equations and processes shown in this section are used in a user GUI, which produces python script capable of being read by the FE package

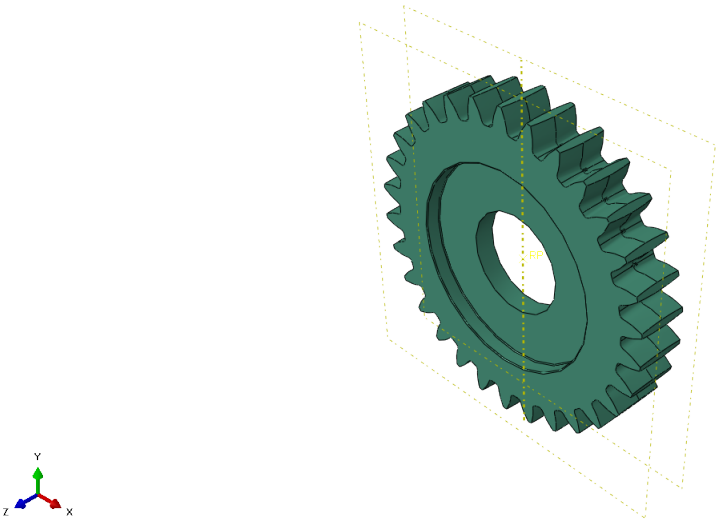

Figure 3.7: Complete crowned gear

ABAQUS to generate various gear sets in contact, where an example of the python script used in ABAQUS to generate a pair of straight cut spur gears is given in Appendix A.1.

3.2 Model Assembly and Gear Positioning

With the gear and pinion created as ABAQUS parts the next step requires them to be positioned in an assembly. This section initially describes the procedure to bring the two gears into perfect alignment and then describes both the various forms of misalignment and the transformations required to misalign the gears. Finally the procedure implemented to perform a parameter study of the various misalignments is discussed.

3.2.1 Perfect Alignment

After being imported into the assembly both the gear and pinion are centered at the global origin (overlapping) with the extruded depth (facewidth) aligned along the z-axis, as shown in Figure 3.8(a); to bring them into perfect alignment firstly they must be separated by the ideal centre distance (C), which can be calculated

as the sum of the pitch circle radii, or:

$$C = \frac{m}{2}\left(N_1 + N_2\right) \tag{3.17}$$

This translation along the x-axis is applied to either the gear or the pinion, as shown in Figure 3.8(b), and the gear teeth are brought into contact by applying a small rotation to one, or both, of the gears. The rotation is applied about the z-axis in the local coordinate systems, whose origins are at the gear centres and which are aligned with the global coordinate frame. The rotation is often a fraction of the pitch angle, and the rotated coordinates of the gears can be found by:

$$\begin{Bmatrix} x^a \\ y^a \\ z^a \end{Bmatrix}_i = \begin{bmatrix} \cos\gamma_i & -\sin\gamma_i & 0 \\ \sin\gamma_i & \cos\gamma_i & 0 \\ 0 & 0 & 1 \end{bmatrix} \begin{Bmatrix} x \\ y \\ z \end{Bmatrix}_i \tag{3.18}$$

where superscript a indicates the aligned coordinates, subscript i indicates the gear and γ is the rotation about the local z-axes. By applying the centre distance translation to the 1st gear (pinion) the aligned coordinates can be found through the following equations.

$$\begin{Bmatrix} x_1^a \\ y_1^a \\ z_1^a \end{Bmatrix} = \begin{bmatrix} \cos\gamma_1 & -\sin\gamma_1 & 0 \\ \sin\gamma_1 & \cos\gamma_1 & 0 \\ 0 & 0 & 1 \end{bmatrix} \begin{Bmatrix} x_1 \\ y_1 \\ z_1 \end{Bmatrix} + \begin{Bmatrix} C \\ 0 \\ 0 \end{Bmatrix} \tag{3.19a}$$

$$\begin{Bmatrix} x_2^a \\ y_2^a \\ z_2^a \end{Bmatrix} = \begin{bmatrix} \cos\gamma_2 & -\sin\gamma_2 & 0 \\ \sin\gamma_2 & \cos\gamma_2 & 0 \\ 0 & 0 & 1 \end{bmatrix} \begin{Bmatrix} x_2 \\ y_2 \\ z_2 \end{Bmatrix} \tag{3.19b}$$

with the resulting aligned gears shown in Figure 3.8(c)

3.2.2 Misalignment

To apply misalignment to the gears a local coordinate system, $O_p - X_pY_pZ_p$, centred at the pitch point with the y-axis aligned along the pressure line, is created

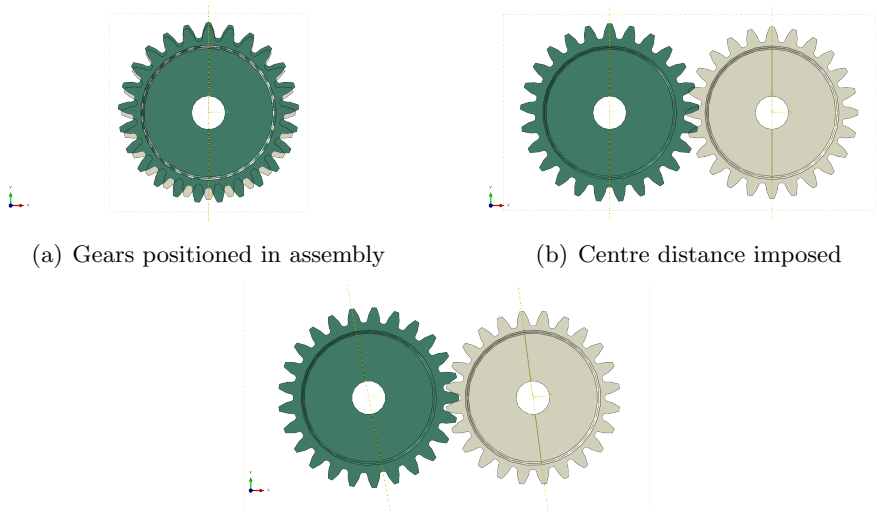

(a) Gears positioned in assembly

(b) Centre distance imposed

(c) Gears rotated

Figure 3.8: Perfect alignment procedure

as illustrated in Figure 3.9.

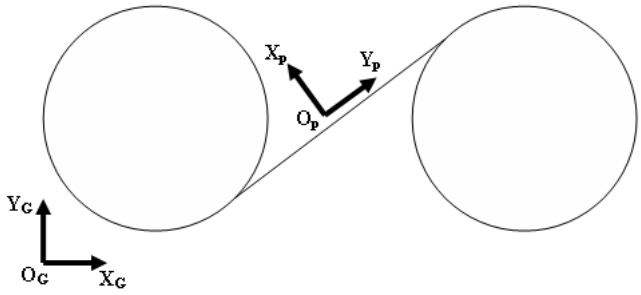

Figure 3.9: Gear coordinate systems used in applying misalignment

Using this figure generic gear misalignment can be decomposed into 4 primary forms, two linear (axial and radial) and two angular (pitch and yaw), where axial misalignment is achieved through a translation along the global z-axis (Z_G) and yaw and pitch misalignment are achieved through rotating the gears about Y_p and Z_p respectively. The final misalignment type is the variation of the centre distance through translation along the global x and y-axes (X_G,Y_G), known as radial misalignment. These individual misalignments are shown schematically in Figure 3.10.

Using Euler angles α and β to represent rotations about X_p and Y_p respec-

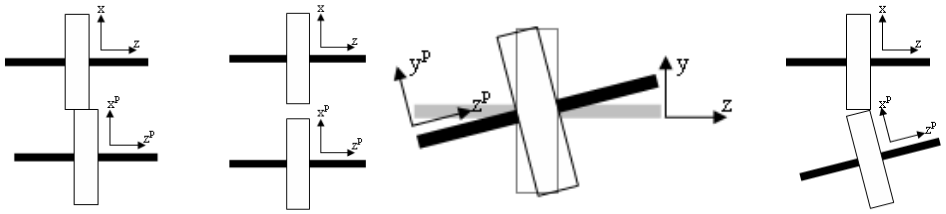

(a) Axial (b) Radial (c) Pitch (d) Yaw

Figure 3.10: Misalignment types

tively and combining them in x-y convention, the positioning of the gears in the analysis is achieved by the equation

$$\begin{Bmatrix} X^m \\ Y^m \\ Z^m \end{Bmatrix} = \mathbf{R} \begin{Bmatrix} X^a \\ Y^a \\ Z^a \end{Bmatrix} + \begin{Bmatrix} X_\delta \\ Y_\delta \\ Z_\delta \end{Bmatrix} \tag{3.20}$$

where $\begin{Bmatrix} X_\delta & Y_\delta & Z_\delta \end{Bmatrix}^T$ are the misalignment displacements and $\mathbf{R}$ is the rotation matrix, which is composed of $\mathbf{R} = \mathbf{R}_Y \mathbf{R}_X$, and where $\mathbf{R}_Y$ and $\mathbf{R}_X$ are determined using Rodrigues' rotation formula of the form.

$$\mathbf{R} = \mathbf{I}\cos\theta + (1 - \cos\theta)\,\mathbf{e}\mathbf{e}^T + \mathbf{e}_\mathbf{x}\sin\theta \tag{3.21a}$$

where $\mathbf{I}$ is a 3x3 identity matrix, θ is the angle of rotation, $\mathbf{e}$ is the axis of rotation given by Equation (3.21b) and $\mathbf{e_x}$ is a matrix derived from the rotation axis as shown in Equation (3.21c)

$$\mathbf{k} = \begin{Bmatrix} x_R & y_R & z_R \end{Bmatrix}^T \tag{3.21b}$$

$$[\mathbf{k}]_x = \begin{bmatrix} 0 & -\mathbf{k}_3 & \mathbf{k}_2 \\ \mathbf{k}_3 & 0 & -\mathbf{k}_1 \\ -\mathbf{k}_2 & \mathbf{k}_1 & 0 \end{bmatrix} \tag{3.21c}$$

When applying Yaw misalignment, the axis of rotation is aligned parallel to the pressure line, i.e. along Y_p, such that the axis of rotation ($\mathbf{k}$) is $\begin{Bmatrix} \sin\phi & \cos\phi & 0 \end{Bmatrix}$

and the resultant rotational matrix is

$$\mathbf{R}_{Yaw} = \begin{bmatrix} \cos\beta + \sin^2\phi\,(1-\cos\beta) & \cos\phi\sin\phi\,(1-\cos\beta) & \cos\phi\sin\beta \\ \cos\phi\sin\phi\,(1-\cos\beta) & \cos\beta + \cos^2\phi\,(1-\cos\beta) & -\sin\phi\sin\beta \\ -\cos\phi\sin\beta & \sin\phi\sin\beta & \cos\beta \end{bmatrix} \tag{3.21d}$$

and Pitch misalignment is applied about an axis perpendicular to the pressure line (X_p) with a axis vector of $\begin{Bmatrix} -\cos\phi & \sin\phi & 0 \end{Bmatrix}$ and a rotation matrix of:

$$\mathbf{R}_{Pitch} = \begin{bmatrix} \cos\alpha + \cos^2\phi\,(1-\cos\alpha) & \cos\phi\sin\phi\,(1-\cos\alpha) & \sin\phi\sin\alpha \\ \cos\phi\sin\phi\,(1-\cos\alpha) & \cos\alpha + \sin^2\phi\,(1-\cos\alpha) & -\cos\phi\sin\alpha \\ -\sin\phi\sin\alpha & \cos\phi\sin\alpha & \cos\alpha \end{bmatrix} \tag{3.21e}$$

Using the above equations the gears can be positioned in various configurations within the assembly to study different misalignment cases, and by using the geometry generated for the gear set as a template the application of misalignment can be automated within ABAQUS using a parameter study. The modified simulation file and associated parameter study file are presented in Appendix B, where they have been reduced to exclude the vast majority of nodal and element information.

3.3 Material Definition

With the gear geometry imported into ABAQUS other simulation properties can be assigned, such as the material definition. The gears of interest are manufactured using BS 970 080M40 (EN8) steel, and therefore it is assumed that the material properties are both homogeneous and isotropic; it is also assumed that the stress-strain relationship remains in the elastic region, such that the stresses and strains can be determined through the Young's Modulus and the Poisson's Ratio alone. The values of the material properties are constant throughout the analysis, set at 210GPa and 0.3 for the Young's Modulus and Poisson's Ratio respectively.

3.4 Contact Formulation

In many finite element analyses of gears the contact conditions are modelled using non-linear gap elements, where non-linear springs are placed between contacting nodes to determine the transfer of forces between bodies. A problem associated

with the use of gap elements is that they are unable to model considerable relative sliding of the contacting surfaces and where limited sliding is present gap elements require *a priori* knowledge of the contacting pairs. To accommodate the large sliding present in gear contact and the unknown position of the contacting points under load, ABAQUS also offers a pure master-slave contact algorithm, where possible contacting points are determined during the analysis.

Contact can be assigned by two methods in ABAQUS, the first is a general contact procedure, which does not require any definition of possible contacting surfaces and allows self-contact of a surface. The second method of assigning contact is through the contact pair algorithm, where possible contacting faces are selected and paired together, which although faster than general contact requires knowledge of possible contacting surfaces. General contact also automates the assignment of master and slave surfaces, whereas within the contact pairs algorithm the master and slave surfaces must be explicitly stated before the analysis.

Using the contact pairs approach a greater deal of control is available in defining the contact properties, which will be discussed in the proceeding sections.

3.4.1 Contact Discretization

During analysis, constraints that approximate contact are applied to various points on the contacting surfaces; the position and conditions of the constraints are determined through the contact discretization procedure selected, of which there are two, node-to-surface and "true" surface-to-surface contact discretization.

The node-to-surface contact discretization defines contact between the nodes on the slave surface and the surface of the master surface. Projections are draw between the master surface and slave nodes; where each contact constraint involves a single slave node and a group of adjacent master nodes, meaning the contact direction is therefore based on the normal of the master surface. The slave nodes are constrained to not penetrate the master surface; however this condition does not necessarily hold true for penetration of the master nodes into the slave surface.

Conversely the surface-to-surface contact discretization method enforces the

contact constraints in an average sense in an area near the slave node, as opposed to strictly at the slave node with node-to-surface, which can result in slight penetration of slave nodes into the master surface, and vice-versa; however the large master node penetration capable in the node-to-surface discretization is avoided.

Although more computationally intensive due to the additional nodes required per contact constraint, surface-to-surface discretization has many advantages compared to node-to-surface discretization, such as more accurate contact stress and pressure results, where errors in the node-to-surface contact discretization arise from the strict enforcement of zero penetration of slave nodes. This results in a build-up of forces at the nodal positions, and consequently peaks and troughs in the contact pressure across the face. Because contact conditions are averaged around the slave nodes, surface-to-surface discretization is less dependent on the assignment of master and slave surfaces when compared to node-to-surface, and these are the reasons why in determining the contact discretization method the surface-to-surface method will be used in the analysis of gear contact.

3.4.2 Contact constraint enforcement

As mentioned in the previous section, once two bodies enter contact the contact conditions must be enforced, either strictly or in an average sense across the contacting faces. There are several methods available to implement the contact conditions, however the most common and most appropriate is often hard contact, which states that bodies are unconnected until their clearance is less than or equal to zero, and will remain in contact until the pressure being transmitted through them is less than zero; once a negative pressure is detected the contact points will start to move apart. The hard contact constraint enforcement also stipulates that any pressure can be transmitted through the contacting face, when in contact, which can be seen in Figure 3.11(a).

In Figure 3.11(a) the contact constraint is directly enforced through the use of Lagrange multipliers, since the penetration of constrained nodes is forbidden; however this can lead to convergence issues or increased convergence times. To

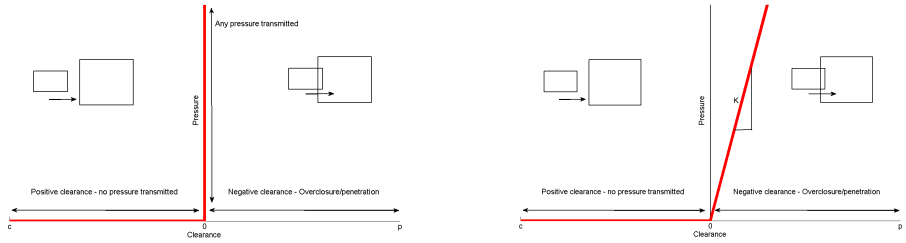

(a) Direct Enforcement (b) Penalty method

Figure 3.11: Hard contact enforcement methods

improve the solution convergence a stiff approximation to hard contact, known as the penalty method, can be used, which effectively introduces a stiff spring, of the order of 1000 times a characteristic element stiffness, to resist penetration of the two contacting surfaces. This improves convergence and also decreases solution time due to the omission of the Lagrange multiplier degrees of freedom associated with hard contact. These advantages are offset by the introduction of some penetration of the surfaces, as shown in Figure 3.11(b).

Figure 3.11(b) illustrates the linear penalty method, however a non-linear formulation is also available, where on initial overclosure the penalty stiffness is low to improve convergence and when penetration increases the penalty stiffness also increases to limit the amount of penetration. This method is not illustrated here.

Other pressure-overclosure relationships available include Exponential, Tabular and Linear, as shown in Figure 3.12, which are based on softened contact and generally only used for specific cases and in most common applications are dismissed in favour of direct hard contact or the penalty method.

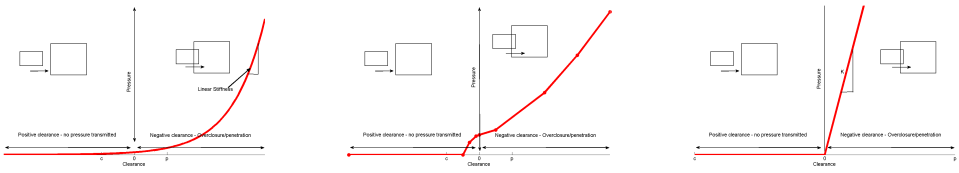

(a) Exponential (b) Tabular (c) Linear

Figure 3.12: Pressure-Overclosure relationships

Similarities can be observed between the Linear Penalty method and the

linear pressure-overclosure method, however the main difference between the two is the calculation of the penetration stiffness, where the penalty method calculates it's value on an underlying element stiffness, the linear pressure-overclosure method determines its penetration stiffness based on a user submitted value.

In the following analyses contact is approximated as hard contact, since although the softening type pressure-overclosure relationships illustrated in Figure 3.12 might be better at approximating the contact of gears through a lubricating film, such as the gearbox oil, the output results will be highly dependent on the precise modelling of the pressure-overclosure relationship, and there might be unforeseen problems in obtaining a converged solution. To overcome possible problems with convergence the penalty method is used to approximate hard contact, as the limited penetration it affords may be neglected as its values will be only a tiny fraction of the global deflections.

3.4.3 Contact tracking

Once in contact, the relative position of the contacting nodes on the slave surface, with respect to the master surface, need to be tracked as they slide along the master surface. ABAQUS has two methods for tracking the contact evolution, the finite-sliding and the small sliding formulations, where the finite-sliding is intended for arbitrary sliding of contacting surfaces and small-sliding is primarily used when the relative sliding of contacting nodes is of the order of a couple of elements on the contacting faces. Figure 3.13 compares the two methods available to track contact.

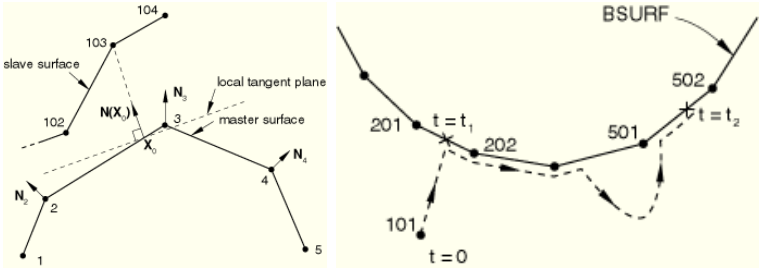

(a) Small-Sliding (b) Finite-Sliding

Figure 3.13: Comparison of contact tracking formulations, taken from the ABAQUS Analysis Users Manual [99]

For small-sliding the slide plane is derived from the initial geometry, i.e. before simulation, and is taken as a plane perpendicular to the contacting normal, as shown in Figure 3.13(a); throughout the simulation the points on the slave surface are constrained to slide along this predetermined plane. When using the finite-sliding formulation the sliding plane is updated throughout the simulation based on the current geometry of the master surface, such that for large sliding the contacting nodes on the slave surface can accurately follow the master surface, as shown in Figure 3.13(b). Since the contacting plane is constantly updated throughout the simulation, the use of finite-sliding contact tracking adds some computational cost to the simulation, however since during gear contact the contacting planes are constantly changing and there is considerable sliding of contacting teeth, the use of the finite-sliding technique is required during the analysis.

3.4.4 Tangential behaviour

ABAQUS has a number of friction formulations available during the modelling of sliding contact, where the most common are based on the Coulomb model; however since friction will be modelled in a dynamic sense through the dynamic gearbox model, no friction is considered in the static analysis of gear contact and no shear is generated on the gear teeth as a result.

3.4.5 Solution methodology

The solution of non-linear problems in ABAQUS, such as contact or plasticity, are dealt with through the use of the Newton-Raphson technique, where during a simulation a small load increment (ΔP) is applied to the model, and based on the current stiffness (K_0) state of the model an equivalent displacement correction (c_a) can be determined. Updating the model configuration using the displacement correction yields stresses in the model and internal forces (I) based on the non-linear response curve of the structure, and by comparing the internal and external forces a residual force can be determined. If the residual force is below a set tolerance the system is said to have converged, however if it is not a new tangent stiffness is derived, and together with the residual force a new displacement correction is deter-

mined and the system is again updated to find the internal forces. This continues until the system converges, or divergence is detected; when this occurs the initial force increment is reduced until a converged solution can be found. The solution of a non-linear response described above is illustrated in Figure 3.14 for clarity.

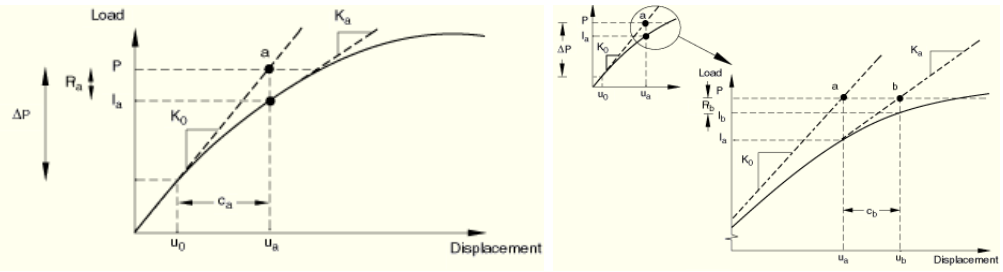

Figure 3.14: Newton-Raphson solution technique, taken from the ABAQUS Analysis Users Manual [99]

The Newton-Raphson technique applied to contact within ABAQUS is specifically shown in Figure 3.15 to include the variations in the contact conditions, where the variations in contact conditions are constantly updated whilst searching for a converged solution.

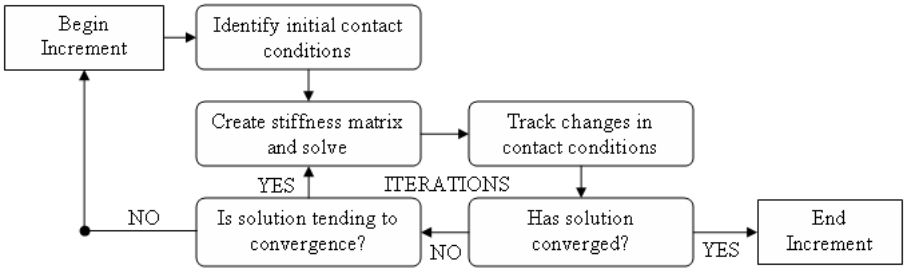

Figure 3.15: Non-linear solution flow chart

In Figure 3.15 the increment begins with a set increment size, where a system of equations are determined considering the initial contact states of the contacting nodes; these are solved and changes in the contact conditions are checked. The solution is then checked for convergence, based on, among other data, the residual forces and the displacement correction, and if converged the increment ends; if not additional checks are performed to detect if the solution is tending towards a converged solution. If the solution is likely to converge the system equation are

recalculated and solved, and the cycle repeats; if not the increment size is reduced and the cycle begins again.

3.5 Loads and Boundary Conditions

During simulation loads and boundary conditions are applied to the two gears through their respective local centres, where the local centres are coupled to the rest of the gear using a kinematic link to the inside of the gear-to-shaft hole, as shown in Figure 3.16. This means that the nodal degrees-of-freedom (DOF) on the inside of the gear-to-shaft hole are governed by the DOF of the control node at the gear centres.

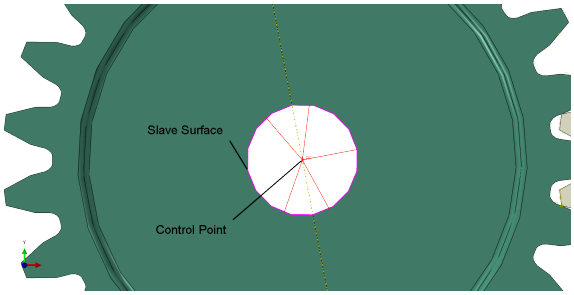

Figure 3.16: Gear kinematic coupling

Both the gear and pinion central control points, are restricted to allow only rotation about their local z-axes, such that there is no linear rigid body motion of the gears, and in general the torque loads are applied through the gear and the rotational displacements are applied to the pinion. The magnitudes of the torques and displacement vary depending on the analysis step.

3.6 Analysis Steps

For a convergent solution to be obtained the simulation of contacting bodies must be achieved in three steps known as the contact step, the load step and the rotation step, with each of these steps having varying boundary conditions.

3.6.1 The contact step

In the initial configuration the two gears are considered to be unconnected and if any forces were to be applied to the system convergence would be unlikely.

To understand why, a simple example is given, as illustrated in Figure 3.17, where a simple spring element comes into contact with a rigid surface.

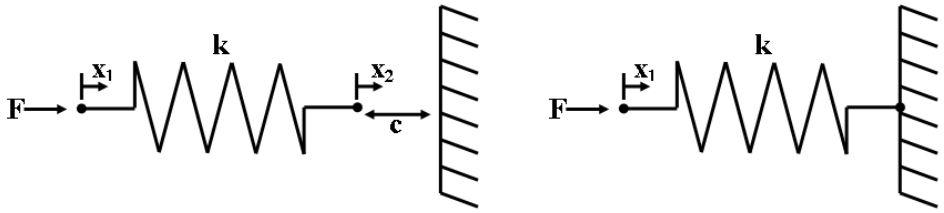

(a) Bodies unconnected (b) Bodies in contact

Figure 3.17: Initialization of contact

In Figure 3.17(a) the bodies are unconnected and a force is applied to node 1 to bring the spring into contact with the rigid surface; physically and intuitively there should be no problem with this scenario, however by observing the system of equations a problem is found.

$$\begin{bmatrix} k & -k \\ -k & k \end{bmatrix} \begin{Bmatrix} x_1 \\ x_2 \end{Bmatrix} = \begin{Bmatrix} F \\ 0 \end{Bmatrix} \tag{3.22}$$

Here the determinant of the stiffness matrix is zero and a solution for the nodal displacements can not be obtained; in contact (Figure 3.17(b)) additional boundary conditions are enforced and the system of equations becomes.

$$\begin{bmatrix} k & 0 \\ 0 & 1 \end{bmatrix} \begin{Bmatrix} x_1 \\ x_2 \end{Bmatrix} = \begin{Bmatrix} F \\ 0 \end{Bmatrix} \tag{3.23}$$

The determinant of the stiffness matrix is now non-zero and the displacements can be determined from the applied load.

It can now be appreciated that for unconnected bodies, contact cannot be initiated by applying a force to the system in isolation. Two methods can be used to overcome this difficulty, the first is the introduction of contact stabilization, the second is to initiate contact through displacement boundary conditions. By introducing contact stabilization the bodies are effectively in contact, this can be

visualized by introducing a spring (k_s) between node 2 and the rigid surface of Figure 3.17(a), and with this the stiffness matrix becomes positive definite (non-zero determinant) as shown in Equation (3.24) and a solution can be obtained.

$$\begin{bmatrix} k & -k & 0 \\ -k & k+k_s & 0 \\ 0 & 0 & 1 \end{bmatrix} \begin{Bmatrix} x_1 \\ x_2 \\ x_3 \end{Bmatrix} = \begin{Bmatrix} F \\ 0 \\ 0 \end{Bmatrix} \tag{3.24}$$

During the contact initialization step the stiffness of the connecting spring is ramped down and eventually removed to bring the two surfaces into contact.

Using the second method a displacement is applied to node 1, rather than a force, and since there is zero external force the displacement of node 2 can be determined through rigid body motion, and the two bodies can be brought into contact. At that point internal stresses are generated within the contacting bodies.

In general, contact stabilization is used when contact is uncertain and the clearance between contacting surfaces is unknown. Since in gear contact the possible contacting faces are known and the distance between contacting faces is relatively small, convergence is better achieved by applying rotational displacement boundary conditions to the gear centres rather than applying contact stabilization. Therefore the procedure employed in the contact initialization step, is to apply a small rotation to the pinion, while the gear is constrained in all DOF.

3.6.2 The load step

One problem associated with using displacement boundary conditions in developing contact is that the internal stresses generated are not in line with the desired external loading. To obtain the required internal stresses the design load is applied to the gear while the pinion is reset to its starting position; in this step the gear is allowed to rotate freely.

3.6.3 The rotation step

After the load step, appropriate stresses are generated within the gears and with the load maintained the pinion is rotated through a single gear contact cycle,

which is equivalent to the pinion pitch angle, where results are obtained at 51 rotational increments throughout the analysis to develop a static response of the system with respect to the pinion rotation angle.

The analysis steps and the variations in the boundary conditions and loads are summarised in Table 3.1, where only the rotations and forces about the local z-axes are considered since the gears are constrained in all other DOF and no other external forces are applied to the system.

	Gear		Pinion	
	UR3	T_{U3}	UR3	T_{U3}
Contact	0	0	γ_{contact}	0
Load	Free	T	0	0
Rotate	Free	T	γ_P	0

Table 3.1: Variation of boundary conditions through steps

Here γ is a rotation about the local z-axis and T is a torque applied about the local z-axis; in the Load and Rotation step the gear is not constrained in rotation and is free to rotate depending on the rotation of the pinion.

3.7 Output Parameters

To simplify gear contact in the hybrid dynamic model three main static outputs are sought, these are the mesh stiffness, the Load-Sharing Ratio (LSR) and the gear centre reaction forces. The mesh stiffness simplifies the deflection of the gear system at a given pinion rotation angle, the LSR states the proportion of the total transmitted load which is applied to individual teeth for a given pinion angle, and the reaction forces define forces which arise from misaligned gear contact. The methods used to determine these parameters and their importance in the hybrid dynamic model will be discussed in the following section.

3.7.1 Mesh Stiffness

In idealized gear contact the transmitted forces act along a theoretical line tangential to the gear base circles known as the pressure line, as shown in Figure 3.18, where the forces associated with gear contact are decomposed into their vertical

and horizontal components.

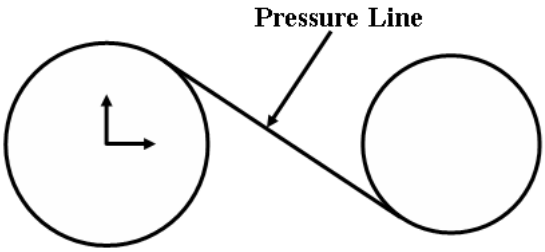

Figure 3.18: Idealized gear contact line

For perfectly rigid gears with perfect involute form the position of the driven gear (θ_1) can be determined from the position of the driving gear (θ_2) through the gear ratio (GR), such that:

$$\theta_1 = \theta_2 \mathrm{GR} \tag{3.25a}$$

where

$$\mathrm{GR} = N_2/N_1 \tag{3.25b}$$

and N_i are the number of teeth on the respective gears. However since gears are never perfectly rigid, various deformations occur during contact, such as tooth bending, Hertzian contact deformation and gear body deformation, which invalidates the assumption that the driven gear position can be determined solely from Equation (3.25a). The difference between the idealized rotational position calculated through Equation (3.25a) and the actual position of the driven gear is called the rotational transmission error (TE), which can be calculated directly as.

$$\mathrm{TE} = \theta_1 - \theta_2 \frac{N_2}{N_1} \tag{3.26}$$

Since the TE is effectively a bulk deformation, a generalized rotational stiffness can be determined from the known applied load (T); this is the rotational mesh stiffness ($k_{m\theta}$).

$$k_{m\theta} = \mathrm{T}/\mathrm{TE} \tag{3.27}$$

The rotational mesh stiffness is acceptable when modelling only the rotational vi-

brations, however it is unable to couple together the rotational and lateral forces that occur during gear contact. A method for coupling together these motions was described by Howard *et al* [31], where a linear mesh stiffness (k_m) acting along the pressure line is calculated based on the normal forces along the pressure line. As shown in Equation (3.27) the rotational mesh stiffness can be determined from the ratio of the applied torque to the angular deflection; with the knowledge of the applied torque the force acting along the pressure line can be determined as the torque multiplied by the perpendicular distance to the pressure line, which is the base circle radius. The linear deflection along the pressure line (δ) can also be determined from the arc length associated with the angular deflection, such that the rotational TE equals the deflection along the pressure line divided by the base radius. This transformation can be seen in Equation (3.28).

$$k_{m\theta} = \frac{\mathrm{T}}{\mathrm{TE}} = \frac{Fr_b}{\mathrm{TE}} = \frac{Fr_b}{\delta/r_b} = \frac{Fr_b^2}{\delta} \tag{3.28}$$

Therefore, since the linear stiffness is the ratio of the normal contact force to the linear deflection, a transformation between the rotational stiffness and the linear stiffness can be determined.

$$k_m = \frac{k_{m\theta}}{r_b^2} \tag{3.29}$$

The linear mesh stiffness can then be used in the dynamic model to determine the dynamic rotational deflection, along with the vertical and horizontal forces at the gear centre. These three forces are referred to in this thesis as the Line-of-Action (LOA) forces as they act along the LOA (pressure line), all other forces are classed as Off-Line-of-Action (OLOA) forces.

3.7.2 Load Sharing Ratio (LSR)

Although the mesh stiffness described above determines gross gear deflection and forces based on the total transmitted load, some gear forces require knowledge of the forces applied to individual teeth. The formulation of friction, which is shown in Section 6.3.2, is one such example, where the friction coefficient depends on

the sliding direction of the surfaces and different teeth may have different sliding directions, along with different normal loads.

To calculate the LSR, first the integral of the normal contact forces across individual teeth is calculated; this gives the total load transmitted through each tooth pair in contact at a given pinion angle, next the LSR is calculated as the ratio of the load transmitted through the tooth to the total transmitted load through all teeth, as shown in Equation (3.30).

$$\mathrm{LSR}_1(\gamma) = \frac{F_1(\gamma)}{\sum_{i=1}^{N} F_i(\gamma)} \tag{3.30}$$

The LSR should equal 1 for all teeth in contact, such that for a gear with a contact ratio of between 1 and 2 the LSR will be 1 for a portion of the gear contact where only a single tooth is in contact, during double tooth contact the LSR will be less than 1, however the sum of the LSR on the two teeth will always equal 1.

3.7.3 Reaction forces

The reaction forces are the forces required to constrain the gears in their current positions, where the gears are being forced by the forces generated at the contacting teeth. They are used in the hybrid dynamic model to model the effects of misalignment on the OLOA forces, which cannot be included through the mesh stiffness described above.

The reaction forces are calculated directly from the Finite Element Analysis and are taken from local coordinate systems at the gear centres described in Section 3.5. The lateral forces are reffered to from this point onwards as RF1, RF2 and RF3 with moments about the axes referred to as RM1, RM2 and RM3, as shown in Figure 3.19, where RF1, RF2 and RM3 are the LOA forces and RF3, RM1 and RM2 are the OLOA forces.

3.8 Mesh Selection

In finite element analyses the selection of the mesh type and size can have a large impact on the validity of the results obtained. Both gears are meshed

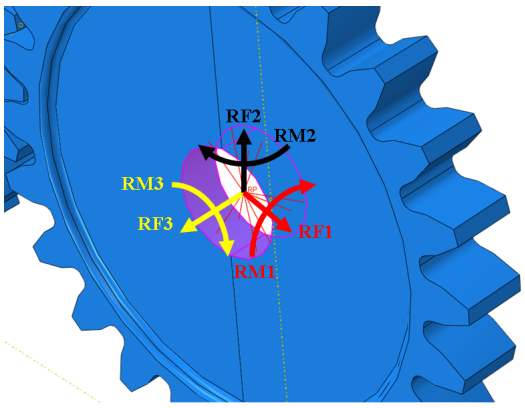

Figure 3.19: Coordinate system convention for reaction forces

using 8-node linear brick elements as these are well regarded in the modelling of contact problems, where they are capable of resolving the contact pressure across the contacting faces accurately. Linear elements are used because quadratic elements, where extra nodes are placed along the element edges and the underlying element shape functions are formed on quadratic equations, can have difficulties in resolving the contact pressure into nodal forces at the mid-side nodes. Linear elements are disadvantaged when compared to quadratic elements in some regards, for example more elements are required to accurately define curved surfaces as the element edges are straight lines, as opposed to quadratic elements which can have curved surfaces due to the mid-side node, and although computationally faster more linear elements are generally required to obtain a converged solution.

During the analysis of gear contact a great deal of effort has been afforded to generate accurate involute profiles for the gear teeth, however once meshed the gear tooth will be described by a number of nodes on the involute curve connected by straight lines, such that some accuracy in the involute will be lost. To minimize this the contacting faces are discretized with a highly refined finite element mesh, which will allow accurate representation of the contacting surfaces and the deformation of the contact zone.

Another major source of gear deformation occurs as a result of cantilever beam bending of the gear tooth, therefore for the gear in contact, the non-contact tooth faces and the gear root should be relatively accurately meshed. It is also

necessary to mesh these regions with some degree of accuracy since the transition of the mesh from the finely meshed surface on the contacting face to the non contacting face needs to be gradual. Large variations in element sizes between adjacent elements can lead to numerical inaccuracies when using isoparametric elements, and since the contacting gear teeth are critical in the analysis the number of numerical errors in the teeth must be minimized.

Since the analysis is performed over a rotation equal to the pitch angle only 3 teeth on the gear and pinion are in contact, meaning the majority of the gears contribute little to the overall response of the system, and therefore the mesh accuracy can be relaxed in these areas. This reduces the number of degrees of freedom of the model and the number of floating point operations (flops) required to reach a solution.

By using the three regions described above the gears can be meshed using three different element sizes, which allow refinement of the mesh in areas of interest and reduce the number of elements in areas with less influence to reduce computational cost. The resulting mesh can be seen in Figure 3.20, where the mesh is shown on the gear, and where the top land has a biased mesh, which means that towards the contacting face the element size is equal to that on the contacting face and as the elements get further away from the contacting surface the element sizes increase linearly to the same size as the non-contacting face.

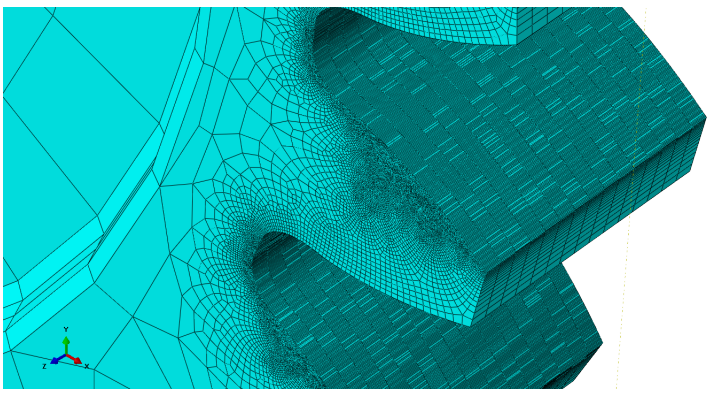

Figure 3.20: Finite element mesh

In Figure 3.20 the mesh is swept about the axial direction (z-axis), where

there are 15 elements across the tooth face, to maintain a reasonable number of elements and reduce computational cost.

3.9 Conclusions

In this chapter the development of a gear contact model within ABAQUS has been shown, including the generation of the gear coordinates, the positioning of the gears under perfect alignment and under misaligned conditions, the material properties, the contact algorithms used, the loads and boundary conditions, the analysis steps and the outputs of interest.

Chapter 4

Finite Element Analysis: Results

In this chapter results are presented for the static contact simulation between two steel involute spur gears with zero modification, whose material and geometric properties are given in Table 4.1, and are illustrated in perfect alignment in Figure 3.8(c).

		Gear	**Pinion**
Geometric Properties			
Number of teeth		25	24
Module (mm)		5	
Pressure Angle (°)		20	
Pitch Radius (mm)		62.5	60
Centre Distance (mm)		122.5	
Base Radius (mm)		58.7308	56.3816
Addendum Radius (mm)		67.5	65
Dedendum Radius (mm)		55	52.5
Pitch Angle (°)		14.4	15
Web Thickness (mm)		10	10
Rim Diameter (mm)		98.75	
Material Properties			
Young's Modulus	(GPa)	210	
Poisson's Ratio		0.3	
Friction Coefficient		0	

Table 4.1: Gear properties

To begin, a sensitivity study is performed to determine appropriate element

sizes for the three regions discussed in Section 3.8, where a 2D analysis is used, to reduce computational cost, at a design load of 100 Nm applied to the gear and a pinion rotation of one pitch angle to capture a single gear contact cycle. Convergence will be based on the transmission error maxima, obtained by the method described in Section 3.7.1.

Once an appropriate mesh is determined, based on computation accuracy and cost, analysis will be performed on the aligned gear pair under loads of 50, 100, 150, 200 and 250 Nm. The final study investigates the various misalignments under the same loads as the aligned scenario, where Table 4.2 illustrates the various tests concisely.

		Torque (Nm)				
Misalignment (mm or °)		**50**	**100**	**150**	**200**	**250**
	0.00	R/A/Y/P	R/A/Y/P	R/A/Y/P	R/A/Y/P	R/A/Y/P
	0.01	R/A/Y/P	R/A/Y/P	R/A/Y/P	R/A/Y/P	R/A/Y/P
	0.02	R/A/Y/P	R/A/Y/P	R/A/Y/P	R/A/Y/P	R/A/Y/P
	0.03	R/A/Y/P	R/A/Y/P	R/A/Y/P	R/A/Y/P	R/A/Y/P
	0.04	R/A/Y/P	R/A/Y/P	R/A/Y/P	R/A/Y/P	R/A/Y/P
	0.05	R/A/Y/P	R/A/Y/P	R/A/Y/P	R/A/Y/P	R/A/Y/P
	0.06	Y/P	R/A/Y/P	Y/P	Y/P	Y/P
	0.07	Y/P	R/A/Y/P	Y/P	Y/P	Y/P
	0.08	Y/P	R/A/Y/P	Y/P	Y/P	Y/P
	0.09	Y/P	R/A/Y/P	Y/P	Y/P	Y/P
	0.10	R/A/Y/P	R/A/Y/P	R/A/Y/P	R/A/Y/P	R/A/Y/P
	0.20	Y/P	R/A/Y/P	Y/P	Y/P	Y/P
	0.30	Y	R/A/Y	Y	Y	Y
	0.40	✗	R/A/Y	✗	✗	✗
	0.50	R/A/Y	R/A/Y	R/A/Y	R/A/Y	R/A/Y
	0.60	✗	R/A/Y	✗	✗	✗
	0.70	✗	R/A/Y	✗	✗	✗
	0.80	✗	R/A/Y	✗	✗	✗
	0.90	✗	R/A/Y	✗	✗	✗
	1.00	R/A/Y	R/A/Y	R/A/Y	R/A/Y	R/A/Y

Table 4.2: Misalignment test cases: R = radial, A = axial, Y = yaw, P = pitch misalignment

For simulations involving yaw or pitch misalignment a small amount of radial misalignment (0.1mm) is included to avoid interference between the non-contacting faces, which limits the maximum amount of pitch misalignment to 0.3°, and the yaw misalignment to 1°.

4.1 Mesh Sensitivity

To establish appropriate element sizes for the 3 regions described in Section 3.8, a 2D plane strain FEA was performed on the gear pair with varying mesh

densities.

For the contacting tooth faces a default element size of 0.05mm was used while varying the other regional element sizes, and the element sizes were varied from 0.025mm to 1mm. The non-contacting tooth faces (on the contacting teeth) were given a default mesh size of 0.5mm, to reduce computational cost, and varied in the range 0.06mm to 1mm, and the global elements were given a default size of 5mm and decreased to 0.5mm, where the computation time was deemed too high.

Figure 4.1 shows the influence of the mesh size in the three regions on the rotational deflection of the gear mesh.

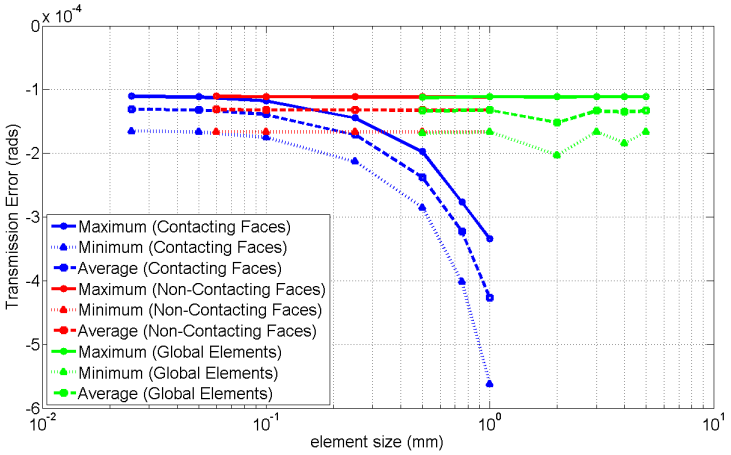

Figure 4.1: Mesh size vs. Transmission Error

In Figure 4.1 the contacting face mesh size has the greatest impact on the results, however variation below an element size of 0.05mm is minimal when compared to the additional computational cost incurred. All other element sizes had little effect on the results for transmission error, with the only other variation seen in the global seeds minimum results, which is due the final point of contact being much lower than expected as shown in Figure 4.2. However there is no relationship present between the size of the global elements and the occurrence of this contact extension, and therefore the erroneous results are not considered and the proceeding results are check for this anomaly.

To gain a converged solution a contact mesh size of 0.05mm is chosen and with this, to maintain a reasonable transitional mesh across the tooth face the non-

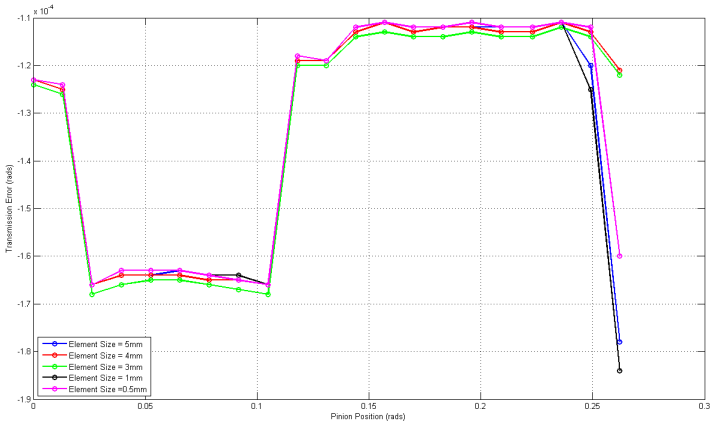

Figure 4.2: TE vs. Pinion angle for various global element sizes

contacting element sizes are set to 0.5mm, and the global seeds are set at 5mm as they have little effect on the results and the use of few elements will reduce the computational cost of analysis.

The results of the finite element model were corroborated with the analytical formula of Kuang and Yang [48, 100] for tooth bending and Hertzian contact stiffness. These stiffnesses were modified to account for the deformation of the gear body through the use of linear finite element models of the gear body under load. In this analytical model the Hertzian contact stiffness, the tooth bending on gear 1 and gear 2 and the gear body bending on gears 1 and 2 are combined as a set of individual stiffness elements in series.

The gear stiffness along the line of action determined by both the finite element contact model and the analytical approach is shown in Figure 4.3.

Figure 4.3 shows that the finite element results are in reasonable agreement with the analytical method. The lower magnitude of mesh stiffness can be attributed to the omission of the shear deformation, axial compression and fillet foundation deformation in the analytical model, while the greater variations during double tooth contact can be attributed to the omission of the complex load sharing relationships during this period. Instead the double tooth contact stiffness is simply taken as the addition of two out of phase tooth stiffnesses.

Of additional note is the smoothing behavior around the transition between

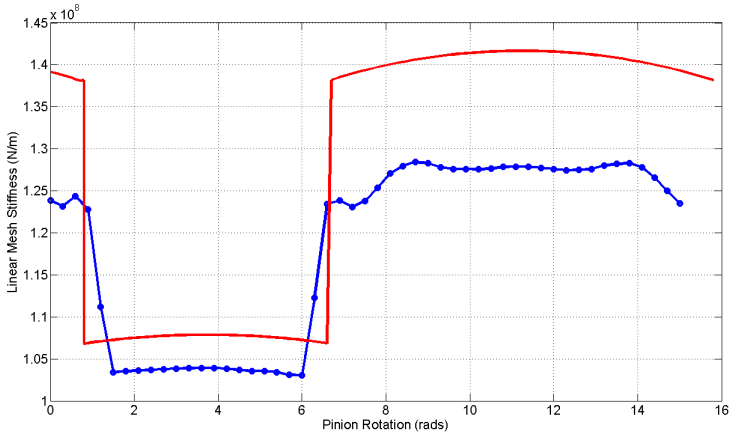

Figure 4.3: Comparison between the finite element derived mesh stiffness and analytical mesh stiffness

single and double tooth contact, which is not seen in the analytical model. This has in the past been attributed to the lengthening of the line of contact as a result of tooth bending.

4.2 Results

This section splits the results up into the various alignment cases, where results from the perfect alignment case at a design load of 100 Nm will be presented first, then variations in the load will be investigated under this alignment. Next the linear misalignment (radial and axial) results will be shown in the same load sequence; and finally the angular misalignments will be shown in the same manner. Where appropriate theoretical relationships are compared against the finite element results to ascertain relationships that can be utilized in the dynamic model to represent the effects seen in contact.

4.2.1 Perfect alignment

With the gears positioned as described in Section 3.2.1 results are obtained at 51 increments over the pinion pitch angle of 15°. Results are given for the mesh stiffness, the load sharing ratio and the reaction forces and compared to theoretical predictions based on the undeformed gear geometry and the free-body forces.

Mesh Stiffness

As described in Section 3.7.1, the mesh stiffness is calculated from the transmission error, which is in turn calculated from the rotational positions of the gears. Figure 4.4 shows the linear mesh stiffness as a function of the pinion rotation angle, where clear regions of single tooth contact (STC) and double tooth contact (DTC) can be seen.

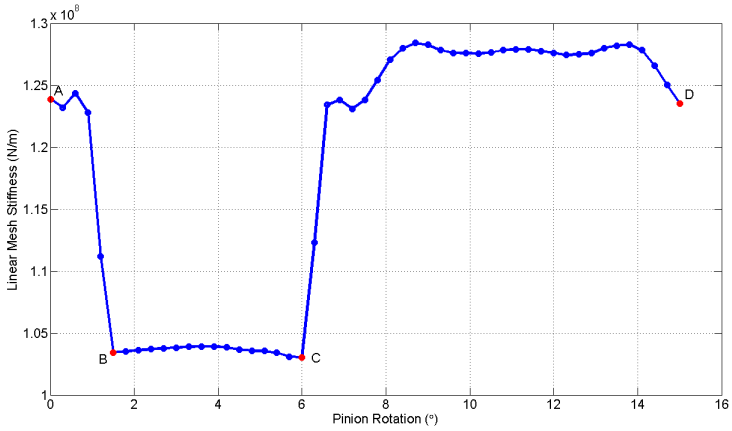

Figure 4.4: Linear mesh stiffness vs. Pinion angle [Perfect Alignment @ 100 Nm]

Between points A to B and C to D, there are two teeth in contact that share the transmitted load; this means that the area of contact is increased and the contact pressure on any individual tooth is decreased. This consequently leads to less deformation of the gears and an increase in the effective stiffness of the gear pair.

Figure 4.4 also indicates mesh stiffness is not constant during single and double tooth contact, this is due to varying tooth stiffness's depending on the position of the loading point along the tooth face. Taking the example of single tooth contact between points B and C; at point B the load is transmitted through a point close to the tooth tip on gear 1 and the tooth root on gear 2, which increases tooth deflection and reduces stiffness. As contact progresses the contact point moves towards the pitch point and the mesh stiffness reaches a maximum. From this point the gears begin to exit contact and the contact point moves towards the tooth tip on gear 2 and the root on gear 1, which in turn decreases the mesh stiffness, much in the same

manner as when the teeth were approaching the pitch point. Due to the comparable sizes of the gears the variation in the mesh stiffness is relatively symmetrical about the pitch point, however this may not hold true with gears of different sizes. The complex nature of the double tooth contact stiffness is most likely due to the different loading positions on the multiple teeth in contact, and the variation in their positions at different rotation angles; it may also be affected by the variation in the load transmitted through the teeth in contact, which will be discussed in the next section.

Another noticeable feature of Figure 4.4 is the softening behaviour at the transition between STC and DTC, which has interesting implications when considering the method of including the time varying nature of the mesh stiffness into the dynamic hybrid model. In some vibration models the mesh stiffness is modelled as a square wave with a severe discontinuity at the transition point [19, 20], however the results obtained from the finite element analysis suggest that this treats the transition to sharply, and ignores the load sharing implications at this point. This concern has been raised recently by Han [101] who investigated the effects of the softening behaviour on the stability of a transmission system under high speed and heavy loading, using Floquet theory. Other methods of representing the mesh stiffness, such as through a sine wave, or a Fourier expansion allow for this softening, however the sine wave cannot easily model the continuous periods of STC or DTC and the Fourier expansion often introduces too much softening around the final transition points (Points B and C) as shown in Figure 4.5.

Also evident from Figure 4.5 is that even with a high order fit the Fourier results over emphasize the small variations during STC and DTC, and only a very high order fit would be able to smooth out these regions.

Since there is no effective analytical method of representing the Finite Element mesh stiffness data in the dynamic model, the best method is to interpolate the data points based on the current pinion rotational position.

The softening seen in Figure 4.4 has been attributed to an effect known as transmission error outside the normal path of contact by previous researchers

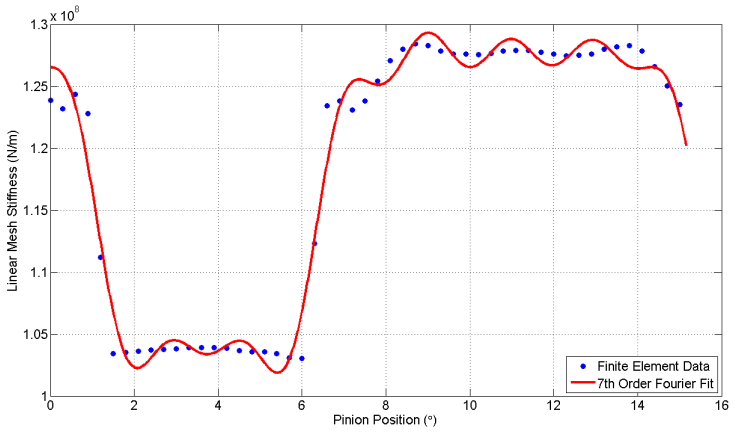

Figure 4.5: 7^{th} order Fourier fit of Mesh Stiffness Data

[101–104] and has been studied in early work performed on gear design leading to the common practice of tooth profile modification, through tip relief [41, 105, 106]. This phenomena occurs as result of tooth bending or pitch errors, which result in the lengthening of the line of contact such that the total angle of contact for a single tooth, and hence the involute contact ratio, increases.

To show the increase in the length of the line-of-action, the contact ratio can be determined approximately from Figure 4.4, by dividing the angle occupied by single tooth contact by the pitch angle, which will give the percentage of time spent in single tooth contact and which can then be used to calculate the contact ratio; this equals 1.62. The theoretical contact ratio can be calculated as.

$$\varepsilon = \frac{\sqrt{r_{a1}^2 - r_{b1}^2} + \sqrt{r_{a2}^2 - r_{b2}^2} - C' \sin\phi'}{P \cos\phi'} \tag{4.1}$$

Where r_a is the addendum radius, r_b is the base radius, C' is the current centre distance, P is the circular pitch and ϕ' is the current pressure angle:

$$\phi' = \cos^{-1}\left(\frac{r_{b1} + r_{b2}}{C'}\right) \tag{4.2}$$

where the perfectly aligned gears described in Table 4.1 have a contact ratio of 1.607, which shows that the results obtained through the FEA of gear contact show

lengthening of the line of action, based on the rotational position of the gears.

Load Sharing Ratio

As previously mentioned the LSR is an important parameter when considering load dependent effects on individual teeth, such as friction, and is derived from the integral of the normal nodal forces across the tooth face. Figure 4.6 shows the LSR for a single contact cycle, where it is compared against a theoretical LSR suggested by Pedrero *et al* [76]. This relationship states that between contact initialisation and the start of single tooth contact the load transmitted through the tooth increases linearly between a third and two thirds (Points A - B), and that at the lowest point of STC the LSR increases instantly to one (Point B - C). As a new tooth enters behind the current tooth the LSR reduces from one to two thirds (Point D - E) and as the current tooth exits contact the LSR reduces from two thirds to one third (Point E - F). Pedrero *et al* [76] state that this LSR form remains relatively consistent independent of the tooth geometry and transmitted load being analysed; however this has not been analysed.

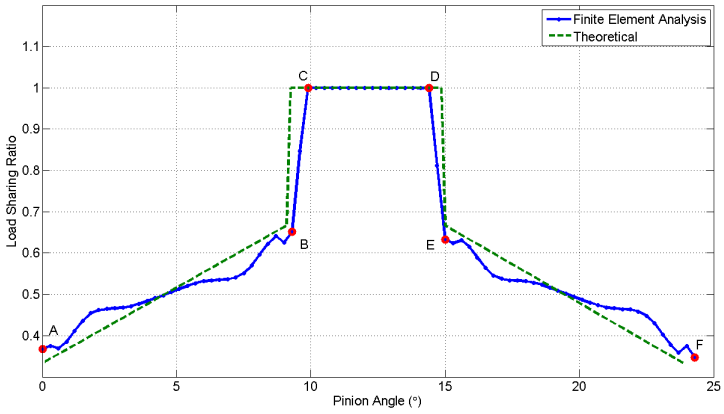

Figure 4.6: Finite Element and Theoretical LSR vs. Pinion Angle

To construct the theoretical LSR, knowledge of the pinion angles corresponding to the points A - F in Figure 4.6 is needed, where if Point A is taken as zero, Point D/E is equal to the pitch angle (θ_P) and Point F is the angle of action (θ_δ). To calculate the angle of action requires knowledge of the contact ratio acquired through Equation (4.1), which can be used to calculate the length of the arc of

action on the pitch circle (δ) and subsequently the angle of action (θ_δ) as shown.

$$\delta = \varepsilon P \tag{4.3a}$$

$$\theta_\delta = \delta / r_2' \tag{4.3b}$$

where r_2' is the current theoretical pitch radius of gear 2

$$r_2' = \frac{C' r_{b2}}{r_{b1} + r_{b2}} \tag{4.3c}$$

Therefore Point B/C can be taken as the difference between the total contact angle and the pitch angle ($\theta_\delta - \theta_P$), as summarised in Table 4.3.

Description	Point	Angle (°)
Tooth enters contact	A	0
Beginning of STC	B/C	$\theta_\delta - \theta_P$
End of STC	D/E	θ_P
End of contact	F	θ_δ

Table 4.3: Summary of contact points in Figure 4.6

As can be seen in Figure 4.6 the biggest discrepancies occur at the transitions between single and double tooth contact and at the end of contact, this is thought to be due to the softening behaviour seen in the mesh stiffness results and the lengthening of the line of contact slightly. In general the theoretical relationship proposed by Pedrero *et al* [76] represents the finite element derived LSR well, and allows for a simpler linear piecewise relationship of the LSR to be formulated for calculation of individual tooth loads, which will be derived in Section 6.3.2.

Reaction forces

In perfectly aligned spur gear contact all forces transmitted through the teeth act along the line-of-action LOA, no axial forces (RF3) exist and the moments about the vertical (RM2) and horizontal axes (RM1) are balance about the centre of mass. In the finite element analysis the OLOA forces are small compared to the LOA forces as can be seen in Table 4.4, which compares the finite element derived

reaction forces with ratios to the normal tooth load for translational forces and to the applied torque for reaction moments.

	Pinion		Gear		Theory	
	Absolute	%	Absolute	%	1	2
Normal	1702.68	100	1702.68	100	1702.68	1703.11
Torque	100	100	96	100	N/A	N/A
RF1	582.87	34.2	-582.87	34.2	582.35	582.5
RF2	1600.05	94	-1600.05	94	1600	1600.4
RF3	-0.0007	4e-5	0.0002	1e-5	0	0
RM1	6.7e-5	6.7e-5	-6.7e-5	7e-5	0	0
RM2	2.1e-5	2.1e-5	6.7e-5	7e-5	0	0
RM3	0	0	96.005	100	96	96.024

Table 4.4: Average reaction forces/moments - Aligned contact, 100 Nm load

Table 4.4 shows that the finite element derived OLOA reaction forces are negligible compared to the gross forces along the LOA, and compare well with theoretically derived formula of normal contact. Theory 1 uses the known applied torque of 100 Nm and multiplies by the base radius of gear 2 (gear) to achieve the normal tooth load along the LOA, whereas Theory 2 calculates the normal tooth load as the average of the finite element derived normal forces throughout contact.

The slight differences in the reaction forces present in the LOA (RF1 and RF2) are due to the variations in the theoretical and finite element normal tooth load and slight variations in the pressure angle as a result of tooth bending, however under perfect alignment and limited bending the variations are very small and therefore the normal forces can be determined from the pressure angle and the tooth loading.

Force analysis

The results above show the variation in the mesh stiffness, load sharing ratio and the reaction forces under perfect alignment and a design load of 100 Nm. Theoretical prediction are made based on the undeformed gear geometry and these must be tested against variations in loading conditions. Figure 4.7 shows the variation in the rotational mesh stiffness for loads between 50 and 250 Nm, where it can be seen that force has an effect on the stiffness value and the shape of the mesh stiffness.

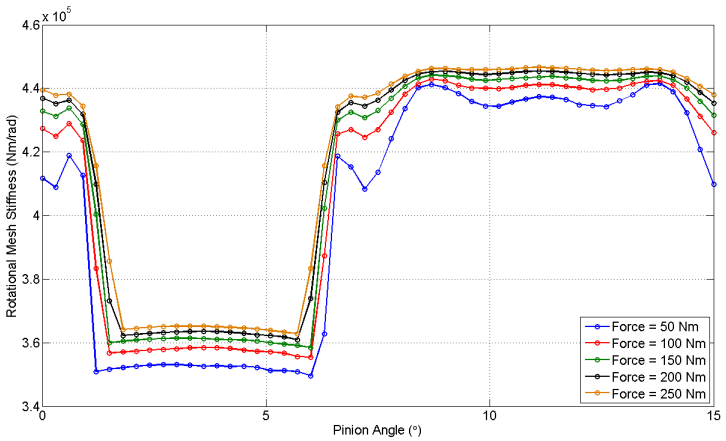

Figure 4.7: Mesh stiffness vs. pinion angle under various applied loads

Increased loading appears to increase the stiffness of the gear contact, which is likely due to nonlinearities either through contact or through bending of the gear tooth; however the range of forces studied are particularly wide and it is not envisaged that the fluctuations in the dynamic contact forces will be this great. Even over this range of forces the mesh stiffness only varies by around $\pm 2\%$ in regions of single and double tooth contact; there is however greater variation during the transition between single and double tooth contact due to increased softening. This softening is caused by increased tooth bending and lengthening of the line of contact, which reduces the peaks present in the low load mesh stiffness results just before and after single tooth contact, where contact is made through the tooth tip. At this point the tooth tip is represented by a single finite element and contact is made soley through that element; similar reductions can be achieved by introducing a small fillet at the tooth tip so that contact can be spread across a number of elements, with the resulting mesh stiffness's illustrated in Figure 4.8.

The introduction of the fillet at the tooth tip reduces the softening of the transition between single and double tooth contact as the fillet reduces the effects of contact outside the normal path of action and corner contact, which results in sharper transitions and a longer period of single tooth contact. This feature of tooth modification is often why it is used within gear design, to reduce contact outside the normal path action and hence vibration at specified design loads caused by excessive

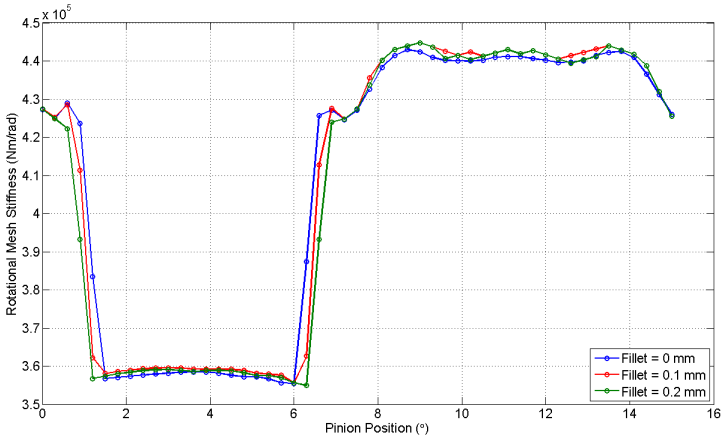

Figure 4.8: Mesh stiffness vs. pinion angle for various tooth fillets

tooth bending.

The tooth bending can also be witnessed in the LSR plots at varying loads given in Figure 4.9 where there is a clear extension of the line of action at high load, resulting in an increased angle of action and a shorter period of single tooth contact. There is also evidence of greater softening of the transitions as present in Figure 4.7; however it is noted again that the range of forces is much wider than expected and that the variations under dynamic loading will be much smaller, and could be neglected. This indicates that the LSR assumption made by Pedrero *et al* [76], which is based purely on the undeformed geometry and independent of the transmitted load, is reasonable for the load cases envisaged.

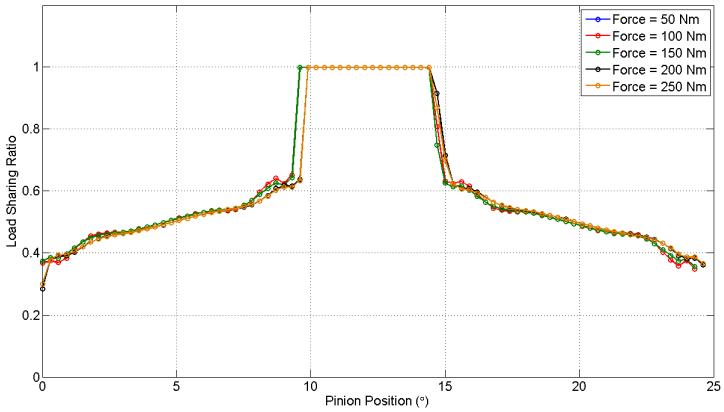

Figure 4.9: Load Sharing Ratio under perfect alignment and varied load

Finally, studying the reaction forces in the previous section the forces in the vertical and horizontal direction were determined from the applied torque (T) and the undeformed pressure angle (ϕ) in the form:

$$RF1 = (T/r_b)\sin\phi \tag{4.4a}$$

$$RF2 = (T/r_b)\cos\phi \tag{4.4b}$$

where r_b is the base radius of the gear. This relationship is tested for the investigated loads and compared in Figure 4.10 with the finite element derived loads, and shows good agreement with errors between 0.06 and 0.26% over the load range for RF1 and even less for RF2. The increases in error are likely due to the variation in the true pressure angle as a result of increased tooth bending under higher load.

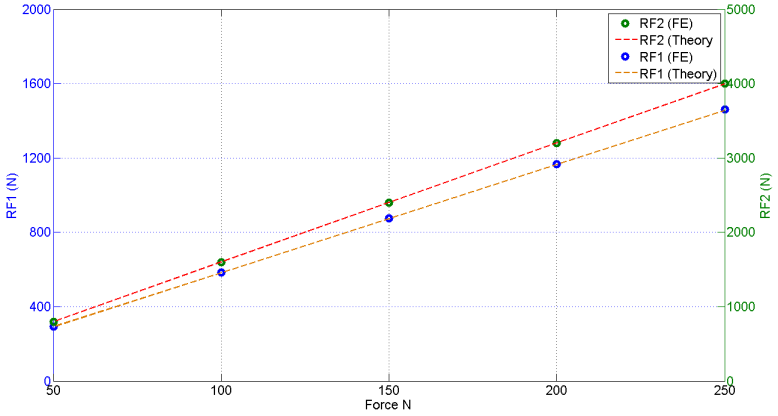

Figure 4.10: Mean reaction forces under perfect alignment and varied load

Through the finite element derived reaction forces the true pressure angles can be determined through the inverse tangent of the ratio RF1/RF2, which are given in Table 4.5. This clearly shows the increased pressure angles as a result of increased load, however the errors attributed to the variation in pressure angle are small compared to the gross load and as such can be neglected.

Conclusions

Observing the finite element analysis results under perfect alignment it has been found that in the dynamic model the mesh stiffness must be represented as

Load (Nm)	Forces (N)		Pressure Angle (°)
	RF1	RF2	
50	291.355	800.041	20.0104
100	582.874	1600.049	20.0159
150	874.710	2400.056	20.0245
200	1167.145	3200.171	20.0376
250	1459.633	4000.238	20.0464

Table 4.5: Variation in pressure angle with applied load

an interpolation of the finite element results, since the softening of the transitions between single and double tooth contact and the varying tooth stiffness under single and double tooth contact mean the use of a square wave approximation is unsuitable. The other possible methods of representing the stiffness as a sine wave or as a Fourier expansion are also unsuitable, with the former unable to model continuous periods of single/double tooth contact and the latter requiring a very high order expansion to correctly model the response and avoid "over-softening" the transition points. The mesh stiffness also increases as the applied load increases and more pronounce softening is found under higher loads, however the effects are small over the range of forces of interest and therefore can be neglected.

The LSR has be determined and compared to the theoretical relationship proposed by Pedrero *et al* [76], where softening is present around the transition points as with the mesh stiffness and slight lengthening of the line of action is also observed. As with mesh stiffness the increased applied load introduces more softening and also increases the length of the line of action through additional tooth bending, however the amount can again be neglected due to the range of forces of interest. The theoretical prediction based on the tooth geometry has been shown to fairly represent the LSR for the gear under load, and as such is a fast method of determining the individual tooth loads.

The finite element reaction forces taken from the gear centres have been determined and compared against theoretical results based on free-body force balancing. As predicted the OLOA reaction forces are negligible compared to the applied loading and the main reaction forces in the LOA directions. Small errors

have been found in the determination of the the lateral LOA reaction forces due to variations in the pressure angle, which increase as the loads are increased; however in general the theoretical forces have compared well and the variations over the range of loads studied due to varying pressure angles are insignificant and can therefore be neglected.

4.2.2 Radial Misalignment

As mentioned in Section 3.2.2 radial misalignment is effectively a variation in the centre distance between mating gears and it is predicted that since the contacting faces remain parallel and the contact lines are uniformly distributed along the tooth width that no additional OLOA forces will be generated. It is also believed that since the contact points move closer to the tooth tip there will be increased tooth bending and a reduction in the mesh stiffness for greater radial misalignments. It is also predicted that with the contact moving predominately towards the tip the length of the line of action will be reduced and therefore the contact ratio will reduce.

Mesh Stiffness

In Section 3.6 the analysis procedures (Steps) are described, where the gears are rotated slightly to bring them into contact; when radial misalignment is introduced the gear teeth no longer sit perfectly together and there is a gap between the contacting faces, known as backlash. With increased radial misalignment comes increased backlash, and when calculating the mesh stiffness, as described in Section 3.7.1, the transmission error results include the free rotation of the gear to overcome the backlash. This backlash rotation must be known and removed from the transmission error results before calculating the gear mesh stiffness, which can be achieved through the use of the involute function to calculate the arc on the pitch circle that describes the backlash, as shown in Equation (4.5a):

$$b_c = 2C' \left(\text{inv}\phi' - \text{inv}\phi\right) \tag{4.5a}$$

Where C' is the actual centre distance, ϕ is the original pressure angle at the ideal centre distance (C), ϕ' is the pressure angle at C' and inv is the involute function

calculated for ϕ as.

$$\text{inv}\phi = \tan\phi - \phi \tag{4.5b}$$

The angular backlash that is required, to be subtracted from the calculated transmission error, can then be found as.

$$b_\theta = b_c / r_2' \tag{4.5c}$$

where r_2' is the gear pitch radius at a centre distance of C'. In the above equations the parameters ϕ' and r' can be calculated using Equations (4.2) and (4.3c) respectively, and the new centre distance can be calculated by the addition of the ideal centre distance, given in Equation (3.17), to the radial misalignment.

The rotational mesh stiffness results for radial misalignments of 0, 0.05, 0.1, 0.5 and 1 mm are given in Figure 4.11 for a design load of 100 Nm. In this figure it is clearly seen that increased radial misalignment reduces the mesh stiffness, which is most likely due to increased tooth bending, rather than increased contact deformation since the contacting force and shape remains unchanged.

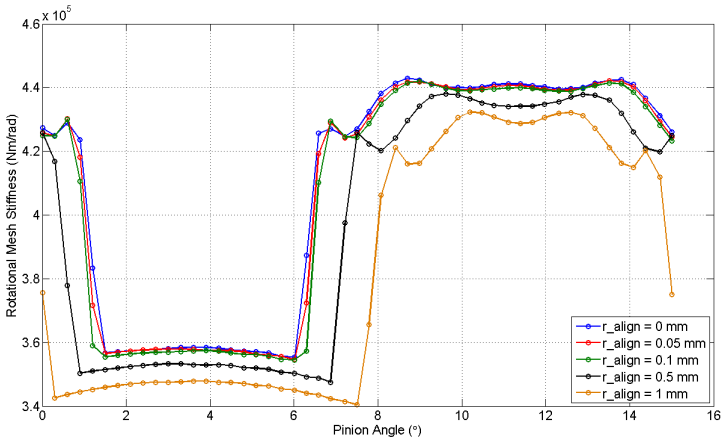

Figure 4.11: Rotation mesh stiffness vs. pinion rotation for various radial misalignments at 100 Nm

The variation in the mesh stiffness is illustrated in Figure 4.12, which includes all the radial misalignments studied at 100 Nm and shows the variation of maximum, minimum and mean mesh stiffness as a function of radial misalignment. This figure

shows that the maximum mesh stiffness is reduced by about 2.5% while the minimum mesh stiffness is reduced by around 4%.

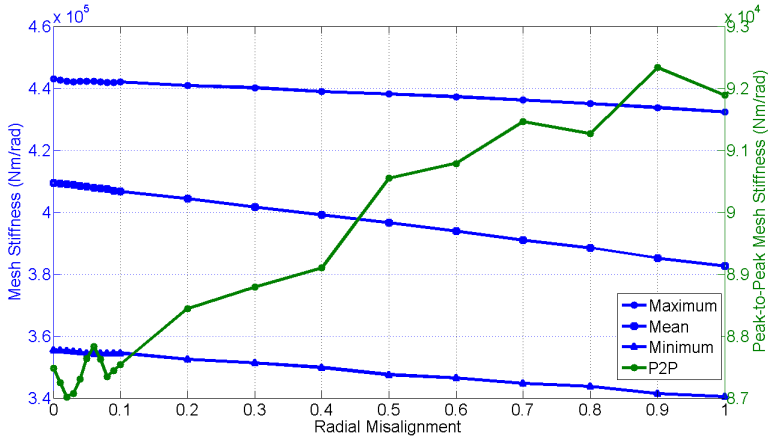

Figure 4.12: Rotation mesh stiffness vs. radial misalignment at 100 Nm

The reduction in mean mesh stiffness observed in Figure 4.12 is much greater than the maximum and minimum mesh stiffness and is solely due to the reduction in the contact ratio, which results in a higher percentage of single tooth contact (low stiffness). This can be seen clearly in the mesh stiffness plots of Figure 4.11 and in the load sharing ratio results.

Load Sharing Ratio

In Section 4.2.1, the LSR is compared against a theoretical relationship based on the geometric contact positions under perfect alignment. When radial misalignment is introduced the contact positions described in Table 4.3 vary, however in Equations (4.1) to (4.3) the parameters used to calculate the angle of action are based on an arbitrary centre distance, and the pitch angle is independent from the radial misalignment. This means that under any radial misalignment the theoretical load sharing ratio can be drawn, as shown in Figure 4.13, where again a reasonable approximation can be made.

This theoretical LSR assumption is found to be valid for all radial misalignments studied, when based on contact positions given in Table 4.3, and Equations (4.1) to (4.3). Figure 4.14 below shows the LSR plots for various misalignments, where the reduction in the contact ratio can be clearly observed as an increase in

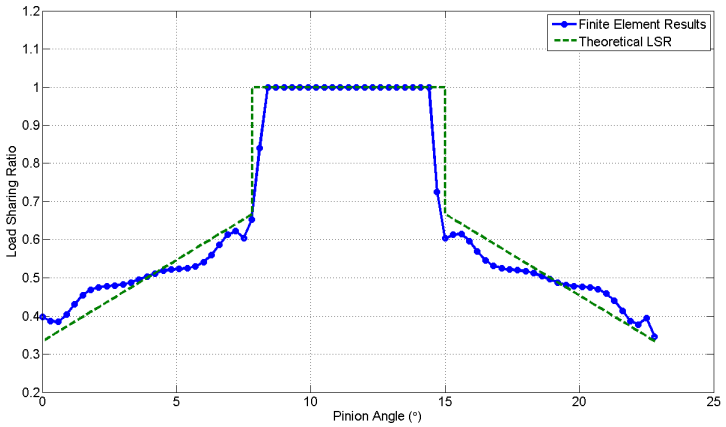

Figure 4.13: LSR at 100 Nm and 0.5 mm radial misalignment, compared to theoretical assumption

the portion of single tooth contact coupled to the reduction in the angle of contact.

In Figure 4.14 the LSR is plotted against sample points during the finite element simulation to illustrate the varying angles at which the teeth enter and leave contact. In each simulation the gears are rotated by the pinion pitch angle, which is equal to 15°, and there are 51 sample during the simulation equating to an angular increment of around 0.3° per sample point. This shows that the reduction in the complete angle of action due to a radial misalignment of 1 mm is around 3°, and since the pitch angle remains unchanged, this leads to an increase in the angle of single tooth contact of 3°.

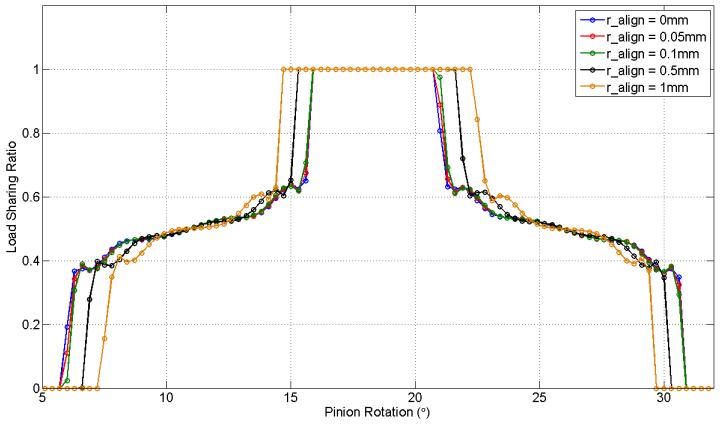

Figure 4.14: LSR vs. sample points for various radial misalignments at a load of 100 Nm

Reaction Forces

As with the load sharing ratio a theoretical relationship has been determined while analysing the reaction forces under perfect alignment, and as with the load sharing ratio the decomposition of the normal tooth loads into the vertical and horizontal directions is dependent on the current pressure angle determined in Equation (4.2). Utilizing Equation (4.2) along with Equations (4.4), the theoretical reaction forces can be determined as seen in Figure 4.15, where they are compared against the finite element derived reaction forces.

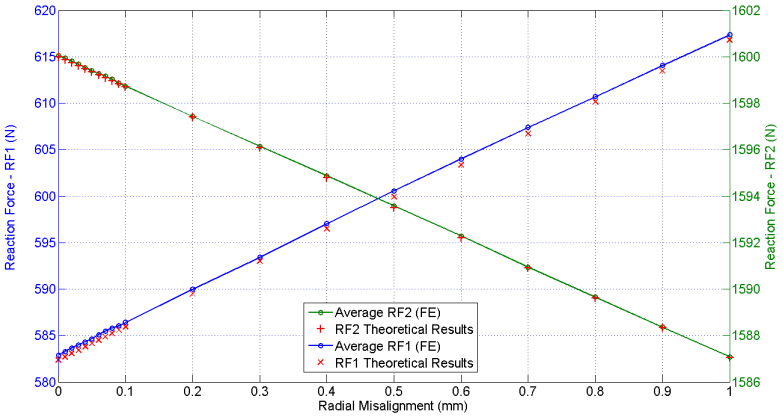

Figure 4.15: Mean reaction forces vs. radial misalignment: comparison between finite element and theoretical results

In Figure 4.15 the theoretical reaction forces for RF1 are approximately 0.075% lower than the finite element results across the misalignment range, while the results for RF2 are even closer at 0.003% at all misalignments. This would indicate that the extra tooth bending leading to variations in the pressure angle and decomposition of the normal tooth loads are negligible compared to the theoretical loads based on free-body assumptions.

It is also assumed that the OLOA forces are again negligible compared to the LOA forces because the normal loads still act solely along the LOA and the load is evenly distributed across the tooth face; and as shown in Table 4.6 this is a reasonable assumption. In this table the axial force (RF3) is around 4E-05% of the normal tooth load, while the reaction moments are constantly much smaller than

the applied load of 100 Nm, indicating that the OLOA forces can be neglected under radial misalignment.

Radial Misalignment	OLOA Forces		
	RF3 (N)	RM1 (Nm)	RM2 (Nm)
0.00 mm	-7.0E-04	6.7E-05	2.1E-05
0.05 mm	-7.0E-04	6.8E-05	2.0E-05
0.10 mm	-7.1E-04	6.8E-05	2.1E-05
0.50 mm	-7.1E-04	9.0E-05	1.2E-05
1.00 mm	-7.2E-04	1.2E-04	1.4E-06

Table 4.6: Radial misalignment OLOA forces

Force analysis

With techniques in place to predict the mesh stiffness, load sharing ratio and reaction forces under radial misalignment, these predictions are analysed under varying loads to determine if they are still applicable. By investigating the mesh stiffness under varying load and misalignment, Figure 4.16 illustrates the variation in the mesh stiffness with the rotational position of the pinion under different applied load, for radial misalignments of 0, 0.1, 0.5 and 1 mm.

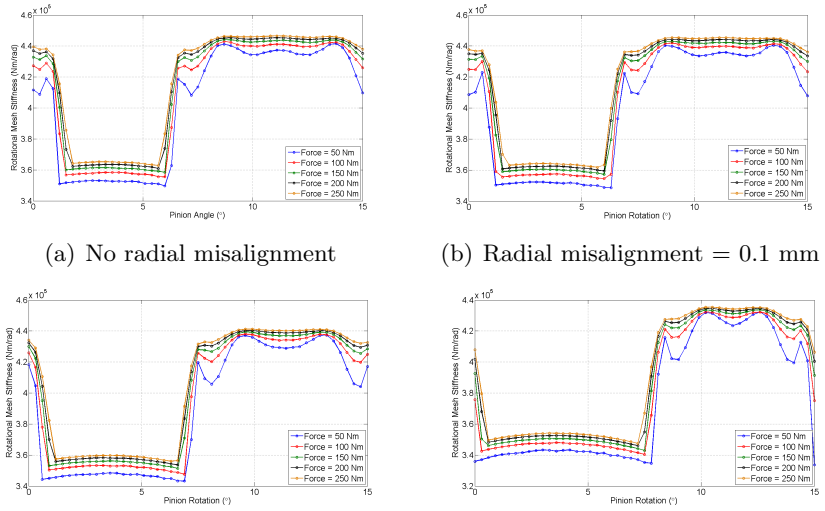

(a) No radial misalignment

(b) Radial misalignment = 0.1 mm

(c) Radial misalignment = 0.5 mm

(d) Radial misalignment = 1 mm

Figure 4.16: Effects of load on mesh stiffness under various radial misalignments

Figure 4.16 shows that the variation in the mesh stiffness due to load is independent of the radial misalignment, since the variations under different loads can be

seen as comparable across the misalignment range. This can be better illustrated by taking the normalized mesh stiffness results, by dividing all the position dependent data by the results at 100 Nm, and plotting individual surface plots for each load case. These results are displayed in Figure 4.17, where it can be seen that the variation in the normalized mesh stiffness remains constant during periods of single and double tooth contact and is therefore independent of the radial misalignment. The peaks in the data occur at the transitions between single and double tooth contact and are due to variations in the contact positions as a result of radial misalignment, as observed in Figure 4.11, which give unrealistic peaks due to comparing single tooth contact points with double tooth contact.

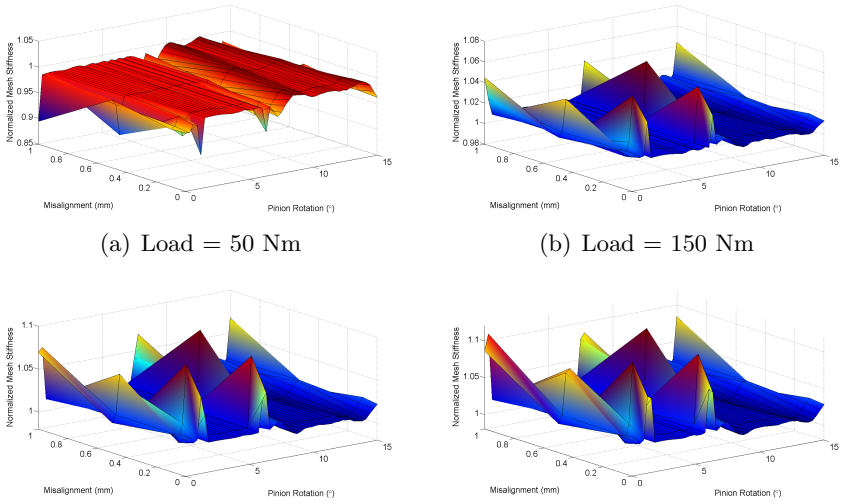

(a) Load = 50 Nm

(b) Load = 150 Nm

(c) Load = 200 Nm

(d) Load = 250 Nm

Figure 4.17: Effects of load and radial misalignment on normalized mesh stiffness with respect to design load

As with perfect alignment the small variation of the mesh stiffness over the large range of applied loads indicates that the effects on the mesh stiffness of load under radial misalignment can be neglected. It is believed that the slight non-linearities in the mesh stiffness are due to the increased Hertzian contact stiffness under applied load.

It has been shown in the finite element analysis of perfectly aligned gears that the LSR is only slightly altered by increased applied load, through increased

tooth bending and the lengthening of the line of contact. Figure 4.18 shows the variation in the LSR as a result of varying load for the design cases illustrated in Figure 4.16.

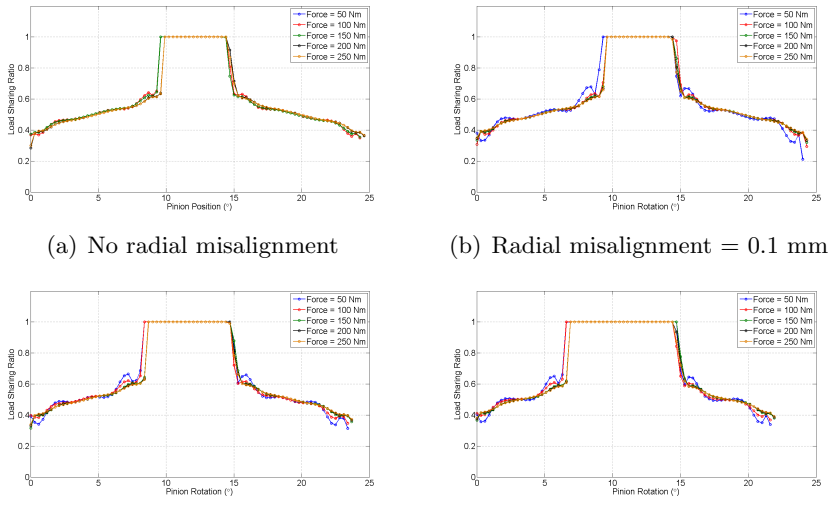

(a) No radial misalignment

(b) Radial misalignment = 0.1 mm

(c) Radial misalignment = 0.5 mm

(d) Radial misalignment = 1 mm

Figure 4.18: Effects of load on load sharing ratio under various radial misalignments

From these LSR plots, the same conclusions can be reached as with the perfectly aligned scenario, in that the increased load causes increased bending and hence lengthening of the line of contact, however the amount is negligible over the range of loads of interest. The increased load also helps to better define the contact region as it moves through contact since the increased contact area means that more elements are involved in contact and help better define the stress distribution; this is indicated by the smoothing of the double tooth contact areas.

The reaction forces are still assumed to act only along the line of action, and this is proven in the results with negligible axial force (RF3) and negligible moments about the horizontal and vertical axes (RM1 and RM2). In previous sections the reaction forces under perfect alignment and radial alignment are compared again theoretical calculations based on free-body force balancing, which have been able to accurately predict the finite element derived reaction forces. In Figure 4.19 the finite element reaction forces are compared to the theoretical relationship for varying

radial misalignments and loads, where the finite element results are displayed as a surface and the theoretical results are displayed as a 3D scatter plot.

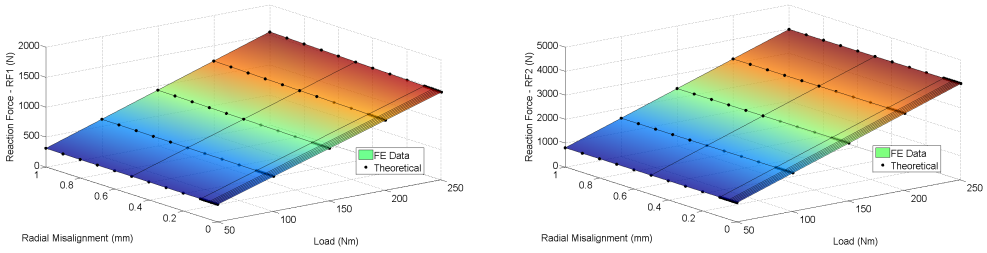

(a) Horizontal reaction force (RF1)

(b) Vertical reaction force (RF2)

Figure 4.19: Effects of load and radial misalignment on the line-of-action forces: Finite element and theoretical results

These figures show that under varying radial misalignment and load the free-body assumptions are an acceptable method of determining the line-of-action forces, and introduce very little error as an assumption.

Conclusions

Through the analysis of gear contact under radial misalignment and varied load it has been found that increased radial misalignment decreases the length of the line of contact and subsequently reduces the contact ratio, which leads to variations in the contact cycle with greater periods of single tooth contact. This has a major impact on the shape of the mesh stiffness curve and the load sharing ratio, where the mesh stiffness must now be determined by the angular position of the pinion and the radial misalignment; however Equations (4.1) to (4.3) have been successful at approximating the load sharing ratio under varying misalignment using the unde-formed gear tooth geometry. Allied to the effect on the contact ratio is a reduction in the mesh stiffness with increased misalignment, as the contact positions move towards the tooth tip, which in turn leads to increased tooth bending.

Under varying load the mesh stiffness and LSR have been found to change little, with the variation in the mesh stiffness comparable across all misalignments and negligible change in the LSR due to lengthening of the line of contact.

The theoretical reaction forces along the line-of-action previously determined

based on free-body force balancing have been further corroborated with varied load and radial misalignment, where the pressure angle used to determine the decomposition of the normal tooth loads into the horizontal and vertical directions has been calculated based on the actual centre distance. Off-line-of-action force have remained insignificant throughout the simulations as predicted.

4.2.3 Axial Misalignment

The second form of lateral misalignment is along the axial direction and is a means of reducing the effective contact width across the tooth face, which is believed to induce greater deformation and introduce OLOA moments due to non-uniform distribution of the load across the tooth face. Misalignments in the range of 0 - 1 mm are investigated to determine the effects on the mesh stiffness, load sharing ratio and the reaction forces as any greater misalignment would be highly visible during installation and unlikely due to dynamic deformation in a real system. Finally the variation in the static parameters under different applied loads are determined to investigate the load dependent effects.

Mesh Stiffness

It is predicted that under axial misalignment there will be a decrease in the contact area across the tooth face leading to increased contact pressure and contact deformation, which will subsequently decrease the mesh stiffness. Figure 4.20(a) shows the mesh stiffness plots for misalignments of 0, 0.1, 0.5 and 1 mm at a load of 100 Nm; from these plots it is apparent that axial misalignment causes a reduction in the mesh stiffness, which is constant throughout the contact cycle. However in Figure 4.20(b) the results are normalized across the contact cycle with respect to the aligned case, which show that axial misalignment has a greater effect on the single tooth contact zone. This is marginal and is likely due to the slight nonlinearity in the contact deformation.

Figure 4.20(b) also suggests that although imposed misalignment may have an impact on the mesh stiffness, the likely degree of dynamic misalignment will have little influence. This is because even at an axial misalignment of 1 mm the

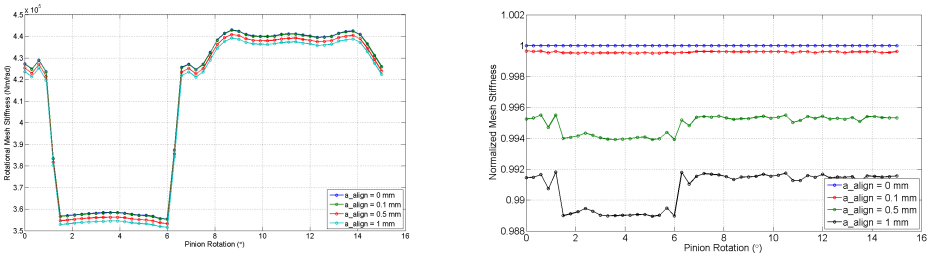

(a) Mesh stiffness (b) Normalized mesh stiffness

Figure 4.20: Mesh stiffness vs. rotation under varied axial misalignment at 100 Nm

mesh stiffness is on average only reduced by around 1%, such that under likely dynamic misalignments the variation in mesh stiffness will be much lower and could be neglected.

Load Sharing Ratio

As in previous sections the LSR is determined for a single tooth over its contact cycle at various misalignments under an applied load of 100 Nm, with the results for axial misalignments of 0, 0.1, 0.5 and 1mm given in Figure 4.21 to illustrate a spread of the obtained results over the misalignment range.

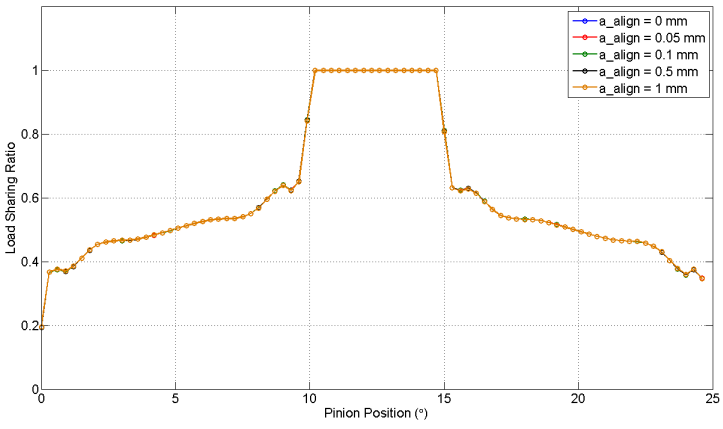

Figure 4.21: Effect of axial misalignment on LSR

This figure shows that even with the decreased mesh stiffness described in Figure 4.20(a) the LSR is unchanged for increased axial misalignment, and can therefore be considered independent of axial misalignment for the range considered. This is likely due to the LSR being more susceptible to tooth bending while increased

axial misalignment does not vary this significantly; this suggests that axial misalignment in this range increases deformation through contact deformation rather than through tooth bending.

Reaction Force

It is predicted that since axial misalignment moves the contact area towards one edge of the tooth, and away from the other, that the introduction of axial misalignment will generate moments in the OLOA direction about the gear centre of mass. It is also predicted that since the angle and direction of the line-of-action is unchanged, the normal LOA forces will remain constant; this is proved in the finite element simulations, where the reaction forces RF1 and RF2 vary by -0.005% and 0.0002% respectively across the misalignment range. This corroborates the assumption that increased axial misalignment has little effect on the tooth bending, which would lead to greater variation in the pressure angle and the composition of the LOA reaction forces.

Figure 4.22 illustrates the variations in the reaction moments RM1 and RM2 as a function of the axial misalignment, where there is seen to be an almost linear relationship.

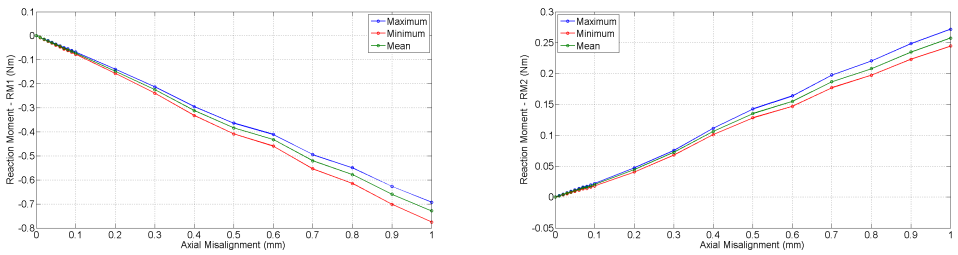

(a) Reaction moment RM1 (b) Reaction moment RM2

Figure 4.22: Effects of axial misalignment on the off-line-of-action reaction moments

To predict this behaviour analytically, the active tooth width, the area in contact, can be split into a discrete number of points and a uniformed distribution of the normal load, decomposed into vertical and horizontal forces, can be applied. The moments about the horizontal (RM1) and vertical (RM2) axes can then be

found using the axial distance to the centre of mass, which can be assumed to be the centre of the facewidth; these are then summed across the facewidth to determine the total moment. This can be summarized in the equation below,

$$RM1 = \frac{N \cos \phi}{n} \sum_{i=1}^{n} z_i \tag{4.6a}$$

$$RM2 = \frac{N \sin \phi}{n} \sum_{i=1}^{n} z_i \tag{4.6b}$$

where N is the normal tooth load, n are the number of discrete points along the tooth face and z_i is the axial position of the ith discrete point from the centre of mass. In general, when using a uniformed distribution, it is found that the reaction moments can be found through multiplication of the decomposed normal contact forces ($N \cos \phi$ and $N \sin \phi$) and the centre of contact, which is equal to half the axial misalignment. When comparing this approximation to the finite element derived data it is found that the theoretical prediction overestimates the reaction moments, for example at 1 mm misalignment the theoretical prediction is 9.75% higher for RM1 (0.8 vs 0.729 Nm) and 13.1% higher for RM2 (0.291 vs 0.257 Nm). This can be attributed to two features, the first is that the force is not uniformly distributed across the tooth face and therefore the centre of pressure is not exactly half the axial misalignment, and the second is that a further moment exists due to an axial force.

When a misalignment is introduced the symmetry of the tooth load distribution may not be satisfied, which can be seen by taking an example of an axial misalignment of 0.5 mm at 100 Nm load, where it is predicted using the uniform distribution model that the reaction moments will equal 0.4 Nm (RM1) and 0.1456 Nm (RM2). Figure 4.23 shows the gear reaction moments as a function of the pinion angle, where the average moments are 0.3837 Nm (RM1) and 0.1353 Nm (RM2), 4% and 7% lower than the theoretical predictions respectively.

In the theoretical model the centre of pressure equals 0.25 mm from the centre of the tooth face; however in Figure 4.24(a) the centre of the contact pressure is tracked through a single contact cycle for three teeth in contact, which shows that

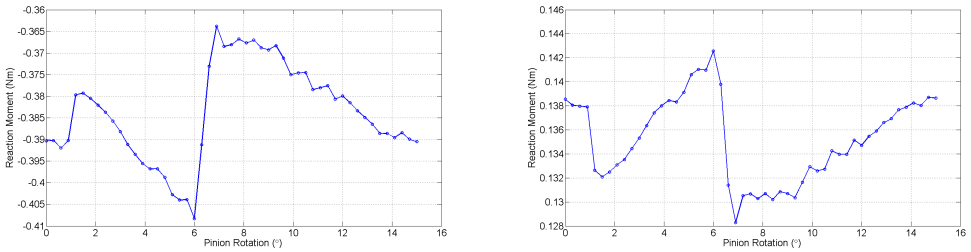

(a) RM1 (b) RM2

Figure 4.23: Reaction moments vs. pinion rotation. 0.5 mm axial misalignment and 100 Nm load.

the centre of pressure varies during contact. By multiplying the centre of pressure by the normal tooth loads decomposed into RF1 and RF2 a comparison between the reaction moment and the moment due to the offset of the centre of pressure can be determined, which is shown in Figure 4.24 for both RM1 and RM2.

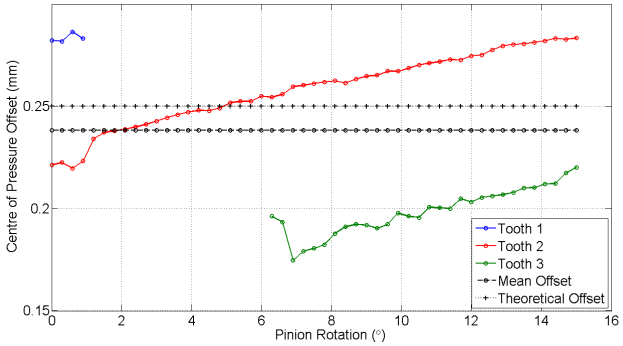

(a) Centre of pressure variation

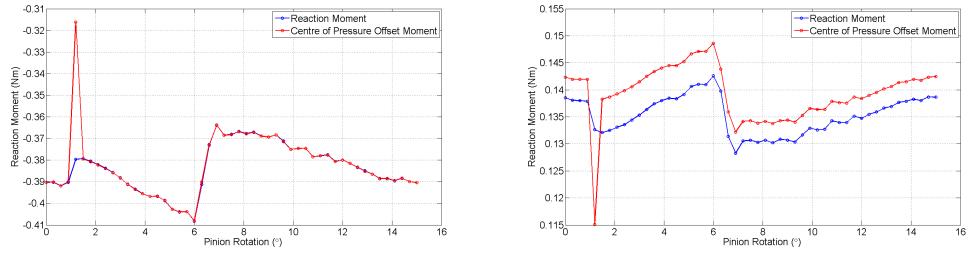

(b) RM1 (c) RM2

Figure 4.24: Reaction moments vs. pinion rotation. 0.5 mm axial misalignment and 100 Nm load compared against moment due to offset of centre of pressure.

The variation in the centre of pressure through contact is due to the tilting of the teeth as they travel through contact; for example, as two teeth enter contact

the load is transmitted through the tip of tooth 1 and the root of tooth 2. The deformation of tooth 1 is greater than tooth 2 and since an axial misalignment is imposed tooth 1 tilts more than tooth 2 and the centre of pressure moves towards the leading edge. As the teeth move through contact the load begins to move to the root of tooth 1 and the tip of tooth 2, therefore tooth 2 deforms more than tooth 1 and the centre of pressure moves accordingly. This tilting is shown in Figure 4.25 where the deformed coordinates of a line traveling across the face of the tooth are plotted in reference to its theoretical rigid body coordinates at two contact positions.

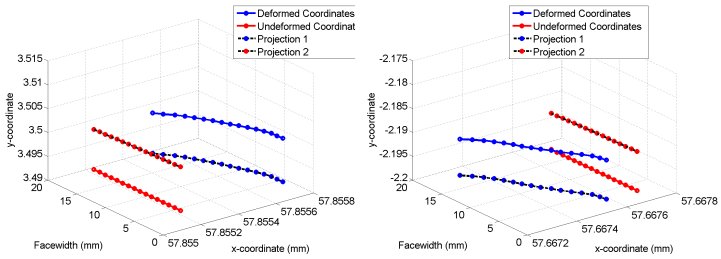

(a) Pinion rotation = 3° (b) Pinion rotation = 8.1°

Figure 4.25: Comparison between deformed tooth coordinates and rigid body coordinates

These figures show that at a pinion rotation of 3° the elements on the far side of the tooth face deform less than those on the nearside, where the variation across the tooth face is more prevalent in the x-coordinates since the overall deformation in this direction is less than in the y-coordinate. This suggests that the pressure on the nearside is slightly higher than on the far side and therefore the contacting faces are not parallel in contact. The effect is then reversed at 8.1° where more deformation is seen on the far side, which suggests that the tilting direction has changed and the centre of pressure moved as a result of this.

The larger variation in RM2 seen in Figure 4.24 is due to the axial force, which causes a moment about the two OLOA axes, as demonstrated in Figure 4.26, where the geometric limits of contact are shown.

Given a constant axial force the moments about the gear are about 5-6 times greater for RM2 compared to the moment RM1, since during contact the geometric

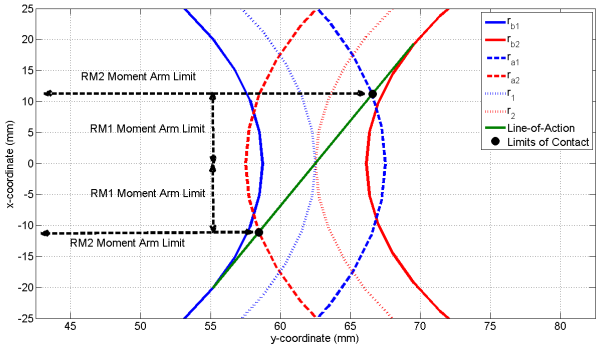

Figure 4.26: Axial force moment arms

moment arm about the vertical axis has limits of 58.46 and 66.57 mm, while the moment arm about the horizontal axis has limits of -11.1096 and 11.1772 mm. From these values it can also be shown that a contributing factor to the close accuracy between the averaged FE and theoretical RM1 values is that during contact the axial force has less impact on the reaction force; this is not only due to the smaller moment arms but also because the moments are balance through contact. During the initial part of contact the moment arms are positive, however as contact moves past the pitch point they become negative and therefore so does the moment, and since the FE values are based on the averaged moments across tooth contact the effect of the axial force is minimized. Conversely, since the moment arms about RM2 are always positive the effects of the axial moments are not removed during the averaging procedure, causing greater difference between the theoretical and FE moments.

A further improvement to the reaction moments seen in Figure 4.24 can be achieved by multiplying the axial tooth forces by the moment arms shown in Figure 4.26, with the resulting plots given in Figure 4.27(a) and 4.27(b).

From the above analyses it can be deduced that the effects of axial misalignment on the OLOA reaction moments can be attributed to the non-uniform load distribution across the tooth face, which creates an offset between the centre of pressure and the centres of mass, and the axial force on the tooth face, which has a time varying moment arm depending on the contact position.

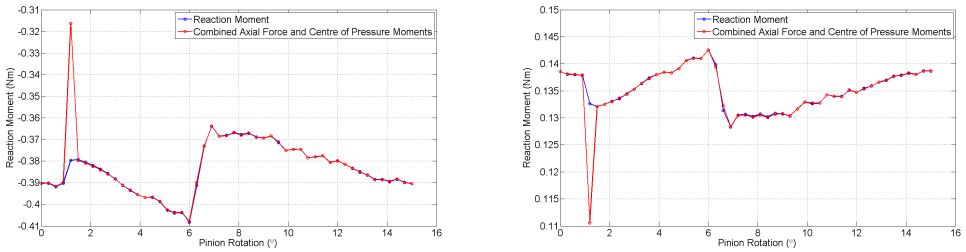

(a) RM1 (b) RM2

Figure 4.27: Reaction moments vs. pinion rotation. 0.5 mm axial misalignment and 100 Nm load compared against moment due to offset of centre of pressure and axial tooth load.

Although increased misalignment induces OLOA moments they remain relatively small compared to the applied loads at less than 1% under an imposed misalignment of 1 mm; however this is could be due to the small facewidth gears in use, where with larger facewidth gears the tilting of the teeth may increase and the centre of pressure may move further towards the edge.

Force Analysis

During the analysis of various degrees of axial misalignment under a load of 100 Nm it has been shown that mesh stiffness is slightly changed due to the increased contact pressure and contact deformation. With varied load it can be shown that the combined effects of axial misalignment and load are similar to the aligned and radial misaligned cases, shown in Figures 4.7, 4.16 and 4.17. Figure 4.28 shows the rotational mesh stiffness results for axial misalignments of 0.1 and 1 mm under various applied loads.

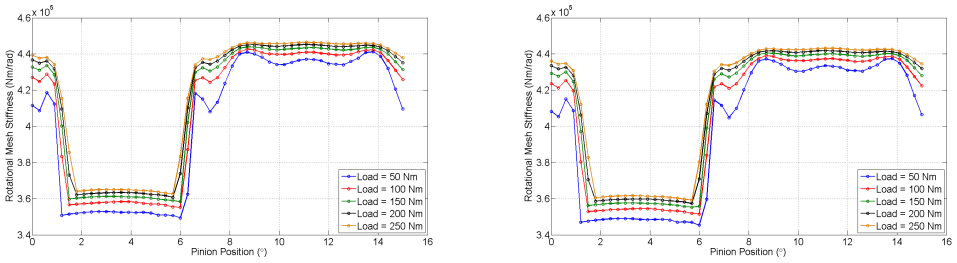

(a) Axial misalignment = 0.1 mm (b) Axial misalignment = 1 mm

Figure 4.28: Mesh stiffness vs. pinion angle under axial misalignment and load

The results show that the increases in mesh stiffness are most likely due to a slight nonlinearity in the contact zone and the tooth bending, where with increased load the area of contact increases and increases the overall contact stiffness, which is the same effect seen in previous analyses of varied load under perfect alignment and radial misalignment. There is also increased smoothing around the transition points and reductions in the amount of single tooth contact, which are again consistent with previous analyses.

The LSR did not vary under axial misalignment and therefore it is believed that the LSR will behave exactly as the perfectly aligned scenario under varied load, which can be proved through Figure 4.29. This figure shows the LSR under axial misalignments of 0.1 and 1 mm and various loads, and it can be seen by comparing the two figures, and with Figure 4.9, that the introduction of axial misalignment does not vary the effects of applied load on the LSR.

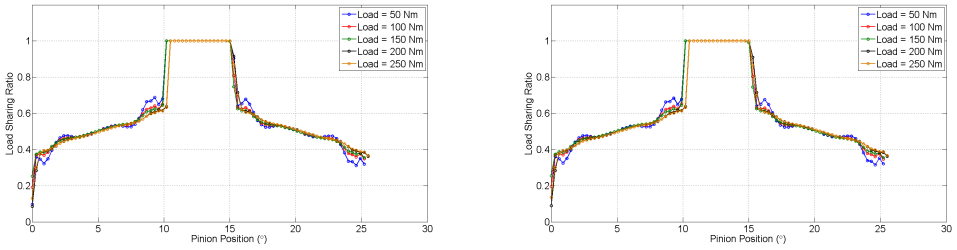

(a) Axial misalignment = 0.1 mm

(b) Axial misalignment = 1 mm

Figure 4.29: Load sharing ratio vs. pinion angle under axial misalignment and load

In both figures the increased load increases tooth bending and reduces the degree of single tooth contact, as shown in the mesh stiffness plot, and also smooths the double tooth contact zones by better describing the contact zone across more elements.

Turning attention to the reaction forces it is found that the variation of the LOA forces under different axial misalignment and loads are minimal when compared to the theoretically derived values; very small variations between the finite element and theoretical results do exist, and these are likely due to small variations in the pressure angle, which have been described previously. The OLOA moments are

however found to increase with increased load as shown in Figure 4.30 where they are compare against theoretical values.

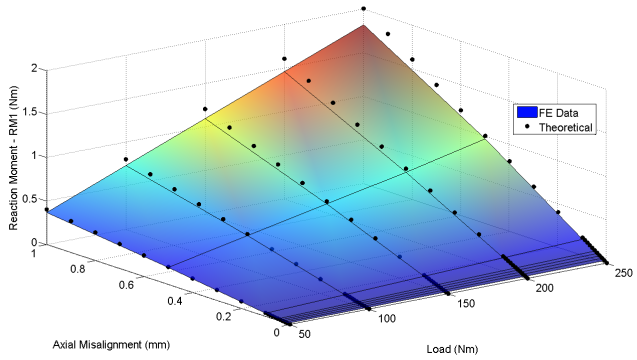

Figure 4.30: Reaction force RM1 vs. axial misalignment vs. applied load

In this figure the variation between the theoretical and finite element results increases with both increased misalignment and load; this is due to the increased tooth twisting, which causes the centre of pressure to move further from the theoretically derived value, and the subsequent increase in the axial force component, which increases its contribution to the overall reaction moment.

Conclusions

The axial misalignment can be seen to only have a limited effect on the static parameters. Slight decreases in the mesh stiffness are found, which can be attributed to the decrease in the contact area and subsequent increase in the contact pressure and deformation; this is however only very slight and at small axial misalignments can be neglected. Under various loads the mesh stiffness behaves as previously seen in the perfectly aligned case, and as such the effects of axial misalignment on the mesh stiffness, under the expected range of misalignment and dynamic loads are found to be small and can therefore be neglected.

The load sharing ratio can also be seen to be insensitive to the amount of misalignment, where no change is seen under applied misalignments and the effects of load are in line with those seen under the perfectly aligned scenario.

The LOA reaction forces are found to alter little across the misalignment and load range when compared to theoretical relationships, with extremely small

variations due to the variation in the pressure angle under varied load. Finally the OLOA reaction forces are found to be the most sensitive to axial misalignments, where the reaction moments RM1 and RM2 are sensitive to the variation in the distance between the centre of pressure and the gear centre of mass, and moments about the centre of mass caused by axial forces across the tooth face. An additional tilting motion of the gear teeth is observed, which causes a variation in the axial position of the centre of pressure throughout contact, and which in turn creates a time varying reaction moment depending on the tilting of the tooth. So far the best theoretical model assumes the OLOA moments are based on a moment arm to the gear centre of half the axial misalignment value, and does not include the tilting motions of the teeth or the moments arising from the axial forces.

4.2.4 Yaw Misalignment

Yaw misalignment is achieved by rotating the gears about the line of action, at an axial point through the centre of the gear faces, which maintains parallel contact between the two tooth faces and maintains the pitch radii at the centre of the facewidths. In this section the effects of yaw misalignment on the mesh stiffness, load sharing ratio and reaction forces are investigated; however it is predicted that since the load distribution will remain relatively constant across the tooth face, and symmetrical about the pitch point, yaw misalignment will not effect the mesh parameters. In the proceeding results a radial misalignment of 0.1 mm has been introduced to avoid the risk of interference between the non-contacting portions of the gear teeth, and as such, when the results are compared against the aligned scenario the gear teeth are under a radial misalignment of 0.1 mm with zero yaw misalignment.

Mesh Stiffness

The effects of yaw misalignment on the mesh stiffness at a load of 100 Nm are shown in Figure 4.31, where yaw misalignments of 0.05°, 0.1°, 0.5° and 1° are compared against the aligned case.

Figure 4.31 proves that yaw misalignment has little effect on the mesh stiff-

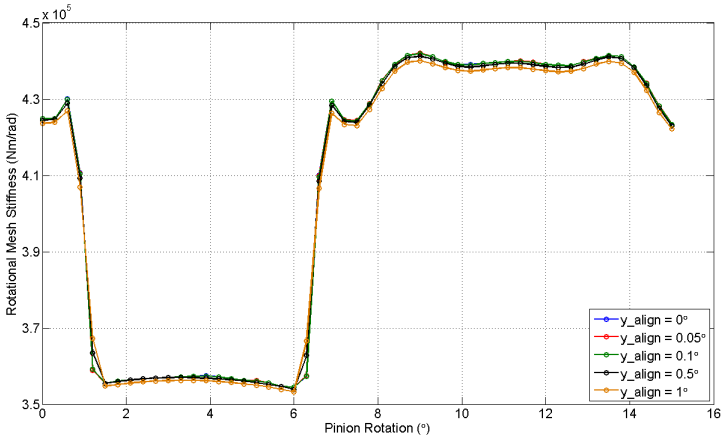

Figure 4.31: Effects of yaw misalignment on the mesh stiffness at 100 Nm.

ness, with noticeable variation only observed at misalignments greater than 0.5°; however even with a large misalignment of 1°, the variation in the average mesh stiffness is still less than 0.5%, and as such the effects of the yaw misalignment on the mesh stiffness can be neglected in this case.

Load Sharing Ratio

Since the purpose of yaw misalignment is to maintain parallel contact between the gear teeth, and yaw misalignment introduces no significant variations in the mesh stiffness, it is predicted that yaw misalignment has little effect on the LSR. This prediction can be corroborated with Figure 4.32, which shows the LSR plots for the same misalignment values as the mesh stiffness results; under a load of 100 Nm.

In this figure it can be seen that the prediction is correct and yaw misalignment has no noticeable effect on the LSR of the gears, and as such can be neglected from the calculation of the LSR.

Reaction Forces

With rotation of the gear teeth about the line of action, the direction of the line-of-action remains unchanged and as such the LOA forces will remain the same, which is demonstrated in the finite element results, where the variation in the LOA reaction forces are found to be very small, 0.0024% for RF1 and 0.0015% for RF2,

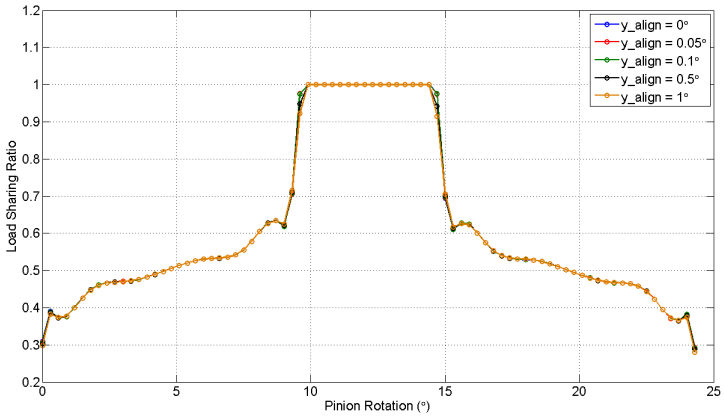

Figure 4.32: Effects of yaw misalignment on the load sharing ratio at 100 Nm.

across the misalignment range.

The OLOA reaction forces also remain negligible, where the axial forces (RF3) under a misalignment of 1° are generally only 0.0002% of the normal contact force (0.004 N vs 1700 N), where the increases in the axial force are shown in Figure 4.33.

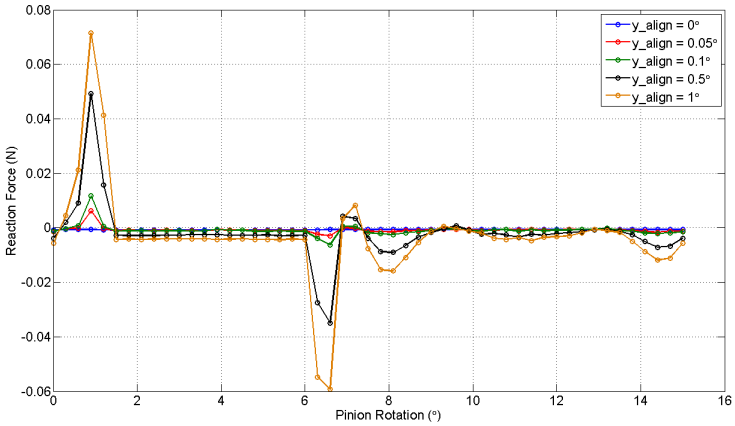

Figure 4.33: Effects of yaw misalignment on the axial reaction force (RF3) at 100 Nm.

In Figure 4.33 there are spikes at the transitions between single and double tooth contact, which are due to contact at the tooth tip, where the contact pressure is concentrated towards one side of the tooth face. The can be seen in Figures 4.34(a) and 4.34(b), which show the stress distribution in the gear at pinion rotation angles

of 0.75° and 8.1°.

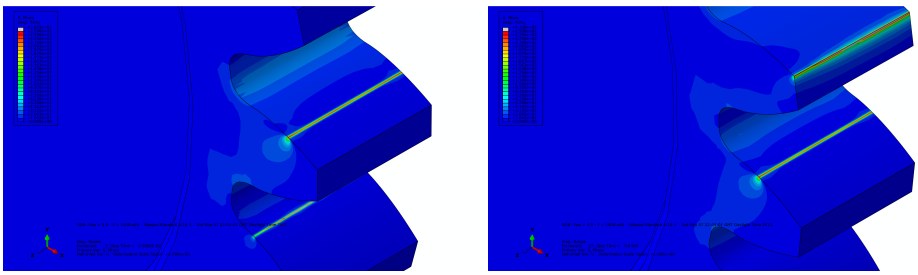

(a) Pinion rotation = 0.75° (b) Pinion rotation = 8.1°

Figure 4.34: Von Mises stress contour plots showing tip contact under yaw misalignment of 0.8° and 100 Nm applied load

Figure 4.34(b) illustrates the imbalance of pressure most effectively, where the stress is higher towards the far side of the gear tooth, which will generate an axial force and moments about the vertical and horizontal axes. However in general the moments about the vertical and horizontal axes are found to be small in comparison to the LOA forces, where at a misalignment of 1° the reaction moments are around 0.035 Nm (RM1) and 0.01 Nm (RM2) in the periods of single and double tooth contact and 0.6 Nm and 0.2 Nm during the transition points. However it is noted that in a real system, these high peaks would be smoothed as wear took place at the tooth tip.

Under the misalignments investigated the effects of yaw misalignment on the reaction forces at the gear centre have been shown to be negligible for the gear pair studied.

Force Analysis

Under an applied load of 100 Nm it has been shown that even considerable yaw misalignment has negligible effects on the mesh stiffness, load sharing ratio and reaction forces. Through load variation it can be seen that under any applied load the effects of yaw misalignment on the mesh stiffness are identical to the perfectly aligned case, where Figure 4.35 compares the mesh stiffness obtained under a radial misalignment of 0.1 mm with the mesh stiffness obtained under a yaw misalignment of 0.1° at various loads.

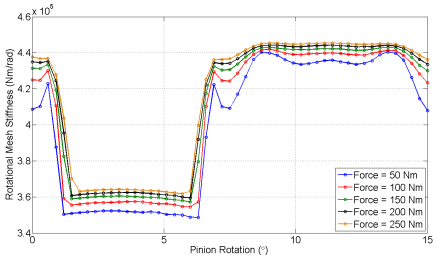

(a) Radial misalignment = 0.1 mm

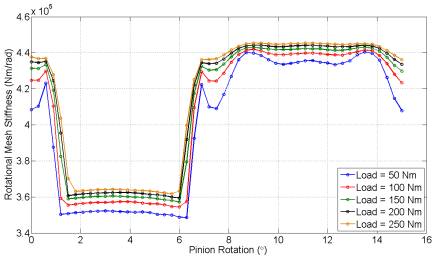

(b) Yaw misalignment = 0.1°

Figure 4.35: Mesh stiffness results under 0.1° yaw misalignment and varied load

From these figures it can be seen that under a range of loads the effects of a yaw misalignment of 0.1° are negligible. The same response can be seen across the misalignment range, such that it can be concluded that for this gear pair the effects of yaw misalignment on the mesh stiffness, under any load can be neglected.

The load effects on the LSR are also identical under applied yaw misalignments when compared to the LSR under a radial misalignment of 0.1 mm as can be shown in Figure 4.36, where the LSR plots under the same two misalignment scenarios as Figure 4.35 are compared under varied load.

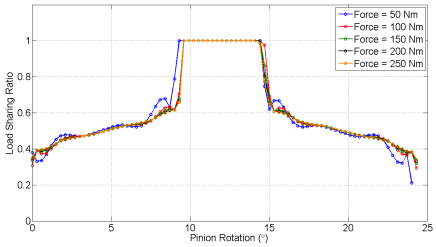

(a) Radial misalignment = 0.1 mm

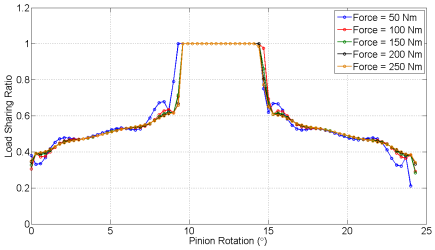

(b) Yaw misalignment = 0.1°

Figure 4.36: Load sharing ratio results under 0.1° yaw misalignment and varied load

The results present in Figure 4.36 are repeated in all other yaw misalignment cases, which indicates that yaw misalignment can be omitted in the determination of the load sharing ratio, regardless of the applied load.

Finally, in the previous section reaction moments have been found to exist under yaw misalignment due to the variation in the contact positions across the tooth face and the subsequent moment arms about the gear centres; however these

were very small compared to the applied loads and were therefore neglected. Under a load of 250 Nm and a yaw misalignment of 1° the maximum OLOA moments are still only 0.1 Nm (RM1) and 0.03 Nm (RM2) and can be ignored, while the LOA forces remain in line with the predicted values at 1465.29 N vs 1464.81 N (RF1) and 3996.92 N vs 3996.74 N (RF2). Therefore, even at these large misalignments and load, the effects are extremely small and are not considered within the research.

Conclusions

Yaw misalignment has been shown to contribute little to the contact parameters under investigation, which is likely due to the maintained symmetry across the tooth face, and the maintained parallel contact. The largest variations occur in the OLOA reaction moments where the variation in the contact positions across the tooth face cause an imbalance in the reaction moments about the gear centre of mass; however since the facewidth of the gears is small the effects are small compared to the applied loads and this may not hold true for gears with larger facewidths.

4.2.5 Pitch Misalignment

As opposed to yaw misalignment, which is obtained by rotating the gears about the line of action, pitch misalignment is introduced by rotating the gears about a line perpendicular to the line of action and passing through the pitch point at the centre of the tooth faces. The introduction of pitch misalignment invalidates parallel contact of the tooth surfaces seen in previous misalignment cases, which causes contact to be concentrated at the edges of the tooth faces, which can subsequently have a large impact on the contact shape and stresses produced.

As performed during the investigation of yaw misalignment, a small radial misalignment of 0.1 mm is introduced to add a degree of backlash to the system, which allows pitch misalignment to be introduced without interference between the contacting and non-contacting tooth faces. However, unlike yaw misalignment, where the backlash remained constant and independent of the imposed misalignment, increased pitch misalignment reduces the amount of backlash as the edges of the teeth translate along the line-of-action as shown in Figure 4.37.

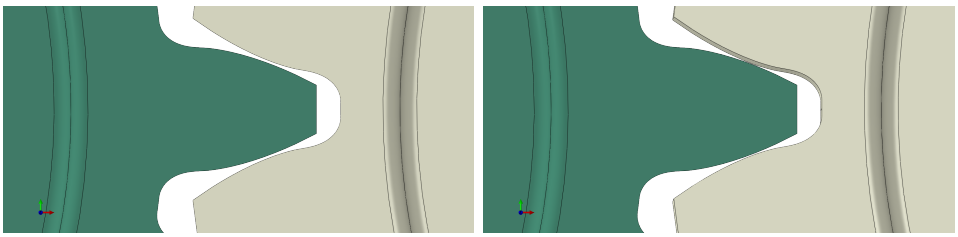

(a) Radial misalignment = 0.5 mm (b) Pitch misalignment = 1°

Figure 4.37: Variation in backlash under pitch misalignment

For a radial misalignment of 0.1 mm, the circular backlash (b_c) along the pitch circle can be calculated as around 0.0731 mm, which equates to a linear backlash (b_l) along the line of action of about 0.0686 mm, using the relationship $b_l = b_c \cos\phi'$. However when pitch misalignment is introduced into the gears the edges transverse the backlash by an amount equal to $\delta_{FW} \sin\theta_{pitch}$, where δ_{FW} is the length of the facewidth and θ_{pitch} is the pitch misalignment angle. With a facewidth of 15 mm this limits the amount of pitch misalignment to around 0.26°, at which point there is interference between the contacting and non-contacting faces of the gears. Using these equations the instantaneous backlash can be determined based on the radial and pitch misalignment, as shown in Equation (4.7)

$$b_\theta = \frac{1}{r'}\left(2C'\left(\text{inv}\phi' - \text{inv}\phi\right) - \frac{\delta_{FW}\sin\theta_{pitch}}{\cos\phi'}\right) \tag{4.7}$$

By using this backlash formulation the transmission error under applied radial and pitch misalignment can be determined, which removes the additional rotation of the gear required to pass through the backlash region and assists in the calculation of the mesh stiffness.

Mesh Stiffness

The mesh stiffness results across the misalignment range of 0 - 0.2° at a radial misalignment of 0.1 mm and a load of 100 Nm are shown in Figure 4.38, which illustrates that pitch misalignment has a large effect on the mesh stiffness of the gears.

In Figure 4.38 the mean mesh stiffness is reduced by over 50% under a mis-

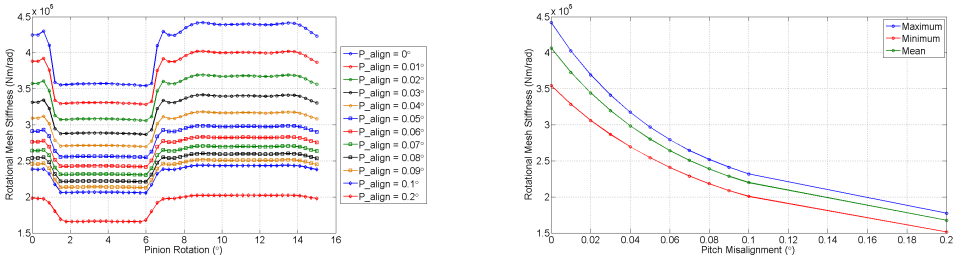

(a) Mesh stiffness vs. pinion angle (b) Mesh stiffness vs. pitch misalignment

Figure 4.38: Variations in mesh stiffness as a result of pitch misalignment at an applied load of 100 Nm

alignment of 0.2°, which is a considerable amount. The reduction in stiffness can be attributed to the tilting of the tooth faces under misalignment, which causes contact to be initiated at a point, rather than along a line, as seen in previous simulations; this point contact increases the deformation in the contact zone and decreases the mesh stiffness. Figures 4.39(a) and 4.39(b) show the contact pressure contour plots on a gear tooth in contact under 0.06° and 0.2° misalignment respectively, where it can clearly be seen that the pitch misalignment has a considerable effect on the shape and size of the contact zone. In Figure 4.39(a) the maximum contact pressure is found to be 766.6 MPa, which increases to 1340 MPa under 0.2° misalignment; this is compared to a maximum contact stress under aligned contact of 621.1 MPa, meaning that under pitch misalignment of 0.2° the contact pressure more than doubles and will have a large effect on the tooth deformation at the contact zone.

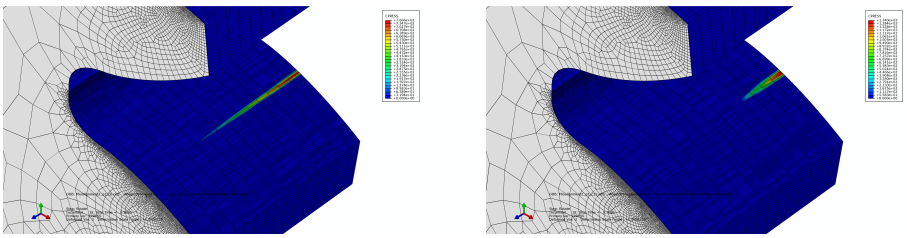

(a) Pitch misalignment = 0.06° (b) Pitch misalignment = 0.2°

Figure 4.39: Contact pressure contour plots at an applied load of 100 Nm

The increased deformation of the contact zone can also be seen by investigating the width of the contact zone, where by comparing Figure 4.39(a) and 4.39(b) it is clear that the contact zone at 0.2° is much wider than at 0.06°, indicating that

the surfaces are deforming more before equilibrium is reached in the contact zone.

It is also possible that with the centre of contact moving towards the edge of the tooth face, there is a considerable bending moment acting about the centre of the tooth, which results in a slight variation in the length of the line of contact, much in the same manner as the tilting of the teeth experienced under axial misalignment. This will explain the softening of the single-to-double tooth contact transitions observed in Figure 4.38(a), which are also observed under increased load and parallel (line) contact, where the increased load increases tooth bending and lengthens the line of contact. The lengthening of the line of action as a result of additional tooth bending can be better visualized through the investigation of the LSR.

Load Sharing Ratio

The LSR plots under a selection of applied misalignments are shown in Figure 4.40(a) where the increase in pitch misalignment slightly decreases the period of single tooth contact, which can be attributed to the lengthening of the line of contact either through tooth bending or variations in the geometry of contact. Specifically, since the rotational vectors of the two gears are no longer parallel, i.e. the axes of the gears are not parallel, the contacting planes of the gears are not parallel either, as can be seen in Figure 4.40(b), which increases the total length of contact, and subsequently decreases the proportion of single tooth contact.

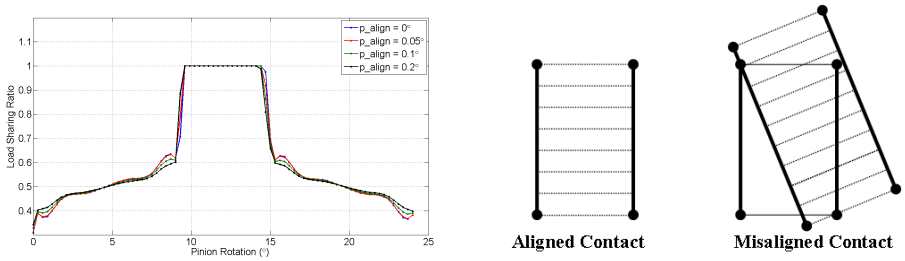

(a) LSR vs. pinion rotation (b) Contact planes

Figure 4.40: Effects of pitch misalignment on load sharing ratio

The pitch misalignment also smooths the double tooth contact regions in the same manner as increased load, where with increased contact pressure and defor-

mation, as shown in Figure 4.39(b), the contact is defined by more elements and a better resolution of the contact forces is found, giving increased solution accuracy. Although the pitch misalignment has some effect on the load sharing ratio the amount is relatively negligible compared to the effects of radial misalignment.

Reaction Forces

Looking firstly at the LOA reaction forces it is observed that the introduction of pitch misalignment has only a marginal effect, where across the misalignment range the reaction forces RF1 and RF2 vary by only 0.19% and 0.01% respectively. These small variations can be attributed to the variation in the pressure angle caused by tooth bending and the slight variation in the gross direction of the normal contact force, caused by the tilting of the tooth faces; however both these effects are small even under considerable misalignment and load.

Greater effects are witnessed in the reaction moments RM1 and RM2, where due to the tilting of the contacting faces the centre of pressure moves sharply towards the edge of the tooth, creating a considerable moment about the axes in a similar process to that seen in the axial misalignment scenarios; however this is to a much greater extent. The movement of the centre of pressure can be seen in Figure 4.39, with the resulting averaged moments under increasing misalignments shown in Figure 4.41, along with the variation in the peak-to-peak reaction moments as a results of misalignment.

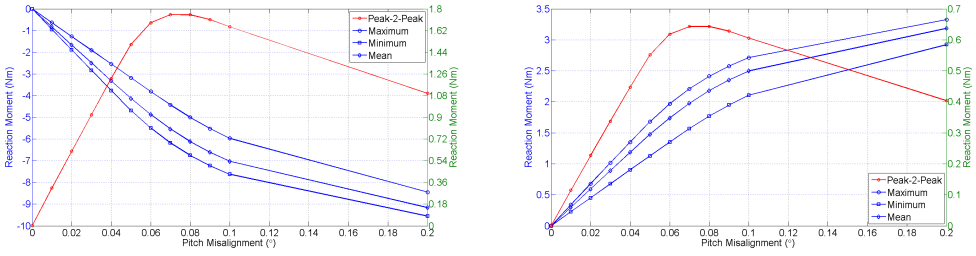

(a) RM1 (b) RM2

Figure 4.41: Effects of pitch misalignment on reaction moments at a load of 100 Nm

These figures show that as the faces tilt the centre of pressure moves to in-

crease the OLOA moments, however the effects of increased misalignment diminish at higher misalignments as a result of the contact moving to the extremities of the tooth face as shown in Figure 4.39(b); where it is imagined that with ever increasing misalignment the reaction moments would decrease as the centre of pressure moves back towards the centre of mass. Another characteristic seen in the OLOA moment plots is the reduction of the peak-to-peak reaction moments past a pitch misalignment of about 0.07 - 0.08°, which is believed to be due to the differences in the size of the contact zone under single tooth contact compared to double tooth contact. Under single tooth contact the applied tooth load is higher and the deformation increases, which in turn increases the contact area; up to around 0.07° pitch misalignment, the contact area, at least under single tooth contact, lies on either side of the centre of the tooth, however higher misalignment sees the contact solely positioned on one side of the face. This is shown in Figure 4.39, where under 0.06° misalignment the contact pressure lies over half way across the tooth width, while under 0.2° misalignment the contact area is much less than half way across the width. This means that the difference in the centre of contact under single and double tooth contact is less above around 0.07° misalignment.

As with axial misalignment, pitch misalignment causes a slight axial force, and again this causes additional moments in RM1 and RM2 dependent on the position of contact; however although these reaction forces are negligible compared to the applied normal load of around 1700 N, at a maximum of less than 3 N, the axial force can act over a large distance and cause considerable variations in the reaction moments, especially in the RM2 direction.

Investigating the reaction moments under 0.05° misalignment, the contribution of these two components, the movement of the centre of pressure and the axial force, can be shown. Figure 4.42 shows the variation in the centre of pressure in the axial direction, which is used in combination with the vertical and horizontal tooth loads to determine the contribution of the movement of the centre of pressure to the OLOA reaction moments. This contribution is also shown in Figure 4.42 compared against the FE derived reaction moments, where some variation is seen. This is

again more pronounced in the RM2 results and can be overcome by including the contribution of the axial force terms multiplied by the horizontal (U1) and vertical (U2) position of the contact points.

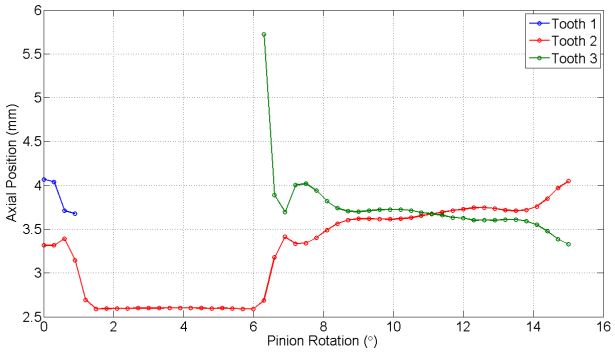

(a) Centre of pressure variation

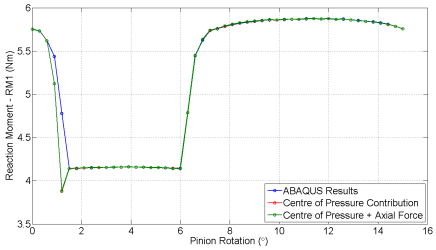

(b) RM1

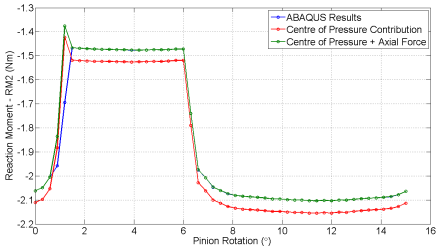

(c) RM2

Figure 4.42: Reaction moments vs. pinion rotation. 0.05° pitch misalignment and 100 Nm load compared against moments due to offset of centre of pressure and axial force.

Force Analysis

In the previously analysed aligned and misaligned results the contact is initiated and developed as line contact and as such the deformation under increased load has remained relatively linear, with mesh stiffness increasing slightly as the contact area increases, and noticeable changes only occurring at large variations in normal load. With pitch misalignment the contact is now initiated at a point and as such the deformation is highly nonlinear, which leads to large changes in the mesh stiffness as shown in Figure 4.43

In these figures it can be seen that as the load increases the increase in the mesh stiffness starts to plateau; this occurs because the load spreads across the

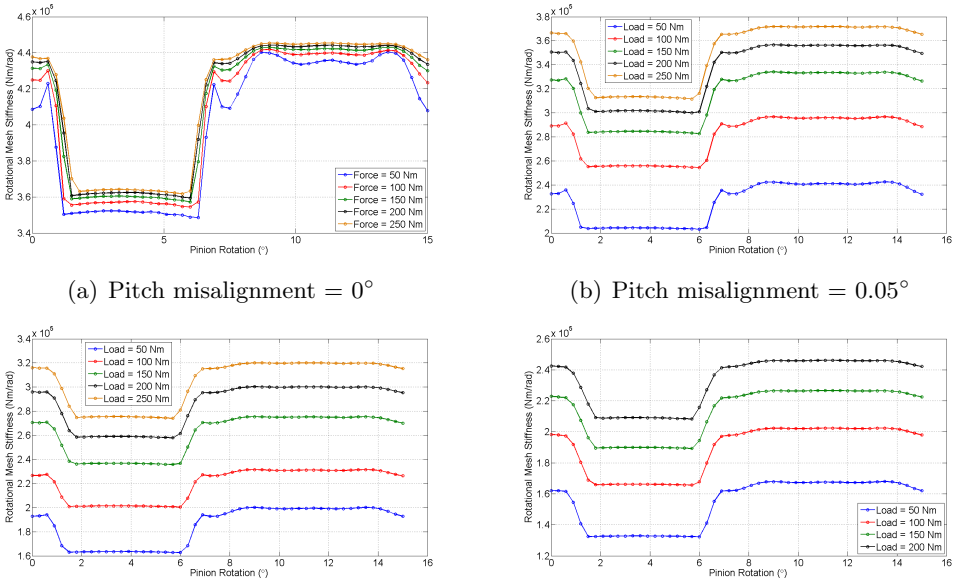

(a) Pitch misalignment = 0°

(b) Pitch misalignment = 0.05°

(c) Pitch misalignment = 0.1°

(d) Pitch misalignment = 0.2°

Figure 4.43: Rotational mesh stiffness variation under varied load and pitch misalignment

tooth face and as such the increase in the load has a more marginal effect on the area in contact, which is more in line with the effects seen under parallel tooth contact. From these figures it can be seen that the combination pitch misalignment and load has a considerable effect on the deformation of the tooth, and subsequently the mesh stiffness. This cannot be easily described functionally, since it has already been shown that the most appropriate technique in modelling the variation in the mesh stiffness is through a linear interpolation of the finite element results, and little theoretical work has been used to describe the mesh stiffness under applied pitch misalignment and load. Therefore although it is known to be a great contributing factor to the mesh stiffness the effect of pitch misalignment must be omitted for now.

Another aspect of the mesh stiffness curves shown in Figure 4.43 is the softening of the transition points between single and double tooth contact, which have previously been shown. These can be better observed in the load sharing ratio curves, where Figure 4.44 shows the LSR curves for a pitch misalignment of 0.2° under various loads.

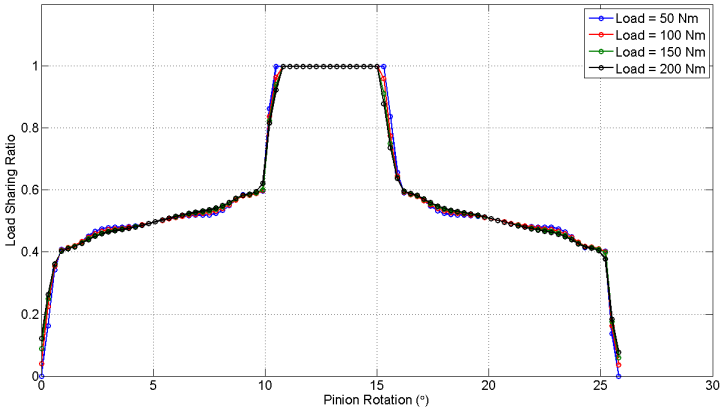

Figure 4.44: Effects of load on the Load Sharing Ratio under a pitch misalignment of 0.2°

Even under large pitch misalignment and load the effects are still relatively small, with variations in the meshing positions through increased tooth bending and softening of transitional points common with the previous alignment and misalignment scenarios. Therefore the same conclusion can be found, that the effects of increased pitch misalignment and load on the load sharing ratio are negligible, which is most likely due to the effects being governed by the tooth bending, not the increased contact deformation associated with pitch misalignment.

Finally looking at the reaction forces, the LOA forces and moments remain in line with the theoretically predicted values based on the free body force balancing, while the OLOA moments are highly dependent on both the misalignment and force. The reaction moment RM1 is shown in Figure 4.45 under various loads and misalignments, however the reaction moment about RM2 is not show since the response is identical to that seen in RM1.

These figures show there is a complex relationship between the pitch misalignment, load and the OLOA reaction moments; as the load is increased the length of the contact line across the face increases and the centre of pressure moves towards the centre of mass, which reduces the moment arm and the overall increase in the moment caused by increasing the applied load. Therefore the increase in the OLOA moment in response to the applied load is nonlinear unlike the response under axial

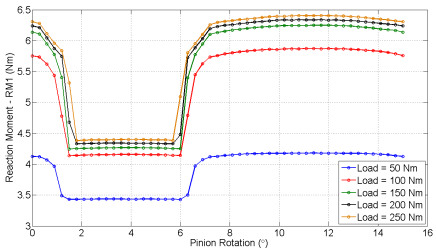

(a) Pitch misalignment = 0.05°

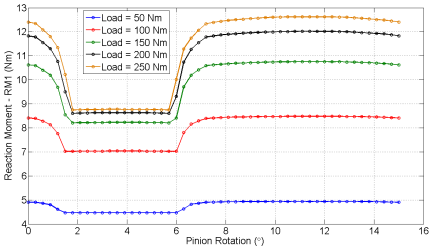

(b) Pitch misalignment = 0.1°

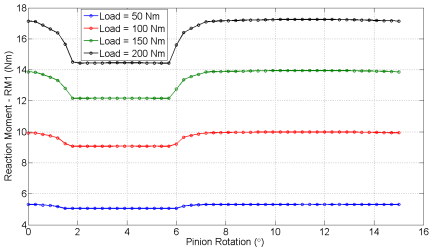

(c) Pitch misalignment = 0.2°

Figure 4.45: Reaction moment (RM1) variation under varied load and pitch misalignment

misalignment. The degree to which the centre of pressure moves under increased load depends on the amount of pitch misalignment, which can be seen in Figure 4.45, where under 0.05° misalignment the moments increase only slightly with ever increasing loads and the results seem to plateau. This is due to the shallow slope between the contacting faces and therefore when compared to a much greater misalignment the increase in the moments is much greater as the centre of pressure moves much less.

Conclusions

Pitch misalignment has been shown to greatly influence the contact parameters, where increased misalignment has greatly changed the size, shape and position of the contact area. This has lead to the increase in contact deformation, which has lead to a decrease in the mesh stiffness under greater misalignments, and the introduction of OLOA moments due to the movement of the centre of pressure towards the edge of the tooth face. Only marginal effects are seen on the load sharing ratio and the LOA reaction forces, where the variation in the LSR is due to the increase in the length of the line of action due to changes in the geometry of the contact

path, and variations in the LOA forces due to the variation in the gross contact angle and the small variation in the pressure angle under load.

With varied load the LOA forces are in line with the theoretical results and the LSR varies only slightly with changes in line with previous misalignment scenarios. The mesh stiffness increases with increased load, however plateau's as the contact line stretches across the complete tooth face, and the OLOA moments increase with increased load but the response is nonlinear due to the shortening of the moment arms as a result of increased load.

4.3 Conclusions

In this chapter results have been shown under many contact conditions and it has been shown that radial misalignment has a large effect on the contact positions governing the amount of single and double tooth contact, which has large effects on the mesh stiffness, load sharing ratio and the decomposition of the normal tooth loads into the LOA force directions. Axial misalignment had little effect on the mesh stiffness, LSR and the LOA forces, however by moving the centre of pressure towards the tooth edge OLOA moments were generated; this lead to the discovery of the tilting of the teeth in mesh which caused the centre of pressure to move during contact. Yaw misalignment was found to have little effect on any of the contact parameters due to the symmetry of contact across the tooth face, however pitch misalignment was shown to have a considerable effect, where contact changed from line contact to point contact. This was found to cause great increases in the contact deformation and resulted in a large reduction of the mesh stiffness, where under increased load the area of contact greatly increased causing an increase in the mesh stiffness, which was proportional to both the pitch misalignment and applied load. The introduction of pitch misalignment also varies the position of the contact, moving it towards the edge of the tooth face, which in turn introduces OLOA moments, which are again nonlinear with respect to pitch misalignment and load.

Chapter 5

Cranfield Test Rig

In Chapter 6 a dynamic model of a gearbox is proposed and developed; this model is based on the physical test rig designed and built at the University of Cranfield, which will be described in this chapter. Unlike traditional rigs used for studying the vibration in gearboxes the Cranfield rig has been designed specifically to allow various misalignments to be introduced through mounting the motor and shaft assembly onto a floating platform, while fixing the load-shaft assembly to ground. This allows the driving gear to be moved in all possible directions to study the vibration under a range of operating conditions, which can be seen in Figure 5.1.

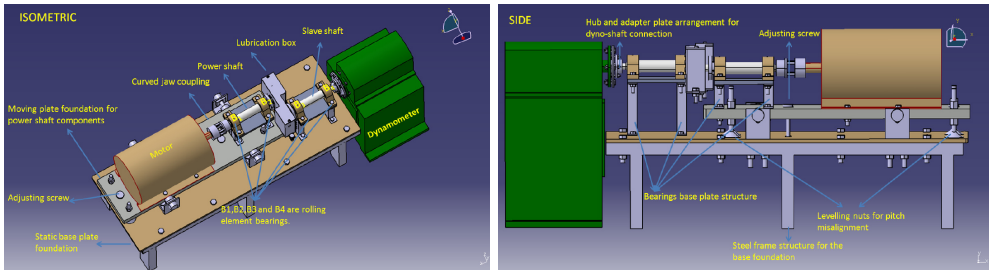

(a) Isometric view (b) Side view

Figure 5.1: CAD model of Cranfield test rig

In Figure 5.1 the bearing configuration is chosen to allow unconstrained rotation of the motor shaft, meaning the rig can be positioned to study the vibration of non-parallel axis gears, such as bevel gears. Radial and angular misalignments are achieved through varying the positions of the vertical and horizontal jacking screws,

which hold the floating platform in place, while axial misalignment is achieved through varying the axial position of the gears using bespoke shaft collars.

The remainder of this chapter will briefly discuss the various rig components, whether bespoke or outsourced, and the instrumentation applied to the rig.

5.1 Bespoke components

Many of the components in Figure 5.1 are bespoke to this test rig; these include the base structure, bearing supports, floating platform, lubricant box and the shaft, where component drawings are given in Appendix C. The base structure shown in Figure 5.2 differs slightly from the CAD drawing of Figure 5.1 with the inclusion of a foundation plate at 90° to the main spur gear foundation plate to allow the study of bevel gears. This means the supporting structure consists of 3 parts, the subframe, the spur gear foundation plate and the bevel gear foundation plate.

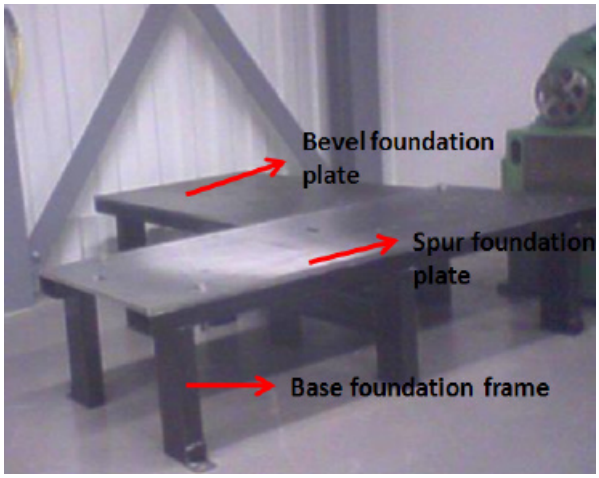

Figure 5.2: Base supporting structure

The physical dimensions of the various components in the base supporting structure means the base structure is very heavy; the subframe is around 56.75 kg, the spur gear foundation 95.8 kg and the bevel foundation 84.18 kg giving a combined foundation mass of 236.73 kg. The significance of this mass is that the natural frequencies of the foundation are of a suitable magnitude to avoid introducing resonance into the system, and should be of a large enough magnitude to reduce the

vibration experienced at the base. This has extra significance in the mathematical modelling of the test rig since the large mass means a datum position can be assumed on the foundation plates and therefore the contribution of the foundation can be excluded from the determination of the vibrational response of the system.

A similar assumption can be made about the floating platform, since along with its large mass of 94.5 kg, it is securely bolted to the base foundation and should move in unison with it. Therefore from a modelling standpoint the floating platform can also be modelled as a datum plane to which zero displacement boundary conditions can be applied. This means that the first structurally significant components in the mathematical model are the bearing supports.

The bearing supports, as shown in Figure 5.3, are manufactured from 40 mm x 40 mm hollow square tubing with a wall thickness of 3 mm welded to 5 mm thick stainless steel plates, meaning their stiffness is sufficiently low to allow measurable movement of the shaft-bearing-gear systems. The bearing supporting structures are linked together by the bearing base plates positioned on the top of the supports, as shown in Figure 5.1, to couple the motions of the shaft and increases the lateral stability of the supports.

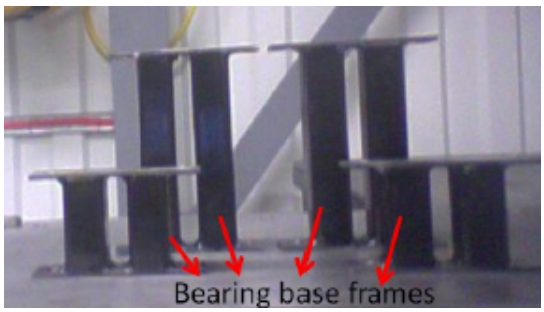

Figure 5.3: Bearing supports

On top of the bearing base plates are the bearings, which are connected to the shafts; these have varying cross sectional areas to accommodate the various bore holes in the couplings, bearings and the gears, with various features and keys to allow secure mounting of these components. At the gear end the shaft is threaded to improve the connection between the gear and shaft and to avoid axial movement

of the gear, whereas at the motor/load end the connection is made through only a keyway. The shaft, as shown in Appendix C, consists of 5 sections with varying diameters and lengths, which are shown in Table 5.1, and is assumed to be made from steel with a Young's Modulus of 210 GPa, Poisson's Ratio of 0.3 and a density of 7850 kgm^{-3}.

Section	Diameter (mm)	Length (mm)
1 (Motor/Load Side)	25	50
2	30	52
3	50	152
4	30	83.5
5 (Gear Side)	25	47.5

Table 5.1: Shaft dimensions

Along the length of the shafts bearings and gears are placed, the bearings are placed at 72 and 300 mm along the shaft from the motor/load ends, while the gears are placed at 357.5 mm along the shaft, however this distance will vary depending on the ammount of axial misalignment imposed on the gear set.

The final bespoke component is the lubrication box, shown in Figure 5.4, which is constructed from two dish shape components separated by a gasket and bolted together around their flanges, with the lubricant being dripped onto the gear contact from above and collected in the base of the lower half using a peristaltic pump. The lubrication box sits over the gears and connects only to the foundation plates; this means it does not interfere with the transmission path to the accelerometers, which is important when considering the modelling approach as the contribution of the lubrication box can be ignored.

5.2 Off-the-Shelf Components

Along with the bespoke components the rig has a number of outsourced parts, such as the motor, dynamometer, couplings, bearings and the gears, where the motor is an 11 kW, 4 pole high efficiency unit sourced from Brook Crompton® (Frame reference: W-DA160MJ), which at full load runs at a speed of 1470 rpm and a load of 71.5 Nm. The most important parameter of the motor, with respect

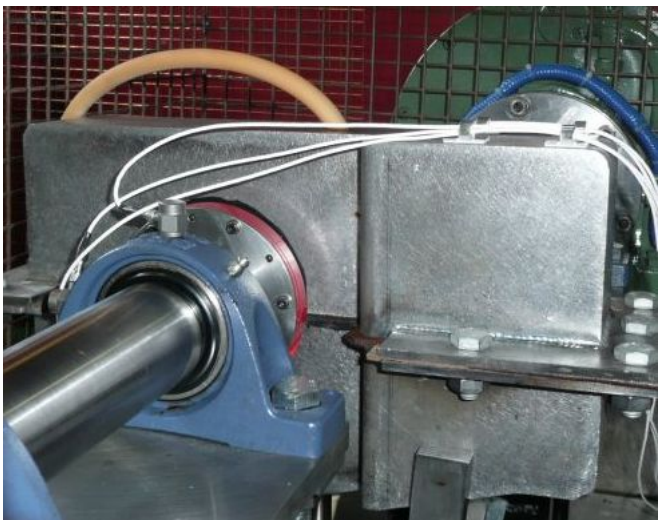

Figure 5.4: Lubrication Box

to the dynamic model is its rotor inertia, which is 0.068 kgm^2 as this contributes to the mass of the system.

The dynamometer is a Borghi & Saveri® FA-50/30 SLV water cooled eddy current unit with maximum power, speed and torque of 44 kW, 12,000 rpm and 102.5 Nm respectively, which is sufficient to match the output of the motor. As with the motor the dynamometer is considered to be fixed to the ground, such that its only mass of interest is its rotary inertia, which is found to be 0.0035 kgm^2. The dynamometer is controlled by a Schenck Test Automation Series 3000 controller, which is able to set the required loading of the gears to an accuracy of 0.05% of the full scale deflection, giving accurate control over the test load.

The motor is connected to the shaft via a Type GR curved jaw coupling sourced from Lenze^{TM}(model 38/45), as shown in Figure 5.5, with dimensions given in Table 5.2. In this coupling Hub A, with bore hole size of 25 mm, is connected to the shaft, while Hub B is connected to the motor output shaft.

Type	Fa	Fb	Fg		E	A	B	H	L	I	M	S	N	G
			A	B										
38/45	25	42	10	12	80	66	80	45	114	37	24	3	18	38

Table 5.2: Coupling dimensions with reference to Figure 5.5 (All dimensions in mm)

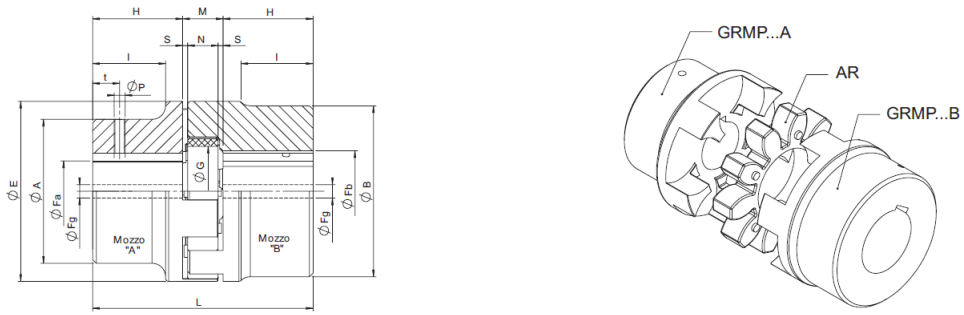

Figure 5.5: Curved jaw coupling

This consists of two cast iron hubs connected through a polyurethane resin spider with a dynamic torsional rigidity of around 23.63 kNm/rad about the shaft rotational axis. The coupling allows free rotation about the other axes up to an angle of 0.9°, which means that its rotational stiffness about these axes can be ignored; this assumption is also made for the axial stiffness, where the coupling allows axial misalignment of 1.8 mm. Vertical and horizontal stiffness are not documented and therefore suitable values must be determined. Mass values have been calculated through CAD drawings of the two hubs, where it is assumed that both are made from cast iron with a density of 7000 kg/m^3, which results in the mass properties given in Table 5.3 with moments of inertia taken about the hubs centre of mass.

	Mass (kg)	Moments of Inertia (kgm^2)		
		Ixx	Iyy	Izz
Hub A	1.13	0.000844	0.000716	0.000716
Hub B	1.25	0.0013	0.000965	0.000965

Table 5.3: Coupling mass properties

The bearings have been sourced from SKF® and specified to avoid failure of the bearings under the subjected loading conditions; the resultant bearings are cast plummer block units (Housing: SYJ 507) with Y-bearings® (YSA 207-2FK) on an adapter sleeve (H 2307), as shown in Figure 5.6. These are 03 dimension series sealed single row deep groove ball bearings with a bore diameter of 30 mm, outside diameter of 72 mm and a width of 19 mm, where Table 5.4 shows the important bearing data required for modelling.

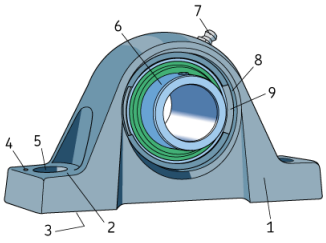

Figure 5.6: Plummer block bearing schematic taken from www.skf.com

N_e	α_0	d_e	PCD_b	$r_{\rho,i}$	$r_{\rho,o}$	r_L	E_b	ν_b
9	0	11.112	53.5	27.41672	26.08328	0.05	208	0.3

Table 5.4: Bearing data table: N_e = number of bearing elements, α_0 = unloaded contact angle (°), d_e = bearing element diameter (mm), PCD_b = bearing pitch circle diameter (mm), $r_{\rho,i}$ and $r_{\rho,o}$ = radii of inner and outer raceway centres of curvature (mm), r_L = radial clearance (μm) and E_b and ν_b = bearing material Young's modulus (GPa) and Poisson's ratio

This information will be shown to be useful in determining the stiffness characteristic of the bearings in the next chapter, while the mass can be obtained from finite element analysis of the bearing CAD drawing. The bearing mass is split into two sections, the first includes all the internal components, as shown in Figure 5.7(a), while the second includes only the bearing block casing and the outer raceway, as shown in Figure 5.7(b).

(a) Internal components (b) External components

Figure 5.7: Bearing CAD models for mass calculation

In Figure 5.7(a) the majority of the components are assumed to be constructed from bearing steel with a density of 7850 kg/m^3, while the seals either side of the ball bearings are assumed to be constructed from rubber with a density of 500 kg/m^3. In Figure 5.7(b) the casing is modelled as cast iron with a density of 7000 kg/m^3 and the outer raceway is modelled as bearing steel, which result in the

mass properties given in Table 5.5 where the moments of inertia are taken about the components centre of mass.

	Mass (kg)	Moments of Inertia (kgm^2)		
		Ixx	Iyy	Izz
Bearing Internals	0.373	0.000163	0.000133	0.000133
Bearing Externals	1.33	0.00328	0.00251	0.00116

Table 5.5: Bearing mass properties

The final outsourced components are the gears; however their physical dimensions have been discussed at length in Chapter 4 and will not be reiterated here. The only physical quantity required for the gears, which has not been discussed is their weight; this has been determined through the finite element model of the gears assuming that they are constructed from steel with a density of 7850 kg/m^3, where the resultant mass properties of the two gears are given in Table 5.6

	Mass (kg)	Moments of Inertia (kgm^2)		
		Ixx	Iyy	Izz
Gear	1.09	0.00244	0.00124	0.00124
Pinion	0.975	0.00202	0.00102	0.00102

Table 5.6: Gear mass properties

5.3 Instrumentation

The Cranfield test rig is highly instrumented to capture the progression of the vibration through the structure and determine its effects on various portions of the system. Starting near the gears, the shaft rotation is monitored with the use of a Renishaw® RESM-20-USA-100^{TM}graduated ring with and outside diameter of around 100 mm and a graduation pitch of 20 μm, resulting in 15,744 graduations and a rotary resolution of 0.008 arc seconds. This is coupled to a Renishaw® Tonic^{TM}T2011-30A rotary read head with a Ti-0004-A-10-A interface, which has a minimum receiver clock frequency of 10 MHz, a resolution of 5μm and a maximum rotary speed of 1910 rpm for the interface and ring of choice. This is sufficient to operate in the speed range of interest

This should be capable of highly accurate determination of the rotational

positions of the shafts and gears, and help to quantify the transmission error of the system.

The shaft position is also monitored through two 1mm MicroStrain® NC-DVRT® non-contact displacement sensors placed at 90° to the shaft axis in the horizontal and vertical direction. These have an accuracy of between ±0.2 and ±1 % and are capable of frequency responses up to 20 kHz.

The final instrumentation of interest are the accelerometers, which are shown in Figure 5.8 along with the optical encoder ring in red. The accelerometers are positioned on the bearing housing, such that they are not unrealistically close to the gear contact, where they are aligned vertically, horizontally and along the axial direction to measure the three-dimensional forces transmitted through the system. The units used are DYTRAN® 3055B2 Low Impedance Voltage Mode accelerometers, which have a sensitivity of 100 mV/g and a range of ±50 g for a voltage output range of ±5 V, with the response of the accelerometers remaining linear to ±2 % this range. The acceleromters have a frequency range of 1 to 10,000 Hz and a resonant frequency of 35 kHz meaning they will be sufficient to sample the acceleration data of interest for the running speed and gears chosen, and won't resonate leading to unreliable readings.

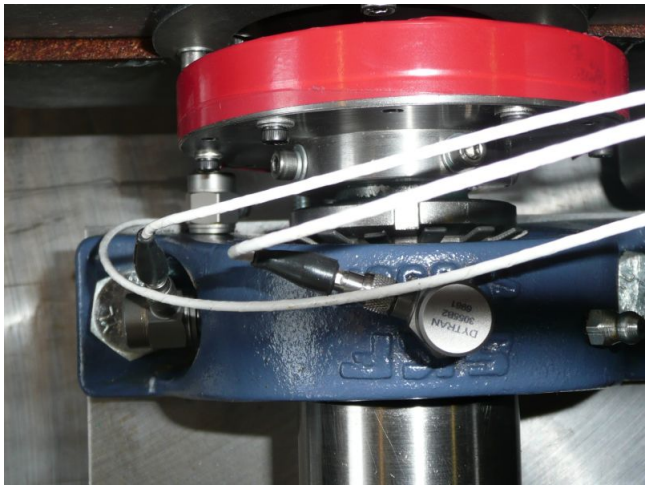

Figure 5.8: Positioning of the accelerometers and the optical encoder ring

The accelerometer, displacement sensor and encoder data is sampled through

National Instruments® Data Acquisition cards installed into a NI cDAQ-9172® chassis, which is connected to a standard desktop PC through a USB. The accelerometer data is sampled through two NI 9234® DAQ cards at a rate of 25.6 kHz, where one card is assigned to a single shaft, while the displacement data is sampled through a NI 9215® DAQ card at the same sampling frequency and the encoder data through a NI 9401® DAQ card at 10 MHz, which should be sufficient to capture the key vibrational frequencies generated within the test rig.

Other instrumentation is included on the rig, such as acoustic sensors and oil debris analysis, however these are not of interest in this current work.

Chapter 6

The Hybrid Dynamic Model

In previous models the transmission of the parametrically excited mesh force from the tooth contact to the point of interest has been achieved through the use of lumped parameter models, which model the shaft as a simple spring with independent stiffness' in each Degree Of Freedom (DOF). It is seen in previous models, such as those proposed by [15, 17, 19–21, 23, 25–31, 107–111], that only one to three DOF of each gear are considered, which usually include a combination of the shaft axial rotation and the translation in the DOF perpendicular to the shaft centroid axis as illustrated in Figure 6.1, which shows the 16 DOF model proposed by Howard *et al* [31]. In this figure the DOF θ_i represent the shaft rotations and X_i represent the translational DOF. The various motions are born from the mesh force, where the shaft rotation is due to the moment caused by this force, the vertical displacements, with correct placement of the gears, can be attributed completely to the normal mesh force, and the horizontal displacements can be gained from the frictional forces. To achieve this the pressure line is aligned with the vertical axis, which greatly simplifies the equations of motion. This approach is adequate when assuming the mesh force acts only in one direction and can be described as a time varying spring, such as under perfectly aligned conditions. However when the gears are brought out of alignment further forces and moments are experienced by the gear, which are not described by this simplified model. An example of this is shown when the moments experienced about the translational DOF X_i introduced through

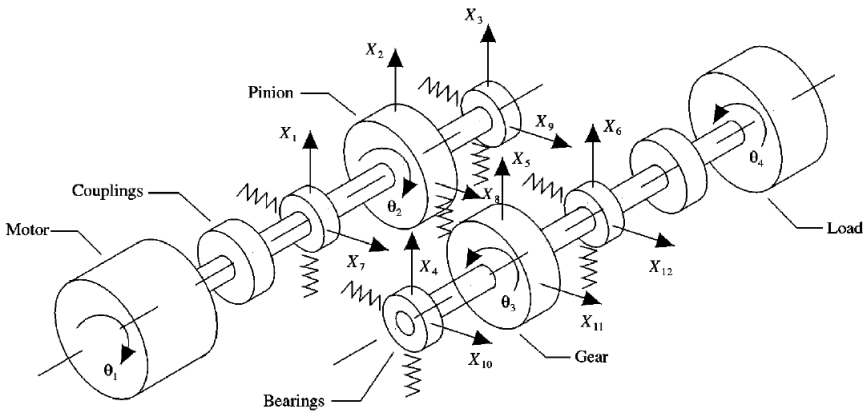

Figure 6.1: 16 DOF model as proposed by Howard *et al* [31]

axial misalignment are investigated; these cause the shaft to deform and vibrate in the translational DOF, which currently cannot be envisaged using the simplified 'independent spring' representation of the shafts. This anomaly is resolved in this chapter by modelling the shaft using finite elements based on Timoshenko beam theory, which will give a more reliable approximation to the shafts stiffness and mass in various directions. The final sections of this chapter use this representation of the shafts and add equations for the stiffnesses and masses of the various ancillary components, such as the bearings, supporting structures, couplings, motor and load. Finally the gear coupling between the two shafts and the sources of vibrations studied are introduced along with the application of boundary conditions and the solution technique applied to the dynamic equations.

6.1 Shaft Modelling

In many previous models of gear train vibration the shafts are modelled as spring elements with rotational stiffness and independent stiffnesses in the lateral DOF; this representation of the shaft implies that there is no coupling between the various motions and results in an inability to transmit moments other than those about the shaft axis. This restriction is overcome by modelling the shafts using the finite element representation of a Timoshenko beam, where the FE representation is preferred to an analytical solution due to the discontinuous nature of the Cranfield test rig shaft cross-section and the inherent complications in analytically solving non-

uniform cross-sectioned beams. The stiffness of the shaft is modelled using the finite element approximation given by Przemieniecki [112], which allows the same basic formulae to be combined with varying parameters relating to the cross-section of the beam to generate a response for the complete shaft. The 12x12 element stiffness matrix is derived directly from the differential equations used in engineering beam theory, where a free-body diagram of a beam element is shown below in Figure 6.2. By choosing the xy and xz planes to coincide with the principle axes of the cross-section the various bending and shearing forces can be considered independently from each other and the complete 12x12 matrix can be constructed from submatrices of size 2x2 and 4x4. One aspect of beam bending that is not introduced through

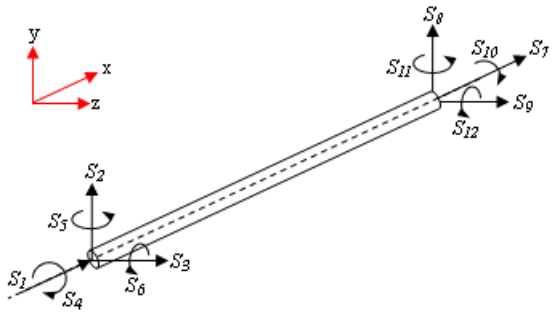

Figure 6.2: Beam Element Free-Body-Diagram

the stiffness matrix of Przemieniecki is the effect of the axial force on bending when the centroid axis is displaced from the undeformed state, however it is believed that the deflection of the shafts will be small enough to neglect the bending moments caused by the axial force.

The stiffness matrix will not be derived here as the methods used are generally well regarded, however the complete matrix is given on page 131 in Equation (6.1) for reference, where E is the Young's Modulus, G is the shear modulus, l is the element length, $m_e(= \rho Al)$ is the element mass, ρ is the material density and A is the cross-sectional area. The term Φ used in Equation (6.1) and defined in Equation (6.2) quantifies the relative importance of the effects of shear deformation, such that setting $\Phi = 0$ indicates that shear deformations are neglected, which in turn results in the stiffness matrix for an Euler-Bernoulli beam. It is also noted here that the

stiffness matrix terms are consistent with the DOF presented in Figure 6.2 such that the displacement vector is given as

$$\mathbf{u}^e = \begin{Bmatrix} u_1 & u_2 & u_3 & u_4 & u_5 & u_6 & u_7 & u_8 & u_9 & u_{10} & u_{11} & u_{12} \end{Bmatrix}^T$$

where subscripts relate to the forces shown in Figure 6.2. In the Cranfield test rig a circular shaft cross-section is used and therefore definitions for the terms used in the matrix, such as the second moment of area (I_y, I_z), the polar second moment of inertia (J), cross-sectional area and effective shear area (A_{sy}, A_{sz}), are given.

$$I_y = I_z = \frac{\pi r_s^4}{4} \tag{6.3a}$$

$$J = \frac{\pi r_s^4}{2} \tag{6.3b}$$

$$A = \pi r_s^2 \tag{6.3c}$$

$$A_{sy} = A_{sz} = \frac{9A}{10} \tag{6.3d}$$

Where r_s is the cross-sectional radius of the shaft element.

Also required in the dynamic analysis of the shafts are the elemental mass and damping matrices. The mass matrix is again taken from the work by Przemieniecki [112] and shown on page 131, whereas the damping matrix can be obtained through Rayleigh damping of the form $[C] = \alpha [M] + \beta [K]$ where $[M]$ and $[K]$ are the global mass and stiffness matrices respectively and α and β are known as the mass proportional and stiffness proportional constants.

The mass matrix is derived using the shape functions of the statically determined system where shear deformations are ignored to simplify the mass matrix formulation, as can be seen by the omission of the Φ terms. Although the use of the shape functions to determine the mass matrix results in an approximate solution to the discretization of the beam mass, by reducing the size of the elements good accuracy can be achieved. The off diagonal terms in the mass matrix, like those in the stiffness matrix, couple together various motions of the shaft, resulting in

$$\mathbf{K}_s^e = \begin{bmatrix}
\frac{EA}{l} & 0 & 0 & 0 & 0 & 0 & \frac{-EA}{l} & 0 & 0 & 0 & 0 & 0 \\
0 & \frac{12EI_z}{l^3(1+\Phi_y)} & 0 & 0 & 0 & \frac{6EI_z}{l^2(1+\Phi_y)} & 0 & \frac{-12EI_z}{l^3(1+\Phi_y)} & 0 & 0 & 0 & \frac{6EI_z}{l^2(1+\Phi_y)} \\
0 & 0 & \frac{12EI_y}{l^3(1+\Phi_z)} & 0 & \frac{-6EI_y}{l^2(1+\Phi_z)} & 0 & 0 & 0 & \frac{-12EI_y}{l^3(1+\Phi_z)} & 0 & \frac{-6EI_y}{l^2(1+\Phi_z)} & 0 \\
0 & 0 & 0 & \frac{GJ}{l} & 0 & 0 & 0 & 0 & 0 & \frac{-GJ}{l} & 0 & 0 \\
0 & 0 & \frac{-6EI_y}{l^2(1+\Phi_z)} & 0 & \frac{(4+\Phi_z)EI_y}{l(1+\Phi_z)} & 0 & 0 & 0 & \frac{6EI_y}{l^2(1+\Phi_z)} & 0 & \frac{(2-\Phi_z)EI_y}{l(1+\Phi_z)} & 0 \\
0 & \frac{6EI_z}{l^2(1+\Phi_y)} & 0 & 0 & 0 & \frac{(4+\Phi_y)EI_z}{l(1+\Phi_y)} & 0 & \frac{-6EI_z}{l^2(1+\Phi_y)} & 0 & 0 & 0 & \frac{(2-\Phi_y)EI_z}{l(1+\Phi_y)} \\
\frac{-EA}{l} & 0 & 0 & 0 & 0 & 0 & \frac{EA}{l} & 0 & 0 & 0 & 0 & 0 \\
0 & \frac{-12EI_z}{l^3(1+\Phi_y)} & 0 & 0 & 0 & \frac{-6EI_z}{l^2(1+\Phi_y)} & 0 & \frac{12EI_z}{l^3(1+\Phi_y)} & 0 & 0 & 0 & \frac{-6EI_z}{l^2(1+\Phi_y)} \\
0 & 0 & \frac{-12EI_y}{l^3(1+\Phi_z)} & 0 & \frac{6EI_y}{l^2(1+\Phi_z)} & 0 & 0 & 0 & \frac{12EI_y}{l^3(1+\Phi_z)} & 0 & \frac{6EI_y}{l^2(1+\Phi_z)} & 0 \\
0 & 0 & 0 & \frac{-GJ}{l} & 0 & 0 & 0 & 0 & 0 & \frac{GJ}{l} & 0 & 0 \\
0 & 0 & \frac{-6EI_y}{l^2(1+\Phi_z)} & 0 & \frac{(2-\Phi_z)EI_y}{l(1+\Phi_z)} & 0 & 0 & 0 & \frac{6EI_y}{l^2(1+\Phi_z)} & 0 & \frac{(4+\Phi_z)EI_y}{l(1+\Phi_z)} & 0 \\
0 & \frac{6EI_z}{l^2(1+\Phi_y)} & 0 & 0 & 0 & \frac{(2-\Phi_y)EI_z}{l(1+\Phi_y)} & 0 & \frac{-6EI_z}{l^2(1+\Phi_y)} & 0 & 0 & 0 & \frac{(4+\Phi_y)EI_z}{l(1+\Phi_y)}
\end{bmatrix} \tag{6.1}$$

$$\Phi_i = \frac{12EI_i}{GA_{si}l^2}, \qquad i = y, z \tag{6.2}$$

$$\mathbf{M}_s^e = m_e \begin{bmatrix}
\frac{1}{3} & 0 & 0 & 0 & 0 & 0 & \frac{1}{6} & 0 & 0 & 0 & 0 & 0 \\
0 & \frac{13}{35} + \frac{6I_z}{5Al^2} & 0 & 0 & 0 & \frac{11l}{210} + \frac{I_z}{10Al} & 0 & \frac{9}{70} - \frac{6I_z}{5Al^2} & 0 & 0 & 0 & -\frac{13l}{420} + \frac{I_z}{10Al} \\
0 & 0 & \frac{13}{35} + \frac{6I_y}{5Al^2} & 0 & -\frac{11l}{210} - \frac{I_y}{10Al} & 0 & 0 & 0 & \frac{9}{70} - \frac{6I_y}{5Al^2} & 0 & \frac{13l}{420} - \frac{I_y}{10Al} & 0 \\
0 & 0 & 0 & \frac{J_p}{3A} & 0 & 0 & 0 & 0 & 0 & \frac{J_p}{6A} & 0 & 0 \\
0 & 0 & -\frac{11l}{210} - \frac{I_y}{10Al} & 0 & \frac{l^2}{105} + \frac{2I_y}{15A} & 0 & 0 & 0 & -\frac{13l}{420} + \frac{I_y}{10Al} & 0 & -\frac{l^2}{140} - \frac{I_y}{30A} & 0 \\
0 & \frac{11l}{210} + \frac{I_z}{10Al} & 0 & 0 & 0 & \frac{l^2}{105} + \frac{2I_z}{15A} & 0 & \frac{13l}{420} - \frac{I_z}{10Al} & 0 & 0 & 0 & -\frac{l^2}{140} - \frac{I_z}{30A} \\
\frac{1}{6} & 0 & 0 & 0 & 0 & 0 & \frac{1}{3} & 0 & 0 & 0 & 0 & 0 \\
0 & \frac{9}{70} - \frac{6I_z}{5Al^2} & 0 & 0 & 0 & \frac{13l}{420} - \frac{I_z}{10Al} & 0 & \frac{13}{35} + \frac{6I_z}{5Al^2} & 0 & 0 & 0 & -\frac{11l}{210} - \frac{I_z}{10Al} \\
0 & 0 & \frac{9}{70} - \frac{6I_y}{5Al^2} & 0 & -\frac{13l}{420} + \frac{I_y}{10Al} & 0 & 0 & 0 & \frac{13}{35} + \frac{6I_y}{5Al^2} & 0 & \frac{11l}{210} + \frac{I_y}{10Al} & 0 \\
0 & 0 & 0 & \frac{J_p}{6A} & 0 & 0 & 0 & 0 & 0 & \frac{J_p}{3A} & 0 & 0 \\
0 & 0 & \frac{13l}{420} - \frac{I_y}{10Al} & 0 & -\frac{l^2}{140} - \frac{I_y}{30A} & 0 & 0 & 0 & \frac{11l}{210} + \frac{I_y}{10Al} & 0 & \frac{l^2}{105} + \frac{2I_y}{15A} & 0 \\
0 & -\frac{13l}{420} + \frac{I_z}{10Al} & 0 & 0 & 0 & -\frac{l^2}{140} - \frac{I_z}{30A} & 0 & -\frac{11l}{210} - \frac{I_z}{10Al} & 0 & 0 & 0 & \frac{l^2}{105} + \frac{2I_z}{15A}
\end{bmatrix} \tag{6.4}$$

interdependency between the transmission of various forces through the system.

Using the shaft dimensions given in Section 5.1, a finite element model of the shaft is produced as both a 3 dimensional solid model and as a beam model using ABAQUS's beam element formulations, to compare against the beam model proposed by Przemieniecki [112]. The ABAQUS beam model is simulated with 50 and 400 elements along its length, while the beam model based on Equation 6.1 is simulated with 7 and 104 elements. The results from simulations under cantilever bending with a tip load of 10kN are given in Table 6.1. From Table 6.1 it can be

Section	Maximum Deflections (mm)				
	Przemieniecki [112]		FEA Beam Model		FEA Solid Model
	7	104	50	400	
1 (0 mm)	0	0	0	0	0
2 (50 mm)	1.157	1.157	1.155	1.155	1.148
3 (102 mm)	4.006	4.006	3.996	3.996	4.061
4 (254 mm)	14.153	14.153	14.112	14.112	14.657
5 (337.5 mm)	20.348	20.348	20.285	20.286	21.262
6 (357.5 mm)	21.928	21.928	21.861	21.861	-
7 (385 mm)	24.143	24.143	24.068	24.068	25.271

Table 6.1: Corroboration of Przemieniecki's Finite Element shaft model against beam and solid FEA models (line 3 = number of elements)

seen that the results obtained from Equation 6.1 are very close to the results of the finite element beam model in ABAQUS, where a maximum difference of only 0.31% is seen. However the results of the solid model tended to be higher than both the prosed beam model and the ABAQUS beam model. This was believed to be attibuted to the behaviour of the solid model at the instantaneous changes in shaft cross section. In the solid model greater deformation occured directly after the changes in cross section due to the flexibility of the connection between the sections.

By comparing the individual sections in isolation (ref Table 6.2) it can be seen that the model proposed by Przemieniecki compares relatively well with the solid model; with variations up to 3.67%. Of interest in Table 6.2 is that the difference between the beam model and the solid model increases with lower aspect ratio sections. This can be attributed to a phenomena known as shear locking, where shear stiffness increases for sections that are short and wide; i.e. have a low aspect ratio.

This tends to increase the stiffness of the very short beam elements and could impact on the results; however at present the results tend to be in reasonable agrement with the finite element solid body and beam element results. With the stiffness matrix

Section	Length	Radius	Aspect Ratio	Max Deflections		% Difference
				Beam	Solid	
5	20.0	25.0	0.800	0.012	0.012	3.67%
6	26.5	25.0	1.060	0.023	0.022	3.40%
2	52.0	30.0	1.733	0.066	0.065	2.67%
1	50.0	25.0	2.000	0.117	0.115	2.44%
4	83.5	30.0	2.783	0.249	0.244	1.90%
3	152.0	50.0	3.040	0.192	0.189	1.75%

Table 6.2: Corroboration of Przemieniecki's Finite Element shaft model against solid FEA model sections

given in Equation (6.1), the mass matrix of Equation (6.4) and the damping matrix given by Rayleigh damping, the shaft can be discretized into a finite number of elements in the matrix equation of motion $[M]\{\ddot{u}\} + [C]\{\dot{u}\} + [K]\{u\} = \{F\}$ to determine its dynamic response. To these matrices the influence of many other system components can be included to obtain the response of the complete test rig describe in Chapter 5.

6.2 System Ancillary Components

To gain a better understanding of the components and how they contribute to the global system matrices a schematic of the experimental rig is given in Figure 6.3, which shows the two shafts connected through the gear mesh, and each shaft connected to ground through the bearings and supports in series. Also shown is the flexible coupling between the motor output shaft and the main gearing shaft on the motor side which has a flexibility much less than that of the shaft to reduce torque fluxtuations. For simplicity in formulation of the required matrices, the shaft nodal numbering direction will always be from the motor/load node towards the mesh. Throughout the chapter the superscripts $s1$, $s2$, c, b and sp relate to the motor-side shaft, load-side shaft, coupling, bearing and support nodes respectively.

In the following sections the system of equations are constructed from the el-

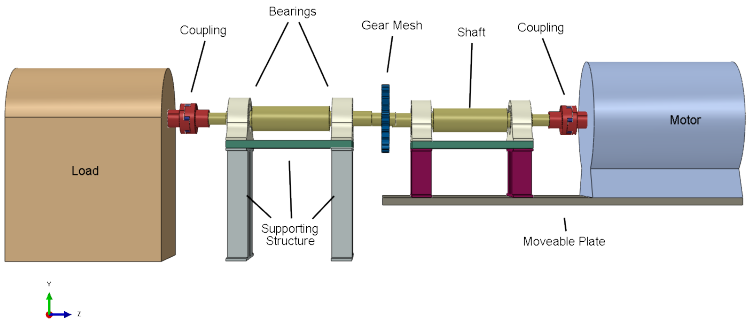

(a) Side view

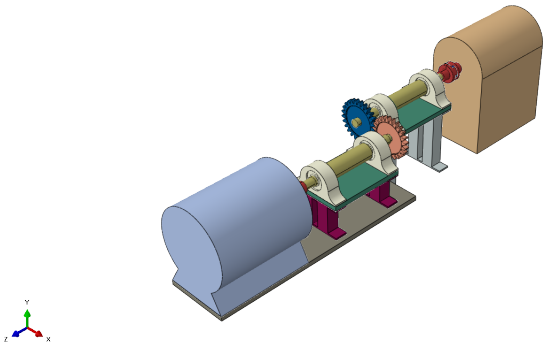

(b) Isometric view

Figure 6.3: Schematic of experimental test rig

ement mass and stiffness matrices for each component. Initially each side is treated separately and the motor-side and load-side shaft matrices are combined and expanded with the matrices of the bearings, supports, load and motor inertias and couplings. The separate shafts are then combined and coupled through the mesh stiffness term either directly through the global stiffness matrix or through the global forcing vector.

6.2.1 Shaft Equations

For a shaft consisting of n elements, a square diagonal matrix of size $6\,(n+1)$ is constructed to account for the mass and stiffness of the shaft and the DOF of the $n+1$ nodes. By splitting the 12x12 stiffness matrix of Equation (6.1) into quarters of size 6x6 such that:

$$\mathbf{K}^{si} = \begin{bmatrix} \mathbf{K}_{11}^{si} & \mathbf{K}_{12}^{si} \\ \mathbf{K}_{21}^{si} & \mathbf{K}_{22}^{si} \end{bmatrix}$$

The individual element matrices can be combined to form the global shaft stiffness matrix using the basic matrix pattern displayed in Equation (6.5), for shaft 1.

$$\mathbf{K^{s1}} = \begin{bmatrix} \mathbf{K}_{11}^{s1,1} & \mathbf{K}_{12}^{s1,1} & 0 & \cdots & \cdots & \cdots & \\ \mathbf{K}_{21}^{s1,1} & \mathbf{K}_{22}^{s1,1} + \mathbf{K}_{11}^{s1,2} & \mathbf{K}_{12}^{s1,2} & & & & \vdots \\ 0 & \mathbf{K}_{21}^{s1,2} & \mathbf{K}_{22}^{s1,2} + \mathbf{K}_{11}^{s1,3} & \mathbf{K}_{12}^{s1,3} & & & \vdots \\ \vdots & & \ddots & \ddots & \ddots & & \vdots \\ \vdots & & & \ddots & \ddots & \ddots & 0 \\ \vdots & & & & \mathbf{K}_{21}^{s1,(n-1)} & \mathbf{K}_{22}^{s1,(n-1)} + \mathbf{K}_{11}^{s1,n} & \mathbf{K}_{12}^{s1,n} \\ 0 & \cdots & \cdots & \cdots & 0 & \mathbf{K}_{21}^{s1,n} & \mathbf{K}_{22}^{s1,n} \end{bmatrix} \tag{6.5}$$

where the numerical superscripts indicate the shaft element number. An identical method is used to develop the stiffness matrix for shaft 2 and their respective global mass matrices ($[M]^{s1/s2}, \mathbf{M^{s1/s2}}$), which therefore will not be derived here.

Using the derived mass and stiffness matrices damping can be applied to the system through Rayleigh damping, where coefficients are applied to the mass and stiffness terms, giving.

$$\mathbf{C} = \alpha\mathbf{M} + \beta\mathbf{K} \tag{6.6}$$

Where in this instance α and β are the mass and stiffness proportional damping coefficients.

These generalised matrices will be used as the basis for the ancillary components such that their stiffness, mass and damping properties can be added to the matrix where needed, using these matrices as the global coordinate system.

6.2.2 Curved Jaw Coupling

The coupling in theory can transmit force in 6 DOF, however stiffness' in all these DOF are not regularly given by manufacturers and the only stiffness available for the coupling in use is around the beam rotational axis, which is 23.63 kNm/rad. In a paper by Saavedra and Ramírez [113] a 10x10 stiffness matrix is proposed, which ignores the torsional rigidity of the coupling, and the effects of applied torque, speed and misalignment in the determination of the stiffness terms. The defence of these omissions included the experimental configuration used, which utilised a non-varying applied torque and speed, and experimental work by Ramírez [114], which

demonstrated that under operating conditions the variation of the stiffness over the misalignment magnitudes is insignificant. This was compared to the variation caused by the angular position of the coupling, which was considered in the paper and is shown in Figure 6.4(b). This variation is due to the varying contact area between the polymer insert (spider) and the coupling jaws and has a periodicity equal to the number of jaws. The coupling was modelled as a system of two rigid

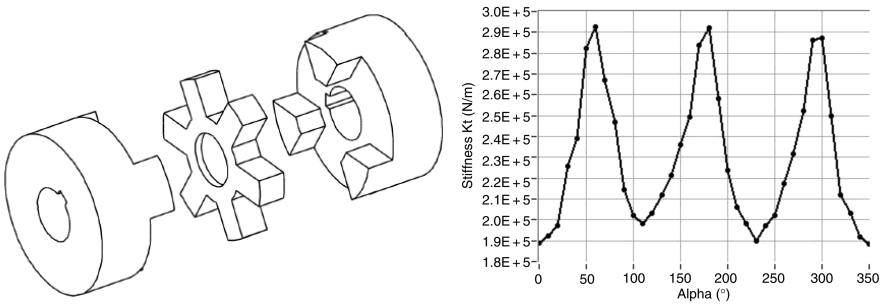

(a) Diagram of three jaw coupling

(b) Variation in coupling transverse stiffness with respect to rotation angle

Figure 6.4: Coupling diagrams

blocks connected by an element, which in turn comprised of five springs accounting for the three translational degrees of freedom (x, y and z) and the rotations about y and z (β and γ). A third spring is included here to account for the torsional stiffness about the x-axis (α), whose value is independent of the angle of rotation. This results in the following 12x12 stiffness matrix.

$$\mathbf{K}_e^c = \begin{bmatrix}
k_x & 0 & 0 & 0 & 0 & 0 & -k_x & 0 & 0 & 0 & 0 & 0 \\
0 & k_y & 0 & 0 & 0 & k_y\frac{l_c}{2} & 0 & -k_y & 0 & 0 & 0 & k_y\frac{l_c}{2} \\
0 & 0 & k_z & 0 & -k_z\frac{l_c}{2} & 0 & 0 & 0 & -k_z & 0 & -k_z\frac{l_c}{2} & 0 \\
0 & 0 & 0 & k_\alpha & 0 & 0 & 0 & 0 & 0 & -k_\alpha & 0 & 0 \\
0 & 0 & -k_z\frac{l_c}{2} & 0 & k_z\frac{l_c^2}{4}+k_\beta & 0 & 0 & 0 & k_z\frac{l_c}{2} & 0 & k_z\frac{l_c^2}{4}-k_\beta & 0 \\
0 & k_y\frac{l_c}{2} & 0 & 0 & 0 & k_y\frac{l_c^2}{4}+k_\gamma & 0 & -k_y\frac{l_c}{2} & 0 & 0 & 0 & k_y\frac{l_c^2}{4}-k_\gamma \\
-k_x & 0 & 0 & 0 & 0 & 0 & k_x & 0 & 0 & 0 & 0 & 0 \\
0 & -k_y & 0 & 0 & 0 & -k_y\frac{l_c}{2} & 0 & k_y & 0 & 0 & 0 & -k_y\frac{l_c}{2} \\
0 & 0 & -k_z & 0 & k_z\frac{l_c}{2} & 0 & 0 & 0 & k_z & 0 & k_z\frac{l_c}{2} & 0 \\
0 & 0 & 0 & -k_\alpha & 0 & 0 & 0 & 0 & 0 & k_\alpha & 0 & 0 \\
0 & 0 & -k_z\frac{l_c}{2} & 0 & k_z\frac{l_c^2}{4}-k_\beta & 0 & 0 & 0 & k_z\frac{l_c}{2} & 0 & k_z\frac{l_c^2}{4}+k_\beta & 0 \\
0 & k_y\frac{l_c}{2} & 0 & 0 & 0 & k_y\frac{l_c^2}{4}-k_\gamma & 0 & -k_y\frac{l_c}{2} & 0 & 0 & 0 & k_y\frac{l_c^2}{4}+k_\gamma
\end{bmatrix} \tag{6.7}$$

where k_x, k_y, k_z, k_α, k_β and k_γ are the stiffness coefficients and l_c is the length of the coupling. As previously mentioned the stiffness coefficients presented in Equation (6.7) are not readily available from manufacturers literature and need to be calculated empirically through the methods described by Saavedra and Ramírez [113]. Simplification of the coupling stiffness has been introduced in previous work, such as Howard *et al* [31], by stating that the coupling only constrains motion in the torsional direction about the beam axis and thus the stiffness values in the remaining 5 DOF are set to zero, or the rows and columns of these DOF are removed completely. Another simplification to the coupling stiffness is the use of constant stiffness coefficients, rather than those dependent on the angle of rotation, which will greatly simplify the computation of the stiffness matrix terms and remove a potentially time consuming step in the solution of the dynamic system. For simplicity constant stiffness terms will be used to model the coupling, where the axial and rotational stiffnesses in u_5 and u_6 are set to zero to account for free movement in these directions and the rotational stiffness is equal to the 23.63 kNm/rad value quoted by the manufacturer. The vertical and horizontal stiffnesses are unknown, however their average values based on the rotational position are assumed to be equal and their values can be varied within the model to determine their importance on the dynamic response.

To include the coupling stiffness in the global stiffness matrix, a similar technique to that used in Section 6.2.1 is applied, where the element matrix is split into quarters and combined with the shaft stiffness matrices. Because the coupling element introduces an extra node into the system the global stiffness matrix is expanded by 6 and the new matrix, shown for shaft 1 ($\mathbf{K^{s1}}$), becomes

$$\mathbf{K^{s1}} = \begin{bmatrix} \mathbf{K}_{11}^{c} & \mathbf{K}_{12}^{c} & \ddots & & \\ \mathbf{K}_{21}^{c} & \mathbf{K}_{22}^{c} + \mathbf{K}_{11}^{s1,1} & \mathbf{K}_{12}^{s1,1} & \ddots & \\ & \ddots & \ddots & \ddots & \ddots \end{bmatrix} \tag{6.8}$$

Also required of the coupling are its mass and damping properties. Since the two

coupling hubs are assumed rigid compared to the spider the mass matrix is modelled as a diagonal matrix where the translational values are simply taken as the mass and the rotational values are the moments of inertia about the principle axes, such that with a coupling comprising of two hubs at points A and B the mass matrix is given as:

$$\mathbf{M}_e^c = \begin{bmatrix} m_A & 0 & 0 & 0 & 0 & 0 & 0 & 0 & 0 & 0 & 0 & 0 \\ 0 & m_A & 0 & 0 & 0 & 0 & 0 & 0 & 0 & 0 & 0 & 0 \\ 0 & 0 & m_A & 0 & 0 & 0 & 0 & 0 & 0 & 0 & 0 & 0 \\ 0 & 0 & 0 & I_{Axx} & 0 & 0 & 0 & 0 & 0 & 0 & 0 & 0 \\ 0 & 0 & 0 & 0 & I_{Ayy} & 0 & 0 & 0 & 0 & 0 & 0 & 0 \\ 0 & 0 & 0 & 0 & 0 & I_{Azz} & 0 & 0 & 0 & 0 & 0 & 0 \\ 0 & 0 & 0 & 0 & 0 & 0 & m_B & 0 & 0 & 0 & 0 & 0 \\ 0 & 0 & 0 & 0 & 0 & 0 & 0 & m_B & 0 & 0 & 0 & 0 \\ 0 & 0 & 0 & 0 & 0 & 0 & 0 & 0 & m_B & 0 & 0 & 0 \\ 0 & 0 & 0 & 0 & 0 & 0 & 0 & 0 & 0 & I_{Bxx} & 0 & 0 \\ 0 & 0 & 0 & 0 & 0 & 0 & 0 & 0 & 0 & 0 & I_{Byy} & 0 \\ 0 & 0 & 0 & 0 & 0 & 0 & 0 & 0 & 0 & 0 & 0 & I_{Bzz} \end{bmatrix} \tag{6.9}$$

The mass values shown in Equation (6.9) have been derived through CAD drawings of the two hubs in Section 5.2 with mass values given in Table 5.3.

This mass matrix is included into the shaft mass matrix using the same method as the coupling stiffness, and again when simplifying the model to only account for the torsional motions of the coupling, only the fourth row and column of the upper half of the mass matrix should be retained.

Since the polymer spider offers greater damping compared to the metallic components in the rig its damping needs to be higher than that of the shaft damping. This can be achieved by applying a higher Rayleigh damping constant to the elemental mass and stiffness matrices before combining with the shaft damping matrix

6.2.3 Bearings

Many rotor dynamics problems involving geared and non-geared systems model bearing elements as translational stiffness or as ideal boundary conditions; this view was challenged in a study by Lim and Singh [115–118], who developed and tested a 6x6 stiffness matrix for both ball and rolling element bearings. Lim and Singh argued, correctly, that although acceptable when considering a system

enclosed in a rigid casing, when considering the transmission of the bearing forces to a flexible casing or surrounding structure the independent spring formulation was incapable of modelling the interconnected motions of the bearing.

The formulation of the stiffness matrix developed by Lim and Singh is based on the classical Hertzian contact theory between the inner-raceway, bearing element and outer-raceway, by relating the relative motions of the inner and outer raceways to the force applied to the bearings, as shown in Figure 6.5; individual bearing element stiffness' were discretely summed across the total number of elements in contact to determine the overall bearing stiffness. This formulation required the as-

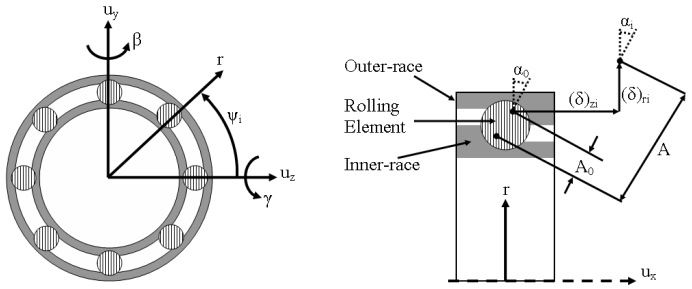

(a) y-z plane (b) r-z plane

Figure 6.5: Bearing model coordinate system adapted from Liew and Lim [119]

sumptions that the contact in ball bearings is elliptical and the loaded contact angle is allowed to change [120]. Also omitted in the calculation of the bearing stiffness matrix were the gyroscopic and centrifugal forces, which were deemed insignificant at the low speeds of interest, tribological effects, such as lubrication, which were deemed to be beyond the scope of the research, and the time varying stiffness parameters depending on the number of rolling element bearings in contact. This final point was addressed by Liew and Lim [119] who modelled the time varying position of the *ith* element as it orbits the inner-race as a function of the inner-race position, assuming pure rolling conditions, such that

$$\psi_i(t) = \frac{1}{2}\left(1 - \frac{r_b}{r_d}\cos(\alpha_0)\right)\Omega_x t + \frac{2\pi(i-1)}{Z}, \qquad i = 1, 2, ...Z. \tag{6.10}$$

where r_b is the rolling element radius, r_d is the inner-race pitch radius for rolling

element bearings, or the inner race curvature centre radius for ball bearings, Ω_x is the mean shaft rotational speed and Z is the number of elements.

In the current test rig ball bearings are used and therefore the remaining equations will be given for ball bearings only. As previously mentioned the loaded contact angle (α_j) is not the same as the unloaded contact angle (α_0), however this can be calculated as

$$\alpha_i(t) = \arctan \frac{A_0 \sin \alpha_0 + (\delta)_{zi}(t)}{A_0 \cos \alpha_0 + (\delta)_{ri}(t)} \tag{6.11}$$

where A_0 is the unloaded relative distance between the inner and outer raceways centres of curvatures and $(\delta)_{zj}$ and $(\delta)_{rj}$ are given by

$$(\delta)_{zi}(t) = u_x^B(t) + r_d \left(u_\beta^B(t) \sin(\psi_i(t)) - u_\gamma^B(t) \cos(\psi_i(t)) \right) \tag{6.12}$$

$$(\delta)_{ri}(t) = u_y^B(t) \cos(\psi_i(t)) + u_z^B(t) \sin(\psi_i(t)) - r_L \tag{6.13}$$

where u_j^B are the translational and rotational bearing displacements in the current coordinate system, shown in Figure 6.2 and 6.5, and r_L is the bearing radial clearance. Also required in the calculation of the bearing stiffness terms is the loaded relative distance between the inner and outer raceways centres of curvatures ($A(\psi_i)$) which is given as

$$A(\psi_i, t) = \sqrt{(\delta^*)_{zi}^2(t) + (\delta^*)_{ri}^2(t)} \tag{6.14}$$

where

$$(\delta^*)_{zi}(t) = A_0 \sin \alpha_i(t) + (\delta)_{zi}(t) \tag{6.15a}$$

$$(\delta^*)_{ri}(t) = A_0 \cos \alpha_i(t) + (\delta)_{ri}(t) \tag{6.15b}$$

The full derivation of the bearing stiffness matrix from the equations above will not be given here, only the resultant stiffness matrix.

$$\mathbf{k}_e^b(t) = \begin{bmatrix} k_{xx}^b(t) & k_{xy}^b(t) & k_{xz}^b(t) & 0 & k_{x\beta}^b(t) & k_{x\gamma}^b(t) \\ k_{yx}^b(t) & k_{yy}^b(t) & k_{yz}^b(t) & 0 & k_{y\beta}^b(t) & k_{y\gamma}^b(t) \\ k_{zx}^b(t) & k_{zy}^b(t) & k_{zz}^b(t) & 0 & k_{z\beta}^b(t) & k_{z\gamma}^b(t) \\ 0 & 0 & 0 & 0 & 0 & 0 \\ k_{\beta x}^b(t) & k_{\beta y}^b(t) & k_{\beta z}^b(t) & 0 & k_{\beta\beta}^b(t) & k_{\beta\gamma}^b(t) \\ k_{\gamma x}^b(t) & k_{\gamma y}^b(t) & k_{\gamma z}^b(t) & 0 & k_{\gamma\beta}^b(t) & k_{\gamma\gamma}^b(t) \end{bmatrix} \tag{6.16a}$$

where the rotational stiffness about the shaft axis is assumed zero due to free rotation and the matrix elements are as follows.

$$k_{xx}^b(t) = K_n \sum_i^z \frac{\left(A\left(\psi_i,t\right)-A_0\right)^n \left(\frac{nA(\psi_i,t)(\delta^*)_{zi}^2(t)}{A(\psi_i,t)-A_0} + A\left(\psi_i,t\right)^2 - (\delta^*)_{zi}^2\left(t\right)\right)}{A\left(\psi_i,t\right)^3} \tag{6.16b}$$

$$k_{xy}^b(t) = K_n \sum_i^z \frac{\left(A\left(\psi_i,t\right)-A_0\right)^n (\delta^*)_{ri}\left(t\right)(\delta^*)_{zi}\left(t\right)\sin\left(\psi(t)\right)\left(\frac{nA(\psi_i,t)}{A(\psi_i,t)-A_0}-1\right)}{A\left(\psi_i,t\right)^3} \tag{6.16c}$$

$$k_{xz}^b(t) = K_n \sum_i^z \frac{\left(A\left(\psi_i,t\right)-A_0\right)^n (\delta^*)_{ri}\left(t\right)(\delta^*)_{zi}\left(t\right)\cos\left(\psi(t)\right)\left(\frac{nA(\psi_i,t)}{A(\psi_i,t)-A_0}-1\right)}{A\left(\psi_i,t\right)^3} \tag{6.16d}$$

$$k_{x\beta}^b(t) = K_n \sum_i^z \frac{r_d\left(A\left(\psi_i,t\right)-A_0\right)^n \cos\left(\psi(t)\right)\left((\delta^*)_{zi}^2\left(t\right) - \frac{nA(\psi_i,t)(\delta^*)_{zi}^2(t)}{A(\psi_i,t)-A_0} + A\left(\psi_i,t\right)^2\right)}{A\left(\psi_i,t\right)^3} \tag{6.16e}$$

$$k_{x\gamma}^b(t) = K_n \sum_i^z \frac{r_d\left(A\left(\psi_i,t\right)-A_0\right)^n \sin\left(\psi(t)\right)\left(\frac{nA(\psi_i,t)(\delta^*)_{zi}^2(t)}{A(\psi_i,t)-A_0} + A\left(\psi_i,t\right)^2 - (\delta^*)_{zi}^2\left(t\right)\right)}{A\left(\psi_i,t\right)^3} \tag{6.16f}$$

$$k_{yy}^b(t) = K_n \sum_i^z \frac{\left(A\left(\psi_i,t\right)-A_0\right)^n \sin^2\left(\psi(t)\right)\left(\frac{nA(\psi_i,t)(\delta^*)_{ri}^2(t)}{A(\psi_i,t)-A_0} + A\left(\psi_i,t\right)^2 - (\delta^*)_{ri}^2\left(t\right)\right)}{A\left(\psi_i,t\right)^3} \tag{6.16g}$$

$$k_{yz}^b(t) = K_n \sum_i^z \frac{\left(A\left(\psi_i,t\right)-A_0\right)^n \sin\left(\psi(t)\right)\cos\left(\psi(t)\right)\left(\frac{nA(\psi_i,t)(\delta^*)_{ri}^2(t)}{A(\psi_i,t)-A_0} + A\left(\psi_i,t\right)^2 - (\delta^*)_{ri}^2\left(t\right)\right)}{A\left(\psi_i,t\right)^3} \tag{6.16h}$$

$$k_{y\beta}^b(t) = K_n \sum_i^z \frac{r_d\left(A\left(\psi_i,t\right)-A_0\right)^n (\delta^*)_{ri}\left(t\right)(\delta^*)_{zi}\left(t\right)\sin\left(\psi(t)\right)\cos\left(\psi(t)\right)\left(1-\frac{nA(\psi_i,t)}{A(\psi_i,t)-A_0}\right)}{A\left(\psi_i,t\right)^3} \tag{6.16i}$$

$$k_{y\gamma}^b(t) = K_n \sum_i^z \frac{r_d\left(A\left(\psi_i,t\right)-A_0\right)^n (\delta^*)_{ri}\left(t\right)(\delta^*)_{zi}\left(t\right)\sin^2\left(\psi(t)\right)\left(\frac{nA(\psi_i,t)}{A(\psi_i,t)-A_0}-1\right)}{A\left(\psi_i,t\right)^3} \tag{6.16j}$$

$$k_{zz}^b(t) = K_n \sum_i^z \frac{\left(A\left(\psi_i,t\right)-A_0\right)^n \cos^2\left(\psi(t)\right)\left(\frac{nA(\psi_i,t)(\delta^*)_{ri}^2(t)}{A(\psi_i,t)-A_0} + A\left(\psi_i,t\right)^2 - (\delta^*)_{ri}^2\left(t\right)\right)}{A\left(\psi_i,t\right)^3} \tag{6.16k}$$

$$k_{z\beta}^b(t) = K_n \sum_i^z \frac{r_d\left(A\left(\psi_i,t\right)-A_0\right)^n (\delta^*)_{ri}\left(t\right)(\delta^*)_{zi}\left(t\right)\cos^2\left(\psi(t)\right)\left(1-\frac{nA(\psi_i,t)}{A(\psi_i,t)-A_0}\right)}{A\left(\psi_i,t\right)^3} \tag{6.16l}$$

$$k_{z\gamma}^b(t) = K_n \sum_i^z \frac{r_d\left(A\left(\psi_i,t\right)-A_0\right)^n (\delta^*)_{ri}\left(t\right)(\delta^*)_{zi}\left(t\right)\sin\left(\psi(t)\right)\cos\left(\psi(t)\right)\left(\frac{nA(\psi_i,t)}{A(\psi_i,t)-A_0}-1\right)}{A\left(\psi_i,t\right)^3} \tag{6.16m}$$

$$k_{\beta\beta}^b(t) = K_n \sum_i^z \frac{r_d^2\left(A\left(\psi_i,t\right)-A_0\right)^n \cos^2\left(\psi(t)\right)\left(\frac{nA(\psi_i,t)(\delta^*)_{zi}^2(t)}{A(\psi_i,t)-A_0} + A\left(\psi_i,t\right)^2 - (\delta^*)_{zi}^2\left(t\right)\right)}{A\left(\psi_i,t\right)^3} \tag{6.16n}$$

$$k^b_{\beta\gamma}(t) = K_n \sum_i^z \frac{r_d^2 \left(A\left(\psi_i,t\right) - A_0\right)^n \sin\left(\psi(t)\right)\cos\left(\psi(t)\right)\left(\left(\delta^*\right)^2_{zi}(t) - \frac{nA(\psi_i,t)(\delta^*)^2_{zi}(t)}{A(\psi_i,t)-A_0} - A\left(\psi_i,t\right)^2\right)}{A\left(\psi_i,t\right)^3} \tag{6.16o}$$

$$k^b_{\gamma\gamma}(t) = K_n \sum_i^z \frac{r_d^2 \left(A\left(\psi_i,t\right) - A_0\right)^n \sin^2\left(\psi(t)\right)\left(\frac{nA(\psi_i,t)(\delta^*)^2_{zi}(t)}{A(\psi_i,t)-A_0} + A\left(\psi_i,t\right)^2 - \left(\delta^*\right)^2_{zi}(t)\right)}{A\left(\psi_i,t\right)^3} \tag{6.16p}$$

where since the matrix $\mathbf{k_e^b}$ is symmetric it is found that $k^b_{ij} = k^b_{ji}$ for $i,j = x,y,z,\beta,\gamma$, and with free rotation about the shaft axis it is seen that $k^b_{i\alpha} = k^b_{\alpha i} = 0$ for $i = x,y,z,\beta,\gamma$, which is already included in the stiffness matrix of Equation (6.16a).

In Equation (6.16) K_n is the Hertzian contact stiffness, which accounts for the Hertzian contact between the inner bearing raceway, the bearing element and the outer bearing raceway. This is calculated for a single sided contact between one raceway and the ball through the equation

$$K_n = \frac{8\sqrt{6}}{3\sqrt{3}} \frac{E^*\sqrt{R_e}}{\lambda^{3/2}} \tag{6.17}$$

which is derived in Appendix D, and where E^* is the effective Young's Modulus, R_e is an effective radius and λ is a constant based on the radii of curvature of the contacting bodies.

Since this only results in a stiffness term for one contact side (i.e. inner raceway - bearing element) the stiffness terms must be added in series from inner (K_i) and outer (K_o) raceway contact.

$$\frac{1}{K_n} = \frac{1}{K_i} + \frac{1}{K_o} \tag{6.18}$$

These individual element stiffness terms are then summed across the complete bearing; however not all the element contributions are considered in the calculation of the bearing stiffness under applied load and rotational angle; only when the inequality $A\left(\psi_i\left(t\right)\right) > 0$ is satisfied will the contribution of the element be used. This omits the negative stiffness effects caused by separation of the inner race from the ball bearing, i.e. an increase in the distance between the raceway centres of curvatures,

in reality these ball bearings would not be loaded.

From these formulations the time varying bearing stiffness' can be calculated and incorporated into the global stiffness matrix, where the 12x12 stiffness matrix for the bearing incorporating two nodes is given simply as:

$$\mathbf{K}_e^b(t) = \begin{bmatrix} \mathbf{k}_e^b(t) & -\mathbf{k}_e^b(t) \\ -\mathbf{k}_e^b(t) & \mathbf{k}_e^b(t) \end{bmatrix} \tag{6.19}$$

This is added to the global system of equations in a similar fashion to the other ancillary components, where the global matrix is increased in size by 6 to account for the increase in the number of nodes, and the quarters of the bearing stiffness matrix are added to the appropriate elements of the matrix. The positioning of the bearing element quarters depends on the shaft node to which the bearing element is attached, such that with a global system of $n-1$ elements (n nodes) where the bearing is attached to node p at one end and a new node at its free end, the bearing stiffness elements are placed as such.

$$\begin{gathered} \mathbf{K}(t)\,(6(p-1)+1:6(p-1)+6, 6(p-1)+1:6(p-1)+6) = \mathbf{k_b^e}(t) \\ \mathbf{K}(t)\,(6(p-1)+1:6(p-1)+6, 6n+1:6n+6) = -\mathbf{k_b^e}(t) \\ \mathbf{K}(t)\,(6n+1:6n+6, 6(p-1)+1:6(p-1)+6) = -\mathbf{k_b^e}(t) \\ \mathbf{K}(t)\,(6n+1:6n+6, 6n+1:6n+6) = \mathbf{k_b^e}(t) \end{gathered}$$

The mass of the bearing is simplified in a similar fashion to the coupling, as shown in Equation (6.9), whereby point masses are assumed and there is no interconnection between the various mass DOF. The first 6 terms of the mass matrix, which are associated with the common shaft node simply account for the mass properties of the bearing internals, while the lower right hand corner is considered to be the mass of the bearing externals including the bearing housing and outer raceway, as shown in Figure 5.7 with mass values derived from CAD drawings given in Table 5.5.

Damping is again approximated through separate Rayleigh damping coefficients applied to the elemental stiffness and mass matrices, however since the stiffness is load and position dependent the stiffness matrices are unknown until the

simulation is underway. Two options are available to model the bearing damping, the first is to simply allow the bearing damping to vary along with the bearing stiffness, the second is to apply a representative deflection to the bearings to obtain an approximate time invariant damping matrix. The first option is more computationally expensive as it requires the global damping matrix to be reformulated for every time increment, however this may be more accurate compared to approximating the types and magnitude of the deflections expected. The second formulation although not time varying can be tweaked by varying the deflection and Rayleigh coefficient values to give a fair representation of the bearing damping without the computational expense. In this study the bearing damping will be time invariant to reduce computational time.

6.2.4 Bearing Supports

Within the test rig the bearings are positioned on top of supporting structures as shown in Figure 6.3. On the motor side shaft the supports are placed on a floating table, which allows the motor/shaft assembly to be moved, and misalignments to be introduced; whereas on the load side shaft the supports are fixed to the main rig base. On both the motor and load sides, the supports are assumed to be fixed at their base, which is deemed acceptable since the mass and stiffness of the main rig base and the floating table are designed to prohibit excessive vibration and act as a suitable datum.

Since the supporting structures are bespoke components little information is known of their mass and stiffness properties, such that under these conditions it is usual to perform a full finite element analysis to determine the structures response to load. However under dynamic loading the solution of the large structural matrices is computationally expensive, and therefore a technique known as Model Order Reduction (MOR), Component Mode Synthesis (CMS) or substructuring is used to reduce the size of the structural matrices for increased computational efficiency. This is obtained by eliminating the majority of the degrees of freedom (DOF), leaving only the DOF that connect the "substructure" or "superelement" to the rest of the

model.

Two techniques used to perform CMS are demonstrated in detail in Appendix E. These are Guyan reduction and Craig-Bampton CMS, where in this thesis Guyan reduction is used to determine the support mass and stiffness matrices. Although Guyan reduction can result in errors in the mass matrix, as it lumps all the mass at the connecting DOF, it has been found and shown in Appendix E that errors are minimal for the current forcing frequency.

As previously described and shown in Figure 6.3 the bearings sit on a plate, which attaches both bearings and supporting frames to each other; the stiffness and mass of this plate is also determined through Guyan reduction and is used as a coupling component between the two bearing/bearing support series, as shown in Figure 6.6. The full matrices for these components are not given here, however

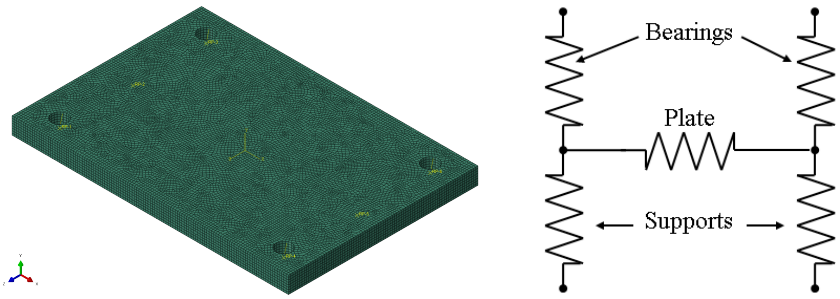

(a) Finite Element model (b) Interconnectivity

Figure 6.6: Bearing base plate FE model and interaction with the bearing supporting structure

they are shown in Appendix F for completeness. The mass and stiffness terms are included into the global matrices by splitting the element matrices into quarters and adding to the existing global matrices, which is similar to the method used for the bearings. The positioning of the element quarters is determined through which bearing the support is attached, as shown in Equation (6.20) for a double bearing/support system, where the bearings are attached to node q and p on the shaft and a is an element in either the global stiffness or mass matrices.

$$
\begin{bmatrix}
a_{11}^{s1} & a_{12}^{s1} & 0 & \cdots & & & & & & & & & \\
a_{21}^{s1} & a_{22}^{s1}+a_{11}^{s2} & a_{11}^{s2} & 0 & \cdots & & & & & & & & \\
0 & \ddots & \ddots & \ddots & & & & & & & & & \\
\vdots & 0 & & a_{22}^{sq}+a_{11}^{s(q+1)}+a_{11}^{b1} & a_{12}^{s(q+1)} & & & a_{12}^{b1} & & & & & \\
 & & & & \ddots & \ddots & & & & & & & \\
 & & & & & a_{22}^{sp}+a_{11}^{s(p+1)}+a_{11}^{b2} & a_{12}^{s(p+1)} & & a_{12}^{b2} & & & & \\
 & & & & & \ddots & \ddots & & & & & & \\
 & & & a_{21}^{b1} & & & & a_{22}^{b1}+a_{11}^{supp1}+a_{11}^{base} & a_{12}^{base} & & a_{12}^{supp1} & & \\
 & & & & & a_{21}^{b2} & & a_{21}^{base} & a_{22}^{b2}+a_{11}^{supp2}+a_{22}^{base} & & & a_{12}^{supp2} \\
 & & & & & & & a_{21}^{supp1} & & & a_{22}^{supp1} & & \\
 & & & & & & & & a_{21}^{supp2} & & & a_{22}^{supp2}
\end{bmatrix}
\tag{6.20}
$$

6.2.5 Motor and Load

The motor and load do not contribute to the stiffness of the system, however they do impose mass and forcing terms, where only the rotational inertia is considered as all other motions of the motor and load are constrained and therefore there are no inertia effects in those DOF. The rotational inertias are added to the global matrices through point masses at the motor/load nodes, which coincide with the coupling node if present.

The forcing characteristics of the model are that the load transmits a constant torque to the system, while the motor torque is proportional to the square of the motor rotational speed.

$$T_M = T_{outcoeff}\dot{\theta}_M^2 \tag{6.21}$$

Where $T_{outcoeff}$ is the coefficient used to determine the final speed and $\dot{\theta}_M$ is the rotational speed of the motor. This allows the system to ramp to a predefined speed and allows some variability in the load applied to the motor, which is not achieved by applying a velocity boundary condition to the motor node.

6.3 Inclusion of gear contact excitations

In the dynamic model the main source of vibration is at the gear mesh, this is either through the variation of the mesh stiffness as a result of changes in the number of gear teeth in contact, frictional forces due relative sliding of the contacting teeth or forces created through misaligned gear contact. This section splits up the gear contact to investigate these phenomena separately, and determines methods of applying their resultant forces to the global system of equations.

6.3.1 Gear Mesh

The gear mesh spans both shafts and is the only connecting element between the two, therefore in a system where the line-of-contact is aligned with the global vertical axis (y), such that $y = \delta$ as shown in Figure 6.7(a), the force coupling

between the two shafts can be given as:

$$N_m(\alpha, t) = -k_m(\alpha)\left(r_{b1}\alpha_1(t) - r_{b2}\alpha_2(t) - y_1(t) + y_2(t)\right) \tag{6.22}$$

Where r_b and α are the base radii and rotational position of the gears respectively and k_m is the mesh stiffness, which is calculated in the dynamic model as a function of the gear rotational position by interpolating the static finite element derived mesh stiffness data shown in Section 4.2. However if the gears are positioned such that the line-of-action is inclined to the vertical axis by the pressure angle (ϕ), as shown in Figure 6.7(b), the contact force (N_m) no longer acts in the global coordinate frame ($y \neq \delta$) but along the LOA, and a transformation of the element parameters is required. The translations along the line-of-action δ_1 and δ_2 are now defined in the

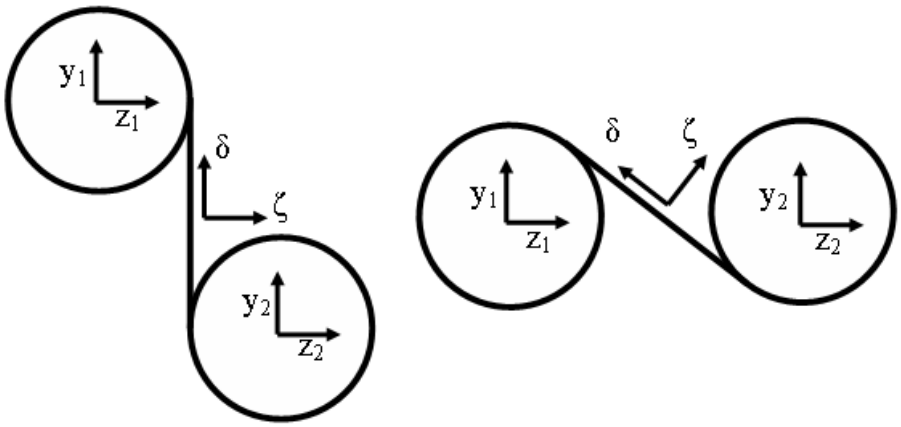

(a) Aligned with global vertical axis (b) Inclined by pressure angle

Figure 6.7: Alignment of local line-of-action coordinate system.

local coordinate system, whereas the rotations α_1 and α_2 remain aligned with the global coordinate system. With these variations in the coordinate system Equation (6.22) is split into terms in the global coordinate system and those in the local system.

$$N_m(\alpha, t) = -k_m(\alpha)\left(r_{b1}\alpha_1(t) - r_{b2}\alpha_2(t)\right) + k_m(\alpha)\left(\delta_1(t) - \delta_2(t)\right) \tag{6.23}$$

To generate the normal contact force along the line-of-action based on the global displacements of the model, the global displacements (v_1, w_1, v_2 and w_2) are converted into displacements along the LOA.

$$\delta_1(t) = v_1(t)\cos\phi'(t) - w_1(t)\sin\phi'(t) \tag{6.24a}$$

$$\delta_2(t) = v_2(t)\cos\phi'(t) - w_2(t)\sin\phi'(t) \tag{6.24b}$$

Using this transformation and Equation (6.22), a description of the normal contact force along the LOA based on the global displacements is obtained.

$$N_m(\alpha,t) = k_m(\alpha)\begin{bmatrix}\cos\phi'(t) & -\sin\phi'(t) & -r_{b1} & -\cos\phi'(t) & \sin\phi'(t) & r_{b2}\end{bmatrix}\begin{Bmatrix}v_1(t)\\ w_1(t)\\ \alpha_1(t)\\ v_2(t)\\ w_2(t)\\ \alpha_2(t)\end{Bmatrix} \tag{6.25}$$

However the forces generated along the LOA must then be further converted into forces acting in the global coordinate system, where.

$$N_y(\alpha,t) = N_m(\alpha,t)\cos\phi'(t) \tag{6.26a}$$

$$N_z(\alpha,t) = -N_m(\alpha,t)\sin\phi'(t) \tag{6.26b}$$

$$N_{\alpha i}(\alpha,t) = -N_m(\alpha,t)r_i(t) \tag{6.26c}$$

It is appropriate at this point to identify the coordinate systems used in the dynamic model, therefore by referencing Figures 6.2 and 6.7(b) it can be shown that the positive axial direction (x-axis) of the left gear (gear 1), as shown in Figure 6.7(b), is into the page, while the positive axial direction of the right gear (gear 2) is out of the page. All rotations are determined by the right hand rule as shown in Figure 6.2 and from this the responses of the system under the applied load of the mesh can be determined, which is based on the various motions of the gear centres.

These applied forces from the gear mesh can be represented by a 12 DOF

stiffness matrix based on the above coordinate transform equations, which determines the mesh forces in the global coordinate system based on the displacements in the global coordinate system.

$$\mathbf{N_m}(\alpha,t) = k(\alpha)\begin{bmatrix} 0 & 0 & 0 & 0 & 0 & 0 & 0 & 0 & 0 & 0 & 0 & 0 \\ 0 & c^2 & -cs & -r_{b1}c & 0 & 0 & 0 & -c^2 & cs & r_{b2}c & 0 & 0 \\ 0 & -cs & s^2 & r_{b1}s & 0 & 0 & 0 & cs & -s^2 & -r_{b2}s & 0 & 0 \\ 0 & -r_{b1}c & r_{b1}s & r_{b1}^2 & 0 & 0 & 0 & r_{b1}c & -r_{b1}s & -r_{b1}r_{b2} & 0 & 0 \\ 0 & 0 & 0 & 0 & 0 & 0 & 0 & 0 & 0 & 0 & 0 & 0 \\ 0 & 0 & 0 & 0 & 0 & 0 & 0 & 0 & 0 & 0 & 0 & 0 \\ 0 & 0 & 0 & 0 & 0 & 0 & 0 & 0 & 0 & 0 & 0 & 0 \\ 0 & -c^2 & cs & r_{b1}c & 0 & 0 & 0 & c^2 & -cs & -r_{b2}c & 0 & 0 \\ 0 & cs & -s^2 & -r_{b1}s & 0 & 0 & 0 & -cs & s^2 & r_{b2}s & 0 & 0 \\ 0 & r_{b2}c & -r_{b2}s & -r_{b1}r_{b2} & 0 & 0 & 0 & -r_{b2}c & r_{b2}s & r_{b2}^2 & 0 & 0 \\ 0 & 0 & 0 & 0 & 0 & 0 & 0 & 0 & 0 & 0 & 0 & 0 \\ 0 & 0 & 0 & 0 & 0 & 0 & 0 & 0 & 0 & 0 & 0 & 0 \end{bmatrix}\begin{Bmatrix} u_1(t) \\ v_1(t) \\ w_1(t) \\ \alpha_1(t) \\ \beta_1(t) \\ \gamma_1(t) \\ u_2(t) \\ v_2(t) \\ w_2(t) \\ \alpha_2(t) \\ \beta_2(t) \\ \gamma_2(t) \end{Bmatrix} \tag{6.27}$$

Where $c = \cos\phi'(t)$ and $s = \sin\phi'(t)$.

Using Equations (6.27) the mesh coupling can be applied to the system by two means; firstly by expanding the matrix equation the mesh forces can be applied directly to the forcing matrix and excite the system externally, in this method the stiffness terms of Equation (6.27) are not included into the global stiffness matrix. The alternative method is to vary the mesh stiffness, which parametrically excites the system, this second method will have effects on the systems natural frequencies as the mesh stiffness values vary depending on the rotational position of the gears and is used here.

6.3.2 Friction

Friction is considered by many researchers as an important contributor to gear dynamic responses, which is understandable as, under perfect alignment conditions, it operates single-handedly in the Off-Line-of-Action (OLOA) direction, in such that it creates an alternating force in a direction perpendicular to the pressure line. At present all forces developed and transferred in the dynamic model act along the LOA, which reduces the total system Degrees of Freedom and the available motions of study.

To include these frictional forces a description of the friction as a function of

time and dynamic force is required, where the simplest methodology is the sliding Coulomb friction model where the frictional force for a single tooth ($F_{f,i}$) is taken as.

$$F_{f,i}(t) = \mu(t) N_m(t) \tag{6.28}$$

Where $\mu(t)$ is the time varying friction coefficient and $N_m(t)$ is the dynamic normal force, which is determined from the output of the dynamic model as described in Section 6.3.1. This method of representing the forcing term, in terms of the system variables, as apposed to using forces obtained from quasi-static conditions, implies that the friction force is modelled as a time varying parameter much like the mesh stiffness. When using quasi-statically obtained normal forces the friction force does not contain any terms which are present on the left hand side of the equations of motion and therefore is simply modelled as a forcing term.

Coefficient of Friction

As previously mentioned, and described in the literature review, there are many methods of determining the coefficient of friction [29, 88, 89], such as the empirical formulation of Kelley and Lemanski [91], the pure Coulomb model and the smoothed Coulomb model, which will be used here and is given as

$$\mu(t) = (2\mu_0/\pi) \tan^{-1}(V_s(t)/V_0) \tag{6.29}$$

Where μ_0 is the reference Coulomb coefficient of friction, V_s is the tooth sliding velocity and V_0 is a reference velocity, which determines the transition between positive and negative sliding velocities and hence the sign convention of the friction coefficient as shown in Figure 6.8, where arbitrary values of the above parameters are used. Figure 6.8 shows that with low reference velocity the smoothed Coulomb model closely resembles the square wave representation of the coefficient of friction. In the square wave formulations there is a singularity present at the pitch point where the direction of sliding changes. As mentioned in the literature review, experimental

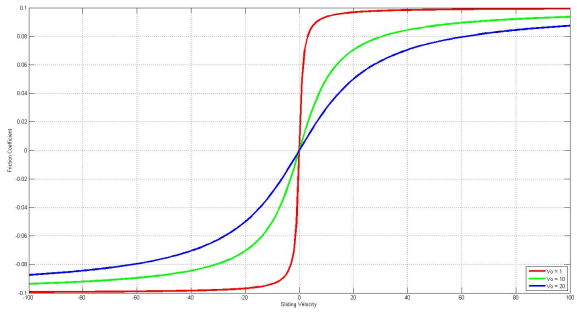

Figure 6.8: Coulomb friction coefficient variation

studies have shown that this is not necessarily the case and that there is a gradual change in friction coefficient, especially under boundary layer lubrication regimes [90]. It is found that a reference velocity value of around 1% of the maximum sliding velocity value gives reasonable results for the coefficient of friction.

The sign of the friction coefficient and the subsequent direction of the friction force are determined by the direction of the sliding velocity, since friction forces tend to resist relative motion. As with the contacting force the method of determining and representing of the sliding velocity impacts the terminology by which the modelling approach is described, as well as the available solution methods. When the velocity is an explicitly described function of time, i.e. the velocity is determined geometrically, the model is linear, whereas when the friction coefficient is determined from instantaneous model velocities the model exhibits an implicit nonlinearity. Using the smoothed Coulomb model the nonlinear sliding velocity can be given as

$$V_s(t) = \xi_p(t)\left(\Omega_2 + \dot{\delta}_2(t)\right) - \xi_g(t)\left(\Omega_3 + \dot{\delta}_3(t)\right) - \ldots$$
$$\left(\dot{y}_1(t)\sin\phi'(t) + \dot{z}_1(t)\cos\phi'(t)\right) + \left(\dot{y}_2(t)\sin\phi'(t) + \dot{z}_2(t)\cos\phi'(t)\right) \quad (6.30)$$

Where ξ_p and ξ_g are the distances between the pinion/gear centres from the contact point along the pressure line, as shown in Figure 6.9, Ω_2 and Ω_3 are the mean angular speeds of the pinion and gear respectively, δ_2 and δ_3 are the angular deviations from the mean position, $\dot{y}_i$ and $\dot{z}_i$ are the vertical and horizontal velocities of the two

gears and ϕ' is the instantaneous pressure angle. It can be seen here that the velocity terms in the first two brackets are equal to the complete instantaneous rotational velocity of the gears, which is already an output of of the dynamic model in the global coordinate system.

From the above equation it can be seen that the variation in the position of the contact point during meshing ($\xi_p(t)$, $\xi_g(t)$) is required. Although this can be taken as a function of time it is more desirable to describe its variation in terms of the rotational angle of the driven gear as it can then be linked to the output of the dynamic model. Figure 6.9 below shows an extremely simple representation of two gears in contact with required dimensions for the determination of the position of the contact point along the line of contact. The required parameters seen in

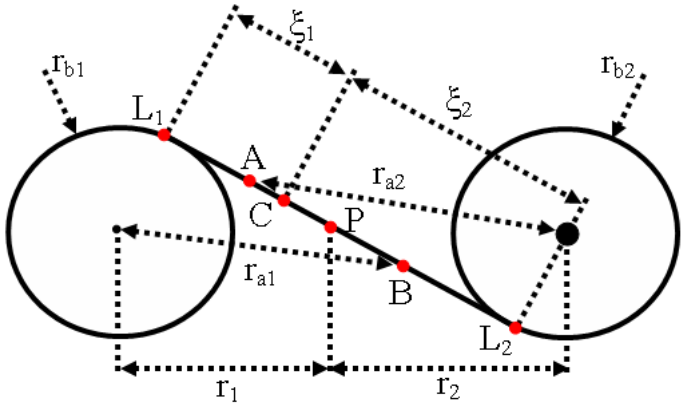

Figure 6.9: Contact position geometry diagram

Figure 6.9 include the gear pitch radii (r_1, r_2), the gear base radii (r_{b1}, r_{b2}) the gear outside/addendum radii (r_{a1}, r_{a2}), the pitch point (P) and the position of the contact point C along the line of action from the gear centres (ξ_g, ξ_p). In this geometric gear pair, contact is initiated when the addendum circle of one of the gears crosses the line of contact (A), the gears then remain in contact until the addendum circle of the opposing gear crosses the line of contact on the other side of the pitch point (B). The complete length of the line of contact (L_1L_2), from its tangent points with the gear base circles can be calculated simply from Pythagoras'

theorem in the form

$$L_1L_2(t) = L(t) = \sqrt{(r_1'(t))^2 - r_{b1}^2} + \sqrt{(r_2'(t))^2 - r_{b2}^2} \tag{6.31}$$

Again the length from the base circle of gear 2 to the initial point of contact (L_2A) and the length from the base circle of gear 1 to the final point of contact (L_1B) can be given respectively as

$$L_2A = \xi_2(A) = \sqrt{r_{a2}^2 - r_{b2}^2} \tag{6.32a}$$

$$L_1B = \xi_1(B) = \sqrt{r_{a1}^2 - r_{b1}^2} \tag{6.32b}$$

And subsequently the corresponding distances (L_2B, L_1A) are taken as the difference between the total length of the line of contact and the distances given in Equations (6.32a) and (6.32b) such that

$$L_2B(t) = \xi_1(A)(t) = L(t) - \xi_2(A) = \sqrt{(r_1'(t))^2 - r_{b1}^2} + \sqrt{(r_2'(t))^2 - r_{b2}^2} - \sqrt{r_{a2}^2 - r_{b2}^2} \tag{6.32c}$$

$$L_1A(t) = \xi_2(B)(t) = L(t) - \xi_1(B) = \sqrt{(r_1'(t))^2 - r_{b1}^2} + \sqrt{(r_2'(t))^2 - r_{b2}^2} - \sqrt{r_{a1}^2 - r_{b1}^2} \tag{6.32d}$$

It is assumed that the variation in the position of contact will vary linearly with the gear angle, which is true when considering conjugate action, since this implies that there is constant rotation of both gears and therefore constant velocity along the LOA. Therefore a relationship between the points determined above and the angles they subtend is required to fully describe the sliding velocity in terms of the instantaneous roll angle and rotational velocity. This is obtained from knowledge of the angle of action described in Section 3.2.2, which can be used to fully describe the variation of the contact point lengths with respect to the gear rotation angles from a purely geometric stand point. This representation is given in Equation (6.33),

with reference to Equations (6.32a)–(6.32d) and the angle of action (θ_{AB}), as a set of linear mathematical equations. The angle corresponding to the initiation of contact can be determined from the mesh stiffness curves as the point where the mesh stiffness has a sudden increase, which for convenience is taken as θ_0 in Equation (6.33).

$$\xi_p(\theta,t) = \left((\theta-\theta_0)\left(\frac{\xi_1(B)-\xi_1(A)(t)}{\theta_{AB}(t)}\right)+\xi_1(A)(t)\right) \tag{6.33a}$$

$$\xi_g(\theta,t) = \left((\theta-\theta_0)\left(\frac{\xi_2(B)(t)-\xi_2(A)}{\theta_{AB}(t)}\right)+\xi_2(A)\right) \tag{6.33b}$$

It is noted here that due to flexibilities of the gears, and the variation in loading caused by the number of teeth in mesh, the contact point may deviate slightly during the meshing period, however the amount is imagined to be insignificant compared to the effect of the rigid body motion of the gears. It is also believed that the variation in rotation position due to the gear flexibilities should be captured in some part via the use of instantaneous rotation angles in the determination of the contact position and contact lengths.

Using Equations (6.28) - (6.30) with Equation (6.33) and the normal tooth force the frictional force for a single tooth can be obtained, however for large portions of the contact cycle more than one tooth is in contact and the interaction between the numerous friction forces must be known.

Multiple Tooth Contact

Thus far the OLOA forces associated with friction have only been considered under single tooth contact, however under gear design guidelines, which suggest that no gear pair should have an involute contact ratio of less than 1.2, there will be situations where the load is shared among multiple teeth. The relative sliding velocities of these gear teeth pairs could, at various gear angles, be opposed or paralleled, resulting in a reduction or increase in the frictional force.

To gain a better understanding of the OLOA forces generated during mesh

a scenario for a gear pair with a gear ratio of between 1 and 2 is given, where the initialisation of the mesh is defined as the moment when a second tooth pair comes into contact. The mesh cycle is then split into 4 distinct points, which are described below.

#1 - Highest point of single tooth contact (HPSTC) - This is defined as the point of double tooth contact initialisation, where the gear load is shared between two teeth and the sliding velocities of the two tooth pairs are, in this situation, opposed.

#2 - Lowest point of single tooth contact (LPSTC) - The first tooth leaves and the complete load is transferred via the second tooth.

#3 - Pitch Point - The second tooth passes the pitch point and the direction of the sliding velocity and hence the frictional forces changes.

#4 - HPSTC - A third tooth enters contact and the cycle begins again.

For a complete tooth contact cycle an additional point #5 is added where the second tooth leaves contact, which is equal to the angle of action. It can also be argued that point #3 could occur before point #2 for some gear geometries and that in this situation the friction force under the initial double tooth contact will be roughly equal to that of single tooth contact. It is also seen that certain angles correspond to the different stages described above, for example the angle between point #1 and #4 is equal to the pitch angle. From these assumptions angles can be attributed to the various points in mesh, such that if point #1 is taken as $\theta = 0°$, point #2 is taken as the difference between the angle of action (θ_{AB}) and the pitch angle (θ_P), point #3 is determined as the point where the sliding velocity is zero (θ_{V_0}) and point #4 is taken as the pitch angle. This is summarised in Table 6.3 below. By using these points the sliding velocities of three teeth are shown in Figure 6.10, where Tooth 2 enters contact with a large relative sliding velocity, which gradually reduces to zero at the pitch point then increases in magnitude as the tooth leaves mesh. This occurs in a linear fashion with respect to the gear angle and because

Point #1	$\theta = 0°$
Point #2	$\theta = \theta_{AB} - \theta_P$
Point #3	$\theta = \theta_{V_0}$
Point #4	$\theta = \theta_P$

Table 6.3: Angular occurrence of key meshing events

in this scenario the number of teeth on the gear and pinion are similar, and hence the gear geometries are similar, the maximum approach and recess velocities are similar in magnitude. If there were many more teeth on either gear compared to the other there would be a variation in the arc of approach and arc of recess and hence a variation in the entrance and exit sliding velocities. In a paper by Vaishya and Singh

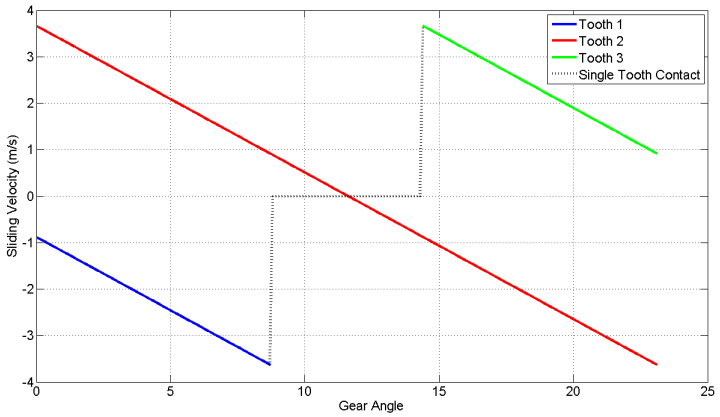

Figure 6.10: Multiple tooth sliding velocity

[20], investigating the effect of friction, a similar plot was presented of gear sliding velocities under quasi-static conditions for a gear pair consisting of 25 and 31 teeth and an involute contact ratio of 1.433. Their plot, given in Figure 6.11, shows 2 teeth represented by the solid line and the dashed line and suggests that the relative sliding velocity of the second gear tooth is always negative, which is incorrect, and that the sliding velocity of the first gear tooth pair is only negative for a very small fraction of the mesh cycle. This is obviously incorrect and the plot also assumes that there are always two teeth in contact although as previously mentioned the involute contact ratio is not equal exactly to 2. This can be seen by the lack of a period of time in the mesh cycle where the relative sliding velocity of one of the gear teeth

is zero, which would indicate that the teeth are out of mesh and no friction force would be generated. It also appears from the figure that the tooth sliding velocities of the two teeth are always in phase with each other, whereas in Figure 6.10 it is observed that peak sliding velocities for each tooth are out of phase. Figure 6.11

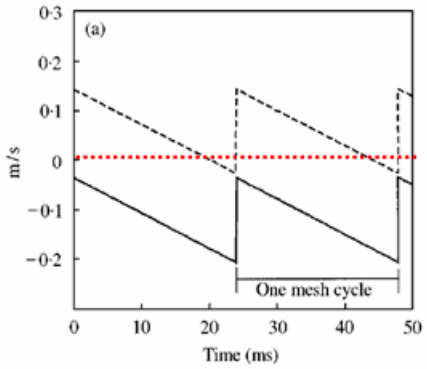

Figure 6.11: Tooth sliding velocity by Vaishya and Singh [20, 21]

could exhibit a simple mistake which would account for a portion of the variations with the assumed sliding velocities given in Figure 6.10. It could be assumed that the dashed line only accounted for the sliding velocity of tooth 1 for the period up to the sharp increase in sliding velocity, approximately $0 \leq t \leq 25$ms, and for the next period, marked as one mesh cycle in Figure 6.11, the tooth is represented by the solid line. This would cause the sliding velocity graph to exhibit the behaviour expected, in such that both gear tooth pairs would experience positive and negative relative sliding velocities, which are periodic and have peak values offset from each other. This small alteration in the data would not however alter the assumption implied by Figure 6.11, which is that two teeth are constantly in contact.

As well as multiple sliding velocity conditions, double tooth contact also effects the friction force through how the load is apportioned to the various teeth, which is often referred to as the Load Sharing Ratio (LSR). In its simplest form it can be assumed that when two pairs of teeth are in contact the load is shared equally between the two pairs, giving a square wave approximation to the LSR. This has the effect of completely nullifying the friction force when two pairs of teeth are in contact with opposing sliding velocities. This technique has been used by many

studying the effect of friction on gear dynamics [20, 21], however as shown in papers by Wang and Howard [65], Pedrero *et al* [76] and the work performed in Chapter 4 this load approximation is not accurate.

It is believed that the LSR representation proposed by Pedrero *et al* [76], where under double tooth contact the LSR varies linearly between a third and two thirds and under single tooth contact the LSR is 1, is a reasonable approximation of the realistic LSR. This approximation is free from the softening type interaction at the initiation and termination of contact due to the effects of loading and tooth bending in these areas. From knowledge of the key meshing event angles as shown in Table 6.3 it is possible to represent the load sharing ratio for a single gear tooth as a piecewise function based on the three main areas of contact. These equations are given below, however in these equations the initialisation of tooth contact occurs at $\theta = \theta_0$.

$$\mathrm{LSR}(\theta,t) = \begin{cases} \frac{1}{3}\left(\left(\frac{\theta-\theta_0}{\theta_{AB}(t)-\theta_P}\right)+1\right) & \theta_0 \leq \theta \leq \theta_{AB}(t)-\theta_P+\theta_0 \\ 1 & \theta_{AB}(t)-\theta_P+\theta_0 \leq \theta \leq \theta_P+\theta_0 \\ \frac{1}{3}\left(\left(\frac{\theta_{AB}(t)+\theta_0-\theta}{\theta_{AB}(t)-\theta_P}\right)+1\right) & \theta_P+\theta_0 \leq \theta \leq \theta_{AB}(t)+\theta_0 \end{cases} \tag{6.34}$$

Mathematical Representation of the Frictional Force

With this approximation to the load sharing ratio, the dynamic normal force and the description of the friction coefficient given in Equations (6.29), (6.30) and (6.33), a piecewise description of the total friction can be derived using the Coulomb friction model given in Equation (6.28) for single and double tooth contact. This representation is given below for a mesh cycle beginning at $\theta = \theta_0$, however since the equations are periodic with a period of θ_P only two piecewise equations describing the period $\theta_0 \leq \theta \leq \theta_0 + \theta_P$ are required. After this period Tooth 2 is represented by the equations of Tooth 1 and Tooth 3 is represented by the equations of Tooth 2, and so the cycle continues. The force equation, as seen in Equation (6.35), is unchanged during the mesh cycle, however its components ($\xi_{i,1}$, $\xi_{i,2}$ and LSR_i) are not linear during the complete mesh period and are therefore represented as linear

piecewise functions as shown in Equations (6.36)

$$F_f(\theta,t) = \sum_{i=1}^{2} \mu_i(\theta,t) N_i(\theta,t) \tag{6.35a}$$

$$\begin{aligned} F_f(\theta,t) = \sum_{i=1}^{2} (2\mu_0/\pi) \tan^{-1} \Big(\Big(\xi_{i,1}(\theta,t) \left(\Omega_2 + \dot{\delta}_2(t) \right) - \dots \\ \xi_{i,2}(\theta,t) \left(\Omega_3 + \dot{\delta}_3(t) \right) - \left(\dot{y}_1(t) \sin\phi'(t) + \dot{z}_1(t) \cos\phi'(t) \right) + \dots \\ \left(\dot{y}_2(t) \sin\phi'(t) + \dot{z}_2(t) \cos\phi'(t) \right) \Big) / V_0 \Big) \mathrm{LSR}_i(\theta,t) N(t) \end{aligned} \tag{6.35b}$$

For the period $\theta_0 \leq \theta \leq (\theta_{AB} - \theta_P + \theta_0)$ the angular dependent parameters for the current tooth in mesh (Tooth 1) are given below.

$$\xi_{1,1}(\theta,t) = \left((\theta + \theta_P - \theta_0) \left(\frac{\xi_1(B) - \xi_1(A)(t)}{\theta_{AB}(t)} \right) + \xi_1(A)(t) \right) \tag{6.36a}$$

$$\xi_{1,2}(\theta,t) = \left((\theta + \theta_P - \theta_0) \left(\frac{\xi_2(B)(t) - \xi_2(A)}{\theta_{AB}(t)} \right) + \xi_2(A) \right) \tag{6.36b}$$

$$\mathrm{LSR}_1(\theta,t) = \frac{1}{3} \left(\left(\frac{\theta_0 - \theta}{\theta_{AB}(t) - \theta_P} \right) + 2 \right) \tag{6.36c}$$

with the second tooth (Tooth 2) parameters taken as.

$$\xi_{2,1}(\theta,t) = \left((\theta - \theta_0) \left(\frac{\xi_1(B) - \xi_1(A)(t)}{\theta_{AB}(t)} \right) + \xi_1(A)(t) \right) \tag{6.36d}$$

$$\xi_{2,2}(\theta,t) = \left((\theta - \theta_0) \left(\frac{\xi_2(B)(t) - \xi_2(A)}{\theta_{AB}(t)} \right) + \xi_2(A) \right) \tag{6.36e}$$

$$\mathrm{LSR}_2(\theta,t) = \frac{1}{3} \left(\left(\frac{\theta - \theta_0}{\theta_{AB}(t) - \theta_P} \right) + 1 \right) \tag{6.36f}$$

During the period $(\theta_{AB} - \theta_P + \theta_0) \leq \theta \leq (\theta_P + \theta_0)$ the parameters for the two teeth are given as

$$\xi_{1,1}(\theta,t) = 0 \tag{6.36g}$$

$$\xi_{1,2}(\theta,t) = 0 \tag{6.36h}$$

$$\mathrm{LSR}_1(\theta,t) = 0 \tag{6.36i}$$

$$\xi_{2,1}(\theta,t) = \left((\theta-\theta_0)\left(\frac{\xi_1(B)-\xi_1(A)(t)}{\theta_{AB}(t)}\right)+\xi_1(A)(t)\right) \tag{6.36j}$$

$$\xi_{2,2}(\theta,t) = \left((\theta-\theta_0)\left(\frac{\xi_2(B)(t)-\xi_2(A)}{\theta_{AB}(t)}\right)+\xi_2(A)\right) \tag{6.36k}$$

$$\mathrm{LSR}_2(\theta,t) = 1 \tag{6.36l}$$

By removing the dynamic mesh force from the summation in Equation (6.35b) the friction coefficient can be given as a function of both instantaneous gear rotational velocities and gear angles. Using the mean rotational velocity of the gears Figure 6.12 illustrates the variation in friction coefficient with gear angle. This shows clearly

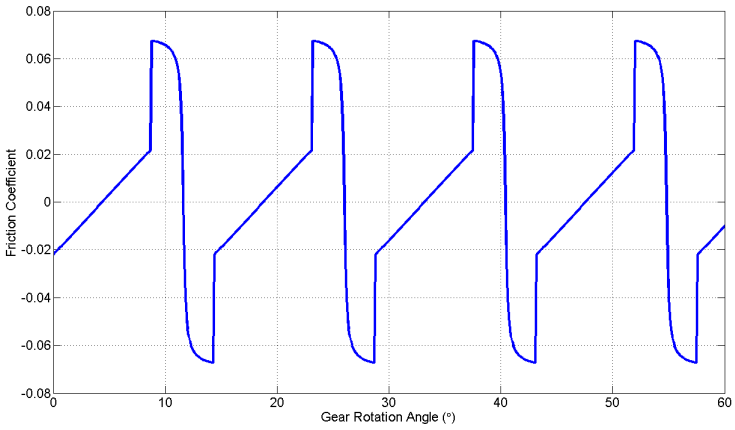

Figure 6.12: Friction coefficient variation

the linear variation of the friction force due to transfer of the load from the gear leaving mesh to the gear entering mesh, which causes a change in the direction of the friction coefficient. The load is then taken by a single tooth and is represented by the form shown in Figure 6.8 and again there is a sudden change in the direction of the friction coefficient as the contacting tooth passes the pitch point. Finally in the last section of the mesh period the friction coefficient follows a similar form to that of the first section. This means that for every mesh period the direction of the friction force will alternate three times, however it is imagined that due to its sudden nature the pitch point reversal of direction will have the biggest effect on the system dynamics.

The theoretical static friction force depicted in Figure 6.12 can be compared against experimental work performed by Rebbechi *et al* [50, 121], where quasi-static friction results are shown in Figure 6.13. These results were obtained on the NASA

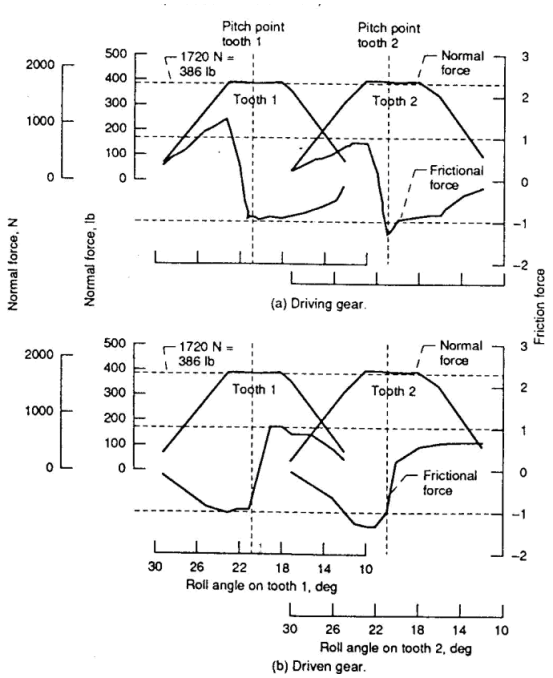

Figure 6.13: Experimental quasi-static friction forces conducted by Rebbechi *et al* [50, 121]

Lewis gear noise rig by instrumenting the tooth root fillets with strain gauges on the loaded and unloaded side and decomposing the strain data into normal and tangential forces. In general the results shown in Figure 6.13 match well with the theoretical results of Figure 6.12, however there is a large discrepancy that occurs in the transitions between single and double tooth contact. This is due to tip relief of around 0.023 - 0.025 mm at 24° roll angle included in the test data; the effect of which can be seen in the normal load results that do not exhibit the sharp increase and decreases at the initiation and end of single tooth contact witnessed in the LSR results of Section 4.2.1.

Inclusion of Friction

The tangential tooth force associated with friction, as shown in Figure 6.12, can be applied directly to the global forcing matrix using the pressure angle to de-

compose the tangential force into the global vertical and horizontal direction. Using the coordinate system shown in Figure 6.7 the frictional forces can be determined as:

$$F_{fy}(\theta, t) = F_f(\theta, t) \sin \phi'(t) \tag{6.37a}$$

$$F_{fz}(\theta, t) = F_f(\theta, t) \cos \phi'(t) \tag{6.37b}$$

Where ϕ' is the current pressure angle and the forces on the gear teeth are opposing, such that the vertical and horizontal forces on gear 1 are positive and the forces on gear 2 are negative at the initialization of contact; however as contact moves past the pitch point and the direction of sliding changes the sign of these forces will also change. Normal sliding of the tooth surfaces also introduces a torque about the gear centre due to the moment arm along the LOA, as shown in Figure 6.9; therefore the frictional torque about the axial direction (x-axis) can be calculated for both gears through the modification of Equation (6.35) and the parameters defined in Equations (6.36).

$$T_{f,1}(\theta, t) = \sum_{i=1}^{2} \xi_{i,1}(\theta, t) \mu_i(\theta, t) N_i(t) \tag{6.38a}$$

$$T_{f,2}(\theta, t) = \sum_{i=1}^{2} \xi_{i,2}(\theta, t) \mu_i(\theta, t) N_i(t) \tag{6.38b}$$

The frictional torque must be calculated on individual teeth due to the varying nature of the frictional forces and moments arms between different teeth. It is also noted that the frictional torques are again opposed with a negative torque on gear 1 and a positive torque on gear 2 at the initialization of contact.

Using the equations derived in this section the frictional forces and moments associated with normal sliding of the gear teeth can be determined; these generate forces in the normal plane of the gears, in the LOA directions. However the gears are also capable of sliding in the axial direction, which will generate further forces acting outside of this normal plane of action, and which will be discussed in the

proceeding section.

6.3.3 Axial Friction

Within the dynamic model the gears are free to move in 6 DOF and as a result there will be relative sliding in the axial direction. This can be decomposed into the translational axial motion (x-axis) and axial motion as a result of rotation about the global vertical axis (y-axis), where due to the coordinate system in use the total axial sliding velocity can be determined as.

$$V_a(t) = \dot{x}_1(t) + \dot{x}_2(t) + r'_1(t)\dot{\beta}_1(t) + r'_2(t)\dot{\beta}_2(t) \tag{6.39}$$

where $\dot{x}_i$ are the translational velocities in the axial direction, r'_i are the instantaneous pitch radii and $\dot{\beta}_i$ are the angular velocities about the vertical gear axes. The axial friction forces can then be obtained by applying this velocity to the smoothed Coulomb friction model given in Equation (6.29) and multiplying by the total normal contacting force, which is acceptable because the axial sliding directions do not vary from tooth-to-tooth in this formulation. The total axial friction force acting in the axial direction can therefore be summarized as.

$$F_{f,a}(t) = \sum_{i=1}^{2} (2\mu_0/\pi) \tan^{-1}\left(\left(\dot{x}_1(t) + \ldots \right.\right.$$
$$\left.\left. \dot{x}_2(t) + r'_1(t)\dot{\beta}_1(t) + r'_2(t)\dot{\beta}_2(t)\right)/V_0\right) N(t) \tag{6.40}$$

However using the generalized normal tooth load is not acceptable when considering the moments generated about the vertical and horizontal axes as a result of axial sliding, since the moment arms between the contact points and the gear axes varies between teeth as shown in Figure 6.14. These moment arms (δ_y and δ_z) can be calculated using the known base radii of the gears and the distance along the LOA of the contact points (ξ), as shown below for all gears (j) and all contacting teeth (i).

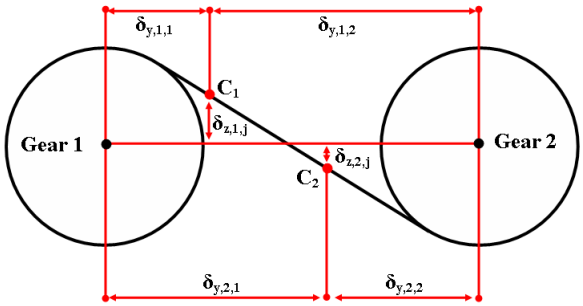

Figure 6.14: Schematic of axial friction moment arms

$$\delta_{y,i,j}(\theta,t) = r_{bj}\cos\phi'(t) + \xi_{i,j}(\theta,t)\sin\phi'(t) \tag{6.41a}$$

$$\delta_{z,i,j}(\theta,t) = r_{bj}\sin\phi'(t) - \xi_{i,j}(\theta,t)\cos\phi'(t) \tag{6.41b}$$

Combining Equation (6.40) with Equation (6.41) and the LSR given in Equation (6.34) to determine the individual tooth effects, generates four equations describing the axial moments about the vertical and horizontal axes on each gear.

$$T_{a,y,j}(\theta,t) = \sum_{i=1}^{2} \delta_{y,i,j}(\theta,t)\mathrm{LSR}_i(\theta,t)F_{f,a}(t) \tag{6.42a}$$

$$T_{a,z,j}(\theta,t) = \sum_{i=1}^{2} \delta_{z,i,j}(\theta,t)\mathrm{LSR}_i(\theta,t)F_{f,a}(t) \tag{6.42b}$$

These axial forces and moment can then be applied to the global force matrix to act as a time varying loading parameter on the gears, where using the predefined coordinate system, the translational friction force described by Equation (6.40) will be negative on both gears due to there opposing positive directions, the frictional moment about the vertical axis will be negative on gear 1 and 2, and the frictional moment about the horizontal axis will initially be positive on gear 1 and negative on gear 2, then as the contact point moves past the pitch point ($\delta_{z,i,j}(\theta,t)$ becomes negative) the sign of the forces will change.

Another friction force may exist where the contacting faces of the teeth rotate, which has previously been described as yaw rotation in Section 3.2.2. This will

not be investigated further in this chapter and is a topic for further investigation in the derivation of a more complete friction formulation for full 6 DOF motion of the contact point.

6.4 Calculation and Application of Misalignments

One of the major contributions of this research is to understand the effects of instantaneous translational misalignments on the dynamics of gear contact. To achieve this it is necessary to transform the global positions of the gear nodes within the dynamic gear model into local misalignments at the gear contact, which have been extensively investigated in Chapter 4. Methods of including the effects of misalignment witnessed in the Finite Element results are also needed so that dynamic effects on the system parameters can be investigated.

6.4.1 Transforming Global Displacements into Local Misalignments

Within the dynamic test rig model the translations and rotations are taken at the gear centre and about the global axes, whereas when defining the effects of misalignment the rotations are about the pitch point and are aligned parallel and perpendicular to the line of action, which is angled to the global coordinate system by the pressure angle. A transformation from the nodal coordinates to the local (LOA) coordinate system is required to define the current misalignment state of the gears.

Axial and Radial Misalignment

Here the local and global coordinate systems are defined according to the dynamic model, where the axial, vertical and horizontal directions in the global coordinate system are the x, y and z-axes respectively. This is illustrated in Figure 6.7(b) along with the local coordinate system along the pressure line.

The translations along the global coordinate frame manifest themselves as contributions to the radial and axial misalignment, where the axial component is simply the sum of the global axial components, since the global and local axial

directions are identical. Hence the axial alignment can be defined as:

$$a\_align(t) = x_1(t) + x_2(t) \tag{6.43}$$

The radial misalignment is a variation in the centre distance and involves translations along both the y and z axes; the current operating centre distance can be found from the equation:

$$a'(t) = \sqrt{\left(a\cos\left(\phi'(t)\right) + x_1(t) - x_2(t)\right)^2 + \left(y_1(t) - a\cos\left(\phi'(t)\right) - y_2(t)\right)^2} \tag{6.44}$$

where a' is the instantaneous centre distance and a is the ideal centre distance. The instantaneous radial misalignment caused by global translation along the y and z axes can then be taken by subtracting the ideal centre distance.

$$r\_align(t) = a'(t) - a \tag{6.45}$$

As well as translation the gear centres are also subjected to rotation due to the bending of the shaft, and this bending will play an important role in defining the types and extent of misalignment at the contact points. Bending about the vertical (y) axis will introduce further, albeit small, radial and axial misalignment since there is an intrinsic moment arm present between the y-axis and the pitch point, as shown in Figure 6.15. From this figure the effects of rotational position on the

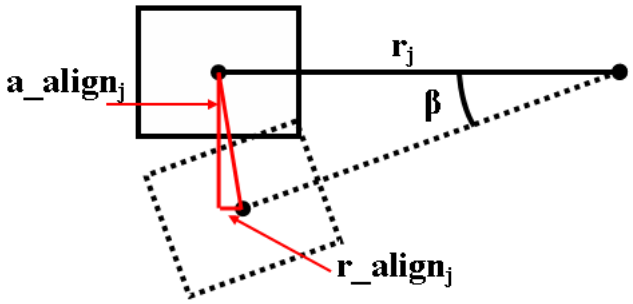

Figure 6.15: Contribution of rotation about global y-axis to the lateral misalignments

radial and axial misalignment can be given mathematically as

$$r\_align_j(t) = r'_j(t) - r'_j(t)\cos\left(\beta_j(t)\right) \tag{6.46a}$$

$$a\_align_j(t) = r'_j(t)\sin\left(\beta_j(t)\right) \tag{6.46b}$$

Where r'_j and β_j are the pitch radii and rotations about the vertical axes respectively for each gear, which are shown in Figure 6.15. Using the above equations and their lateral contributions the complete axial and radial misalignments can be determined from the global nodal locations, as described below.

$$a\_align(t) = x_1(t) + x_2(t) + r'_1(t)\sin\beta_1(t) + r'_2(t)\sin\beta_2(t) \tag{6.47a}$$

$$\begin{aligned} r\_align(t) = & \\ & \sqrt{\left(a\cos\left(\phi'(t)\right) + x_1(t) - x_2(t)\right)^2 + \left(y_1(t) - a\cos\left(\phi'(t)\right) - y_2(t)\right)^2} \\ & - a + r'_1(t)\left(1 - \cos\beta_1(t)\right) + r'_2(t)\left(1 - \cos\beta_2(t)\right) \end{aligned} \tag{6.47b}$$

Pitch and Yaw Misalignment

When considering the effects of angular misalignments on the contact parameters using the finite element method, pitch and yaw misalignment were applied about the local coordinate system along the LOA, however in the dynamic gearbox model the angular rotations are derived about the vertical and horizontal axes at the gear centres. Therefore pitch and yaw misalignment must be obtained from the rotations about the vertical and horizontal axes by transforming these known rotations into a local coordinate system aligned with the pressure line, as shown in Figure 6.7(b). To achieve this the Rodgrigues rotation formula, as described in Section 3.2.2, is employed to generate a transfer matrix describing the rotations about the global axes using the local LOA coordinate system as a datum. This results in axes vectors ($\mathbf{e}$) for rotations about the global vertical (y) and horizontal (z) axis of $\begin{Bmatrix}\cos\phi'(t) & \sin\phi'(t) & 0\end{Bmatrix}^T$ and $\begin{Bmatrix}-\sin\phi'(t) & \cos\phi'(t) & 0\end{Bmatrix}^T$ respectively, such that by assigning Euler angles of β and γ to describe rotations about y and z

two rotational matrices can be determined.

$$\mathbf{R_{y,j}}(t) = \begin{bmatrix} \cos\beta_j(t) + c^2\left(1-\cos\beta_j(t)\right) & cs\left(1-\cos\beta_j(t)\right) & s\sin\beta_j(t) \\ cs\left(1-\cos\beta_j(t)\right) & \cos\beta_j(t) + s^2\left(1-\cos\beta_j(t)\right) & -c\sin\beta_j(t) \\ -s\sin\beta_j(t) & c\sin\beta_j(t) & \cos\beta_j(t) \end{bmatrix} \tag{6.48a}$$

$$\mathbf{R_{z,j}}(t) = \begin{bmatrix} \cos\gamma_j(t) + s^2\left(1-\cos\gamma_j(t)\right) & -cs\left(1-\cos\gamma_j(t)\right) & c\sin\gamma_j(t) \\ -cs\left(1-\cos\gamma_j(t)\right) & \cos\gamma_j(t) + c^2\left(1-\cos\gamma_j(t)\right) & s\sin\gamma_j(t) \\ -c\sin\gamma_j(t) & -s\sin\gamma_j(t) & \cos\gamma_j(t) \end{bmatrix} \tag{6.48b}$$

Where $c = \cos\phi'(t)$ and $s = \sin\phi'(t)$. A problem occurs when combining the two matrices into a complete rotational matrix since multiplication of the matrices is not commutative, i.e. $\mathbf{R_y R_z} \neq \mathbf{R_z R_y}$. An approximation is made here that since the rotations about x and y are small ($< 1°$) the variation due to the multiplication sequence of the rotational matrices is negligible; this is proven in Appedix G along with the multiplications leading to the pitch and yaw misalignments and the rotation about the shaft axis given in the equations below.

$$\theta_{pitch,j}(t) = \sin^{-1}\left(\cos\phi'(t)\sin\gamma_j(t) + \sin\phi'(t)\cos\gamma_j(t)\sin\beta_j(t)\right) \tag{6.49}$$

$$\theta_{yaw,j}(t) = \tan^{-1}\left(\cos\phi'(t)\tan\beta_j(t) - \frac{\sin\phi'(t)\tan\gamma_j(t)}{\cos\beta_j(t)}\right) \tag{6.50}$$

$$\theta_{z,j}(t) = \tan^{-1}\left(\frac{\cos\gamma_j(t) - \cos\beta_j(t) - \tan\phi'(t)\sin\gamma_j(t)\sin\beta_j(t)}{(\cos\gamma_j(t)(1/\tan\phi'(t))) + \cos\beta_j(t)\tan\phi'(t) - \sin\gamma_j(t)\sin\beta_j(t)}\right) \tag{6.51}$$

Using these equations the complete yaw and pitch misalignment can be determined by combining the influence of the individual gear misalignments. Since the positive vertical and horizontal axes' directions are the same on both gears the combination of misalignment is achieved through subtraction, such that:

$$y\_align(t) = \theta_{yaw,1}(t) - \theta_{yaw,2}(t) \tag{6.52a}$$

$$p\_align(t) = \theta_{pitch,1}(t) - \theta_{pitch,2}(t) \tag{6.52b}$$

These equations generate an understanding of the misalignments from the global displacements of the gear nodes and although the effects of angular misalignment

are not included in the dynamic model, this is a useful exercise to determine the degree of angular misalignment under dynamic conditions and gain some insight into its possible effect on the system parameters.

6.4.2 Inclusion of Misalignment Effects

In the previous section the misalignments have been calculated from the global displacements of the dynamic system and with this knowledge their effects, determined from the static FE results in Chapter 4, can be included into the dynamic model. This is achieved through the variation of the system parameters associated with the gear mesh, such as the mesh stiffness term, the meshing positions and LSR, and the forces generated at the gear mesh. This section splits up the effects of the two translational misalignment, where their effects on the system parameters are discussed, and a possible method for the inclusion of angular misalignments is presented.

Radial Misalignment

As previously mentioned the mesh stiffness term (k_m) used to couple together the shaft motions is position dependent and obtained in the dynamic model through the interpolation of the static finite element results. Section 4.2.2 shows that radial misalignment greatly effects the length of the line of contact and subsequent contact ratio, which leads to variations in the proportion of single and double tooth contact. This results in variations in the shape of the mesh stiffness curve, meaning the effects of radial misalignment cannot be included as a scaling function applied to the mesh stiffness under perfect alignment. To overcome this the mesh stiffness value is interpolated by both the instantaneous gear rotations and radial misalignment, based on the nodal gear displacements in the global coordinate system.

Another consequence of varying the contact ratio as a result of radial misalignment is that the shape of the load sharing ratio curve changes to accommodate the different contact positions. In the determination of the load sharing ratio the length of the line of action, and hence the angle of action, are calculated through

the contact ratio, which is given here for reference.

$$\varepsilon(t) = \frac{\sqrt{r_{a1}^2 - r_{b1}^2} + \sqrt{r_{a2}^2 - r_{b2}^2} - C'(t)\sin\phi'(t)}{P\cos\phi'(t)} \tag{6.53}$$

The contact ratio is based on the instantaneous centre distance and pressure angle, which are both dependent on the radial misalignment, where the variation in the pressure angle, which has been shown previously, can be calculated as

$$\phi'(t) = \cos^{-1}\left(\frac{r_{b1} + r_{b2}}{C'(t)}\right) \tag{6.54}$$

The variation in the load sharing ratio as a result of radial misalignment effects the determination of the friction forces, however the radial misalignment also affects the size and angle of the line of contact. With an increase in the centre distance as a result of radial misalignment there is an increase in the respective pitch radii of the two gears, as described in Chapter 4 and reiterated here in Equation (6.55), which leads to variations in the limits of contact described in Section 6.3.2 and subsequent variations in the tooth contact positions along the LOA.

$$r_1'(t) = \frac{r_{b1}C'(t)}{(r_{b1} + r_{b2})} \tag{6.55a}$$

$$r_2'(t) = C'(t) - r_1'(t) \tag{6.55b}$$

The effects of radial misalignment on the tooth contact positions along the line of contact and the pressure angle also determine the inclusion of the frictional forces into the global system of equations, since the pressure angle is required to decompose the OLOA friction force into the global vertical and horizontal directions and the position of the contact point along the LOA is required as the moment arm in calculating the frictional moments about the axial direction.

The LSR, position of the contact points along the line of action, pressure angle and the pitch radii are also used in the calculation of the axial friction forces and as such the radial misalignment also has an impact on these forcing terms.

The radial misalignment has been shown to effect the determination of the OLOA forces due to friction through variations in the contact positions and length of the line of contact, however radial misalignment also has a large effect on the LOA forces. As with the inclusion of friction into the global force matrix, the variation in the pressure angle caused by radial misalignment alters the decomposition of the normal tooth contact force into the global coordinate frame. This can be captured in the dynamic model through variations in the gear mesh stiffness matrix given in Equation (6.27), or through variations in the forces generated as a result of this stiffness.

In conclusion radial misalignment effects the contact ratio, pressure angle, centre distance and the pitch radii, which all have subsequent effects on the gear contact equations described in previous sections and therefore where necessary the instantaneous values are prescribed.

Axial Misalignment

In the static FE study performed as part of this research, the effects of axial misalignment have been confined to the OLOA moments, with negligible effects on the mesh stiffness, LSR and LOA forces. During analysis of the OLOA moments their effects have been attributed to the movement of the centre of pressure from the centre of mass, which coincides with the gear nodes in the dynamic model, and the moments caused by a slight axial force. Another phenomena where the gear teeth twist during contact causing further variation in the centre of pressure has also been witnessed, however this will not be included in the model due to the modelling approach used for the gear contact.

The movement of the centre of pressure has been found to result in variations in the moment arms associated with not only the normal contact force, which were observed in the finite element analyses, but also in the moment arms of the frictional force. Both forces are therefore included in the determination of the axial misalignment moments.

In the dynamic model the effect of the axial misalignment on the OLOA

moments will be accounted for through the assumption that the load is uniformly distributed across the tooth faces; this results in equations for the various OLOA moments of the form.

$$T_y(t) = \frac{a\_align(t)}{2}\left(N(t)\sin\phi'(t) - F_f(\theta,t)\cos\phi'(t)\right) \tag{6.56a}$$

$$T_z(t) = \frac{a\_align(t)}{2}\left(N(t)\cos\phi'(t) + F_f(\theta,t)\sin\phi'(t)\right) \tag{6.56b}$$

The moments attributed to the axial force will not be included as their effects are negligible when compared against the moments due to variations in the centre of pressure; there are also difficulties in determining the axial force using the current modelling technique and a change in the representation of the contact area would be required to include its effects.

Due to the directions of the normal forces, which act in opposing directions of gear 1 and gear 2, a positive axial misalignment introduces negative reaction moments about both the horizontal and vertical axes on both gear 1 and gear 2.

Angular Misalignment

The angular misalignments are not included in the dynamic model for two reasons, the yaw misalignment is omitted because it has been shown in the FE results that it has negligible effects on the system parameters, while the effects of pitch misalignments are unable to be included accurately using the current single spring gear contact model. An alternative approach to modelling the contact position or mesh stiffness has been suggested by both Blankenship and Singh [35] and Eritenel and Parker [38], where the tooth surface is discretized into a number of springs across the tooth width allowing for representation of the contact stiffness and forces under non-parallel contact, as shown in Figure 6.16. Figure 6.16 illustrates this modelling approach under two conditions; perfect alignment is shown in Figure 6.16(a), where the contacting tooth faces are parallel to each other and the complete tooth face is in contact along its width, and pitch misalignment, which is shown in Figure 6.16(b), where the contacting faces are no longer parallel and the contact does not span the complete facewidth.

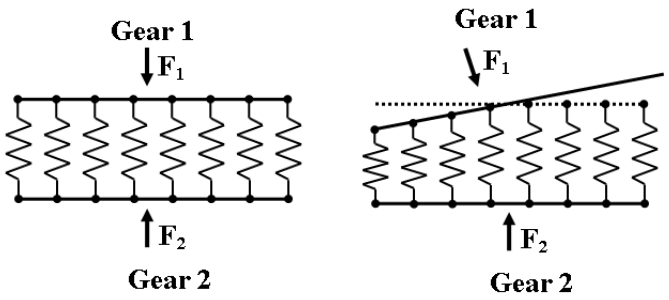

(a) Parallel contact (b) Inclined contact

Figure 6.16: Alternative model of gear contact, taken from Blankenship and Singh [35] and Eritenel and Parker [38]

With accurate modelling of the individual spring stiffnesses this modelling approach is able to accurately calculate the mesh stiffness under any combination of axial and pitch misalignment, as well as model the OLOA forces by summing the individual force contributions of the springs about the centre of the gear face. Deriving a methodology for the calculation of the individual spring stiffnesses from the finite element results and applying this new modelling approach is beyond the scope of this project; however it can be considered as vital further work in determining the effects of misalignment as pitch misalignment has been shown to be influential in the static FE results.

6.5 Force Matrix

In the above sections the application of the frictional forces and the misalignment forces at the gear mesh have been discussed and whilst the normal contacting forces are found as part of the system stiffness, these excitation effects are used as forcing parameters at the gear mesh. Using the coordinate frame shown in Figure 6.2 and Figure 6.7(b), where for both gears u_2 is aligned with the vertical (y) axis, u_3 is aligned with the horizontal (z) axis, u_1 is into the page for gear 1 and out of the page for gear 2 (Figure 6.7(b)), and the rotations are determined by the right hand rule as shown in Figure 6.2, the forcing terms at the gear mesh can be shown, with correct polarity, to be.

$$\begin{Bmatrix} F_1 \\ F_2 \\ F_3 \\ F_4 \\ F_5 \\ F_6 \\ F_7 \\ F_8 \\ F_9 \\ F_{10} \\ F_{11} \\ F_{12} \end{Bmatrix} = \begin{Bmatrix} -F_{f,a}(t) \\ F_f(t)\sin\phi'(t) \\ F_f(t)\cos\phi'(t) \\ -T_{f,1}(t) \\ -T_{a,y}(t) - T_{f,a,y,1}(t) \\ -T_{a,z}(t) - T_{f,a,z,1}(t) \\ F_{f,a}(t) \\ -F_f(t)\sin\phi'(t) \\ -F_f(t)\cos\phi'(t) \\ T_{f,2}(t) \\ -T_{a,y}(t) - T_{f,a,y,2}(t) \\ -T_{a,z}(t) + T_{f,a,z,2}(t) \end{Bmatrix} \tag{6.57}$$

Where $F_{f,a}$ is the axial friction force, F_f is the normal sliding friction force, ϕ' is the instantaneous pressure angle, $T_{f,i}$ is the torque derived from the normal sliding friction on gear i, $T_{a,y}$ and $T_{a,z}$ are the moments about the y and z axes due to axial misalignment, and $T_{f,a,y,i}$ and $T_{f,a,z,i}$ are the moments due to axial friction about the y and z axes on gear i.

6.6 Boundary Conditions

Within the dynamic model unconstrained rigid body motion must be avoided by applying boundary conditions to the system; this can be applied to any nodal DOF within the model by setting all off diagonal terms in the mass, damping and stiffness matrices associated with this DOF to zero and by setting the diagonal term to 1. Also the external forcing term associated with this DOF should be set to zero, which can be seen in the simple example below for an arbitrary system consisting of 3 DOF.

$$\begin{bmatrix} M_{11} & M_{12} & M_{13} \\ M_{21} & M_{22} & M_{23} \\ M_{31} & M_{32} & M_{33} \end{bmatrix} \begin{Bmatrix} \ddot{x_1} \\ \ddot{x_2} \\ \ddot{x_3} \end{Bmatrix} + \begin{bmatrix} C_{11} & C_{12} & C_{13} \\ C_{21} & C_{22} & C_{23} \\ C_{31} & C_{32} & C_{33} \end{bmatrix} \begin{Bmatrix} \dot{x_1} \\ \dot{x_2} \\ \dot{x_3} \end{Bmatrix} + \begin{bmatrix} K_{11} & K_{12} & K_{13} \\ K_{21} & K_{22} & K_{23} \\ K_{31} & K_{32} & K_{33} \end{bmatrix} \begin{Bmatrix} x_1 \\ x_2 \\ x_3 \end{Bmatrix} = \begin{Bmatrix} F_1 \\ F_2 \\ F_3 \end{Bmatrix} \tag{6.58a}$$

This system by its nature is semi-definite and therefore cannot be solved, due to there being no inverse of the system matrices; however by constraining the first DOF (x_1) the system of equations can be depicted as.

$$\begin{bmatrix} 1 & 0 & 0 \\ 0 & M_{22} & M_{23} \\ 0 & M_{32} & M_{33} \end{bmatrix} \begin{Bmatrix} \ddot{x_1} \\ \ddot{x_2} \\ \ddot{x_3} \end{Bmatrix} + \begin{bmatrix} 1 & 0 & 0 \\ 0 & C_{22} & C_{23} \\ 0 & C_{32} & C_{33} \end{bmatrix} \begin{Bmatrix} \dot{x_1} \\ \dot{x_2} \\ \dot{x_3} \end{Bmatrix} + \begin{bmatrix} 1 & 0 & 0 \\ 0 & K_{22} & K_{23} \\ 0 & K_{32} & K_{33} \end{bmatrix} \begin{Bmatrix} x_1 \\ x_2 \\ x_3 \end{Bmatrix} = \begin{Bmatrix} 0 \\ F_2 \\ F_3 \end{Bmatrix} \tag{6.58b}$$

If constrained correctly this system of equations is now positive definite and can be solved. Within the dynamic model boundary conditions are applied to the motor and load nodes and the supporting structures, where the motor and load nodes are constrained in all DOF except the rotational about the shaft axis (α) and the bearing supports are constrained in all DOF at their base, referring to the datum plane of the floating platform and spur gear foundation plate.

6.7 Solution Technique

Once the global matrices have been built, based on the individual element matrices, and boundary conditions applied the system of dynamic equations can be compiled, which can be simplified to show the time varying/position dependent forcing and stiffness arrays in the form.

$$\mathbf{M}\ddot{\mathbf{x}}(t) + \mathbf{C}\dot{\mathbf{x}}(t) + \mathbf{K}(x,t)\mathbf{x}(t) = \mathbf{F}(x,t) \tag{6.59}$$

This second order nonlinear system of equations can be solved by splitting it into two first order equations, which can be solved numerically, where the two first order systems are given as

$$\dot{\mathbf{x}}(t) = \mathbf{z}(t) \tag{6.60a}$$

$$\dot{\mathbf{z}}(t) = \mathbf{M^{-1}F}(x,t) - \mathbf{M^{-1}Cz}(t) - \mathbf{M^{-1}K}(x,t)\mathbf{x}(t) \tag{6.60b}$$

The technique specified for the solution of these nonlinear equations is the explicit fixed time step Runge-Kutta method of 4^{th} order accuracy, which is applied to both sets of first order equations to calculate the displacement and velocities at time $t+h$ from the system parameters at time t. This can be summarized as

$$\mathbf{z}\,(t+h) = \mathbf{z}\,(t) + \frac{h}{6}\left(k_{1z} + 2k_{2z} + 2k_{3z} + k_{4z}\right) \tag{6.61a}$$

$$\mathbf{x}\,(t+h) = \mathbf{x}\,(t) + \frac{h}{6}\left(k_{1x} + 2k_{2x} + 2k_{3x} + k_{4x}\right) \tag{6.61b}$$

Where h is the time increment, $\mathbf{x}$ and $\mathbf{z}$ are the system displacements and velocities respectively and k_i are the coefficients, which are based on the gradients at various points throughout the simulation, where k_1 is based on the slope at the beginning of the interval and can be calculated from

$$k_{1z} = \mathbf{M^{-1}F}\,(x_0,t) - \mathbf{M^{-1}Cz_0}\,(t) - \mathbf{M^{-1}K}\,(x_0,t)\,\mathbf{x_0}\,(t) \tag{6.61c}$$

$$k_{1x} = \mathbf{z_0} \tag{6.61d}$$

These gradients are used to specify the displacement and velocity values at the midpoint of the increment, such that

$$\mathbf{z_1} = \mathbf{z_0} + \frac{1}{2}k_{1z} \tag{6.61e}$$

$$\mathbf{x_1} = \mathbf{x_0} + \frac{1}{2}k_{1x} \tag{6.61f}$$

Using these displacement and velocity values to update the force and stiffness matrices to their configuration at the midpoint of the interval a second gradient at the midpoint can be determined.

$$k_{2z} = \mathbf{M^{-1}F}\left(x_1, t+\tfrac{h}{2}\right) - \mathbf{M^{-1}Cz_1}\left(t+\tfrac{h}{2}\right) - \mathbf{M^{-1}K}\left(x_1, t+\tfrac{h}{2}\right)\mathbf{x_1}\left(t+\tfrac{h}{2}\right) \tag{6.61g}$$

$$k_{2x} = \mathbf{z_1}\left(t + \tfrac{h}{2}\right) \tag{6.61h}$$

Again these gradients are used to define the displacements and velocities at the midpoint, which can be used to update the force and stiffness matrices and generate a further gradient at the midpoint.

$$\mathbf{z_2} = \mathbf{z_0} + \frac{1}{2}k_{2z} \tag{6.61i}$$

$$\mathbf{x_2} = \mathbf{x_0} + \frac{1}{2}k_{2x} \tag{6.61j}$$

$$k_{3z} = \mathbf{M^{-1}F}\left(x_2, t + \tfrac{h}{2}\right) - \mathbf{M^{-1}C z_2}\left(t + \tfrac{h}{2}\right) - \mathbf{M^{-1}K}\left(x_2, t + \tfrac{h}{2}\right)\mathbf{x_2}\left(t + \tfrac{h}{2}\right) \tag{6.61k}$$

$$k_{3x} = \mathbf{z_2}\left(t + \tfrac{h}{2}\right) \tag{6.61l}$$

These gradients are then used to calculate the velocities and displacements at the end of the time increment and subsequently calculate the gradient at $t + h$

$$\mathbf{z_3} = \mathbf{z_0} + k_{3z} \tag{6.61m}$$

$$\mathbf{x_3} = \mathbf{x_0} + k_{3x} \tag{6.61n}$$

$$k_{4z} = \mathbf{M^{-1}F}\left(x_3, t + h\right) - \mathbf{M^{-1}C z_3}\left(t + h\right) - \mathbf{M^{-1}K}\left(x_3, t + h\right)\mathbf{x_3}\left(t + h\right) \tag{6.61o}$$

$$k_{4x} = \mathbf{z_3}\left(t + h\right) \tag{6.61p}$$

These gradients are then averaged, as shown in Equations (6.61a) and (6.61b), with greater weight afforded to the gradients at the midpoint. Using these equations and stepping through the time domain at fixed increments, the nonlinear response of the system can be generated, which includes the transient response under start-up and the steady state response. However it is noted that since this Runge-Kutta technique is an explicit time advancing scheme the increment (h) must be selected carefully so that a stable solution can be found; it is possible to include a variable time step technique to allocate appropriate increments, however it has been found that the benefit is small when compared to the extra computational cost of varying

the time increment.

6.8 Conclusions

This chapter has described the development of a unique dynamic model of a gearbox, aimed at improving the description of the transmission path and increasing the complexity of the gear contact through the inclusion of friction, variations in contact parameters as a result of radial misalignment and OLOA forces due to axial misalignment. The modelling approach is based around the Finite Element formulation of the shaft stiffness and mass matrices as Timoshenko beams, to which the stiffnesses and masses of the system components derived from theoretical predictions and finite element techniques, such as the couplings, bearings, supporting structures, motor load and gear mesh can be added. Damping has been added to the model through Rayleigh damping, where stiffness and mass proportional damping terms are derived for each component and combined to form a global damping matrix; unlike the global stiffness matrix the damping and mass matrices are time independent, with values based on time independent system parameters.

The effects of the various excitations at the gear contact, including the variations in the mesh stiffness, the frictional forces and the effects of translational misalignments, have been discussed and included into the mathematical model as position and time dependent parameters and forcing terms. Finally a technique to apply boundary conditions to the model and solve the nonlinear system of equations has been discussed based on the 4^{th} order Runge-Kutta method.

Chapter 7

Results: Parametric Study

With the hybrid dynamic model developed in Chapter 6 and the derived finite element mesh stiffness from Chapter 4 at various radial misalignments and 100 Nm load, simulations can be performed to determine the dynamic response of the gear box system under load.

In this chapter different configurations of the gearbox are examined with varying system parameters to determine the effect of the stiffness and damping factors on the response of the system. Initially the gearbox is analysed in a purely rotational configuration, which excludes lateral motion of the gears and hence omits the influence of the bearing and supporting structure compliances and the effects of misalignment. In this configuration the shaft, gear mesh and coupling damping are varied, along with the frictional parameters and applied load, to determine their effect on the dynamic rotational transmission error.

Configuration 2 introduces lateral motion and therefore includes the compliances of the bearings and the supporting structure, this configuration omits the effects of misalignment and friction, such that all forces transmitted through the system are solely due to the normal tooth contact. Again the shaft, mesh and coupling damping are varied, along with the bearing and supporting structure parameters. In Configuration 2 the outputs of interest are the lateral accelerations of the bearing-to-support node, depicted in Figure 6.6(b).

Configuration 3 expands the coupled lateral-rotational hybrid gearbox model

by including normal sliding friction as described in Section 6.3.2, while Configuration 4 expands this further by introducing the effects of the axial friction described in Section 6.3.3.

Finally lateral misalignments are included and the effects of both imposed and instantaneous misalignments on system vibrations are examined.

7.1 Configuration 1

As described, in Configuration 1, the model is constrained such that only axial rotation is permitted; the bearings and supporting structures are therefore omitted and fixed boundary conditions are assumed in all other DOF associated with the system nodes.

7.1.1 Undamped System

Initially the system is considered with shaft, coupling and gear properties as given in Chapters 4 and 5, and friction and damping values as summarized in the table below.

Test Configuration	Damping Values			Friction Values	
	Coupling	Shaft	Mesh	μ	$V_0(m/s)$
Without Coupling	N/A	0	0	0	N/A
With Coupling	0	0	0	0	N/A

Table 7.1: Configuration 1 - Test 1 - Damping and friction values

This results in a dynamic transmission error (DTE), as shown in Figure 7.1, which is obtained by subtracting the actual rotational position of the gear (load shaft), from the theoretical gear position based on the rotational position of the pinion (motor shaft) and the gear ratio.

In Figure 7.1 undamped DTE results are given for two gearbox systems; in the first the motor and load are connected directly to the shaft, while in the second a flexible coupling is inserted between the motor and shaft to reduce the influence of torque fluctuations at the motor. This precaution is not deemed necessary on the load shaft since the input torque is constant. One point of note is that in Figure 7.1(c) the x-axis is chosen to highlight the gear contact frequency and its harmonics,

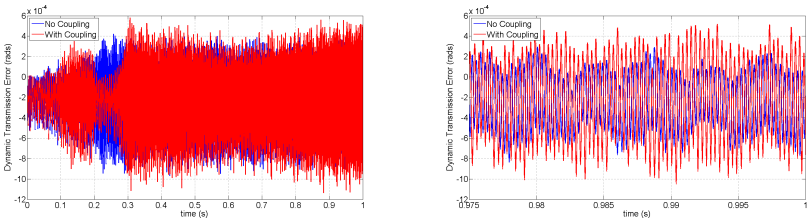

(a) Time domain (0 - 1 s)

(b) Time domain (0.975 - 1 s)

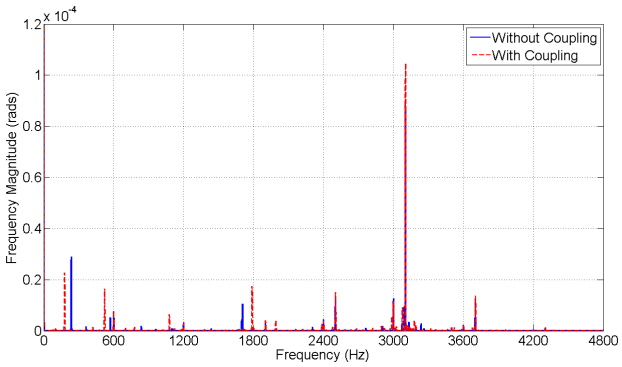

(c) Frequency domain

Figure 7.1: Dynamic transmission error results (Configuration 1 - Test 1)

which for a motor speed of 1500 rpm and 24 teeth on the motor shaft gear, results in a gear frequency of 600 Hz.

The first observation that can be made from Figure 7.1(b) is that the introduction of the coupling increases the overall magnitude of the DTE; this is as expected since the coupling is chosen to have a much lower torsional stiffness than the shaft and will increases the torsional bending and the DTE. The introduction of the coupling also causes a decreases in the DTE shortly after start-up, which is believed to be due to the "'wind-up"' and "'wind-down"' motion of the coupling under load, this effect can be decreased by increasing the various damping terms or by increasing the stiffness of the coupling, which will be shown later.

Looking at the frequency domain results of Figure 7.1(c), it can be seen that the introduction of the coupling has little effect on the mesh harmonics, however the 3rd harmonic (1800 Hz) looks increased due to interaction with another nearby frequency. Other frequencies are present, which do not correspond to the meshing frequency, and it is believed that these are caused by the different torsional stiffnesses

along the shaft and the torque fluctuations at the motor.

7.1.2 Coupling Damping

Through the inclusion of various coupling damping values, as summarized in Table 7.2, the previously described decrease in the DTE shortly after start-up is reduced (Figure 7.2(a)).

The introduction of coupling damping also appears to reduce the overall magnitude of the steady-state DTE, where only stiffness proportional damping terms greater than 1e-8 seem to have any noticeable effect on the system response.

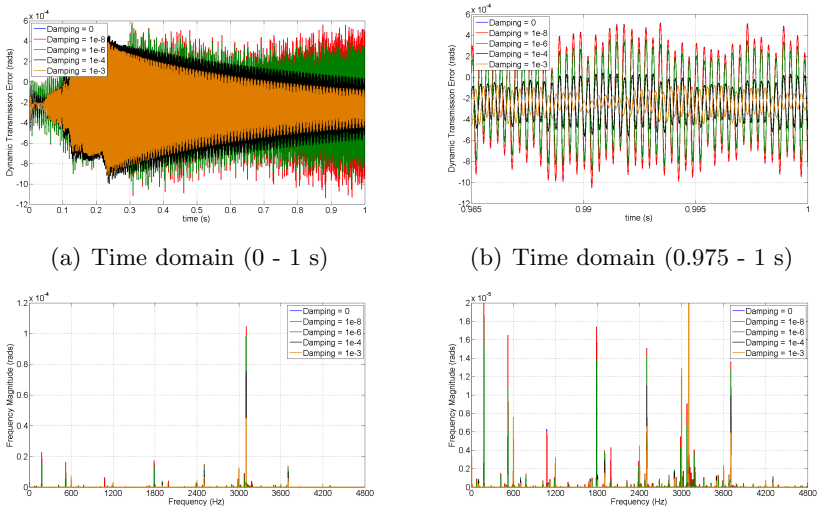

(a) Time domain (0 - 1 s)

(b) Time domain (0.975 - 1 s)

(c) Frequency domain

(d) Expanded frequency domain

Figure 7.2: Dynamic transmission error results (Configuration 1 - Test 2)

Test Configuration	Damping Values			Friction Values	
	Coupling	Shaft	Mesh	μ	$V_0(m/s)$
With Coupling	0, 1e-8, 1e-6, 1e-4, 1e-3	0	0	0	N/A

Table 7.2: Configuration 1 - Test 2 - Damping and friction values

Damping terms greater than 1e-4 cause the DTE to decay to a more pronounced steady-state response, since the damping reduces the fluctuations in the input torque to an acceptable level. This can be proven by observing the time and frequency plots of the motor torque in Figure 7.3, which have pronounced fluctuations above a damping value of 1e-4 in the time domain. This translate into sub-gear-mesh harmonic frequencies in the frequency domain. These are clearly

present in the DTE results of Figure 7.2, and with increased damping the influence of these components are reduced.

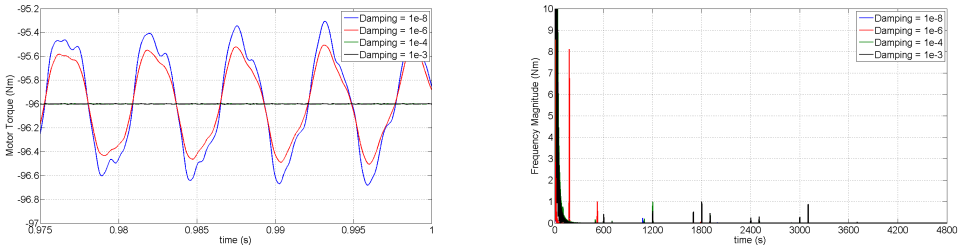

(a) Time domain (b) Frequency domain

Figure 7.3: Motor torque fluctuations (Configuration 1 - Test 2)

Although a true steady-state response is not obtained within 1 second from start-up in Figure 7.2(a) the Fourier transform has been taken from midway through the simulation (0.5 - 1 sec) to determine the frequency domain response. Since the DTE decay is at such a low frequency, it is envisaged that this will not interfere with the underlying steady-state results. From these frequency domain results it can be seen that high damping of above 1e-4 completely removes the non-meshing frequencies bellow around 1800 Hz; however above this frequency many other frequencies still exist, including the large peak at around 3100 - 3200 Hz.

7.1.3 Shaft Damping

By applying damping to only the shaft nodes, which acts to reduce the torsional fluctuations along the shaft length, the influence of these higher vibrational frequencies can be reduced, as shown in Figure 7.4 for the system with and without the coupling.

Test Configuration	Damping Values			Friction Values	
	Coupling	Shaft	Mesh	μ	$V_0(m/s)$
Without Coupling	N/A	0, 1e-8, 1e-6, 1e-5	0	0	N/A
With Coupling	0	0, 1e-8, 1e-6, 1e-5	0	0	N/A

Table 7.3: Configuration 1 - Test 3 - Damping and friction values

Figure 7.4 shows that beyond a shaft damping value of 1e-6 the only frequency components of significance are the gear mesh harmonics. The last frequency

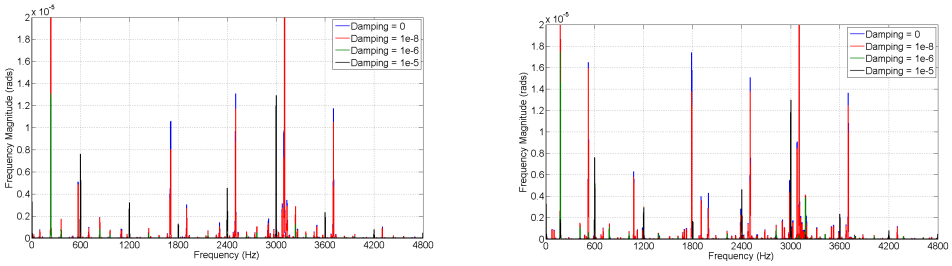

(a) Without Coupling (b) With Coupling

Figure 7.4: Dynamic transmission error results - Frequency Domain (Configuration 1 - Test 3)

component to be damped out in this manner is the torque fluctuation from the motor, which is slightly more prominent and of a lower frequency when the coupling is introduced. The effects of this lower frequency fluctuation can be seen in the time domain responses below, where the lower damping results increase and decreases periodically at a rate lower than the meshing frequency; in these results a step input type response can be seen, which is attributed to the meshing action.

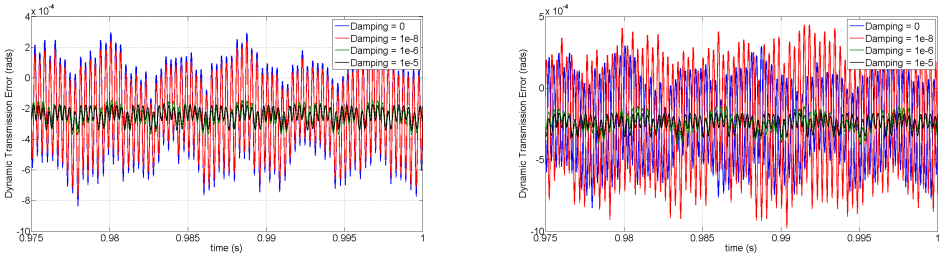

(a) Without Coupling (b) With Coupling

Figure 7.5: Dynamic transmission error results - Time Domain (Configuration 1 - Test 3)

7.1.4 Mesh Damping

Another observation obtain by examining the frequency domain plots of Figure 7.4, is that with high shaft damping the dominant frequency remains the 5^{th} mesh harmonic (3000 Hz) even though the cluster of frequencies in that range have been completely damped out. This issue is addressed by introducing mesh damping, which influences the main source of vibration in the model, such that with increased mesh damping the magnitude of the transmission error is reduced (ref Figure 7.6).

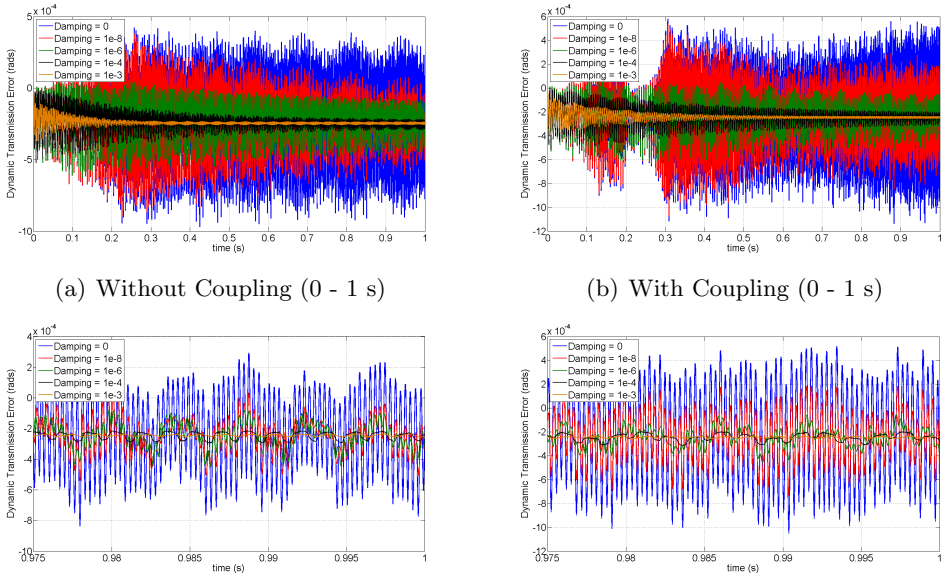

(a) Without Coupling (0 - 1 s)

(b) With Coupling (0 - 1 s)

(c) Without Coupling (0.975 - 1 s)

(d) With Coupling (0.975 - 1 s)

Figure 7.6: Dynamic transmission error results - Time Domain (Configuration 1 - Test 4)

Test Configuration	Damping Values			Friction Values	
	Coupling	Shaft	Mesh	μ	$V_0(m/s)$
Without Coupling	N/A	0	0, 1e-8, 1e-6, 1e-4, 1e-3	0	N/A
With Coupling	0	0	0, 1e-8, 1e-6, 1e-4, 1e-3	0	N/A

Table 7.4: Configuration 1 - Test 4 - Damping and friction values

By comparing Figures 7.6(c) and 7.6(d) the influence of the coupling can clearly be seen even under high mesh damping, where its presence introduces a lower frequency vibration imposed on the mesh forcing vibration due to its lower torsional rigidity. This, along with the lower influence of the higher mesh harmonics with increased mesh damping, can be observed clearly in the frequency domain of Figure 7.7, where the influence of the coupling is most obvious with a mesh damping of 1e-4. At this damping value the influence of the lower frequency vibrations in the range 200 - 300 Hz are clearly higher when the coupling is present, with the most dominant peak around 3 times higher with the coupling. There is also a frequency shift in these lower vibrations, which is most likely due to the decreased torsional stiffness.

The mesh damping clearly reduces the the influence of the higher mesh har-

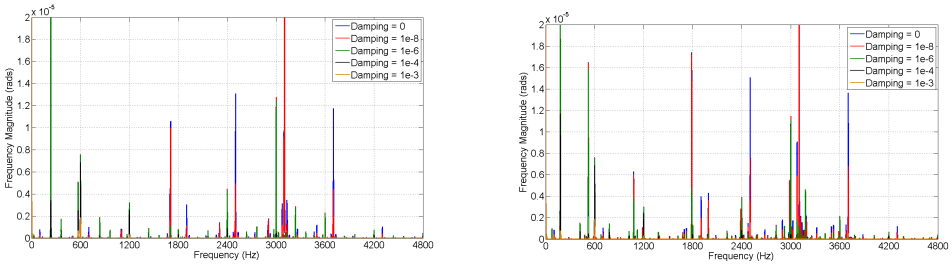

(a) Without Coupling

(b) With Coupling

Figure 7.7: Dynamic transmission error results - Frequency Domain (Configuration 1 - Test 1)

monics, which is to be expected and is illustrated in the time domain response through the smooth form of the transmission error. Up to a mesh damping value 1e-6 the greatest influence of the damping is on the non-gear mesh frequencies, with the only exception being the low frequency components; above a damping value of 1e-6 the non gear mesh frequencies are almost completely damped out and the gear mesh excitation is overdamped, which is more clearly observed in the time domain response with the mesh stiffness variation acting as a step input. Overdamping has a large effect on the frequency components of the response, with higher mesh harmonics ($\geq$ 1800 Hz) being severely reduced, and the primary mesh harmonic also being reduced due to the slow response of the system to the mesh stiffness change.

7.1.5 Friction

In the previous section the vibration source was solely attributed to the normal tooth forces at the gear mesh and the variation in the motor torque as a result of changes in the rotational speed of the shafts. In this section a secondary source of vibration is introduced at the gear mesh through the normal sliding of the gear teeth as they enter and exit contact; this causes a frictional torque about the shaft axis and further contributes to the DTE.

Friction Coefficient

Firstly the undamped response to normal tooth contact and sliding friction is observed in Figure 7.8, for frictional coefficients of 0, 0.05, 0.1 and 0.5 and a reference velocity of 0.1 m/s. It is noted here that the following simulations have

been performed with the coupling placed between the motor and shaft, with a torsional stiffness of 26.36 kNm/rad.

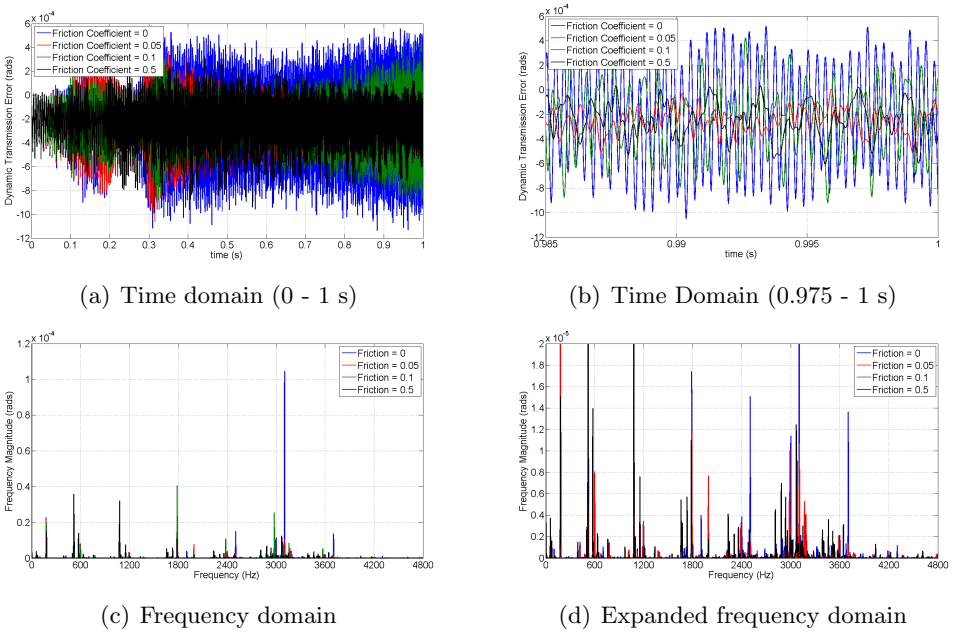

(a) Time domain (0 - 1 s)

(b) Time Domain (0.975 - 1 s)

(c) Frequency domain

(d) Expanded frequency domain

Figure 7.8: Dynamic transmission error results (Configuration 1 - Test 5)

Test Configuration	Damping Values			Friction Values	
	Coupling	Shaft	Mesh	μ	$V_0(m/s)$
With Coupling	0	0	0	0, 0.05, 0.1, 0.5	0.1

Table 7.5: Configuration 1 - Test 5 - Damping and friction values

From Figure 7.8 it can be seen that increased friction up to 0.1 tends to decrease the overall DTE, and through examining the frequency domain plots in Figures 7.8(c) and 7.8(d), it can be seen that this is mainly due to the reduction of three frequency peaks at around 2500, 3100 and 3700 Hz and the higher mesh harmonics ($\geq$ 1800 Hz), which suggests that the introduction of the frictional torque has a damping effect on the higher mesh frequencies. Above a frictional coefficient of 0.1 the DTE is increased, which is likely due to the higher influence of the first two mesh harmonics, which overcomes the reduction of the higher mesh harmonics and non-gear mesh frequencies.

Another observation from the frequency domain is that the introduction of friction causes a frequency shift in the mesh frequencies, which is due to the

additional frictional torque reducing the speed of the motor shaft and hence the mesh frequency, as shown in Figure 7.9. This can be addressed by varying the motor load coefficient of Equation (6.21) given in Section 6.2.5, however the effects are negligible up to a friction coefficient of 0.1, which is considered a large friction coefficient in lubricated gear contact.

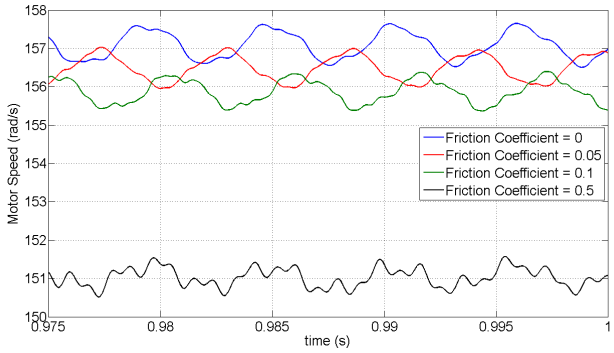

Figure 7.9: Motor speed results (Configuration 1 - Test 5)

In the previous section appropriate overdamped values for the coupling, shafts and mesh were determined; by using stiffness proportional damping values of 1e-4 for the coupling and the gear mesh, and 1e-6 for the shaft, the effects of friction on an overdamped system can be determined. Results for this configuration are shown in Figure 7.10, where the frequency domain shows that all non gear mesh frequency components have been damped to negligible values.

Test Configuration	Damping Values			Friction Values	
	Coupling	Shaft	Mesh	μ	$V_0(m/s)$
With Coupling	1e-4	1e-6	1e-4	0, 0.05, 0.1, 0.5	0.1

Table 7.6: Configuration 1 - Test 6 - Damping and friction values

From the time domain plots it can be seen that due to the high damping the DTE is able to reach a steady state response within 0.3 seconds and that with increased friction coefficients the peak-to-peak DTE is increased. Due to the damping and the reduction of the non-gear mesh harmonic frequencies, the effect of friction on the motor speed and hence gear mesh frequencies is enhanced in both the time and frequency domains, which again is only non-negligible at unrealistic friction

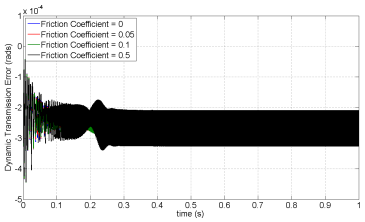

(a) Time domain (0 - 1 s)

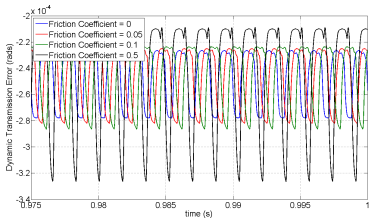

(b) Time Domain (0.975 - 1 s)

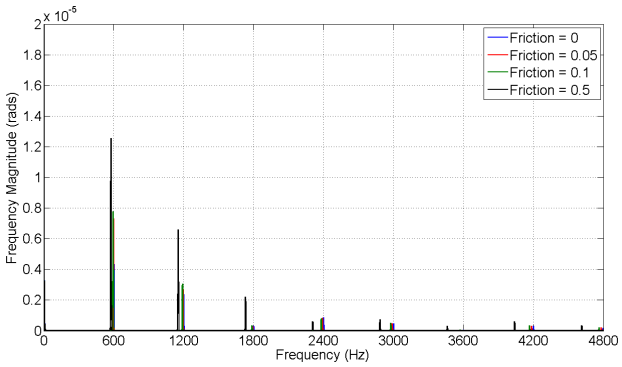

(c) Frequency domain

Figure 7.10: Dynamic transmission error results (Configuration 1 - Test 6)

coefficients.

In the DTE results of Figure 7.10(b) the effect of the load sharing ratio on the frictional torque and hence the DTE can clearly be seen for a friction coefficient of 0.5, where Figure 7.11 compares the time domain plots of the frictional torque on the load shaft, and the DTE.

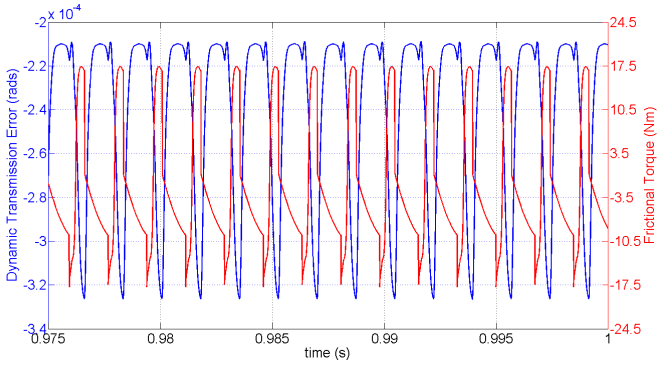

Figure 7.11: Dynamic transmission error and Friction Torque results - $\mu = 0.5$ (Configuration 1 - Test 6)

In Figure 7.11 the sharp decrease in the frictional torque at 0.995 seconds

occurs as the gear pair moves from double to single tooth contact; at this point in the overdamped system without friction the DTE increases as the load is transfered through a single tooth and the mesh stiffness is reduced. However when friction is introduced the frictional torque opposes tooth bending and the DTE decreases until the single tooth pair crosses the pitch point and the direction of sliding changes, causing an increase in the tooth bending and DTE. These effects can be observed in both Figure 7.10(b), where the increased friction coefficients decrease the DTE at the start of single tooth contact and increase DTE once the contacting tooth pair move through the pitch point, and in Figure 7.11.

In the previous section high shaft damping was shown to have similar effects to both the mesh damping and the coupling damping, which is due to the damping being applied to the same nodes and the only difference being in the calculation of the normal tooth load when calculating friction. Figure 7.12 shows the time and frequency domain plots for the DTE with mesh and coupling damping of 1e-4 and shaft damping of 1e-12.

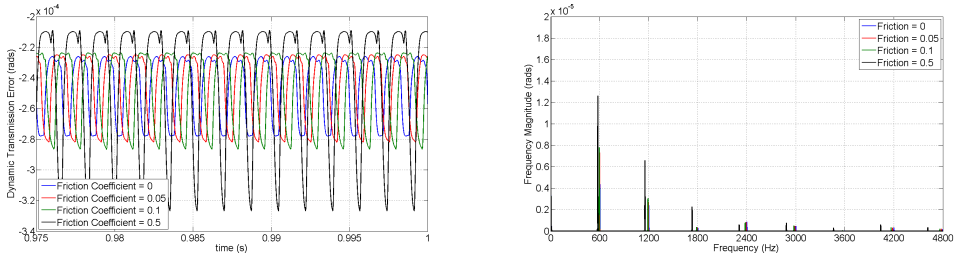

(a) Time domain (0.975 - 1 s)

(b) Frequency domain

Figure 7.12: Dynamic transmission error results (Configuration 1 - Test 7)

Test Configuration	Damping Values			Friction Values	
	Coupling	Shaft	Mesh	μ	$V_0(m/s)$
With Coupling	1e-4	1e-12	1e-4	0, 0.05, 0.1, 0.5	0.1

Table 7.7: Configuration 1 - Test 7 - Damping and friction values

Comparing Figure 7.12 with Figure 7.10, shows that shaft damping has little effect on the DTE results when sufficient mesh and coupling damping are present. Similar patterns with regard to the frictional force are also observed with the lower

shaft damping, meaning that rotational shaft damping has little effect on the over-damped mesh and coupling.

Next the coupling damping is reduced by a factor of 10 to 1e-5, with the mesh and shaft damping remaining at 1e-4 and 1e-12 respectively. The results for these simulations are shown in Figure 7.13, which show similar trends to those in previous simulations; however the transient period illustrated in Figure 7.13(a) differs with a lower damping value. This translates into a lower frequency fluctuation in the DTE seen in Figure 7.13(b) and Figure 7.13(c).

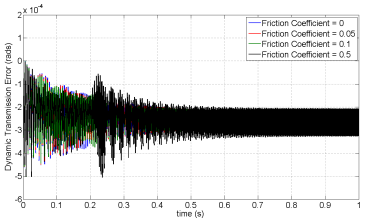

(a) Time domain (0 - 1 s)

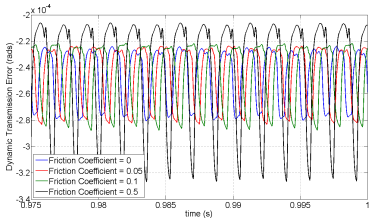

(b) Time Domain (0.975 - 1 s)

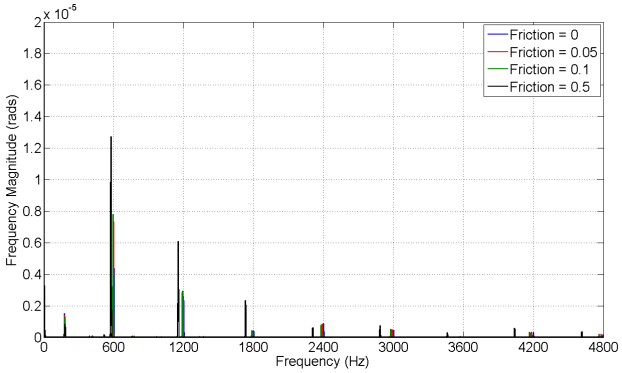

(c) Frequency domain

Figure 7.13: Dynamic transmission error results (Configuration 1 - Test 8)

Test Configuration	Damping Values			Friction Values	
	Coupling	Shaft	Mesh	μ	$V_0(m/s)$
With Coupling	1e-5	1e-12	1e-4	0, 0.05, 0.1, 0.5	0.1

Table 7.8: Configuration 1 - Test 8 - Damping and friction values

This lower frequency component is eventually completely damped out even at lower damping values, and the coupling damping value can be thought of as a useful tool to artificially create a steady state response in a reasonable simulation

time.

Comparing Figure 7.13(b) with previous simulations indicates that the over-damped mesh has the biggest effect on the steady state response of the system since neither the shaft or coupling damping have a significant effect on the steady state DTE. By reducing the mesh damping to 1e-5 and increasing the coupling damping to 1e-4 to ensure a sufficient period of steady state DTE, the effects of friction on the DTE with an underdamped mesh can be investigated. The results are given in Figure 7.14 and show that a steady state response is obtained within half the simulation time, due in part to the high coupling damping.

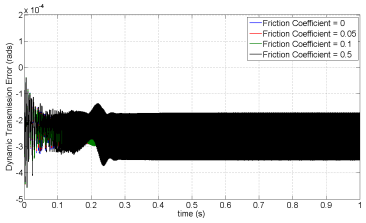

(a) Time domain (0 - 1 s)

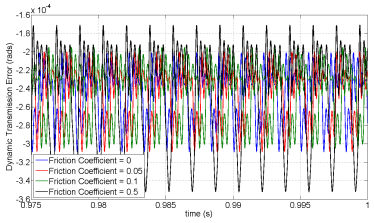

(b) Time Domain (0.975 - 1 s)

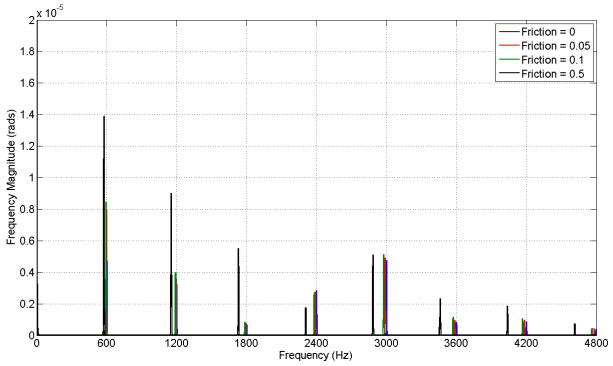

(c) Frequency domain

Figure 7.14: Dynamic transmission error results (Configuration 1 - Test 9)

Test Configuration	Damping Values			Friction Values	
	Coupling	Shaft	Mesh	μ	$V_0(m/s)$
With Coupling	1e-4	1e-12	1e-5	0, 0.05, 0.1, 0.5	0.1

Table 7.9: Configuration 1 - Test 9 - Damping and friction values

Figure 7.14 illustrates that the lower mesh damping causes significant variations in the DTE as a result of the step changes in the mesh stiffness and the system

is clearly underdamped. Comparing the frequency domains it can be deduced that the lower mesh damping increases the contribution of all the mesh frequency components, especially the higher frequency components.

The general effect of increased friction coefficients on this system is similar to previous simulations, where with increased friction coefficients the contribution of most mesh frequency components is increased, with the exception of the 4^{th} mesh harmonic (2400 Hz), which decreases, and the 5^{th} harmonic (3000 Hz), which remained relatively unchanged. The largest variations in the frequency components are seen in the first 3 harmonics, where the increase in the first harmonic is due to the frictional torque increasing gross peak-to-peak DTE, the increase in the second is due to the change in the direction of the frictional torque as the teeth pass through the pitch point and the increase in the third is due to the load sharing characteristics of the teeth causing step changes in the frictional torque.

Reference Velocity

Until this point the reference velocity used to determine the rate of change of the frictional force as the teeth move through the pitch point has been set to 0.1 m/s and through Figure 7.11 it can be seen that this reference velocity causes a relatively sharp increase in the frictional torque. By changing the reference velocity it can be shown that the higher the reference velocity the slower the transition, as shown in Figure 7.15; where the variation in the frictional torque with time at various reference velocities is given for a reference friction coefficient of 0.07, which is deemed reasonable for lubricated steel-to-steel sliding.

Test Configuration	Damping Values			Friction Values	
	Coupling	Shaft	Mesh	μ	$V_0(m/s)$
With Coupling	1e-4	1e-12	1e-5	0.07	0.001, 0.01, 0.05, 0.1, 1

Table 7.10: Configuration 1 - Test 10 - Damping and friction values

In Figure 7.15 the main variations occur between a reference velocity of 0.1 and 1 m/s, where the high reference velocity not only controls the rate of transition but also the maximum frictional force. This is caused by the maximum sliding

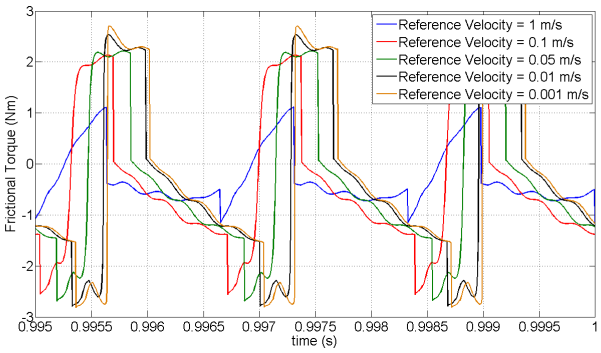

Figure 7.15: Frictional torque results (Configuration 1 - Test 10)

velocity, which is an insufficient fraction of the reference velocity needed to obtain the highest friction coefficient described by Equation 6.29 in Section 6.3.2. As the reference velocity is reduced further, it's effect on the transition and the maximum frictional torque is reduced.

These variations in the frictional torque only have a slight effect on the time and frequency domain responses of the system, where higher reference velocities increase the contributions of the mid range mesh frequencies (1800 - 3000 Hz) and reduce the contribution of the first two mesh harmonics due to the reduced peak torque values and the smooth transfer between the sliding directions. These results can be seen in Figure 7.16, which illustrate the effects of the reference velocity on the DTE in both the steady state time domain and the frequency domain.

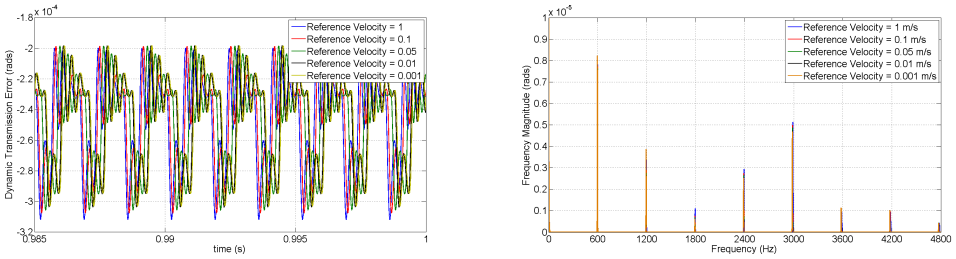

(a) Time Domain (0.975 - 1 s) (b) Frequency domain

Figure 7.16: Dynamic transmission error results (Configuration 1 - Test 10)

In the time domain the effect of the higher mid-range frequency components is to increase the general DTE during single tooth contact, whereas the effects on double tooth contact appear negligible, which could be due to the frictional force

introducing a damping like effect on the transmission error. The variation of the reference velocity also appears to introduce a slight shift in the DTE, which is in line with the results seen in Figure 7.15.

7.1.6 Load Variation

In all previous simulations the applied load has been set to 100 Nm, by varying this load between 10 - 100 Nm in increments of 10 Nm an idea of the effects of the applied load can be obtained. Figure 7.17 shows the effect of applied load on the rotational system with damping values as per Table 7.11.

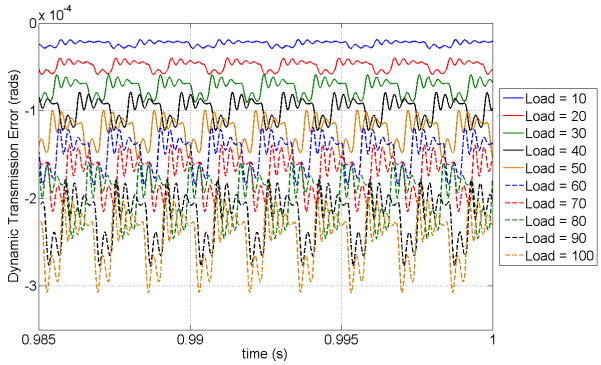

Figure 7.17: Dynamic transmission error results (Configuration 1 - Test 11)

Test Configuration	Damping Values			Friction Values	
	Coupling	Shaft	Mesh	μ	$V_0(m/s)$
With Coupling	1e-4	1e-12	1e-5	0.07	0.1

Table 7.11: Configuration 1 - Test 11 - Damping and friction values

In Figure 7.17 decreased load reduces the overall magnitude of the DTE; however as observed in Chapter 4 a decrease in the applied load has some effect on the mesh stiffness, which is currently not included in this model. The reasoning behind the omission of the loading effects on the mesh stiffness is that over the dynamic range of loads the variation will be small enough to be neglected, however the applied load is of a magnitude where these effects will become non-negligible. In Chapter 4 it is seen that with decreased applied load the mesh stiffness decreases. This means the reduction in the DTE witnessed in Figure 7.17 is overestimated and the decreased mesh stiffness will increase the DTE. This variation in mesh stiffness

introduces a known error into the results of Figure 7.17.

7.1.7 Conclusions

The mathematical model has been constrained to allow only rotation, such that the effects of the coupling, and the various system damping and frictional parameters, on the dynamic transmission error can be investigated. It has been found that the introduction of the coupling increases the transmission error through increased twisting of the shaft, and that through increased coupling damping a sufficient period of steady state response can be obtained in a reasonable simulation time. The shaft damping has been found to have little effect on the response when significant coupling and mesh damping are introduced; however shaft damping can be used to replace the mesh and coupling damping as it acts on similar nodes and is only inadequate when calculating the normal tooth load for the calculation of the frictional force. The mesh damping is seen to have the largest impact on the steady-state response as all vibratory sources within the model emanate from the gear mesh under steady-state conditions. Suitable damping values of 1e-4, 1e-12 and 1e-5 are determined for the coupling, shafts and mesh respectively, which allow for a reasonable period of steady-state response and also ensure that the gear mesh is not too heavily damped.

The frictional parameters, namely the frictional coefficient and reference velocity, have been investigated under undamped, overdamped and underdamped mesh conditions and it has been shown that increased friction coefficients increase the contribution of many of the gear mesh frequencies, especially the first three harmonics, and that with extremely high coefficients the speed of rotation of the motor is affected by the additional frictional torque. The reference velocity has been shown to have a large effect on the frictional torque; however coupled to a reasonable friction coefficient of 0.07 this has limited impact on the DTE in both the time and frequency domain.

The final variable altered has been the applied load, which showed that with decreased load the DTE is reduced. It has been noted however that the reduction

is overestimated due to the reduction in the mesh stiffness under decreased applied load, as seen in Chapter 4.

7.2 Configuration 2

In configuration 2 the rotational model is expanded to include the coupled lateral motions caused by the normal tooth loads. This involves the inclusion of the bearing and support compliances to restrict the lateral motion of the shaft.

7.2.1 Mesh Damping

Initially the model is configured to exhibit zero damping on the bearings and supports, with shaft and coupling damping values equal to Test 11 (Table 7.11). During the simulations the effects of the mesh damping, which was shown to be highly influential in the purely rotational model, were determined.

Damping					Additional Information
Coupling	Shaft	Bearings	Supports	Mesh	
1e-4	1e-12	0	0	1e-6 - 1e-3	None

Table 7.12: Configuration 2 - Test 1 - Damping Values

Figure 7.18 illustrates the accelerations of the node connecting the bearing and support element, which is assumed to be representative of a virtual accelerometer placed on the bearing housing. These results show only the accelerations on the load side shaft; however similar results are present on the motor side and are given in the Digital Appendix (attached to the thesis in CD format), with the only variations being that the major peaks seen in Figure 7.18 are found at slightly higher frequencies.

The reason behind the differences in the peaks on the motor and load shafts is due to the variations in the supporting structure on each side. By setting all the supporting structure parameters equal to each other, the position of these frequency spikes is maintained across both shafts. Figure 7.19 shows the frequency domain plot of the motor and load side vertical accelerations, where the larger support (Figure C.6) has been used universally across the system. These results can therefore be compared directly with the results shown in Figure 7.18(d), where it is found that

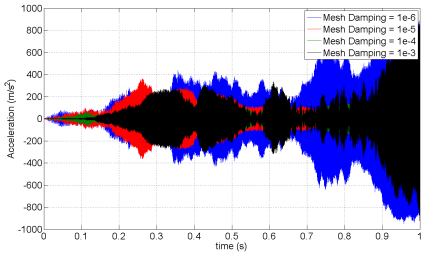

(a) Time Domain (Axial)

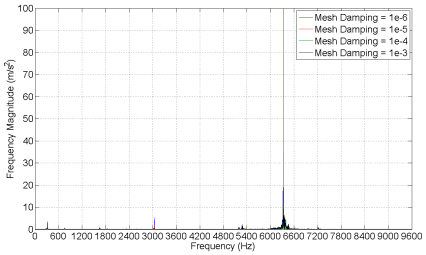

(b) Frequency domain (Axial)

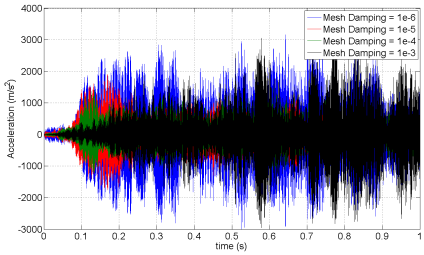

(c) Time Domain (Vertical)

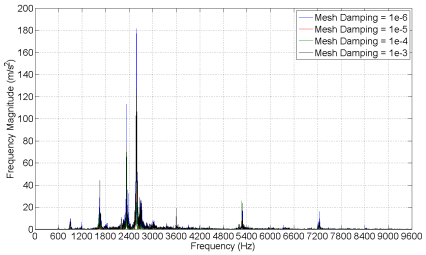

(d) Frequency domain (Vertical)

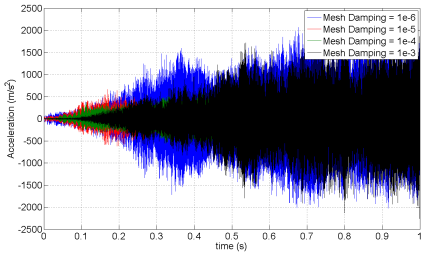

(e) Time Domain (Horizontal)

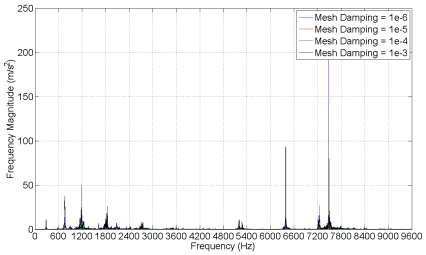

(f) Frequency domain (Horizontal)

Figure 7.18: Load side acceleration results (Configuration 2 - Test 1)

although the magnitudes of the respective frequencies vary, the pertinent frequencies remain the same.

Test	Damping					Additional Information
	Coupling	Shaft	Bearings	Supports	Mesh	
a	1e-4	1e-12	0	0	1e-5	All supports as per Figure C.6
b	1e-4	1e-12	0	0	1e-5	All supports as per Figure C.5

Table 7.13: Configuration 2 - Test 2 - Damping Values

Further simulations were also performed where the supporting structures were set equal to the smaller configuration (Figure C.5), and where the stiffness proportional damping values of the bearing and supporting structure were set to 1e-4, to represent a highly damped system. The results of these simulations, along

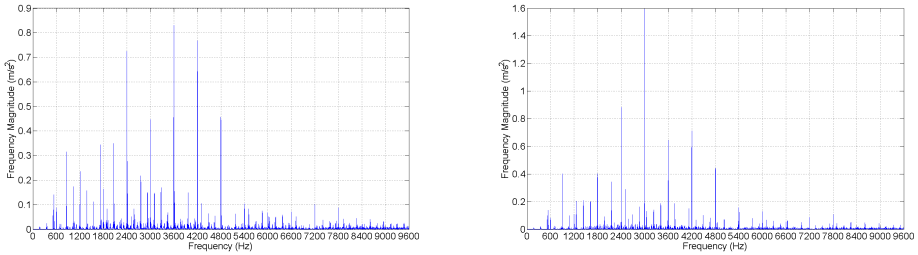

(a) Load side (b) Motor side

Figure 7.19: Vertical acceleration results (Configuration 2 - Test 2a)

with the complete results of Figure 7.19 are present in the Digital Appendix.

Figure 7.18 shows that mesh damping does have an effect on the lateral vibrations of the system; however by removing the results for a mesh stiffness value of 1e-6, it can also be shown that mesh damping above and below the range of 1e-3 and 1e-6 respectively has an adverse effect on the magnitude of vibration (Figure 7.20).

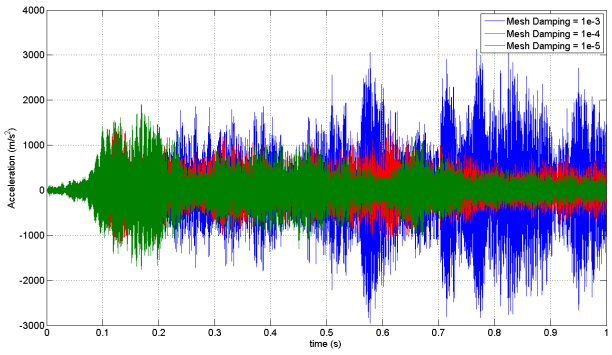

Figure 7.20: Vertical acceleration results (Configuration 2 - Test 1)

Figure 7.20 shows that although mesh stiffness can be used to reduce the magnitude of the bearing vibrations, without further damping of the bearings and supports the response does not reach a steady-state response in the set time frame.

7.2.2 Shaft Damping

In Section 7.1 it was shown that high shaft damping was unnecessary when coupled with other component damping as both coupling and mesh damping acted at the most significant nodes in terms of vibration. In Test 1 it has been shown

that mesh damping has only a limited effect on the lateral vibration at the bearing supports, such that in Test 3 the shaft damping is again varied to ascertain its effect on the lateral motions of the system.

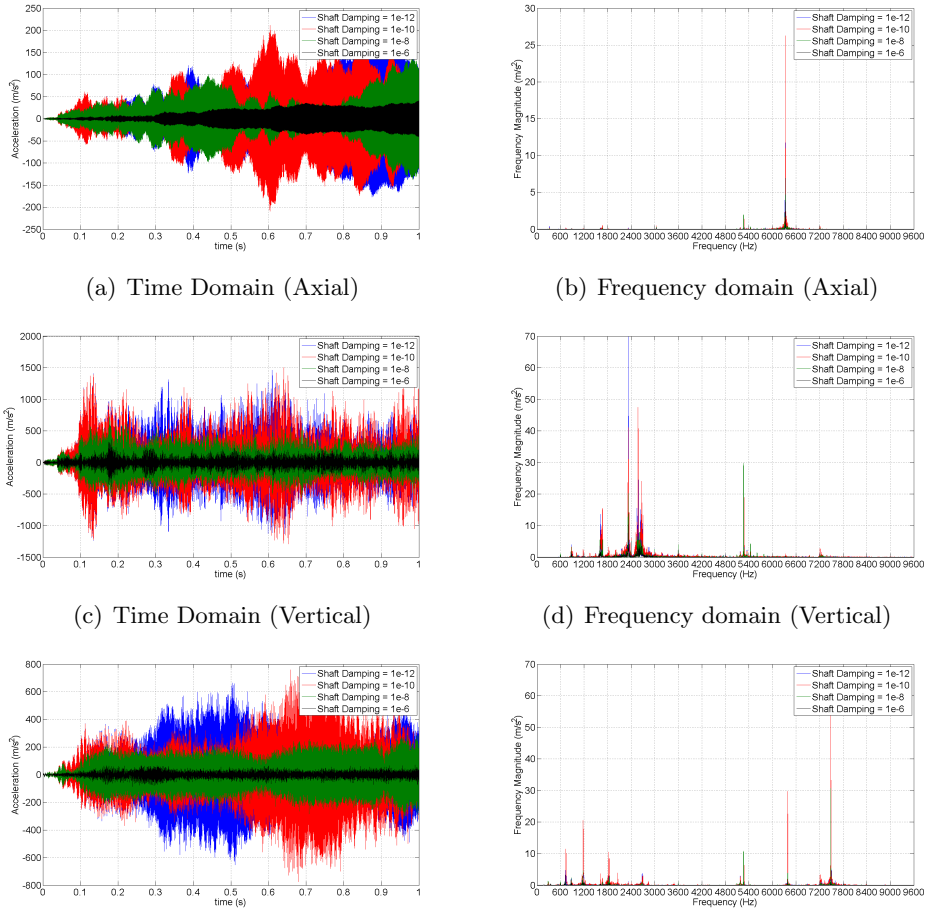

(a) Time Domain (Axial)

(b) Frequency domain (Axial)

(c) Time Domain (Vertical)

(d) Frequency domain (Vertical)

(e) Time Domain (Horizontal)

(f) Frequency domain (Horizontal)

Figure 7.21: Load side acceleration results (Configuration 2 - Test 3)

Damping					Additional Information
Coupling	Shaft	Bearings	Supports	Mesh	
1e-4	1e-12 - 1e-6	0	0	1e-4	None

Table 7.14: Configuration 2 - Test 3 - Damping Values

Figure 7.21 again shows the accelerations on the load side bearing casing, where the motor side results are given in the Digital Appendix. These results show that the shaft damping does help to reduce the magnitude of the casing vibrations, especially at the higher frequency components where shaft damping of 1e-6 has been

shown to completely damp out off mesh frequencies above 5000 Hz in the vertical direction (ref Figure 7.21(d)). However the frequency domain results in the 0 - 3600 Hz region maintain the high off mesh frequency terms, which were seen in Figure 7.18 and were found to mask the effects of the mesh frequencies on the vibrational response.

7.2.3 Bearing Damping

Shaft damping acts to dampen the torsional and lateral vibrations at the shaft nodes, which include the node connecting the shaft to the bearings. Therefore, in portions of the frequency domain, it is envisaged that the shaft damping may show similar effects to the bearing damping. The stiffness proportional bearing damping was subsequently varied between 0 and 1e-4 in Test 4 (ref Table 7.15), with results given in Figure 7.22 and the Digital Appendix.

Figure 7.22 shows that bearing damping has a significant effect on the magnitude of the acceleration response in the time domain. Its introduction also tends to bring about a steady state response within an acceptable time frame, as best depicted in Figure 7.22(c). The greatest variation in the time domain response is seen between damping values of 1e-6 and 1e-4, which suggests that critical damping of the bearings lies between these two values and that at 1e-4 the bearings are overdamped.

Damping					Additional Information
Coupling	Shaft	Bearings	Supports	Mesh	
1e-4	1e-12	0 - 1e-4	0	1e-4	None

Table 7.15: Configuration 2 - Test 4 - Damping Values

Looking at the frequency domain response the effects between 1e-6 and 1e-4 further suggest that the bearings are overdamped at 1e-4, where more pronounced peaks are seen. Of note is that whilst the bearings are overdamped the frequency contributions of the higher frequencies are reduced to negligible values. However with this high damping value the contribution of the primary meshing frequency (600 Hz) is greatly reduced, such that its effects are still negligible compared to

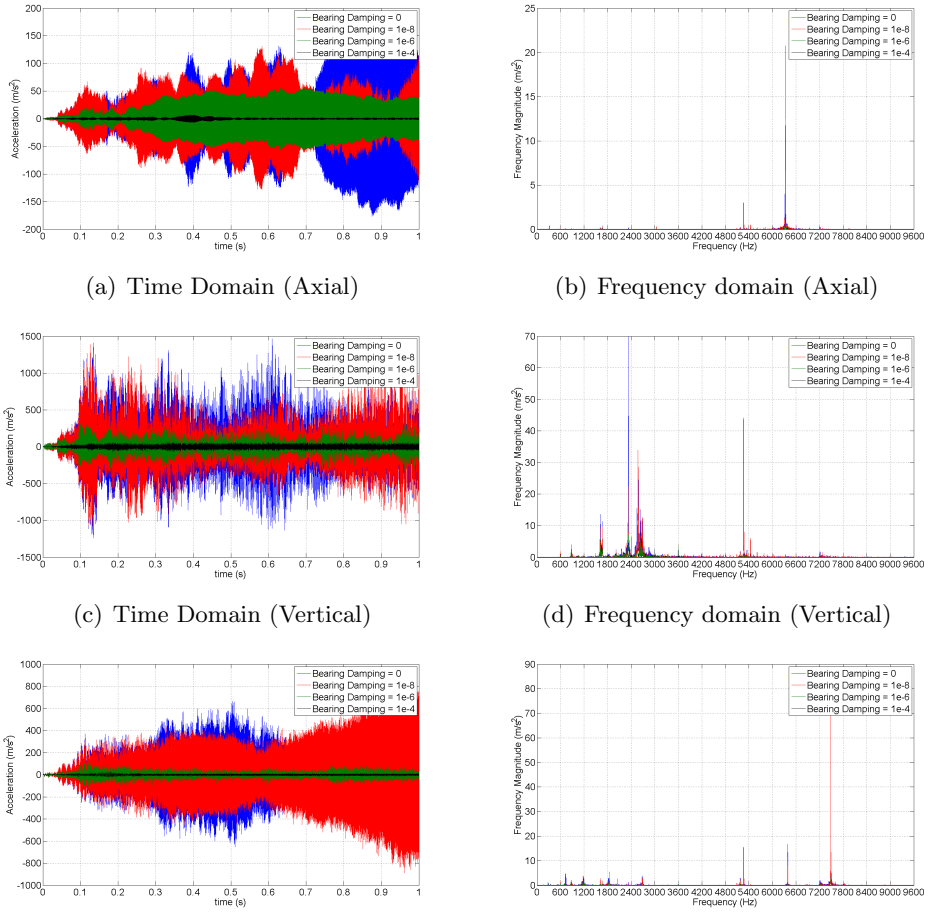

(a) Time Domain (Axial)

(b) Frequency domain (Axial)

(c) Time Domain (Vertical)

(d) Frequency domain (Vertical)

(e) Time Domain (Horizontal)

(f) Frequency domain (Horizontal)

Figure 7.22: Load side acceleration results (Configuration 2 - Test 4)

other frequency peaks; the most notable being at 4 - 8 times the primary frequency (2400, 3000, 3600, 4200 and 4800 Hz). At damping values of 1e-8 or less the primary meshing frequency is the greatest of the meshing frequency harmonics, however it is once again masked by the off-mesh frequency peaks.

7.2.4 Support Damping

The final component damping which can be varied is that of the supports. In Test 5 the stiffness proportional damping term of the supports is varied between 0 and 1e-4 (ref Table 7.16), with results shown in Figure 7.23.

In Figure 7.23 the effects of support damping are shown to decrease the magnitude of the translational accelerations, with RMS values decreasing from 57, 331 and 160 m/s^2 to 0.7, 72 and 47 m/s^2 across the damping range for the axial,

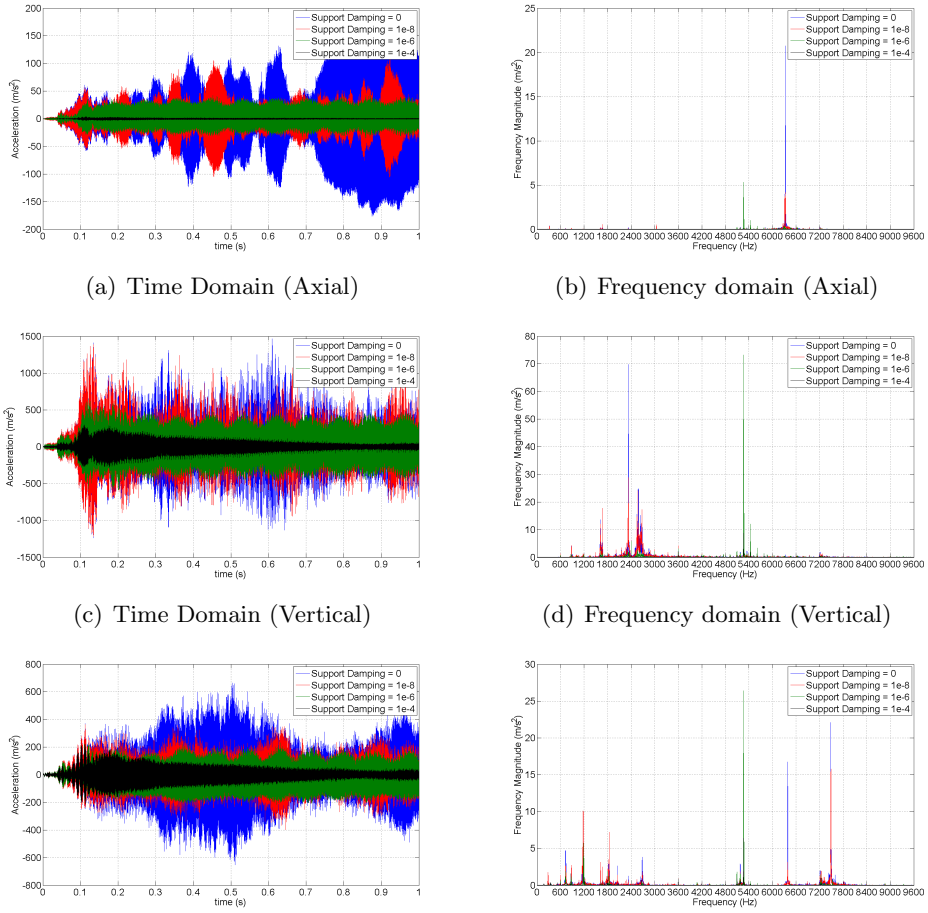

(a) Time Domain (Axial)

(b) Frequency domain (Axial)

(c) Time Domain (Vertical)

(d) Frequency domain (Vertical)

(e) Time Domain (Horizontal)

(f) Frequency domain (Horizontal)

Figure 7.23: Load side acceleration results (Configuration 2 - Test 5)

Damping					Additional Information
Coupling	Shaft	Bearings	Supports	Mesh	
1e-4	1e-12	0	0 - 1e-4	1e-4	None

Table 7.16: Configuration 2 - Test 5 - Damping Values

vertical and horizontal acceleration respectively.

Again it is seen that the component critical damping limit is found between a stiffness proportional damping value of 1e-6 and 1e-4. This is seen in both the time and frequency domains where in the frequency domain the over-damped response results in clearly defined peaks. It is also noted that in the frequency domain, support damping does little to diminish the influence of the off-mesh-frequency at 5400 Hz and therefore it can be deduced that this peak is associated with the bearing

stiffness only. This means that this frequency can only be reduced with increased bearing damping or shifted with varied stiffness values.

Support damping tends to reduce some of the higher frequency mesh components, however it is still found that the contribution of the primary mesh frequency is less than many off-mesh-frequency contributions and those of other mesh harmonics. It is shown that in all DOF support damping is not as effective at reducing the off-mesh component contributions when compared against equivalent bearing damping values.

7.2.5 Coupling Stiffness

It has previously been noted that although the coupling torsional stiffness is quoted in the sales literature, the values for the coupling translational and bending stiffness in other directions are not. In the previous simulations the translational coupling stiffnesses have been set at 1e6 N/m, while the bending stiffnesses have been set to zero. In the proceeding section these stiffness values are changed to investigate their effects on the vibrational response of the system.

Initially the translational stiffness are varied as per Table 7.17, where the damping value of the bearings and supports are set to zero. In Figure 7.24 results are given for the motor side since greater effects were seen on this side, which is expected since the coupling is only present on this shaft.

Damping					Additional Information
Coupling	Shaft	Bearings	Supports	Mesh	
1e-4	1e-12	0	0	1e-4	Lateral Coupling Stiffness = 1e4 - 1e8 N/m

Table 7.17: Configuration 2 - Test 6 - Damping Values

From the time domain results of Figure 7.24, it can be seen that increased lateral coupling stiffness reduces the magnitude of the accelerations; however since in all simulations the stiffness proportional damping term has remained at 1e-4 this could be due to variations in the absolute damping of the system. In the frequency domain it can be seen that the increased lateral stiffness tends to reduce the off mesh frequency magnitudes, which again could be due to the increased damping of

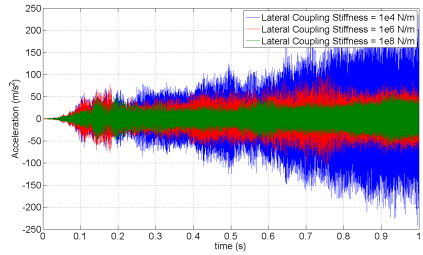

(a) Time Domain (Axial)

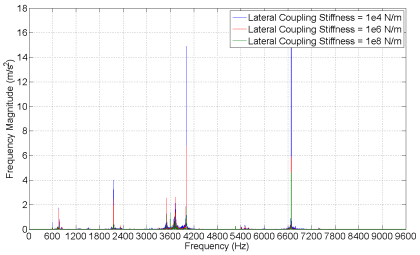

(b) Frequency domain (Axial)

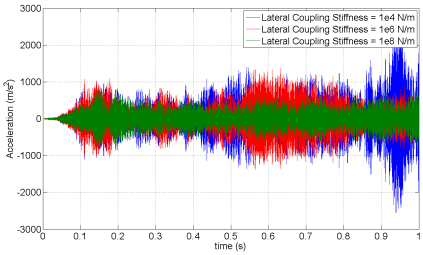

(c) Time Domain (Vertical)

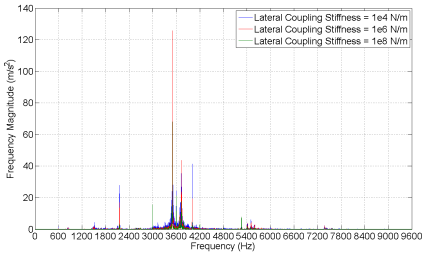

(d) Frequency domain (Vertical)

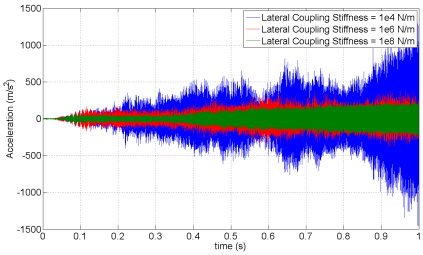

(e) Time Domain (Horizontal)

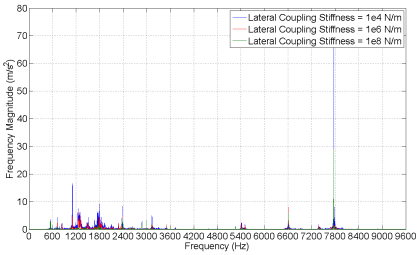

(f) Frequency domain (Horizontal)

Figure 7.24: Motor side acceleration results (Configuration 2 - Test 6)

the coupling. The effect of lateral stiffness on the mesh frequency terms tends to be minimal in the frequency domain, where it is again seen that for all stiffness values the primary mesh frequency at around 600 Hz is smaller than many other harmonics and other off mesh frequencies.

Results for the load side shaft are not given here; however they show less variation between stiffness values. Figures for the load side can be found in the Digital Appendix.

In Figure 7.24 the results were obtained with zero damping applied to the bearings and supports; this resulted in frequency domain plots with poorly defined peaks for the mesh frequencies and many large frequency contributions that were not harmonics of the mesh frequency. By increasing the stiffness proportional damping

terms for the bearings and supports a more defined steady state response can be obtained, where results are shown in Figure 7.25. These results are again shown for the motor side only since no change was observed for the accelerations on the load shaft.

In these results the only variation in accelerations occurs between coupling stiffnesses of 1e6 and 1e8, where the magnitude of the accelerations is reduced. This can be attributed to the reduction in many of the peaks in the frequency domain, especially the two frequency peaks below 600 Hz, which are significantly reduced in the acceleration results for U1 and U3. In U2 the effect of increased coupling stiffness is seen in many mesh harmonic peaks as well as many off-mesh frequencies.

The reductions in the acceleration results of Test 7, although less than Test 6, could be again attributed to the increased damping of the coupling. By reducing the stiffness proportional damping value to 1e-6, for a lateral coupling stiffness of 1e8 N/m, Figure 7.26 shows the load side vertical accelerations for the undamped (Test 6) and overdamped (Test 7) scenarios. These results are compared against the default configuration, where the coupling stiffness is equal to 1e6 N/m and the coupling damping is equal to 1e-4.

Damping					Additional Information
Coupling	Shaft	Bearings	Supports	Mesh	
1e-4	1e-12	1e-4	1e-4	1e-4	Lateral Coupling Stiffness = 1e4 - 1e8 N/m

Table 7.18: Configuration 2 - Test 7 - Damping Values

Figure 7.26 shows similar results to Figures 7.24(c) and 7.25(c) when comparing the variations in the accelerations due to changing lateral coupling stiffnesses. This suggests that the variations in the vibrational response are primarily due to the changes in stiffness rather than the imposed damping values. Full results are given in the Digital Appendix, where slight variations are attributed to the reduced torsional damping as a result of the reduced stiffness proportional damping term.

In previous simulations the bending stiffness of the coupling was assumed to be zero; this was to approximate the ability of the coupling to allow some angular motion without resistance. Results showing the effects of the bending stiffness on

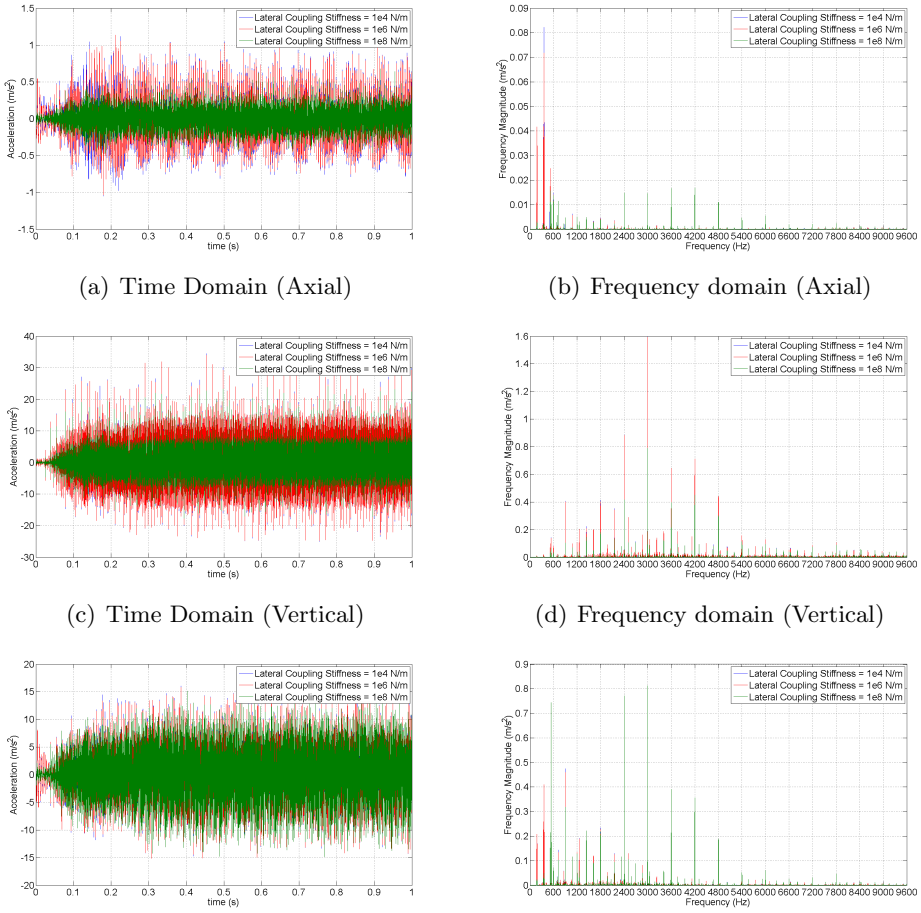

(a) Time Domain (Axial)

(b) Frequency domain (Axial)

(c) Time Domain (Vertical)

(d) Frequency domain (Vertical)

(e) Time Domain (Horizontal)

(f) Frequency domain (Horizontal)

Figure 7.25: Motor side acceleration results (Configuration 2 - Test 7)

the time and frequency domain response for undamped and overdamped systems are given in Figures 7.27 and 7.28 respectively, with system parameters given in Tables 7.19 and 7.20.

From Figure 7.27 little can be deduced with regard to the effect of the bending stiffness on the acceleration results. It is apparent from the time domain responses that the introduction of bending resistance at the coupling decreases the magnitude of the accelerations in all directions; however the mechanism through which this is achieved is not clearly defined in the frequency domain. Instead the introduction of bending resistance tends to reduce the magnitude of a wide range of frequency peaks.

Further investigation into the overdamped response under varied bending

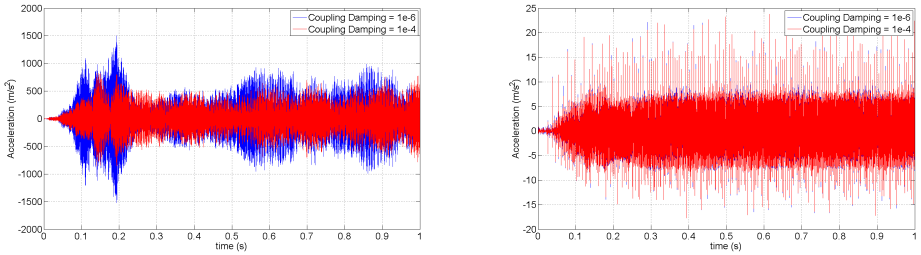

(a) Undamped (as per Test 6)

(b) Overdamped (as per Test 7)

Figure 7.26: Motor side vertical acceleration results (Configuration 2 - Test 8)

stiffnesses, as illustrated in Figure 7.28, shows clearly reduced acceleration magnitudes. Observing the frequency domain results this can clearly be attributed to reductions in defined frequency magnitudes. As with the lateral stiffness results of Tests 6 and 7, the introduction of bending resistance at the coupling tends to reduce two large frequency peaks below 600 Hz in the U1 and U3 directions.

Damping					Additional Information
Coupling	Shaft	Bearings	Supports	Mesh	
1e-4	1e-12	0	0	1e-4	Bending Coupling Stiffness = 0 - 1e6 N/rad

Table 7.19: Configuration 2 - Test 9 - Damping Values

Another result of the increased bending stiffness seen in Figure 7.28 is that the mesh harmonic at 3000 Hz is greatly reduced. This was partially seen in the results of Figure 7.25(d); however this was only in the vertical direction.

Damping					Additional Information
Coupling	Shaft	Bearings	Supports	Mesh	
1e-4	1e-12	1e-4	1e-4	1e-4	Bending Coupling Stiffness = 0 - 1e6 N/rad

Table 7.20: Configuration 2 - Test 10 - Damping Values

The similarities between the responses due to increased lateral and bending stiffness can be attributed to the formulation of the coupling stiffness matrix, as shown in Section 6.2.2. In this formulation a slight bending resistance is introduced through the coupling lateral stiffnesses, with a constant factor of $l_c^2/4$, where l_c is the coupling length. Therefore an increase in the lateral stiffness subsequently increases the coupling bending stiffness.

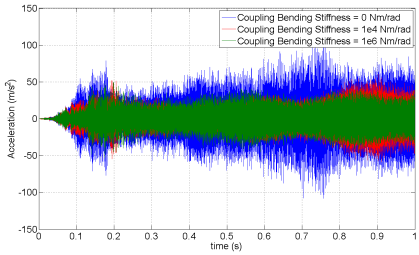

(a) Time Domain (Axial)

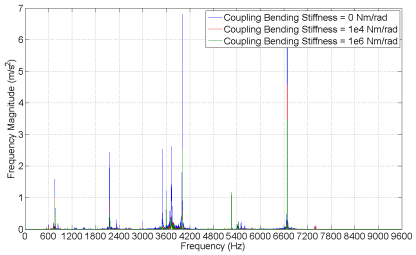

(b) Frequency domain (Axial)

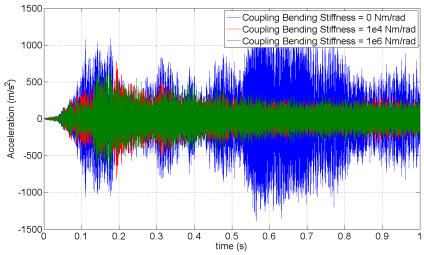

(c) Time Domain (Vertical)

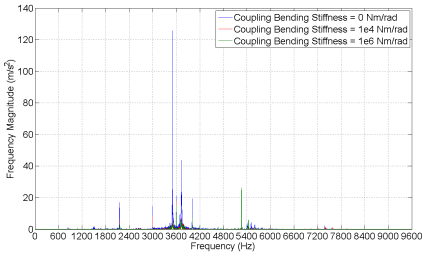

(d) Frequency domain (Vertical)

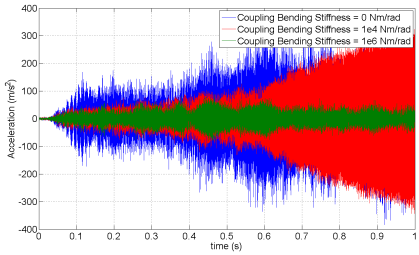

(e) Time Domain (Horizontal)

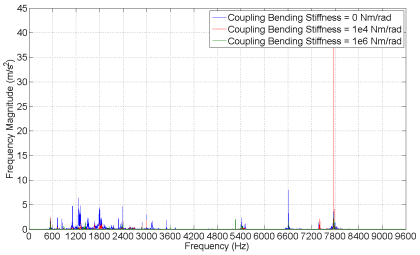

(f) Frequency domain (Horizontal)

Figure 7.27: Motor side acceleration results (Configuration 2 - Test 9)

7.2.6 Bearing Stiffness

Next the bearing contact stiffness (K_n) is varied between 1e7 and 1e11 N/m$^{3/2}$ under undamped and overdamped conditions. The undamped time and frequency domain results are shown in Figure 7.29 for the load side shaft.

Damping					Additional Information
Coupling	Shaft	Bearings	Supports	Mesh	
1e-4	1e-12	0	0	1e-4	Bearing Stiffness = 1e7 - 1e11 N/m$^{3/2}$

Table 7.21: Configuration 2 - Test 11 - Damping Values

In the time domain it can be seen that stiffnesses in the range 1e8 to around 6e9 N/m$^{3/2}$ result in the lowest magnitude vibrational response, which is also the

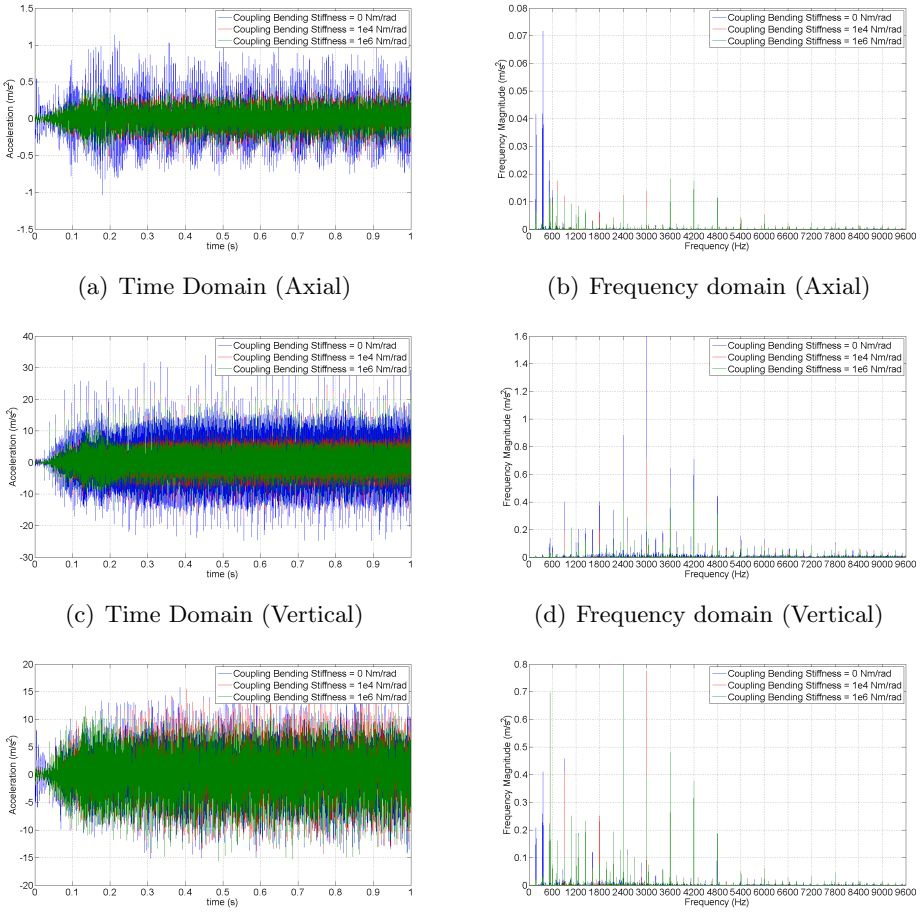

(a) Time Domain (Axial)

(b) Frequency domain (Axial)

(c) Time Domain (Vertical)

(d) Frequency domain (Vertical)

(e) Time Domain (Horizontal)

(f) Frequency domain (Horizontal)

Figure 7.28: Motor side acceleration results (Configuration 2 - Test 10)

case for the motor side shaft vibrations. However it is apparent that in all the undamped results, the vibration increases through the time domain. In the frequency domain large peaks are found in areas not associated with the harmonics of the gear meshing frequency, which again tend to contribute more to the response when compared against the mesh frequencies.

The frequency domain results for the high stiffness bearings show much greater distribution around the frequency peaks, which results in less clearly defined peaks, and therefore few conclusions can be drawn from the frequency domain results of the undamped system.

By increasing the damping at the bearings and supports the effects of bearing stiffness can be determined with more ease (Figure 7.30). In this configuration the

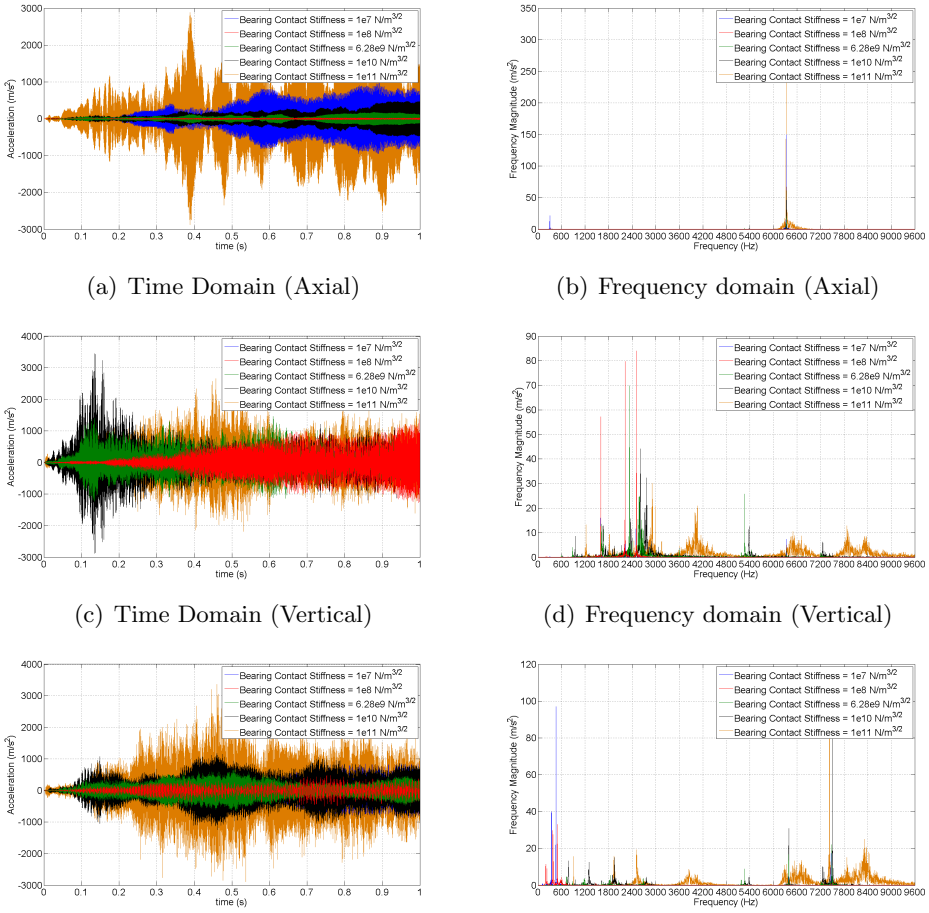

(a) Time Domain (Axial)

(b) Frequency domain (Axial)

(c) Time Domain (Vertical)

(d) Frequency domain (Vertical)

(e) Time Domain (Horizontal)

(f) Frequency domain (Horizontal)

Figure 7.29: Load side acceleration results (Configuration 2 - Test 11)

stiffness proportional bearing damping is maintained at 1e-4, and since the stiffness matrix, and hence the absolute damping, is a function of both the contact stiffness value and the bearing deflection some variations as a result of different damping values are present.

From the time domain results it is clear that a contact stiffness value of 1e7 $N/m^{3/2}$ leads to excessive axial motion, and that as the contact stiffness is increased the magnitude of acceleration increases in the vertical and horizontal directions. At stiffness values of 1e7 $N/m^{3/2}$ and 1e8 $N/m^{3/2}$ the vibration is dominated by the variation in the bearing stiffness, with clear acceleration spikes at intervals of of roughly 0.012 seconds on the load side shaft, which translates to 83.3 Hz. This relates to variations in the bearing stiffness where the fundamental frequency of the

bearing carrier (9.51 Hz) based on a rotational frequency of 24 Hz, and 9 rolling elements result in a bearing frequency of 85.6 Hz. On the motor side shaft the frequency is seen to shift to 85.8 Hz compared to a theoretical value of 89.1 Hz. The difference between the shafts is due to the increased rotational speed of the motor side shaft (25 Hz) and the difference between the calculated and theoretical values is likely due to slight variations in average speed.

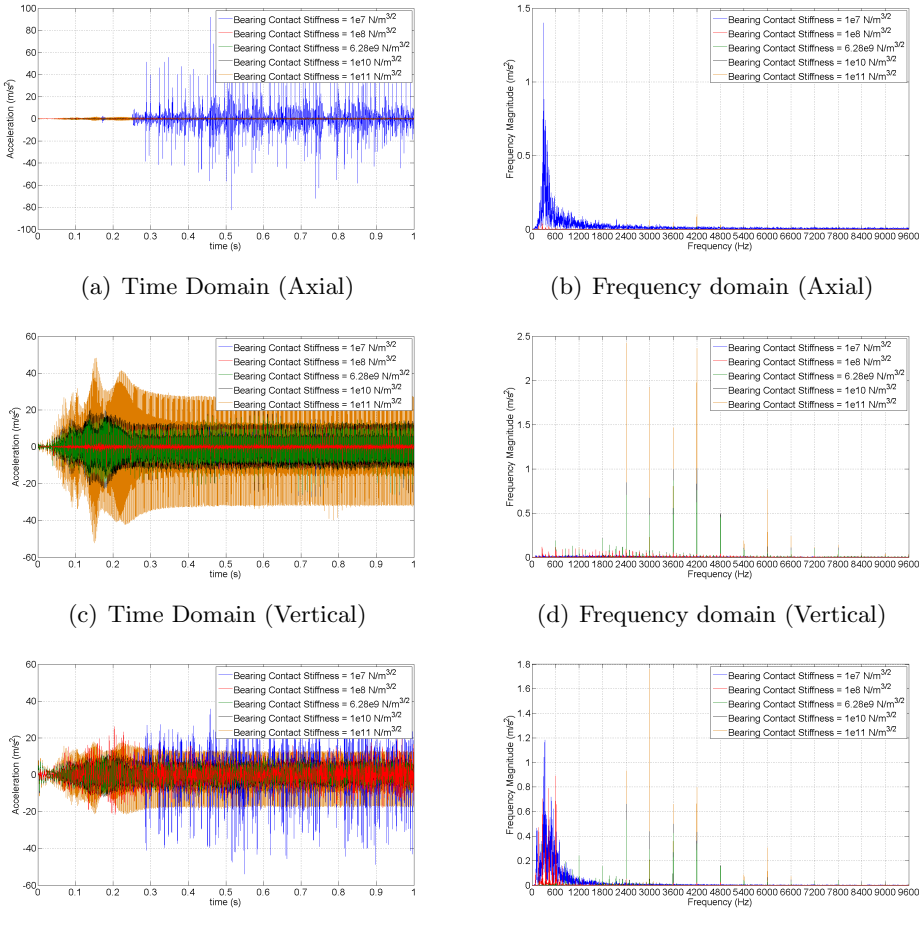

(a) Time Domain (Axial)

(b) Frequency domain (Axial)

(c) Time Domain (Vertical)

(d) Frequency domain (Vertical)

(e) Time Domain (Horizontal)

(f) Frequency domain (Horizontal)

Figure 7.30: Load side acceleration results (Configuration 2 - Test 12)

Damping					Additional Information
Coupling	Shaft	Bearings	Supports	Mesh	
1e-4	1e-12	1e-4	1e-4	1e-4	Bearing Stiffness = 1e7 - 1e11 $N/m^{3/2}$

Table 7.22: Configuration 2 - Test 12 - Damping Values

In the frequency domain plots it can be seen that a contact stiffness of 1e7

$N/m^{3/2}$ is far to low and results in excessive vibration in all DOF. For all stiffness values greater than 1e8 $N/m^{3/2}$ the frequency domain is dominated by harmonics of the meshing frequencies in the range 2400 - 6600 Hz and the influence of the primary meshing frequency is diminished. At 1e8 $N/m^{3/2}$ there is a great reduction in the comparative influence of these higher order harmonics and the primary frequency dominates. There are large harmonic frequencies associated with the bearing vibrations, however these could be due to the decreased bearing damping as a result of the constant stiffness proportional damping used.

On the motor side results, given in the Digital Appendix, a further major frequency spike is seen at 3000 Hz, which has previously been shown to be due to the reduced bending stiffness of the coupling; therefore this can be controlled through proper setting of this value.

7.2.7 Bearing Support Stiffness

The final variation of the system stiffnesses involves the bearing supports shown in Figures C.5 and C.6. As with previous studies in this section the system is analysed under both undamped and overdamped configurations, where the stiffness matrices developed from finite element models of the components, as described in Section 6.2.4, were multiplied by 1/2 and 2 to determine the system response under decreased and increased support stiffness. To obtain constant natural frequencies at the component the derived mass matrices were also subjected to the same manipulation.

Figure 7.31 illustrates the effects of varying the support stiffness/mass on the undamped system, where although little is gained from the time domain due to the unstable solution, the frequency domain suggests that the variation in the support properties has an effect on the position of the dominant frequencies. The only main frequency not associated with the meshing frequency, which remains constant and independent of the support properties is just below 5400 Hz. This frequency has previously been shown to be due to the bearings, and these results corroborate this assertion.

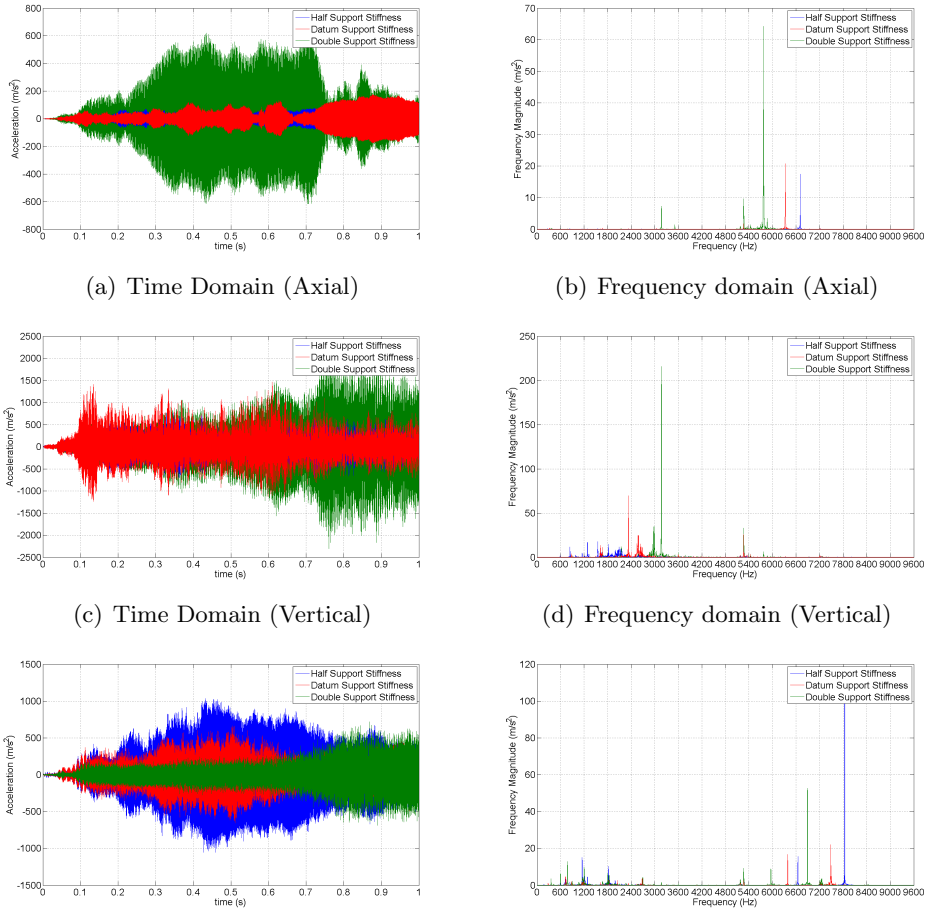

(a) Time Domain (Axial)

(b) Frequency domain (Axial)

(c) Time Domain (Vertical)

(d) Frequency domain (Vertical)

(e) Time Domain (Horizontal)

(f) Frequency domain (Horizontal)

Figure 7.31: Load side acceleration results (Configuration 2 - Test 13)

Damping					Additional Information
Coupling	Shaft	Bearings	Supports	Mesh	
1e-4	1e-12	0	0	1e-4	Support Mass and Stiffness Varied

Table 7.23: Configuration 2 - Test 13 - Damping Values

By introducing damping at the bearings and supports the effects of the support stiffness can be seen more clearly, as shown in Figure 7.32. Here, since the off mesh frequency peaks shown in Figure 7.31 have been damped to insignificant values, increased support stiffnesses have been shown to decrease the overall magnitude of the accelerations without altering the frequency peaks. This can be seen directly in the time domain with decreased acceleration magnitudes and in the frequency domain through reductions in the major frequencies.

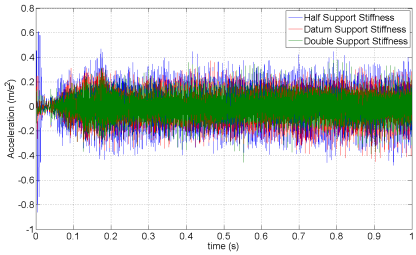

(a) Time Domain (Axial)

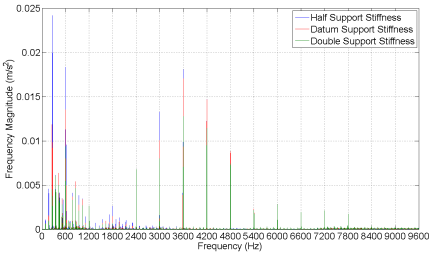

(b) Frequency domain (Axial)

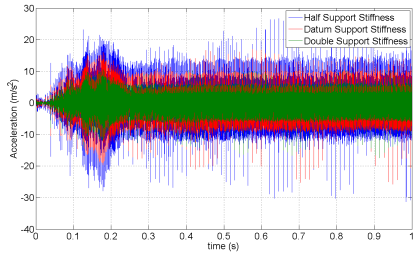

(c) Time Domain (Vertical)

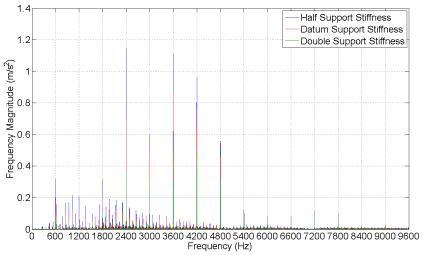

(d) Frequency domain (Vertical)

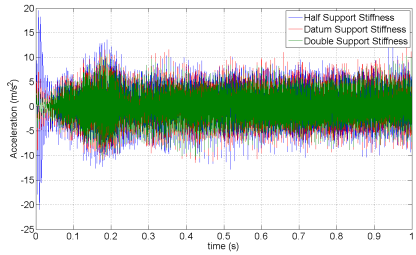

(e) Time Domain (Horizontal)

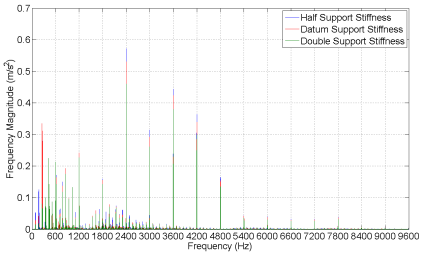

(f) Frequency domain (Horizontal)

Figure 7.32: Load side acceleration results (Configuration 2 - Test 14)

Damping					Additional Information
Coupling	Shaft	Bearings	Supports	Mesh	
1e-4	1e-12	1e-4	1e-4	1e-4	Support Mass and Stiffness Varied

Table 7.24: Configuration 2 - Test 14 - Damping Values

In the frequency domain it is apparent that the support stiffness has the largest impact on the vertical response, and that in the horizontal and axial directions an increased stiffness tends to decrease the first 3 harmonics of the bearing frequencies.

Whilst the magnitude of the accelerations is varied with changes in the support stiffness, the composition of the frequency domain changes little, and the relative impact of the frequency components changes only marginally.

7.2.8 Conclusions

In this section the purely torsional model was expanded to include lateral and bending motion of the gears, shafts, bearings and supports. Various parameters were investigated to determine their effects on the accelerations at the bearing housings. From this it was shown that the mesh and shaft damping had only a marginal effect on the response when considering undamped bearings and supports; however it was noted that they could exhibit larger effects if additional system damping was included. Bearing and support damping however were shown to be extremely effective at reducing the magnitude of the vibration. Both tended to have a large impact on major frequency peaks not associated with the meshing frequency; however it was found that a specific frequency peak at around 5400 Hz was solely attributed to the bearings and could not be affected by the support damping.

Although bearing and support damping reduced the non mesh frequencies, they were also found to reduce the influence of the primary mesh frequency at 600 Hz, such that it was negligible in magnitude compared to its harmonics in the range 2400 - 7200 Hz. This was addressed through reductions in the bearing contact stiffness under damped conditions, which reduced the influence of the higher mesh harmonics and increased the influence of the primary frequency. From this a sensible range of bearing contact stiffnesses were determined as 1e8 to 1e10 $N/m^{3/2}$.

Further stiffness evaluation was performed on the coupling and the supports. The coupling bending and lateral stiffnesses were varied and showed that with damping of the supports and bearings, increased stiffnesses tended to reduce the magnitude of the bearing vibrations on the motor side only. This was achieved in the frequency domain by the reduction of two main frequency regions. In the axial and vertical direction increased coupling stiffnesses reduced large frequency peaks in the sub mesh frequency (<600 Hz) region, whilst in the vertical and horizontal directions it decreased the 5^{th} harmonic (3000 Hz). It is believed that, due to the formulation of the coupling stiffness matrix, increases in both the lateral and bending stiffness act in the same way to reduce these frequency peaks.

Increases in the support stiffness have shown a tendency to reduce the magnitude of vibration, however this was found to be universal across the whole frequency range.

7.3 Configuration 3

In Configuration 3 the coupled torsional-lateral model is expanded to include the influences of normal sliding friction. This introduces nonlinear forcing terms in the vertical, horizontal and torsional directions. In this section the model is configured with specific damping terms, as shown in Table 7.25, whilst the coefficient of friction and the reference velocity, as described in Section 6.3.2, are varied to investigate their effects.

Damping					Additional Information
Coupling	Shaft	Bearings	Supports	Mesh	
1e-4	1e-12	1e-5	1e-8	1e-4	Varied frictional parameters

Table 7.25: Configuration 3 - Damping Values

7.3.1 Coefficient of Friction

The first part of this section investigates the effect of varied frictional coefficients on the load side vibrations. The coefficient of friction is varied between 0 and 0.5 with the reference velocity set to 0.1 m/s. Results are shown in Figure 7.33.

As with the torsional model in Configuration 1, the effect of friction is found to decreases the rotational velocity of the shafts, due to the introduction of the resistive frictional torque. In the vertical and horizontal directions increased friction coefficients have been shown to increase the influence of the 1^{nd}, 2^{nd} and 3^{rd} harmonics of the mesh frequency (600, 1200 and 1800 Hz). The increases in the 2^{nd} and 3^{rd} harmonics have previously been shown to be attributed to the variations in the friction force through a mesh cycle. The increases in the 2^{nd} harmonic are due to the variation in the direction of the friction force as a tooth passes through the pitch point, while the 3^{rd} harmonic has been shown to be due to the load sharing characteristics through a mesh cycle.

In the time domain the effects of increased sliding friction are shown to

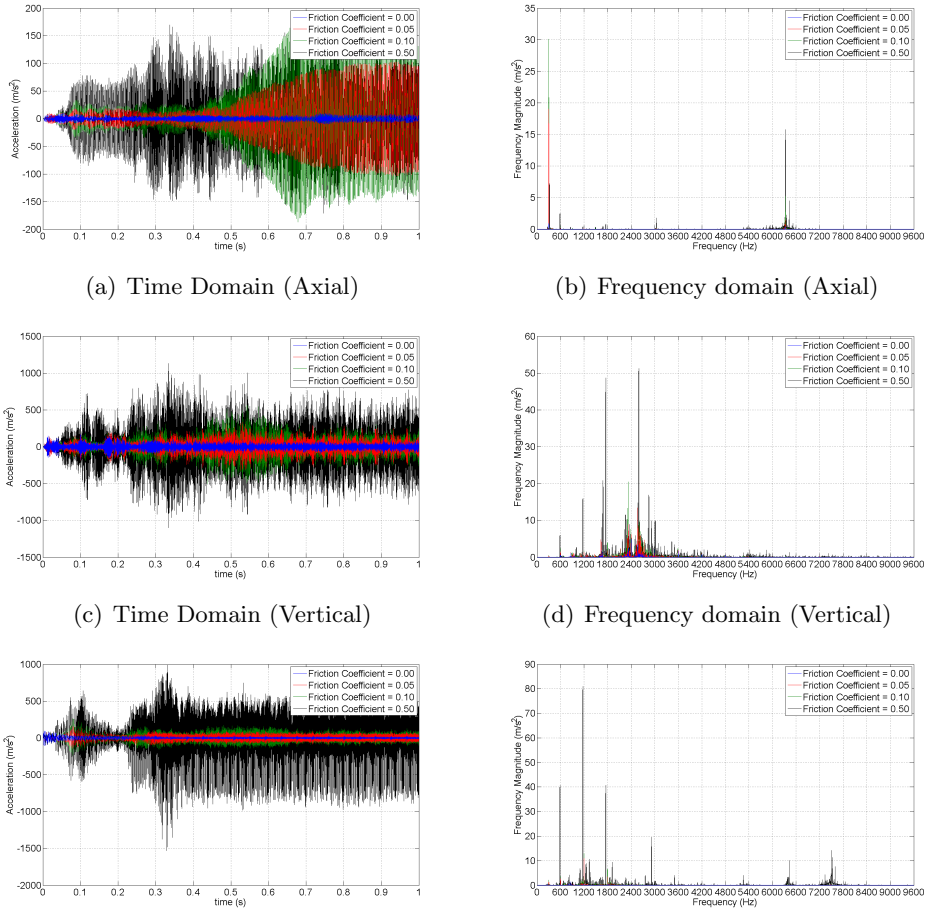

(a) Time Domain (Axial)

(b) Frequency domain (Axial)

(c) Time Domain (Vertical)

(d) Frequency domain (Vertical)

(e) Time Domain (Horizontal)

(f) Frequency domain (Horizontal)

Figure 7.33: Load side acceleration results (Configuration 3 - Test 1)

increase the magnitude of bearing vibration in all translational directions. This again has been shown in the torsional model to be attributed to the increased peak-to-peak transmission error caused by variations in the torsional friction load. However in the combined lateral-torsional model the introduction of further lateral forces from the friction forces also result in increased vibrations.

In the frequency domain the lateral friction forces have been shown to have increased influence in the horizontal DOF compared to the vertical DOF due to the pressure angle. This means that when decomposing the frictional forces into the global vertical and horizontal directions greater forces arise in the horizontal direction.

7.3.2 Reference Sliding Velocity

With the coefficient of friction set to 0.07, the reference velocity is varied between 0.01 and 1 m/s to determine its effect on the bearing vibrations. Damping values remain as per Table 7.25 and results for the load-side bearing lateral vibrations are given in Figure 7.34.

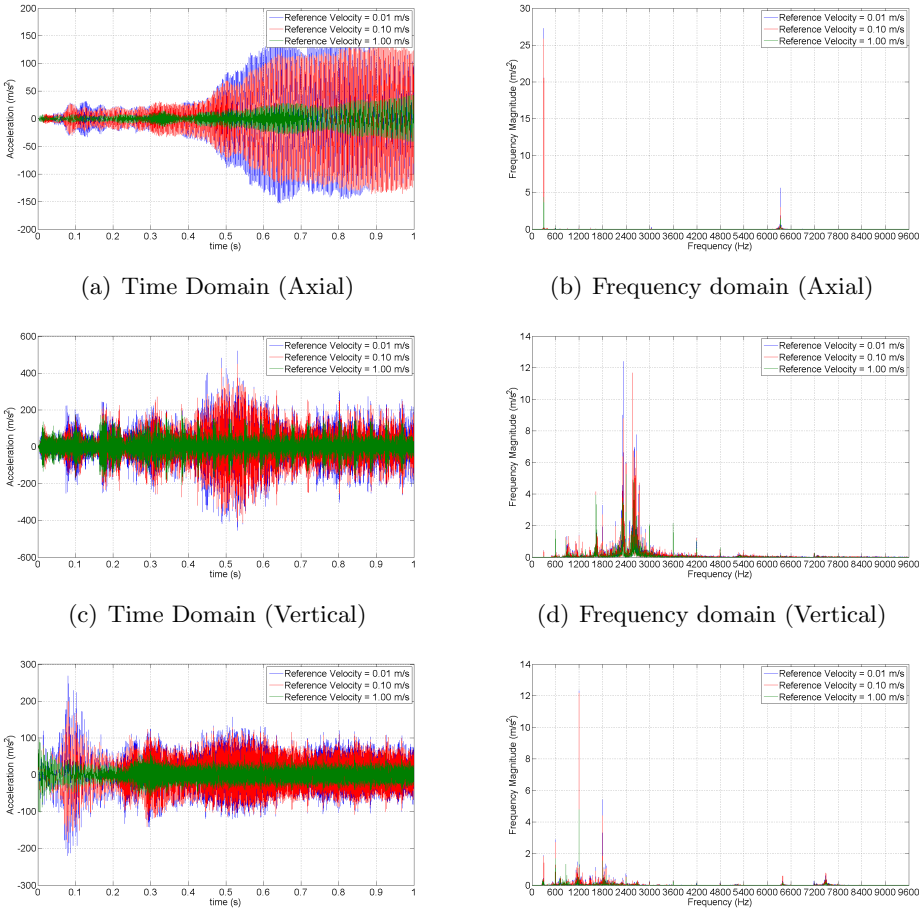

(a) Time Domain (Axial)

(b) Frequency domain (Axial)

(c) Time Domain (Vertical)

(d) Frequency domain (Vertical)

(e) Time Domain (Horizontal)

(f) Frequency domain (Horizontal)

Figure 7.34: Load side acceleration results (Configuration 3 - Test 2)

The time domain results of Figure 7.34 show that, in the vertical and horizontal DOF, the effect of increasing the reference velocity, and subsequently decreasing the severity of the transition in friction force at the pitch point, is that steady state peak-to-peak vibrations are decreased.

In the frequency domain the decreases in the peak-to-peak vibrations can be

attributed to the reduction in the 2^{nd} - 4^{th} mesh harmonics, which have effects that are described in the previous section. The greatest effect is seen between 0.1 and 1 m/s where, as shown in Figure 7.15, the friction force does not reach its maximum value before and after the transition point. This is due to the reference velocity being greater than the maximum and minimum sliding velocities during simulation.

7.3.3 Conclusions

In this section the lateral-torsional model has been expanded to include the effects of normal sliding friction introduced by the sliding action as the gear teeth come into and out of mesh. The effects of the friction coefficient and the reference sliding velocity used to determine the friction force have been varied to observe their effects on the bearing vibrations.

Increases in the friction coefficient have been shown to increase the magnitude of vibration through the increased influence of the 2^{nd} - 4^{th} harmonics. These have previously been shown to be attributed to the transition of the friction force direction at the pitch point and the variations in the friction forces as a result of load sharing. Increased friction coefficient has also been shown to decrease the speed of the shafts due to a resistive torque at the mesh.

The reference velocity has previously been shown to vary the severity of the friction force transition at the pitch point. Increased reference velocity values decrease the severity and allow for a smoother transition at the pitch point; therefore it has been found that increased values tend to decrease the magnitude of bearing vibrations in the time domain. This is seen in the frequency domain as a decrease in the frequency magnitudes of the pertinent mesh harmonics (2^{nd} - 4^{th}).

7.4 Configuration 4

In the previous section the dynamic model was forced by both the variation in the mesh stiffness and the friction force as a result of the sliding contact between teeth as they enter and leave contact. Both these forces act in the plane of the gear. In this section the friction model is expanded to include the effects of teeth sliding in the axial direction. This manifests as an axial force and moments about

the vertical and horizontal axes, as shown in Section 6.3.3.

To ascertain its effects, axial friction is applied to a selection of results from Tests 1 and 2 in Configuration 3 and compared against the original results.

7.4.1 Friction Coefficient

When varying the friction coefficient, as shown in Figure 7.35 for a friction coefficient of 0.07, it is found that axial friction reduces the magnitude of the vertical and horizontal vibrations. This is attributed to the resistive moment generated as a result of axial sliding, which tends to resist the bending and hence vertical and horizontal deflection of the shaft and bearings.

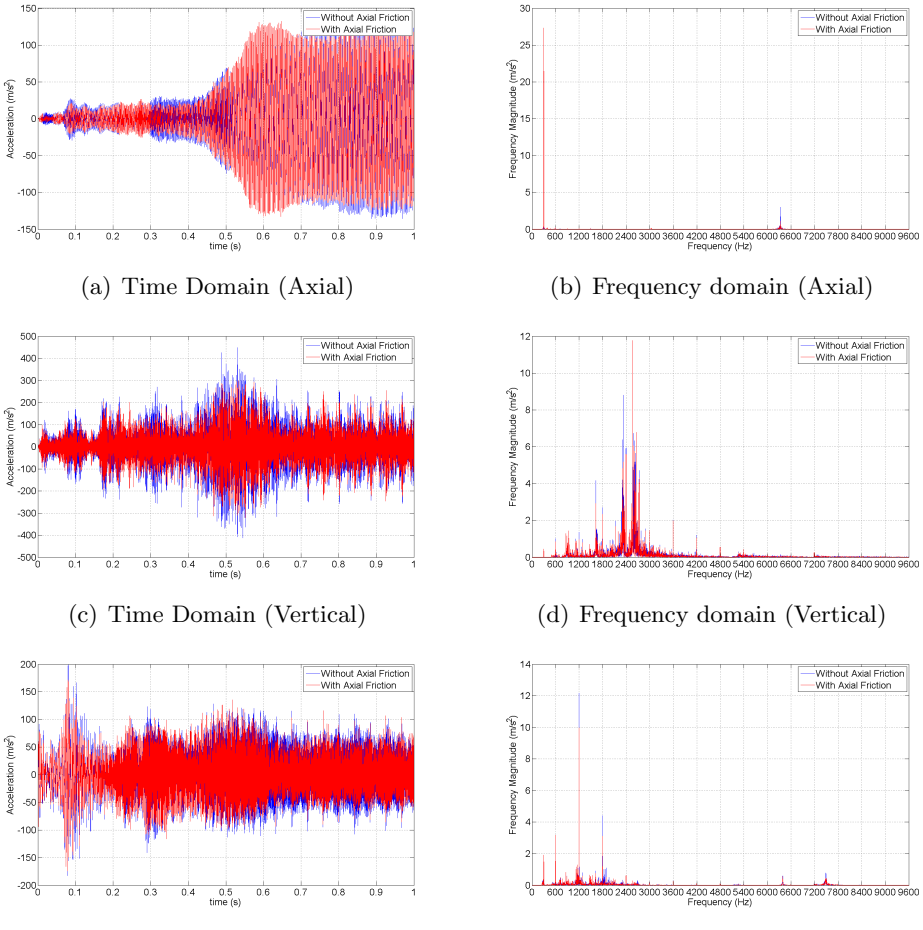

(a) Time Domain (Axial)

(b) Frequency domain (Axial)

(c) Time Domain (Vertical)

(d) Frequency domain (Vertical)

(e) Time Domain (Horizontal)

(f) Frequency domain (Horizontal)

Figure 7.35: Load side acceleration results (Configuration 4 - Test 1)

The axial vibrations do not seem to vary significantly at a friction coefficient of 0.07 when axial friction is included; however it is found that when the friction

coefficient is increased further to 0.5, axial friction does have a more profound effect on the axial vibrations. Figure 7.36 shows the axial vibrations on both the load and motor side at a friction coefficient of 0.5, for cases where axial friction is and is not accounted for.

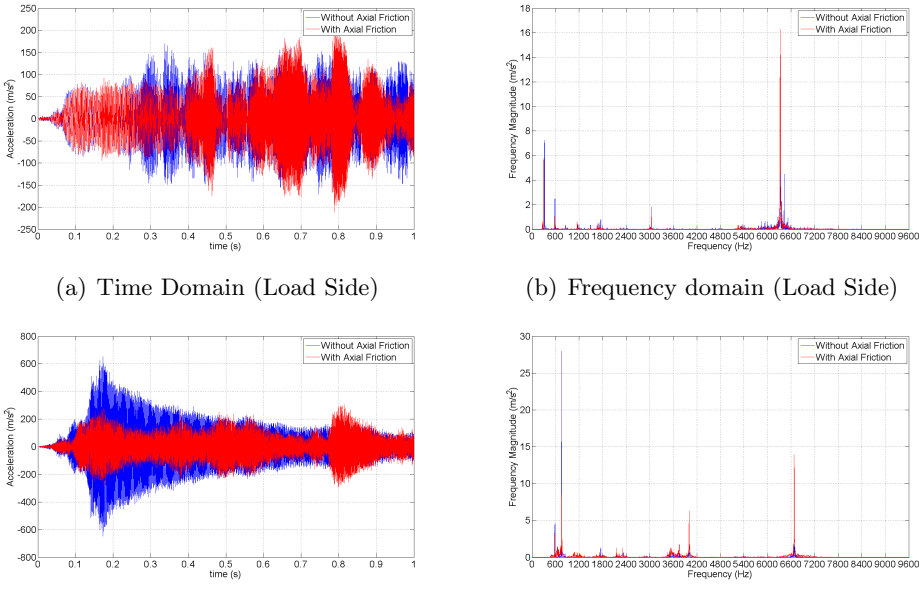

(a) Time Domain (Load Side)

(b) Frequency domain (Load Side)

(c) Time Domain (Motor Side)

(d) Frequency domain (Motor Side)

Figure 7.36: Axial acceleration results (Friction Coefficient = 0.5)

Figure 7.36 shows that the axial friction has a large effect on the axial vibration, where at a friction coefficient of 0.5 the axial vibrations are greatly reduced. It can also be seen that the effects on the motor side are much greater than on the load side, due to the reduced axial stiffness of the shaft assembly caused by the coupling. In the frequency domain there is also variation in the most significant frequencies, which are thought to be due to the variation in the shaft rotation speeds and the coupling stiffness.

Although axial friction has been shown to have an effect on the axial vibration, a friction value of 0.5 is unreasonably high and is only selected to demonstrate an extreme scenario.

Further results for friction coefficient values of 0.07 (ref Test 1), 0.1 (ref Test 2) and 0.5 (ref Test 3) are omitted here, however these can be found in the Digital

Appendix and show similar trends to Figures 7.35 and 7.36.

7.4.2 Friction Reference Velocity

Next the effect of axial friction is studied where the frictional reference sliding velocity is changed. Figure 7.37 shows the effect of the axial friction for a reference velocity of 0.01 m/s and a friction coefficient of 0.07. Again the effect of axial friction is to reduce the magnitude of the vertical and horizontal vibrations. In the frequency domain this is found to be mainly due to reductions in the non-mesh frequency peaks in the vertical DOF and the first three harmonics in the horizontal direction.

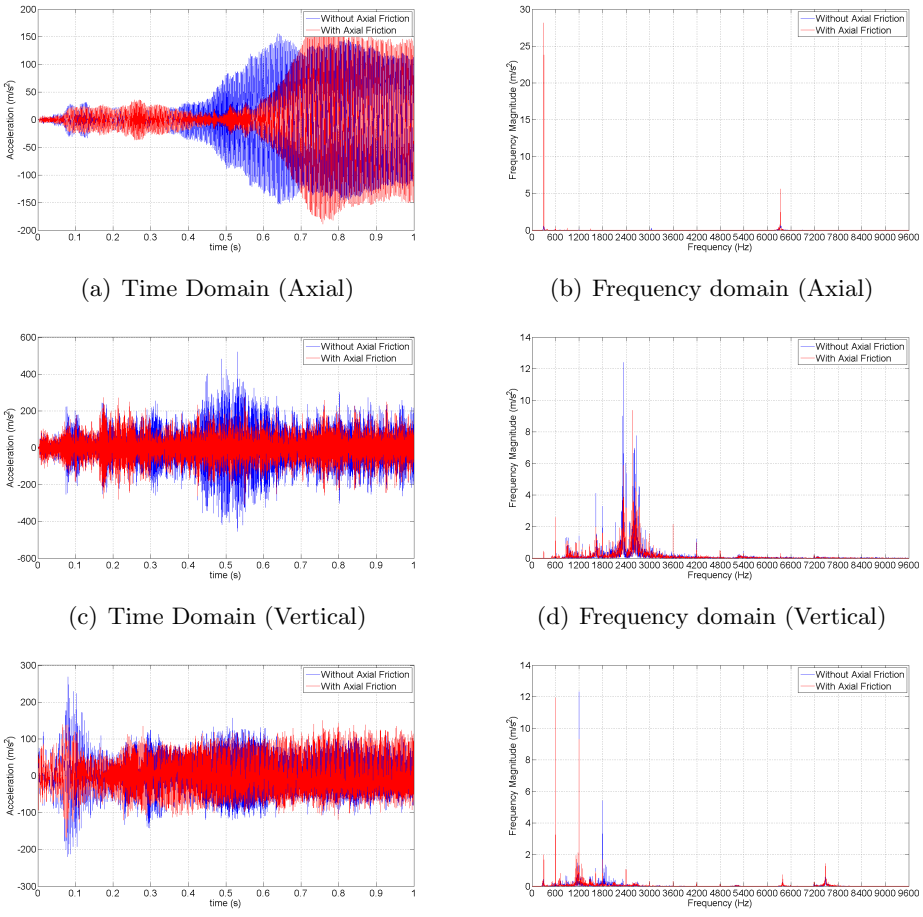

(a) Time Domain (Axial)

(b) Frequency domain (Axial)

(c) Time Domain (Vertical)

(d) Frequency domain (Vertical)

(e) Time Domain (Horizontal)

(f) Frequency domain (Horizontal)

Figure 7.37: Load side acceleration results (Configuration 4 - Test 2)

The effects of axial friction on the vibratory response of the system is mainly seen in the vertical direction, which can be attributed to the length of the moment

arms about the gear centre. Due to the geometry of the gears the distance between the contact point and the vertical axis of the gears is much larger than the distance between the contact point and their horizontal axis, as shown in Figure 6.14. This means that the moment induced about the vertical axis is greater than the horizontal axis, for a given axial force.

Further results for reference velocities of 0.01 (ref Test 4) and 1 m/s (ref Test 5) can be found in the Digital Appendix, which show similar results when compared to Figure 7.37.

7.4.3 Conclusions

In this section the model defined in Configuration 3 is additionally forced in the axial direction as a result of the friction force generated through axial sliding. This introduces lateral forces along the shaft axis and moments about the gear vertical (U2) and horizontal (U3) axes.

The inclusion of axial friction has been shown to reduce the overall magnitude of the vibrations in the horizontal and vertical directions. This was attributed to the resistive moments caused at the mesh as a result of axial friction. In the axial direction the vibrations were shown to decrease due to the resistive axial forces; these were more pronounced at higher friction coefficients and on the motor shaft, since the inclusion of the coupling reduced the axial stiffness of the shaft assembly.

7.5 Configuration 5

In Configuration 5 the current lateral-torsional model is further expanded to include the effects of the lateral system misalignments during operation. These have effects on the system through the variation of the contact conditions as described in Section 6.4.

Initially the effects of the dynamic misalignments on the system accelerations are investigated and compared against previous results, then additional misalignment is applied in the form of axial and radial misalignment. From this the effects of imposed misalignment can be judged.

7.5.1 Dynamic Misalignment

The torsional-lateral model presented in Configuration 4, including normal contact and frictional excitation, is initially investigated to allow the motion of the gear centres to impact on the gear contact conditions. Stiffness and damping properties remain as those given in Table 7.25, with a friction coefficient of 0.07 and a reference sliding velocity of 0.1 m/s.

Figure 7.38 compares the load side bearing accelerations for when the system assumes ideal contact throughout the simulation to the scenario where the system equations are a function of the instantaneous contact conditions.

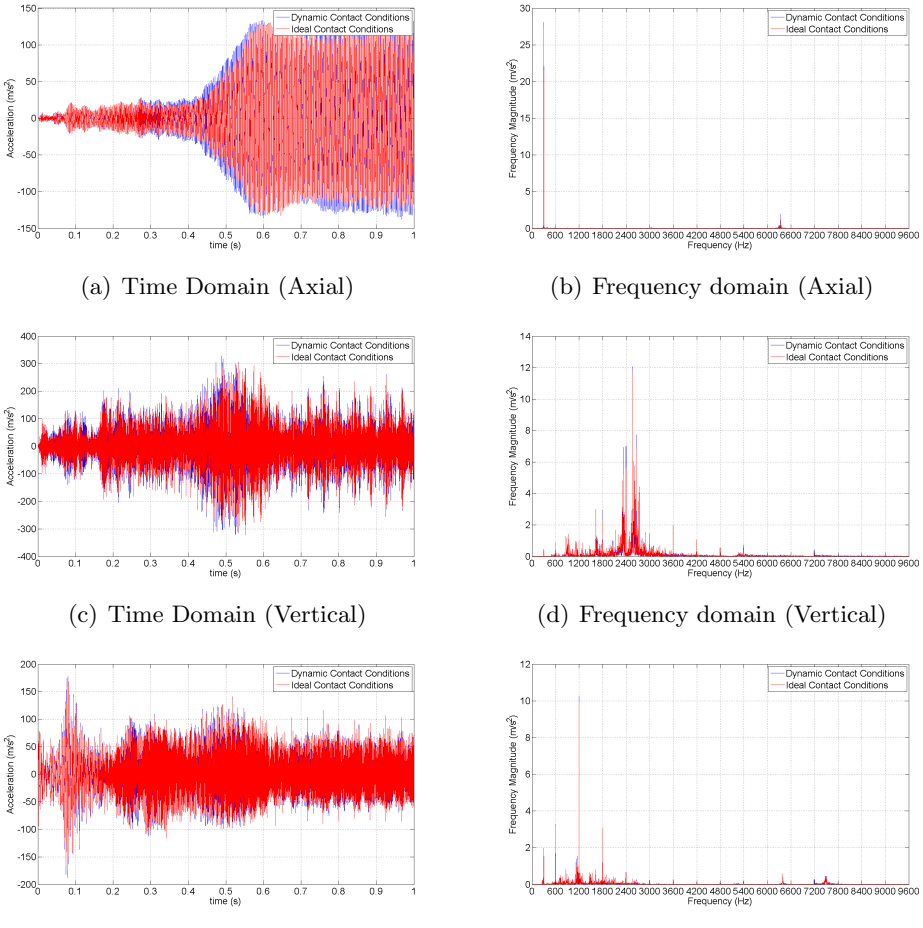

(a) Time Domain (Axial)

(b) Frequency domain (Axial)

(c) Time Domain (Vertical)

(d) Frequency domain (Vertical)

(e) Time Domain (Horizontal)

(f) Frequency domain (Horizontal)

Figure 7.38: Load side acceleration results (Configuration 5 - Test 1)

From the results in Figure 7.38 it can be seen that by allowing the con-

tact conditions to vary throughout the simulation there is a slight increase in the magnitude of vibrations on the load side shaft. Table 7.26 shows the RMS values for the lateral vibrations, which indicate that, on the load side shaft, the dynamic conditions tend to increase the vibrations in all directions. It could be argued that with the variation in the radial misalignment (0.163 mm) and therefore the pressure angle, which during simulation had a mean of 20.2078°, the vertical accelerations should have decreased on the load side; however the decrease in the vertical load as a result of the pressure angle variation (0.133%) could be offset by the increases in peak-to-peak mesh stiffness demonstrated in Section 4.2.2 Figure 4.12, as a result of radial misalignment.

This trend, where the vertical accelerations increase, is not seen on the motor side, which could be due to the inclusion of the coupling or the difference in the support stiffness when compared to the load side. Instead the vertical accelerations decrease and the horizontal accelerations increase, as would be expected when considering the change in pressure angle in isolation.

	RMS Accelerations (m/s^2)					
	Load Side			Motor Side		
	A1	A2	A3	A1	A2	A3
Ideal	54.2	70.8	39.0	20.1	65.6	45.2
Dynamic	57.2 (5.5%)	72.6 (2.6%)	40.1 (2.8%)	19.1 (-4.9%)	64.4 (-1.8%)	47.1 (4.2%)

Table 7.26: Configuration 5 - Test 1 RMS Values

The increases in the time domain RMS values on the load side are attributed to slight increases in the first and second harmonics (600 and 1200 Hz) in the horizontal DOF. In the vertical DOF the increases are attributed to the third and fourth harmonics (1800 and 2400 Hz).

Another noticeable fact from the RMS values in Table 7.26 is that the axial vibrations on the motor side are much reduced when compared to the load side. This could be attributed to the decreased axial stiffness of the coupling, which tends to reduce the reactive stiffness force in the shaft and hence the accelerations.

7.5.2 Imposed Axial Misalignment

In this section axial misalignment is applied to the system prior to simulation to determine its effects on the system vibrations. Identical mass, stiffness, damping and frictional parameters to those used in Configuration 5 Test 1 are applied with misalignment values summarized in in Table 7.27.

	Test 2a	Test 2b	Test 2c	Test 2d
Axial Misalignment (mm)	0.25	0.50	1.00	2.50

Table 7.27: Configuration 5 - Test 2 Misalignment Values

Figure 7.39 illustrates the effect of axial misalignment on the load side bearing vibrations. From these results it can be determined that axial misalignment has little effect on the system vibrations.

Taking a maximum misalignment of 2.5 mm, the axial misalignment moments can be calculated under the quasi-static loads as per Equation 6.56. In this calculation the normal load is based on an applied axial torque of 100 Nm (1703 N) and the frictional force is based on single tooth contact with a friction coefficient of 0.07 (119 N). Under these loads the calculated torques are 0.59 Nm about the vertical axis and 2.05 Nm about the horizontal axis, which are insignificant when compared against the applied torque.

Table 7.28, which shows the RMS values for the simulations given in Figure 7.39, further corroborates the conclusion that axial misalignment has little effect on the bearing vibrations. From the RMS values it can be seen that even at 2.5 mm axial misalignment, the RMS vibrations only vary by a maximum of around 5%. In the results it is again noticed that variations in the axial misalignment have a greater impact on the load side bearings when compared to the motor side shaft, which could be explained through variations in the stiffness and mass properties on either side.

7.5.3 Imposed Radial Misalignment

The final aspect of the parametric investigation is to apply radial misalignment to the system. Again system damping and stiffness parameters remain the

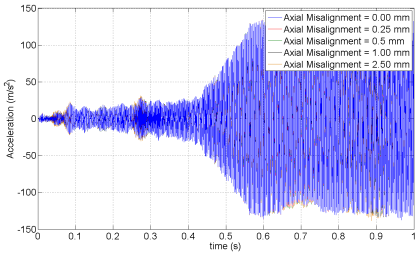

(a) Time Domain (Axial)

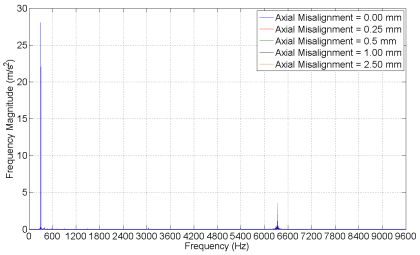

(b) Frequency domain (Axial)

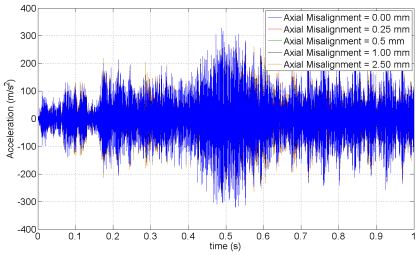

(c) Time Domain (Vertical)

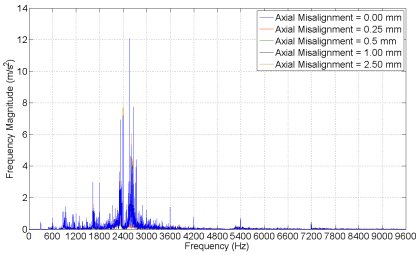

(d) Frequency domain (Vertical)

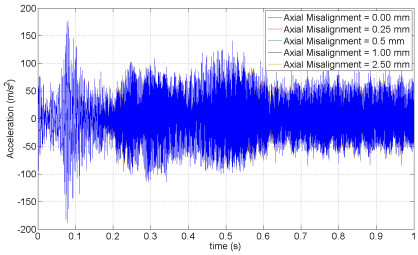

(e) Time Domain (Horizontal)

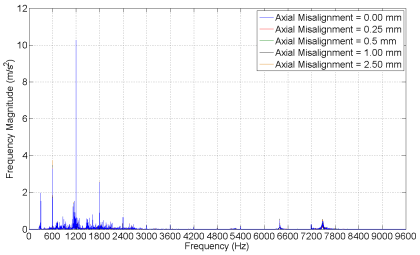

(f) Frequency domain (Horizontal)

Figure 7.39: Load side acceleration results (Configuration 5 - Test 2)

same, as do the frictional properties, while radial misalignments are varied up to 0.75 mm as shown in Table 7.29. These values are restricted by the mesh stiffness dataset produced in Section 4.2.2, which had a range of 0 -1 mm radial misalignment. The maximum value must also allow some additional dynamic misalignment, which under dynamic misalignment and zero imposed misalignment equaled roughly 0.163 mm.

Time and frequency domain results, given in Figure 7.40 for the load side acceleration, show that radial misalignment has a greater effect on the bearing accelerations when compared to axial misalignment.

Table 7.30 summarizes the RMS values for the load and motor sides for the three misalignment cases, and compares them to simulation results with no imposed

	RMS Accelerations (m/s^2)					
	Load Side			Motor Side		
	A1	A2	A3	A1	A2	A3
Test 1	57.2	72.6	40.1	19.1	64.4	47.1
Test 2a	56.8 (-0.61%)	72.5 (-0.25%)	39.9 (-0.42%)	19.1 (-0.40%)	64.3 (-0.08%)	47.1 (0.03%)
Test 2b	56.5 (-1.19%)	72.2 (-0.55%)	39.8 (-0.85%)	19.0 (-0.81%)	64.3 (-0.16%)	47.1 (0.06%)
Test 2c	55.8 (-2.36%)	71.8 (-1.17%)	39.4 (-1.66%)	18.8 (-1.76%)	64.2 (-0.38%)	47.1 (0.12%)
Test 2d	53.8 (-5.89%)	71.4 (-1.76%)	38.5 (-4.10%)	18.6 (-2.59%)	64.0 (-0.67%)	47.2 (0.29%)

Table 7.28: Configuration 5 - Test 2 RMS Values

	Test 3a	Test 3b	Test 3c
Radial Misalignment (mm)	0.25	0.50	0.75

Table 7.29: Configuration 5 - Test 3 Misalignment Values

misalignment.

With an initial misalignment of 0.25 mm the bearing accelerations increase across the load side shaft, which is seen to follow the trend presented in Table 7.26, where progressing from zero misalignments to a degree of dynamic misalignment increased the bearing accelerations on the load shaft. It was previously suggested that this was as a result of variation in the peak-to-peak mesh stiffness, as shown in Section 4.2.2 Figure 4.12, where the reduction in mesh stiffness was accompanied with an increase in peak-to-peak mesh siffness of around 6% across the misalignment range. This could lead to increases in the vibrations at the bearings; however with

	RMS Accelerations (m/s^2)					
	Load Side			Motor Side		
	A1	A2	A3	A1	A2	A3
Test 1	57.2	72.6	40.1	19.1	64.4	47.1
Test 3a	63.4 (11.0%)	74.4 (2.4%)	40.9 (2.0%)	16.3 (-14.7%)	85.4 (32.6%)	50.5 (7.3%)
Test 3b	65.9 (15.4%)	74.0 (1.8%)	41.1 (2.6%)	13.6 (-29.1%)	89.0 (38.2%)	56.1 (19.2%)
Test 3c	68.3 (19.6%)	71.5 (-1.6%)	41.5 (3.6%)	13.0 (-32.2%)	84.2 (30.7%)	60.9 (29.4%)

Table 7.30: Configuration 5 - Test 3 RMS Values

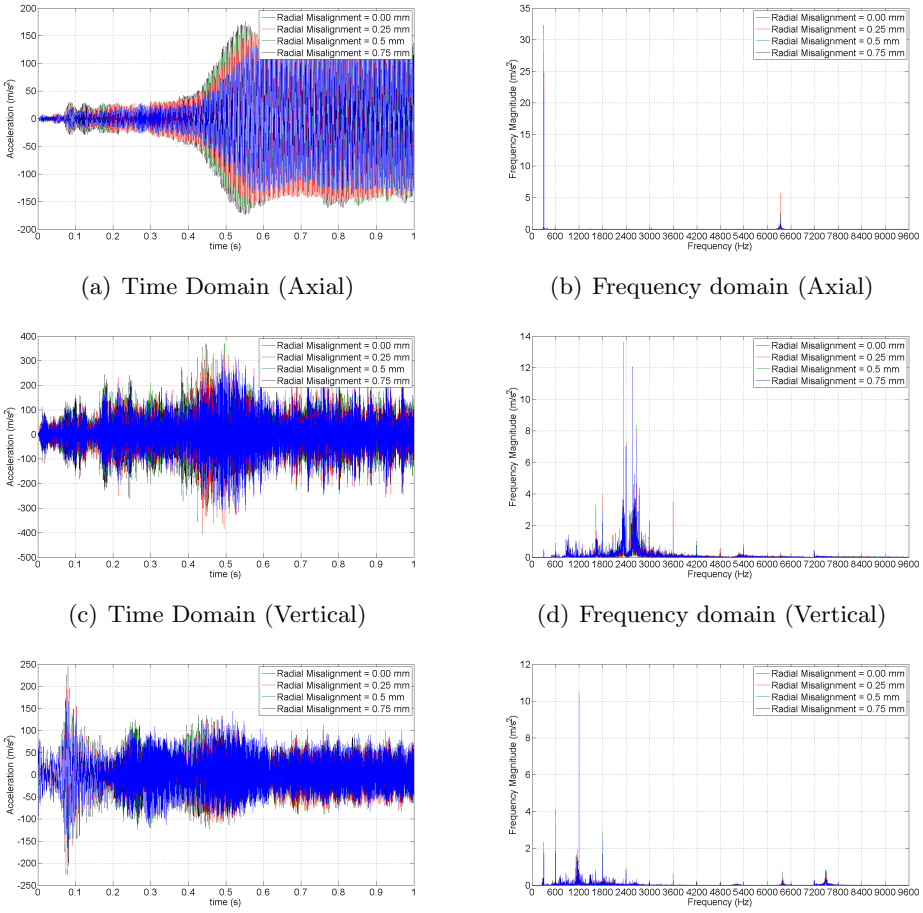

(a) Time Domain (Axial)

(b) Frequency domain (Axial)

(c) Time Domain (Vertical)

(d) Frequency domain (Vertical)

(e) Time Domain (Horizontal)

(f) Frequency domain (Horizontal)

Figure 7.40: Load side acceleration results (Configuration 5 - Test 3)

increased radial misalignment the increases in peak-to-peak mesh stiffness are offset in the vertical direction by the alteration in the pressure angle.

As the radial misalignment is increased, the load side bearing accelerations in the vertical DOF are found to decrease, while the horizontal accelerations are found to increase. This, as previously suggested, is thought to occur through changes in the dynamic contact angle. As witnessed in Test 1, the increases in the frequency domain results for the horizontal DOF (Figure 7.40(f)) are shown to occur at the first two mesh harmonics (600 and 1200 Hz), while again the variation in the vertical accelerations is seen to occur around the 3rd and 4th mesh harmonic (1800 and 2400 Hz). In the vertical DOF additional increases are seen at 3600 Hz for a radial misalignment value of 0.25 mm; however the reasoning behind this is currently not

understood.

Referring to the motor side RMS results given in Table 7.30, it can be seen that, along with the load side results, the introduction of 0.25 mm of radial misalignment tended to increase the magnitude of vibration, especially in the vertical DOF. This does not follow the trend as described in Table 7.26, where the introduction of dynamic misalignment caused the RMS value to decrease. With the multitude of forcing effects it is difficult to pinpoint the reason behind this variation, and more work would be required to assess this phenomena and determine its validity.

The increase in RMS value for the vertical accelerations continues for a radial misalignment of 0.5 mm; however at 0.75 mm the magnitude of vibration decreases, which is as should be expected with the changes in pressure angle. For the horizontal accelerations, it is seen that with increased radial misalignment the magnitude of vibration continues to increase, which again is expected with the changes in pressure angle.

7.5.4 Conclusions

Initially in this section the contact conditions were allowed to vary depending on the degree of lateral misalignment. This influences the system vibrations through variations in the forces generated during contact, along with variations in the contact angle, mesh stiffness and contact ratio. These lead to changes in the normal contact force and frictional forces, along with how these forces are decomposed into the global coordinate system.

When comparing simulations with and without the effects of the instantaneous contact conditions, it was found that the introduction of these effects increased the RMS values of the load side vibrations. It was believed that this was due to the introduction of greater radial misalignment, which, as described in Section 4.2.2, would lead to increases in the peak-to-peak mesh stiffness. This was believed to have a greater effect on the vertical vibrations than the increase in the contact angle as a result of radial misalignment; however this was not true on the motor side shaft, where the vertical accelerations were found to decrease.

From the load side frequency domain results, increases in the RMS values were attributed to greater peaks in the first two harmonics (600 and 1200 Hz) for the horizontal accelerations, and greater peaks around the third and fourth harmonics (1800 and 2400 Hz) for the vertical accelerations.

Next axial misalignment was imposed on the system, and results showed that axial misalignment had only a minor effect on the vibrations, even up to values of 2.5 mm. RMS values were shown to vary by up to only 6% across the misalignment range.

Finally radial misalignments up to 0.75 mm were applied to the gears, and showed that as misalignment is increased the effects are generally to increase the vibrations across all DOF through increases in the peak-to-peak mesh stiffness. However at radial misalignment values greater than 0.5 mm the RMS values for the vertical DOF tended to reduce as a result of variations in the pressure angle.

7.6 Conclusions

In this chapter parametric studies have been performed on various configurations of the proposed model, with varying degrees of complexity. Initially a purely torsional model was investigated with only normal contact forces. This was used to investigate the effects of the coupling between the motor and shaft, and also the damping values assigned to the coupling, shafts and gears. This torsional model was later expanded to investigate the effects of friction and suitable damping and friction values were assigned.

Next the model was expanded to include lateral vibrations, which introduced additional stiffness and mass terms for the bearings and supports. This model was used to further investigate the effects of the component stiffness and damping values.

In the proceeding configurations the gear contact model was expanded to include various friction effects and allow changes to the instantaneous contact conditions. Initially the model was expanded to include the effects of normal sliding friction, which had a large effect on the magnitudes of vibration through the addition of forces perpendicular to the normal contact forces. These increases had the

greatest impact in the horizontal direction due to the decomposition of the friction forces into the global coordinate system, and were shown to be primarily associated with the first three gear mesh harmonics in the frequency domain (600, 1200 and 1800 Hz).

The friction model was then expanded to include the effects of axial friction, which as yet has not been included in any previous work on gear dynamics. This tended to reduce the overall magnitude of vibration as it introduced a further resistive force to gear deflection.

Finally the effects of misalignment were investigated. It was found that axial misalignment tended to have minimal effect on the vibrations in all DOF, with variations in RMS values equal to a maximum of 6% in the axial direction, under misalignment of 2.5 mm. Radial misalignment was found to have a greater impact, where increased radial misalignment changed the peak-to-peak mesh stiffness and tended to increase the RMS value of acceleration. This was combined with changes in the average mesh stiffness and the contact angle. This tended to decrease the forces and accelerations present in the vertical DOF and increase those in the horizontal; however due to the interaction between these effects it was not possible to determine an absloute correlation between the radial misalignment and the accelerations in each DOF.

Chapter 8

Results: Experimental

In Chapter 7 the hybrid dynamic model was modified and varied to understand the effects of the various system parameters. The majority of the parameters pertaining to the off-the-shelf components have been determined through the sales literature, and some parameters have been calculated through the use of finite element analysis and finite element technique. There are however some parameters which are still unknown, with the most prominent being the damping factors applied to the various system components, and the lateral and bending stiffnesses of the coupling.

In this chapter experimental results gained from the test rig at Cranfield University are used to both assume suitable parameter values and corroborate the simulated results.

Initially suitable parameters are determined from the aligned experimental results and similarities between the simulated and experimental results are discussed. Next experimental results for applied axial and radial misalignments are assessed and trends are compared to those witnessed in the simulated data.

8.1 Aligned Results

Through observing the aligned experimental results given in Figures 8.1 and 8.3, and assessing the various impacts of the system parameters discussed in the previous chapter, appropriate damping and frictional parameters were chosen. These are given in Table 8.1.

Damping Values					Friction Values	
Coupling	Shaft	Bearings	Supports	Mesh	μ	$V_0(m/s)$
1e-4	1e-12	1e-4	1e-6	1e-6	0.02	0.5

Table 8.1: Simulation Parameters

It is also noted that stiffness and mass properties are as per Chapters 5 and 6, and Appendix F, with the exception of the coupling, which has stiffness properties as per Table 8.2. In Table 8.2 kx and kα represent the lateral and angular stiffnesses along and about the shaft axis respectively, while ky and kβ act along and about the vertical axis, and kz and kγ act along and about the horizontal axis.

kx	ky	kz	kα	kβ	kγ
1e6 N/m	1e6 N/m	1e6 N/m	2.363e4 Nm/rad	2e4 Nm/rad	2e4 Nm/rad

Table 8.2: Coupling Stiffness

Initially the load side bearing vibrations are assessed (Figures 8.1 and 8.2) and it can immediately be seen that the simulated results are much lower in magnitude than the experimental results. Table 8.3 shows the RMS values for both the experimental and simulated accelerations for the load and motor side bearings, which shows that on the load side, the simulated vertical and horizontal acceleration RMS values are 3.8 and 5.5 times lower respectively when compared to the experimental values. It is also found that the axial accelerations are around 33 times lower.

	RMS Accelerations (m/s^2)					
	Load Side			Motor Side		
	A1	A2	A3	A1	A2	A3
Experimental	41.13	58.38	37.45	117.64	103.55	74.67
Simulated	1.24	15.20	6.86	2.32	30.62	9.46

Table 8.3: Aligned RMS Values

It is believed that this is due to four main factors. Firstly the coefficient of friction is lower than expected in gear contact, since in experiments performed by Rebbechi *et al* [50], the static lubricated friction coefficient was measured at 0.067 and the dynamic coefficient was measure at 0.063 at 800 rpm and 0.04 at 6000

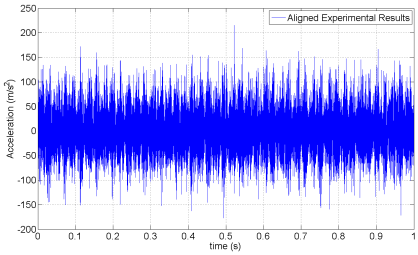

(a) Time Domain (Axial)

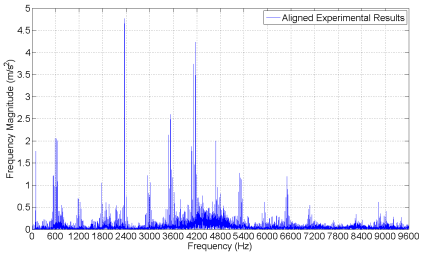

(b) Frequency domain (Axial)

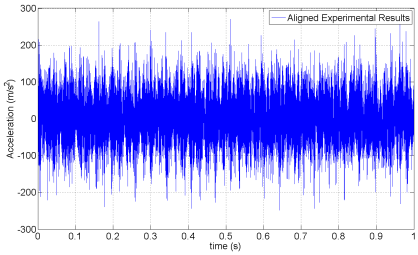

(c) Time Domain (Vertical)

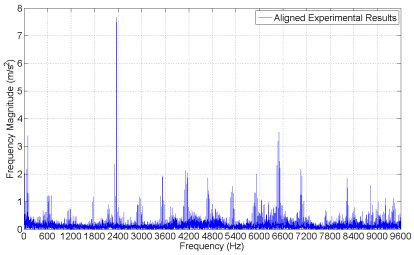

(d) Frequency domain (Vertical)

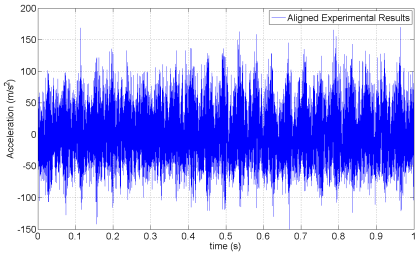

(e) Time Domain (Horizontal)

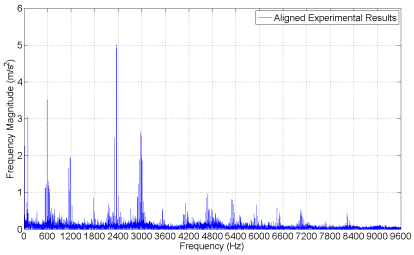

(f) Frequency domain (Horizontal)

Figure 8.1: Load side acceleration results (Experimental - Aligned)

rpm. The reasoning behind the use of the lower friction value is that in the frequency domain the higher frictional forces increase the influence of the first three harmonics, as described in Chapter 7, and dwarf the higher harmonics, which in Figure 8.1 are shown to be important. The increased friction coefficient would have a large impact on the axial vibrations, through the additional axial friction forces, which would be expected to increase more than the vertical and horizontal vibrations.

Secondly it is believed that the damping values employed at the supports are too large. The support damping value of 1e-6 was chosen to ensure a settled response was achieved in a suitable time frame, when the step input of the motor and load torques were applied. If the support damping was decreased this transient period would have increased resulting in a lengthy simulation before an appropriate

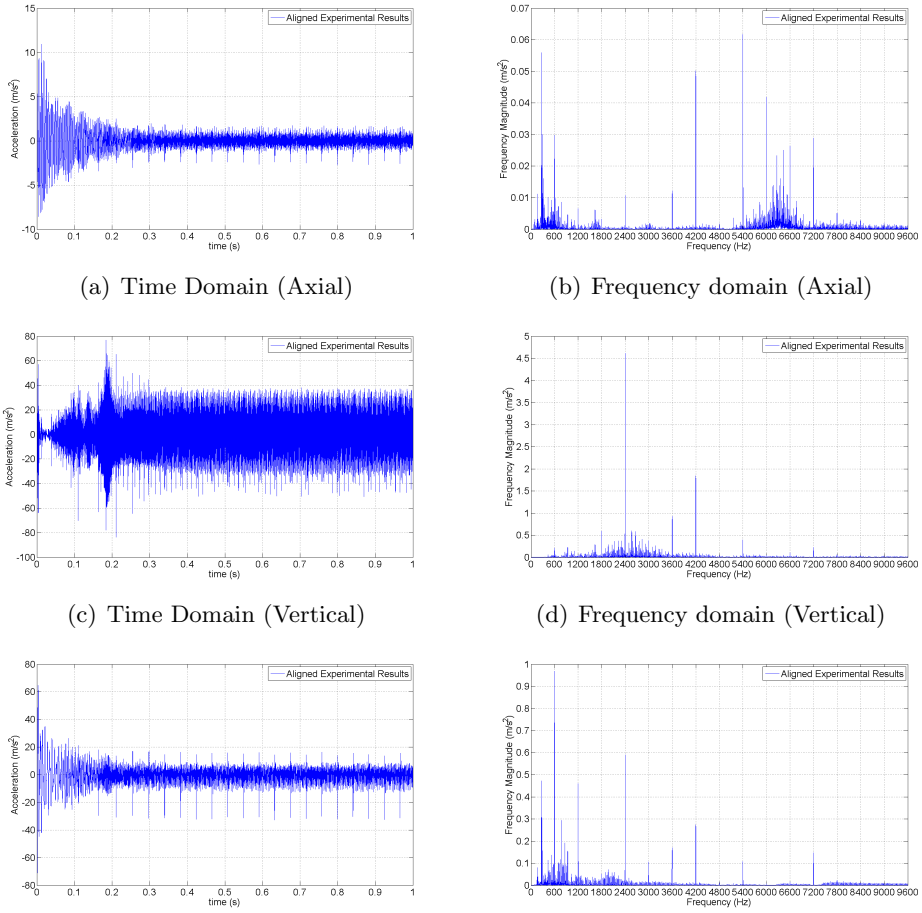

(a) Time Domain (Axial)

(b) Frequency domain (Axial)

(c) Time Domain (Vertical)

(d) Frequency domain (Vertical)

(e) Time Domain (Horizontal)

(f) Frequency domain (Horizontal)

Figure 8.2: Load side acceleration results (Simulated - Aligned)

response was seen. The disadvantage of this approach is that the magnitudes of vibration resulting from varying mesh stiffness, bearing stiffnesses, motor torque fluctuations and dynamic misalignments are reduced in the settled response. This is evident in the frequency domain, where the higher order mesh harmonics are greatly reduced in the simulated results, when compared to their influence in the experimental results.

The third possible reasoning behind the increased magnitude of vibrations could be due to additional forcing within the system. In the simulated results, the model does not account for possible component imbalances, such as along the shaft and at the gears, which would cause vibrations at once per shaft revolution. These are seen in the experimental frequency domain as side bands to the main

mesh frequencies at 24 Hz intervals; however these components are not seen in the simulated results. There is also the possibility of errors in the gears, since the gears were manufactured to a low ISO grade. These errors could manifest themselves as deviations from the perfect involute, or through spacing errors and would lead to increased gear vibrations. As previously explained, this could be included into the model through the unloaded transmission error, which acts as a linear displacement along the line of contact; however since details of the actual gear profile were unknown, this source of vibration was omitted. The final additional source of vibration could be attributed to alignment error, which can never be assumed perfect.

The fourth source of error could be the datum used in the modelling. In the simulated results the datum plane was assumed on the foundation plate for the load side and the movable plate for the motor side. It is known that the foundation was not perfectly rigid and therefore its stiffness could have contributed to the vibration more than imagined. To determine its effects accelerometers would have to be mounted to the base to determine its vibration under operation.

The fifth possible reason behind the variations in acceleration values could be the increased stiffness of the shaft as a result of shear locking. This could lead to smaller deformations and accelerations of the shafts and bearings. This was ruled out in the static results by comparison to finite element models in Chapter 6, however to have 100% confidence that this is not influencing the results it is believed that different shaft models, including a component mode synthesis representation of the shaft, should be used to determine it effect.

By observing the frequency domains of the three lateral vibrations, it can be seen that some of the major peaks in the experimental results are predicted in the simulations. In all DOF the major peaks in the experimental results occur at multiples of the gear mesh frequency; these are slightly offset from the ideal frequency at 1500 rpm (600 Hz), mainly due to the realised motor speed, which is less than predicted.

In the axial direction major peaks are seen at 600, 2400 and 4200 Hz, with

other large peaks at 3600 and 4800 Hz. In the simulated results the peaks at 600 and 4200 Hz are well defined, however the other peaks are not as large (relatively) when compared to the experimental results. It is believed that this is due to the assumption the the dynamometer is rigidly connected to the shaft, which is not true, since a bespoke coupling was used to connect the dynamometer to the shaft. This would have different stiffness characteristics when compared to the modelling assumptions. By looking at the simulated motor side results in Figure 8.4, where a representation of the curved jaw coupling was included between the motor and shaft, it can be seen that the peak at 3600 Hz is increased. It is believed that the peaks at 2400 Hz and 4800 Hz could be attributed to the damping and lack of forcing in the axial direction, since in the vertical and horizontal results the peak at 2400 Hz is clearly seen; however the peak at 4800 Hz, which is a multiple of 2400 Hz, is not recreated in any results. It is believed that the high damping results in this higher frequency term being damped out. The lack of a coupling between the shaft and the dynamometer could also account for the large difference between the simulated and experimental axial accelerations, which are much greater than in any other direction.

To obtain better representation of the axial vibrations the damping of the system would need to be reduced, and a better understanding of the stiffness properties of the coupling would be required.

In the simulated axial results the peak at 5400 Hz has already been shown to be attributed to the bearings, which is most likely an interaction between the number of rolling element bearings (9) and the mesh frequency (600 Hz). Further higher frequency terms are seen between 6600 and 7200 Hz, which have been shown in the parametric study to be due to the supporting structure, and hence it is believed that over time these peaks would reduce. Alternatively it could be argued that the assumptions made in the modelling of the supports was incorrect, since pretension in the bolts holding the bearings to the supports could affect the support stiffness. Also the omission of the foundations could also have an impact on the support stiffness and mass properties, and a full analysis of the structure would be

required to determine this.

In the vertical direction, the major peak at 2400 Hz seen in the experimental results is predicted in the simulation; however the peak at 4200 Hz is overestimated in relation to the other peaks in the simulated results. It is also seen that beyond 4200 Hz the influence of the mesh harmonics is diminished, which is again believed to be due to the high damping used to obtain a settled response in the required simulation time. An elevated peak at 6600 Hz is seen in the experimental results, which has been attributed to the supports.

In the horizontal acceleration the peak seen at 2400 Hz in the simulated results is again corroborated with the experimental results; however the primary meshing frequency at 600 Hz is more dominant in the simulated results when compared against the experimental results. The primary meshing frequency has been found to be highly sensitive to the friction coefficient in the horizontal direction due to the direction of the friction force, which has previously been given as a reason behind the selection of the low friction coefficient. It may be possible to control the influence of this frequency through appropriate damping values, and with decreased system damping it could be possible to bring this in line with the other peaks.

Turning attention to the motor side results it can again be seen that the experimental results are generally larger than the simulated results, which are attributed to the modelling approach, friction values and damping values, as previously described.

In the axial direction the time domain response of the experimental results is found to behave in a strange manner, where accelerations in the negative direction are much greater than in the positive direction. This is explained by the lack of any real tensile stiffness of the coupling, which is not modelled in the simulated results; this means that the stiffness and hence resistance to motion in one direction is less than the other. In the frequency domain of the experimental results the main peaks are seen at 600, 2400, 4200 and 4800 Hz, whereas in the simulated results major peaks are found at 600, 2400, 3600 and 4200 Hz, with an additional bearing frequency at 5400 Hz. The variation in the higher peaks (3600 - 4800 Hz)

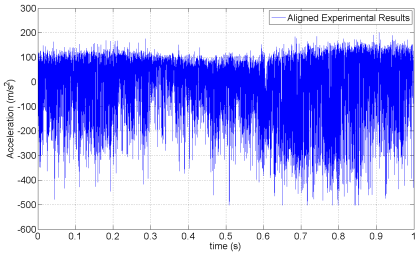

(a) Time Domain (Axial)

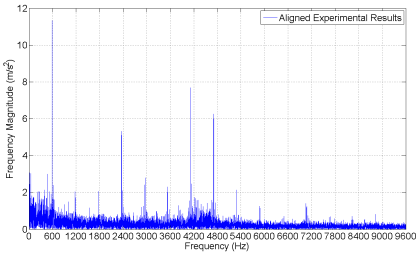

(b) Frequency domain (Axial)

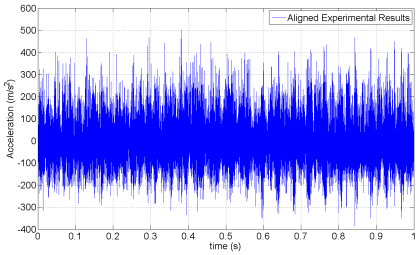

(c) Time Domain (Vertical)

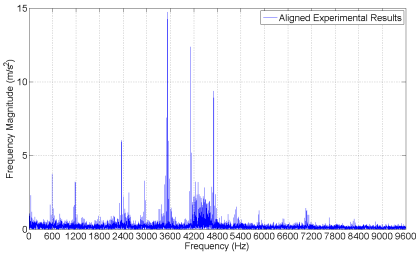

(d) Frequency domain (Vertical)

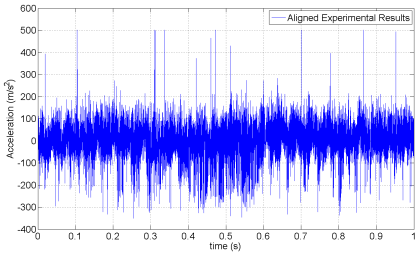

(e) Time Domain (Horizontal)

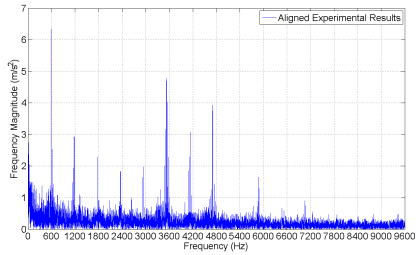

(f) Frequency domain (Horizontal)

Figure 8.3: Motor side acceleration results (Experimental - Aligned)

can be attributed to the modelling of the coupling, where it has been shown in the parameteric study the variation of the coupling stiffness has a major influence on the peak at 3600 Hz, especially under underdamped conditions.

It is noted that the experimental acceleration results are much greater than would be expected, and 50 times greater than those simulated. Since the bearings and coupling offer little axial support it could be envisaged that the introduction of any alternating axial load would result in extreme vibration along the shaft and against the coupling.

Further influence at 2400 and 4800 Hz could be attributed to the time invariant nature of the coupling stiffness. In a paper by Saavedra and Ramírez [113] the lateral stiffness of a curved jaw coupling (3 jaws) was measured at different rota-

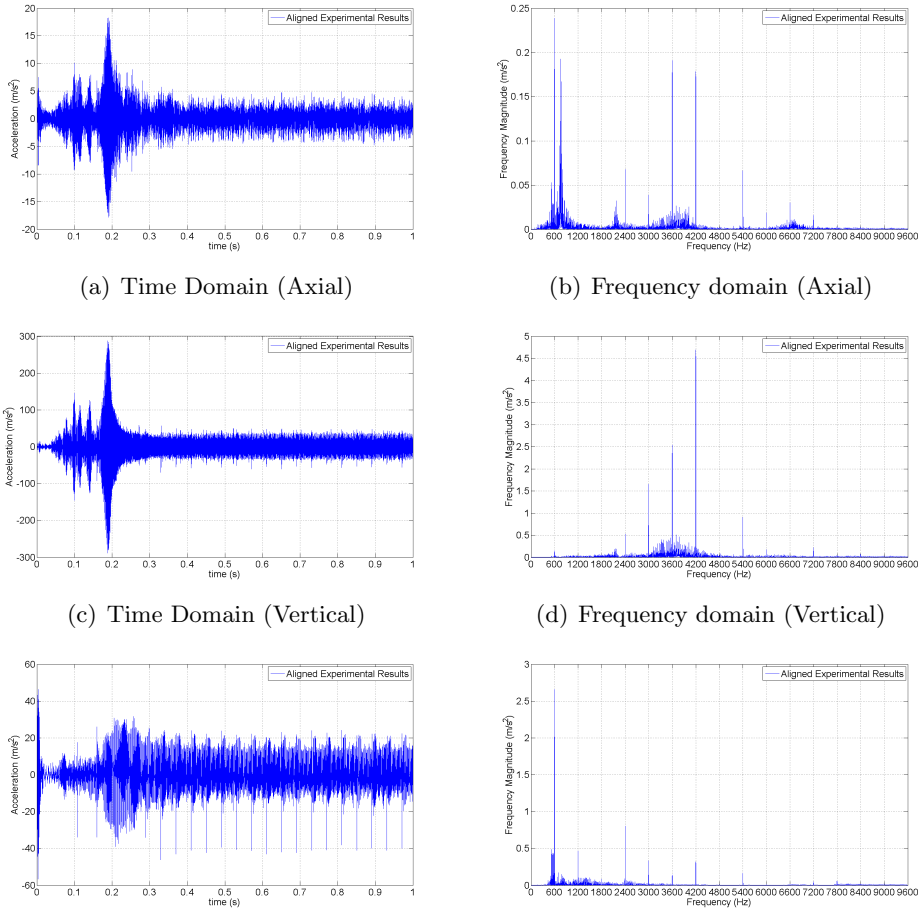

(a) Time Domain (Axial)

(b) Frequency domain (Axial)

(c) Time Domain (Vertical)

(d) Frequency domain (Vertical)

(e) Time Domain (Horizontal)

(f) Frequency domain (Horizontal)

Figure 8.4: Motor side acceleration results (Simulated - Aligned)

tional positions. They found that the coupling stiffness was periodic at three times the rotational speed. In this installation the curved jaw coupling has 4 jaws and therefore it is possible that interaction between the varying stiffness (4 per rotation) and the mesh frequency (600 Hz) results in peaks at 2400 Hz and 4800 Hz (2 * 2400 Hz). To determine the validity of this theory the test would need to be rerun with a coupling with a different number of jaws.

In the vertical acceleration results peaks are again seen in the region 3600 - 4800 Hz, which are attributed to the coupling. These are seen in both the experimental and simulated results, with the exception of the peak at 4800 Hz for the simulated results, which has been explained. The magnitude of the primary meshing frequencies is found to be relatively low in the simulated results when compared

against the other frequencies, which could be due to the low friction values, or the over exaggeration of the higher frequencies.

In the horizontal direction the frequency peaks in the simulated results are relatively comparable to the experimental results, with the exception of the peaks at 2400 and 3600 Hz. The main problem lies with the overall magnitude of the peaks, where in the simulated results these are much less than the experimental results. As previously explained, this could be overcome with a greater friction coefficient and lower system damping; however these would result in longer simulation times before a steady state value was reached.

8.2 Axial Misalignment

To measure the effects of axial misalignment a spacer was inserted on the shaft, which induced a large axial misalignment of 8.76 mm. This may give some indication of the axial misalignment effects; however no correlation between the degree of axial misalignment and its effect on the system accelerations can be determined. To achieve a better understanding further investigations over the range of misalignments would be required.

It is noted here that an 8 mm misalignment would not occur as a result of poor installation or through the dynamic displacement of the shafts; however an offset between the pinion and gear is often prescribed in some applications, which could be of this order of magnitude.

Looking at the load side results in Figure 8.5 and the RMS values in Table 8.4, it can be seen that under this large misalignment the axial vibrations are increased slightly, which mainly occurs through increases in the frequency domain at 600, 1800 and 2400 Hz. These increases could be attributed to the increased tilting at the gear mesh and the slight increase of axial load, which results from this, as described in Section 4.2.3. Another possibly cause could be the reduction in mesh stiffness as a result of axial misalignment, and hence the reduced contact area, described in Section 4.2.3. This effect was omitted in the simulation due to its minor variation over the dynamic misalignment range; however at almost 9 mm (60% along the

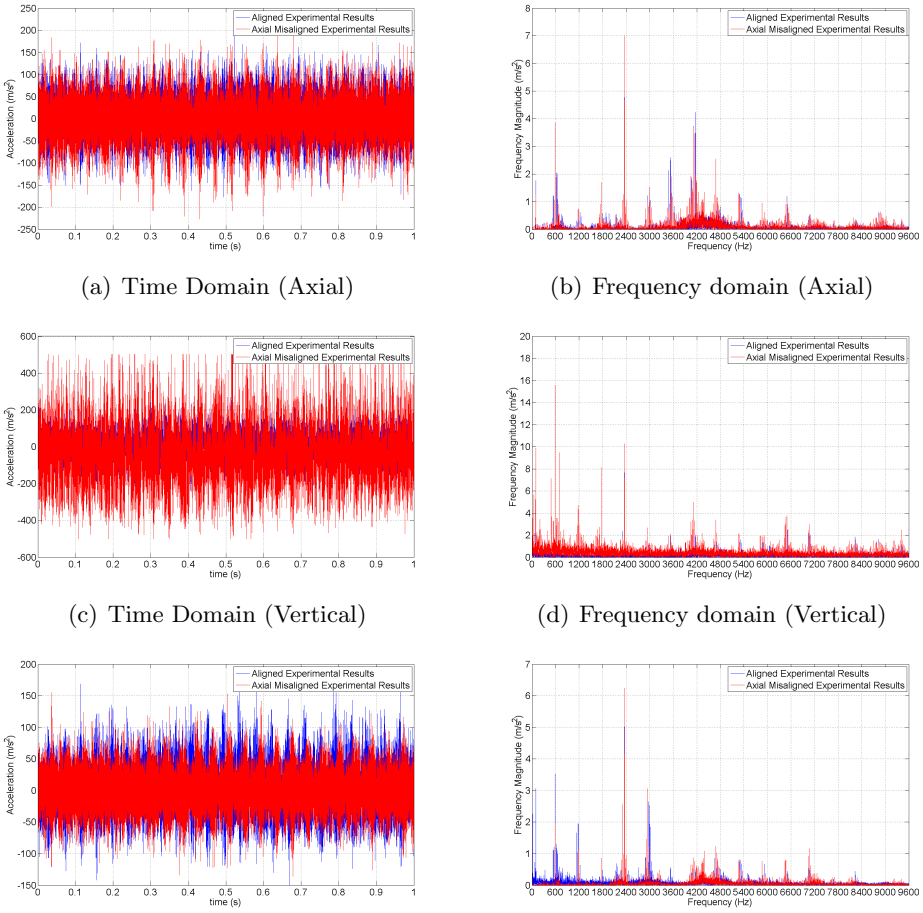

(a) Time Domain (Axial)

(b) Frequency domain (Axial)

(c) Time Domain (Vertical)

(d) Frequency domain (Vertical)

(e) Time Domain (Horizontal)

(f) Frequency domain (Horizontal)

Figure 8.5: Load side acceleration results (Experimental - Axial)

facewidth), the envisaged decrease in contact area and hence increase in contact pressure and deformation, would have a large impact on the actual average mesh stiffness and its peak to peak value.

	RMS Accelerations (m/s^2)					
	Load Side			Motor Side		
	A1	A2	A3	A1	A2	A3
Experimental Aligned	41.13	58.38	37.45	117.64	103.55	74.67
Experimental Axial	47.99	153.12	32.52	127.12	100.32	82.72
Simulated Aligned	1.24	15.20	6.86	2.32	30.62	9.46
Simulated Axial	1.17	18.52	6.79	2.28	27.22	10.00

Table 8.4: Axial RMS Values

When comparing the experimental load side axial accelerations to the sim-

ulated results for 8 mm axial misalignment (ref Figure 8.6) it can be seen that rather than the increase in acceleration magnitude that the experimental results have shown, the inclusion of axial misalignment reduces the RMS acceleration value. This has been described by the exclusion of the axial misalignment effects on mesh stiffness and axial forces because of tilting.

In the simulated frequency domain the reduction in axial vibrations are seen as reduced peaks at 600 and 1200 Hz, while slight increases are seen at 2400, 3600, 4200, 6000 and 7200 Hz.

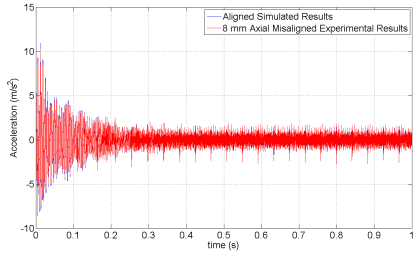

(a) Time Domain (Axial)

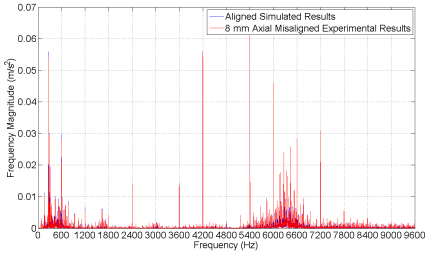

(b) Frequency domain (Axial)

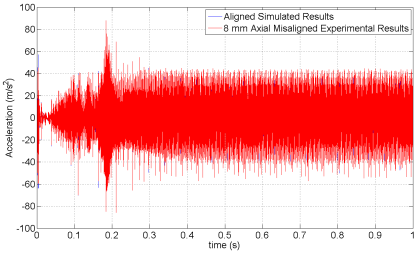

(c) Time Domain (Vertical)

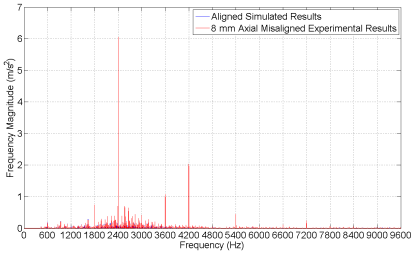

(d) Frequency domain (Vertical)

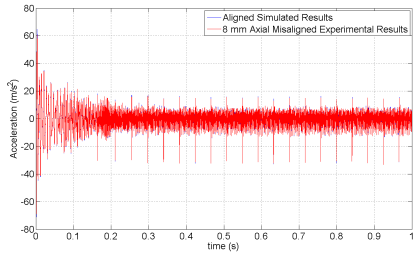

(e) Time Domain (Horizontal)

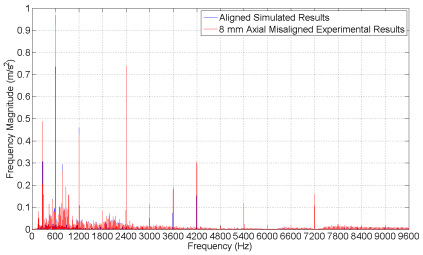

(f) Frequency domain (Horizontal)

Figure 8.6: Load side acceleration results (Simulated - Axial)

In the vertical direction it can be seen that the introduction of axial misalignment has a large impact on the experimental acceleration results, which are believed to be due to the additional forcing terms and the variations in the contacting stiff-

ness. In the frequency domain this is mainly seen as an increase in the meshing frequency at 600 Hz; however throughout the frequency domain the harmonics of the meshing frequency are also seen to increase.

In the simulated results the vertical accelerations are seen to increase, which is believed to be mainly due to the additional forces generated through the axial misalignment. This is seen in the frequency domain as an increase in the frequency peak at 2400 Hz, which is also seen in the experimental results; however the relative increase in this peak is not as great in the experimental results as increases seen in the first three gear mesh harmonics. Therefore it is believed that these increases are mainly due to the variation in the average mesh stiffness and its peak-to-peak values.

Looking at the experimental horizontal accelerations, it is seen that the introduction of axial misalignment appears to slightly reduce the magnitude of vibration. This is manifested in the frequency domain as a reduction in the first 2 mesh harmonics at 600 and 1200 Hz, which appear to have a larger impact on the RMS value compared to slight increases in the higher mesh harmonics. A further reduction is seen in the sub mesh harmonic peak at around 100 Hz; however the reasoning behind this reduction is not known.

From the simulated results, similar trends are seen in the horizontal direction, with a slight decrease in the RMS value at 8 mm axial misalignment. In the frequency domain this reduction is again attributed to decreases in the first two mesh frequencies (600 and 1200 Hz), with slight increases also seen for the higher mesh harmonics.

Moving on to the motor side results it is again seen that with induced axial misalignment the RMS magnitude of the axial vibration is increased. As previously described it is believed that this is due to the induced axial forces, and this is manifested in the frequency domain as increases in the mid range peaks, between 3600 and 4800 Hz. The other notable change in the frequency domain is a considerable decrease in the fourth mesh harmonic (2400 Hz), which is seen to a smaller extent in the simulated results of Figure 8.8(a); however the increases in the mid range

frequencies are not predicted in the simulated results.

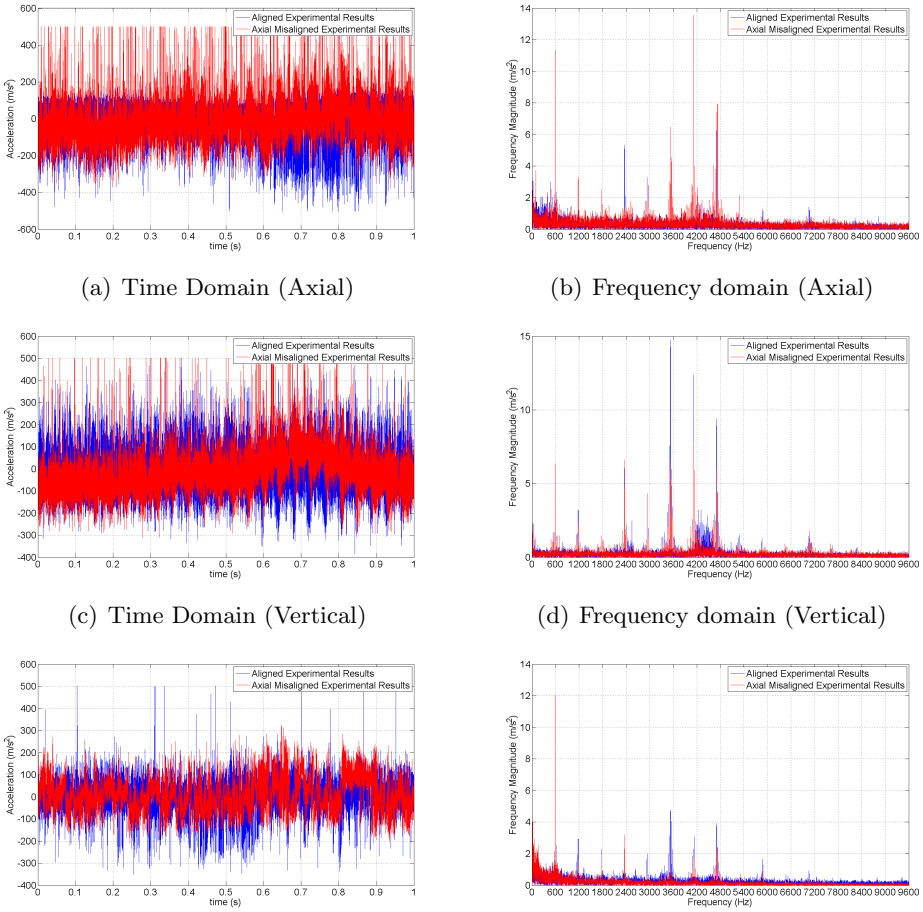

(a) Time Domain (Axial)

(b) Frequency domain (Axial)

(c) Time Domain (Vertical)

(d) Frequency domain (Vertical)

(e) Time Domain (Horizontal)

(f) Frequency domain (Horizontal)

Figure 8.7: Motor side acceleration results (Experimental - Axial)

In the vertical DOF both the experimental and simulated results show a decrease in the total magnitude of vibration. In both results this is attributed to decreases in the mid range frequencies; however in the experimental results this is accompanied by an increase in the primary meshing frequency, which is not seen to the same extent in the simulated results.

Again in the horizontal DOF both the experimental and simulated results show slight increases in the RMS value. In the frequency domain this is seen as an increase in the first mesh frequency (600 Hz), with decreases seen in the mid range frequencies.

From the investigation of the axial misalignment it is clear that treating

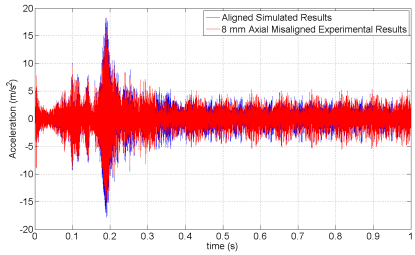

(a) Time Domain (Axial)

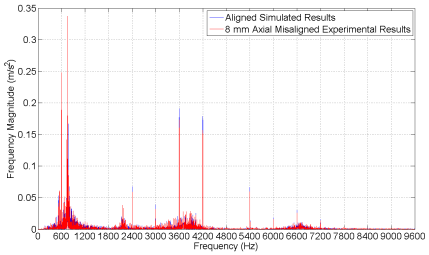

(b) Frequency domain (Axial)

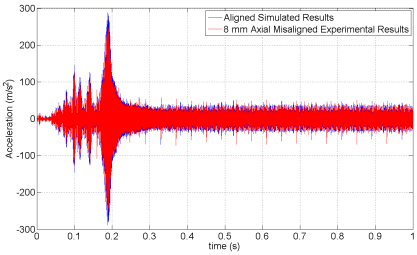

(c) Time Domain (Vertical)

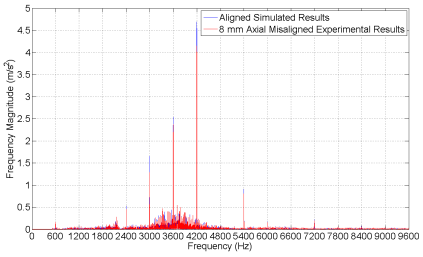

(d) Frequency domain (Vertical)

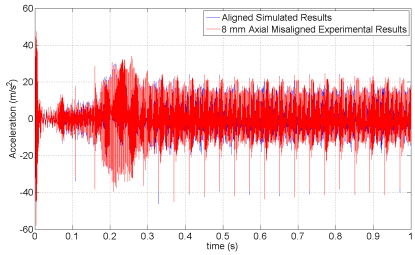

(e) Time Domain (Horizontal)

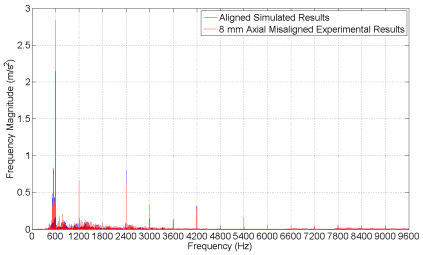

(f) Frequency domain (Horizontal)

Figure 8.8: Motor side acceleration results (Simulated - Axial)

its effects as a pure forcing term does not capture the full response of the system under misalignment. To get a better understanding of the response, appropriate contact parameters under axial misalignment must be used, and under this degree of axial misalignment the effects of the mesh tilting and the axial thrust load must be incorporated.

From the experimental results, although some characteristics are seen under this misalignment, an appreciation of their actual effects is not seen due to the limited experimental data. Therefore any possible reasoning behind the variations in the results must be validated with further experimental and simulated data, and a wider range of misalignments must be studied repeatedly to gain better confidence in the results.

8.3 Radial Misalignment

The final misalignment of study is in the radial direction, which is achieved through the correct positioning of the movable foundation plate. Radial misalignments of 0.25, 0.5, 1 and 2.5 mm are investigated experimentally to try to ascertain its impact on the system vibrations. Simulated accelerations at 0.25, 0.5 and 0.75 mm radial misalignment are compared against the experimental values. As previously explained, the upper limit of 0.75 mm is determined by the dataset used to calculate the mesh stiffness, which has radial misalignment limits of 0 to 1 mm.

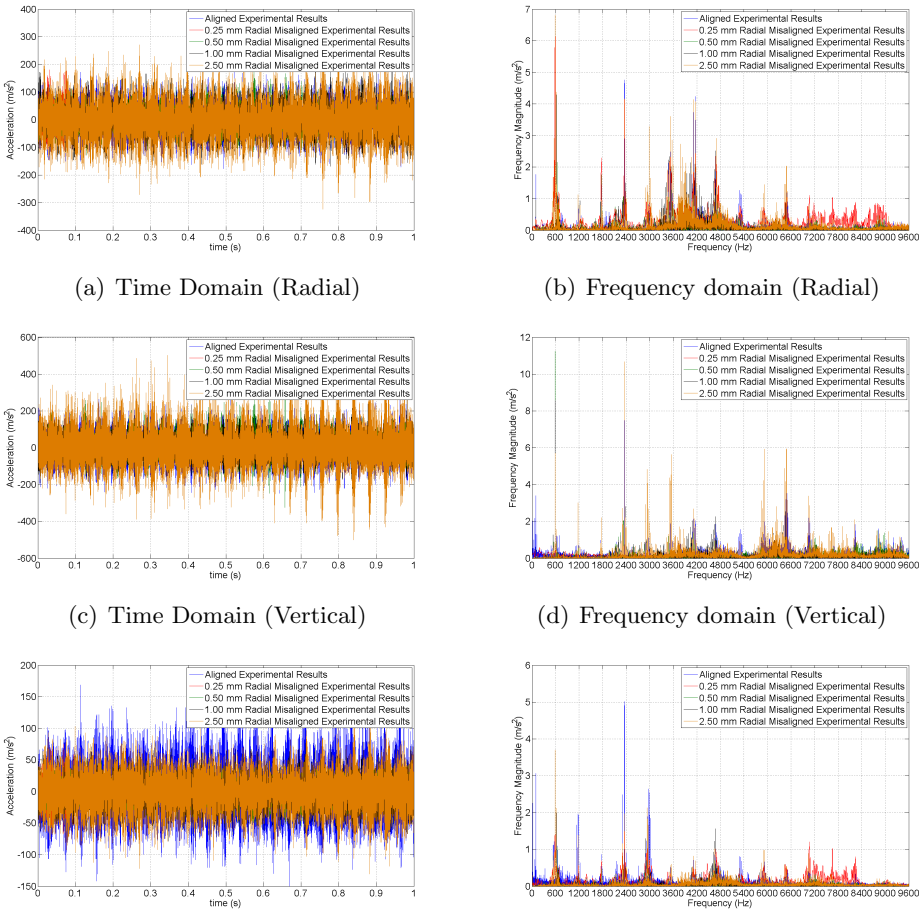

(a) Time Domain (Radial)

(b) Frequency domain (Radial)

(c) Time Domain (Vertical)

(d) Frequency domain (Vertical)

(e) Time Domain (Horizontal)

(f) Frequency domain (Horizontal)

Figure 8.9: Load side acceleration results (Experimental - Radial)

Looking at the experimental results presented in Figures 8.9 and 8.11, and Table 8.5, it can be seen that very little correlation between the amount of misalign-

Misalignment (mm)	RMS Accelerations (m/s^2)					
	Load Side			Motor Side		
	A1	A2	A3	A1	A2	A3
0.00	41.13	58.38	37.45	117.64	103.55	74.67
0.25	38.51	8.98	16.92	155.41	79.56	54.91
0.50	29.56	47.90	11.98	82.29	60.08	72.51
1.00	43.49	49.90	19.16	77.46	52.25	44.91
2.50	62.43	88.61	27.48	92.14	66.64	111.34

Table 8.5: Experimental radial RMS Values

ment and the accelerations exists. When an initial misalignment is introduced the magnitude of vibration is seen to drop in all degrees of freedom bar the motor side axial direction. The drops seen are quite excessive and this is not believed to be wholly a consequence of the radial misalignment, which is relatively small.

A myriad of explanations can be given for this fall in acceleration, such as the movement of the platform, which would mean that along with the intended misalignment, other errors or variations in the contact could be introduced, or after movement of the gear assembly the platform was not secured to the foundation plate with the same tightening torque and hence clamping as before. The gears could also be different and therefore be of different quality, which would effect the accelerations.

With additional misalignment to 0.5 mm, the load side vertical accelerations are seen to increase, which is not as expected when considering the change in the contact angles; however this increase is also found in the simulated results, which could suggest that this variation is due to the radial misalignment and its effects on the mesh forces. This is only a suggestion, since more thorough experimental results would be required to determine if this was indeed an effect of the misalignment and not attributed to other factors.

In the axial and horizontal load side results the ever increasing misalignment causes the RMS values to increase and decrease, while at the maximum, 2.5 mm, misalignment the RMS values across all DOF are seen to increase. This could be due to the induced backlash, which may cause shock loading and increase the

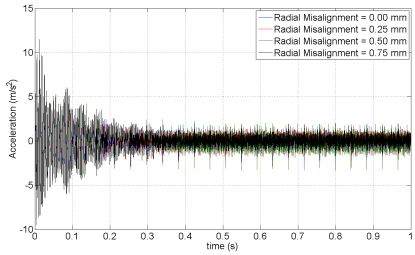

(a) Time Domain (Radial)

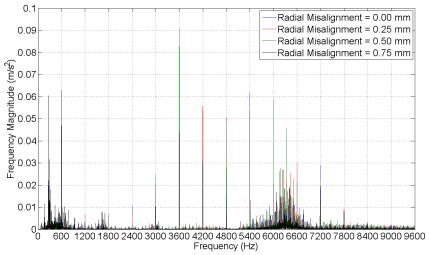

(b) Frequency domain (Radial)

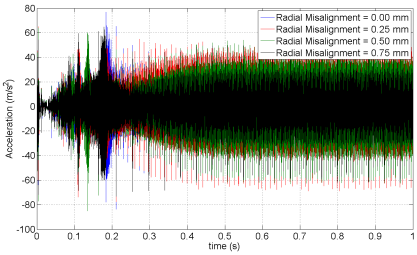

(c) Time Domain (Vertical)

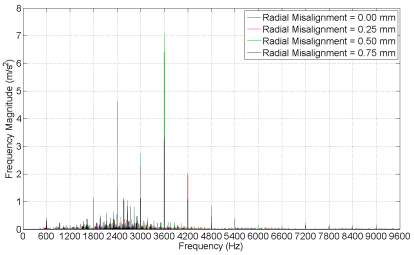

(d) Frequency domain (Vertical)

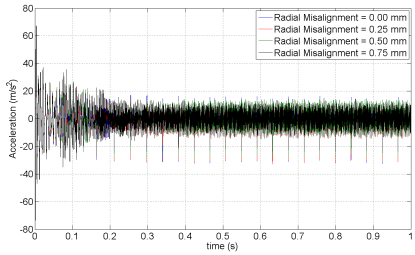

(e) Time Domain (Horizontal)

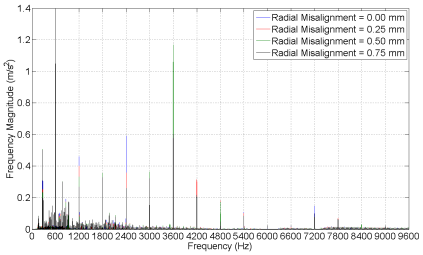

(f) Frequency domain (Horizontal)

Figure 8.10: Load side acceleration results (Simulated - Radial)

magnitude of vibration; however as nonlinearity due to contact loss is not included in the gearbox model, this can not be verified.

In the vertical DOF on the load side shaft, the accelerations are seen to increase with greater misalignment, which is not predicted in the simulated results. It was believed that with the increased misalignment the variation in the contact angle would cause the vertical accelerations to decrease; however this is not found. This could again be attributed to many factors such as random errors in experimentation or the low friction values in the simulated results, which would have a greater effect in the vertical DOF with the variation in the contact angle. The omission of backlash could also contribute to the variations in the results, where the simulated accelerations do not include shock loading.

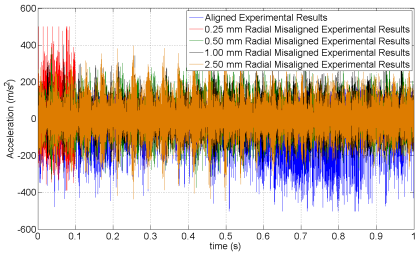

(a) Time Domain (Radial)

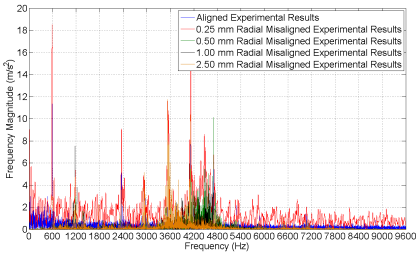

(b) Frequency domain (Radial)

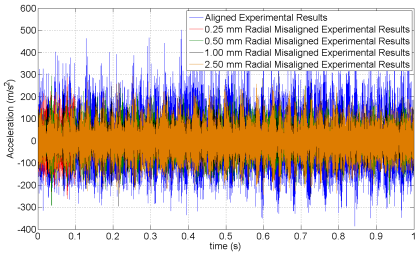

(c) Time Domain (Vertical)

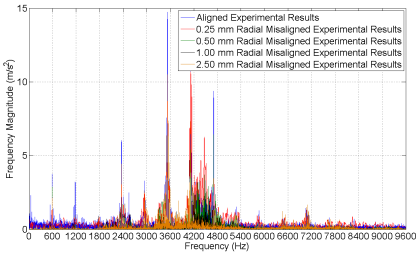

(d) Frequency domain (Vertical)

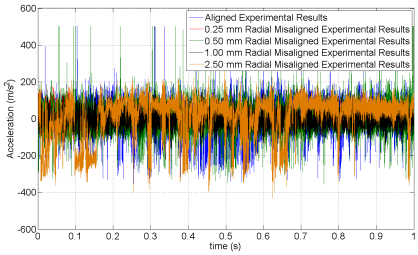

(e) Time Domain (Horizontal)

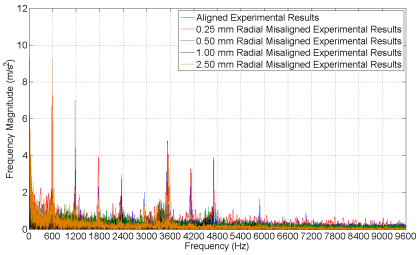

(f) Frequency domain (Horizontal)

Figure 8.11: Motor side acceleration results (Experimental - Radial)

Misalignment (mm)	RMS Accelerations (m/s^2)					
	Load Side			Motor Side		
	A1	A2	A3	A1	A2	A3
0.00	1.24	15.20	6.86	2.32	30.62	9.46
0.25	1.32	18.12	7.39	3.22	42.71	10.58
0.50	1.38	19.79	7.92	3.75	49.24	12.01
0.75	1.40	14.41	8.01	3.00	35.45	12.81

Table 8.6: Simulated radial RMS Values

Focusing on the motor side shaft it can firstly be seen that the magnitudes of vibration are much larger than on the load side, which is realised in the simulated results. In the axial direction some agreement is seen between the experimental and simulated results, where with the addition of misalignment there is an increase in acceleration, and past 0.5 mm misalignment the RMS acceleration value is found to

decrease; however between 0.25 and 0.5 mm misalignment the experimental results predict a large drop in acceleration, while the simulated results suggest the RMS value will increase. Insufficient confidence in the results means that these variations cannot be attributed completely to misalignment.

In the vertical DOF no correlation is seen between the trends in the experimental results and the simulated values, while it is possible that the same could be said for the horizontal accelerations.

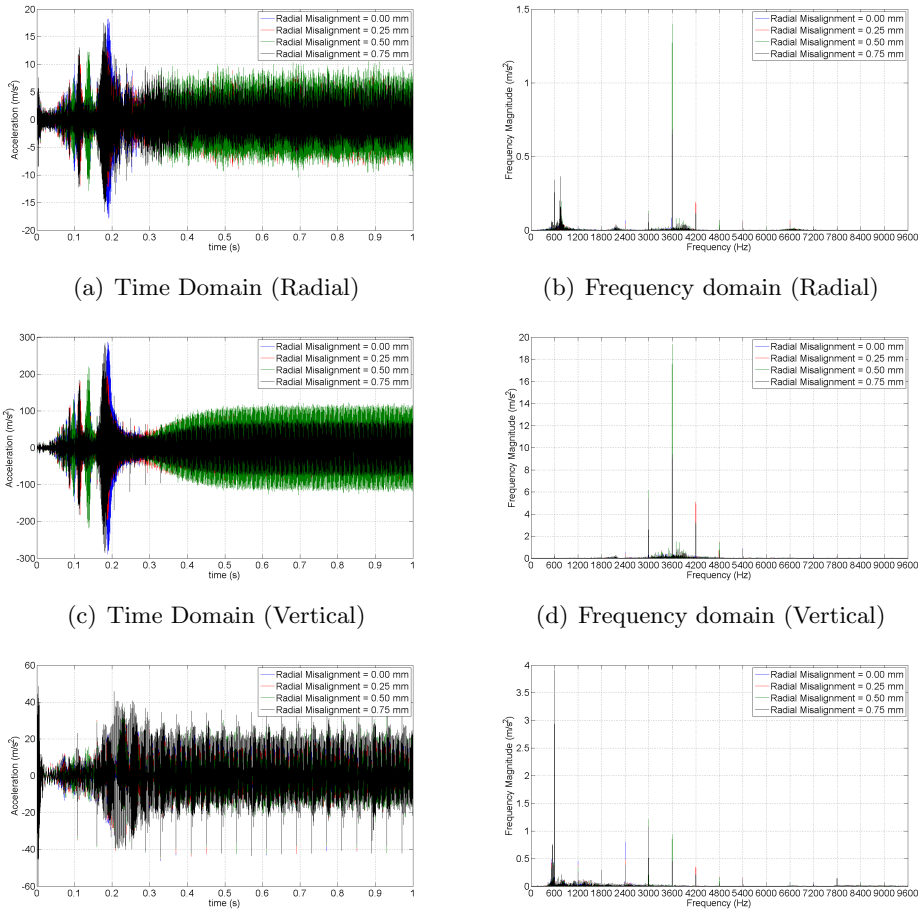

(a) Time Domain (Radial)

(b) Frequency domain (Radial)

(c) Time Domain (Vertical)

(d) Frequency domain (Vertical)

(e) Time Domain (Horizontal)

(f) Frequency domain (Horizontal)

Figure 8.12: Motor side acceleration results (Simulated - Radial)

8.4 Conclusions

In this chapter the experimental results performed at the University of Cranfield are used to verify the simulated results. Initially the aligned experimental re-

sults are used to ascertain appropriate values for the simulation parameters; with special attention given to the damping factors, the coupling stiffnesses and the frictional parameters. From these results it was found that the simulated accelerations were consistently below the experimental values. It was suggested that the reasoning behind these variations were due to the the low friction value used in simulation and the high damping applied to the bearings and supports. The friction value was chosen to prevent the frequency domain from being dominated by the first three mesh harmonics, which are heavily dependent on the friction force, while the high damping values were chosen to ensure a settled response was achieved in a reasonable simulation time. Other possible reasons were also offered, such as the modelling of the foundations and the omission of the various geometric gear errors and angular misalignments.

Next the effect of axial misalignment was investigated, where one experimental set at 8.7 mm misalignment was used to determine its effects. Due to the limited data few concrete conclusions could be drawn from the experimental results; however some correlation between the variation in the RMS values and the frequency domain results was seen between the experimental and simulated results.

Finally the effects of radial misalignment were investigated for misalignment values of 0.25, 0.5, 1 and 2.5 mm. From the RMS, time and frequency domain responses it was found that although the results varied, no correlation between the radial misalignment and the accelerations existed, and therefore it was difficult to conclude whether the variations in the results were as a result of misalignment or other factors. Simulated results were given for radial misalignments of 0.25, 0.5 and 0.75 mm; however the trends in the simulated results did not corroborate the experimental accelerations.

In conclusion although system parameters have been found that are able to predict some features in the frequency and time domain under aligned conditions, it can not be concluded fully that the model predicts the effects of misalignment. This can be attributed to both the simulation assumptions and the experimental methodology, where within the simulation it is known that not all of the effects of

misalignment are included, for example the axial force generated through axial misalignment, and some non linear effects are also omitted, such as clearance/backlash or the effects of angular misalignment.

In the experimental results the data sets provided are not sufficient to categorically state the effects of misalignment, where for axial misalignment only one data point was provided, and for aligned, axial and radial misalignment experiments there was no repetition. In future it is believed that for each misalignment case, multiple results should be gathered, with the rig assembly dismantled and reassembled between each result to remove the effects of the configuration errors. More data points would also be required, especially in the case of axial misalignment.

Chapter 9

Conclusions and Future Work

9.1 Conclusions

The aim of this thesis is to add to the knowledge base with regard to the modelling of gear vibrations. The focal point within the field of gear vibration has been to investigate the effects of misalignments on the vibrational signature of a single stage spur gear pair. This has been achieved through the study of misalignments on gear contact with the use of advanced finite element procedures, and the development of a new dynamic gearbox model from first principles.

The static finite element results have shown the effects of four misalignment types on the mesh stiffness, load sharing ratio and gear reaction forces. The four misalignments of interest consisted of two lateral and two angular misalignment. The lateral misalignments consisted of radial misalignment, which can be thought of as a change in centre distance, and axial misalignment, where the gears are translated along their shafts causing only partial contact along their faces. The angular misalignments are taken about the contact plane, where yaw misalignment was assumed to occur about the line-of-action, such that the contacting planes remained parallel, and pitch misalignment occurred about a line perpendicular to the contacting planes (off-line-of-action) such that the planes were no longer parallel, causing edge loading.

From the finite element analysis it was found that yaw misalignment had a

negligible effect on the forces and deflections at the contact, while axial misalignment introduced additional bending forces in the off-line-of-action DOF and additional axial forces as a result of the tooth tilting motion. This tilting motion was shown to exist in the gear tooth and was shown to vary through a contact cycle as the contact line moved along the teeth. It is believed that this phenomena has not previously been illustrated in any of the available literature. The main variations in the contact parameters were seen through the radial and pitch misalignments, where increased radial misalignment was shown to decrease the mesh stiffness and contact ratio and increase the contact angle. This increased the proportion of single tooth contact and the decomposition of the normal tooth load into the horizontal direction. Pitch misalignment was shown to have a large effect on the mesh stiffness, where increased pitch misalignment resulted in point contact and greater gear deflection. The tilting of the normal contact force and the movement of the centre of contact pressure also introduced large off-line-of-action moments and forces, which have not previously been shown in other works on gear contact.

The parameters and approximations determined from the finite element results were then used to approximate gear contact in a simplified dynamic model. The basis of the model was the shaft, which was modelled as a series of finite element Timoshenko beam elements. A full 6 degree of freedom representation of the shafts was required to transmit the various forces at the gear contact to the bearings and other system components. The bearings were modelled as non-linear, time varying stiffnesses, based on the Hertzian contact between the ball and the inner and outer bearing raceways, while the coupling was treated as a time invariant stiffness element with coupled DOF. The bearing supports were modelled using Guyan reduction, which uses a full finite element model and reduces the numerous DOF to only the necessary connecting nodes, and the motor and loads were modelled as simple inertias.

The gear contact was modelled as a time-varying stiffness, as a result of the number of teeth in contact. Friction was modelled as a non-linear, time varying forcing function, which not only acted in the plane of action, but also introduced

an axial force and moments due to sliding in the axial direction. The inclusion of axial friction has not been found in previous models and is believed to be a unique contribution of this work. The effects of lateral misalignment were also included, through variations in the mesh parameters and through the introduction of additional gear contact forces. The angular misalignments were omitted for two reasons; firstly yaw misalignment was not included since it had marginal effects on the contact parameters and it was not believed to effect the gear vibrations a great deal. Secondly pitch misalignment was omitted since the modelling of the gear contact as a single spring did not allow for the complex modelling of the gear contact under pitch misalignment.

The model was then presented in many configurations to determine the effects of the system parameters on the model response. Initially a constrained torsional model was analysed to ascertain the effects of the coupling, shaft, mesh and frictional parameters on the systems dynamic transmission error. From these simulations appropriate damping, stiffness and frictional parameters were determined to model the coupled, lateral-torsional model.

In this configuration the lateral motion of the bearings and supports were included, and the output of interest was the accelerations at the bearing nodes. Using this model the lateral damping and stiffness values of various components were determined. The model was then expanded to analyse the effects of the normal sliding friction, the axial friction and the lateral misalignments.

The final aspect of the research attempted to corroborate the simulated results against experimental results obtained from the custom built rig at the University of Cranfield. From the aligned results suitable system parameters were chosen to match the experimental results, and with these parameters reasonable similarities in the system responses were found. In general the simulated vibrations were found to be smaller than the experimental results, however this was mainly attributed to the high damping values required to reach a settled response in a reasonable simulation time.

These simulation parameters were then used to corroborate the simulation

results under applied misalignment to similar experimental configurations. From these results it was difficult to conclude with confidence the accuracy of the simulation results when compared to the experimental accelerations. A number of reasons were given for the discrepancies, such as random errors in experimentation that arise from setting up the experiment, or through certain factors in simulation, which were artificially high, such as the damping, or completely omitted, for example the effects of pitch misalignment or backlash.

9.2 Future Work

Following on from this research, a number of additional tasks could be undertaken to further the knowledge on gear vibration.

Develop a new gear mesh model based on finite element results

Within this work the use of a single time-varying spring element to approximate the gear contact has introduced problems in the modelling of misalignment. Through representing the gear contact as a number of springs in parallel, the inclusion of misalignment and partial contact loss would be achievable. This would allow the modelling of the contact tilting and the effects of pitch misalignment on the contact stiffness, which were not modelled in the current work.

Increase solve speed of dynamic model

The current model is programmed using MATLAB, which is an interpreted programming language, and therefore is inherently slower than a compiled programming language, such as C, FORTRAN or python. By rewriting the solver functions in a compiled language the simulation time could be reduced, which would allow the use of lower, more realistic, damping values. An alternative would be to model the system in a commercial FE package, with user subroutines to determine the contact and bearing forces/stiffnesses.

Investigate alternative beam formulations

It has previously been noted that the matrix formulation used to model the shaft stiffnesses can be susceptible to shear locking. It has also been shown that the formulation of the beam elements does not completely agree with a finite element model of the beam, which is most prevalent around the shaft cross-section discontinuities. The effects of changes in the Φ value, which alters the contribution of the shear deformation, should be investigated along with the use of component mode synthesis to model the shafts.

Improve coupling modelling

At present the coupling is modelled as a time invariant stiffness component with assumed stiffnesses and masses. One possibility would be to determine the stiffness of the coupling experimentally at various rotational positions to determine its position dependent properties.

Include clearance

It has previously been shown that the introduction of radial misalignment introduces backlash into the system. This could lead to contact loss under the right conditions, which is not currently available in the model.

Further experimentation comparisons

With the current experimental dataset available it is difficult to determine the effects of misalignment, since it is unknown whether the variations in the experimental results were as a result of misalignment or random errors. Further repeat experiments at a greater number of misalignments are required to eliminate the effects of random error on the results.

References

[1] D Learmount. Rotary woes. *Flight Intenational*, 157(4725):34 – 35, 2000.

[2] K F Fraser. An overview of health and usage monitoring systems (hums) for military helicopters. *DSTO-TR-0061*, 1994.

[3] Air Accidents Investigation Branch, 2009. AAIB Bulletin S5/2009.

[4] H N Ozguven and D R Houser. Mathematical models used in gear dynamics - a review. *Journal of Sound and Vibration*, 121:383–411, 1988.

[5] J Wang, R Li, and X Peng. Survey of nonlinear vibration of gear transmission systems. *Applied Mechanics Review*, 56(3):309–329, 2003.

[6] R G Munro. A review of the theory and measurement of gear transmission error, 1990.

[7] D B Welbourn. Fundemental knowledge on gear noise - a survey, 1979.

[8] J E Shigley and C R Mischke. *Mechanical engineering design.* McGraw Hill, 6th metric edition, 2003.

[9] K C Ludema. *Friction wear and lubrication.* CRC Press, 1996.

[10] A Kahraman and R Singh. Interactions between time-vaying mesh stiffness and clearance non-linearities in a geared system. *Journal of Sound and Vibration*, 146(1):135–156, 1991.

[11] A Parey and N Tandon. Spur gear dynamic models including defects: A review. *The Shock and Vibration Digest*, 35(6):465–478, 2003.

[12] A Parey, M El Badaoui, F Guillet, and N Tandon. Dynamic modelling of a spur gear pair and application of emperical mode decomposition-based statical analysis for early detection of localized tooth defect. *Journal of Sound and Vibration*, 294:547–561, 2006.

[13] V K Tamminana, A Kahraman, and S M Vijayakar. A study of the relationship between the dynamic factors and the dynamic transmission error of spur gear pairs. *Journal of Mechanical Design*, 129:75–84, 2007.

[14] A Kahraman and R Singh. Non-linear dynamics of a spur gear pair. *Journal of Sound and Vibration*, 142(1):49–75, 1990.

[15] G W Blankenship and A Kahraman. Steady-state forced response of a mechanical oscillator with combined parametric-excitation and clearance type nonlinearity. *Journal of Sound and Vibration*, 185(5):743–765, 1995.

[16] A Kahraman and G W Blankenship. Interatcions between commensurate parametric and forcing excitations in a system with clearance. *Journal of Sound and Vibration*, 194(3):317–336, 1996.

[17] A Kahraman and G W Blankenship. Experiments on nonlinear dynamic behaviour of an oscillator with clearance and periodically time-varying parameters. *Journal of Applied Mechanics*, 64:217–226, 1997.

[18] S Theodossiades and S Natsiavas. Non-linear dynamics of gear-pair systems with periodic stiffness and backlash. *Journal of Sound and Vibration*, 229(2): 287–310, 2000.

[19] M Vaishya and R Singh. Analysis of periodically varying gear mesh systems with coulomb friction using floquet theory. *Journal of Sound and Vibration*, 243(3):525–545, 2001.

[20] M Vaishya and R Singh. Sliding friction induced non-linearity and parametric effects in gear dynamics. *Journal of Sound and Vibration*, 248(4):671–694, 2001.

[21] M Vaishya and R Singh. Strategies for modeling friction in gear dynamics. *American Society of Mechanical Engineers Journal of Mechanical Design*, 125: 383–393, 2003.

[22] M Faggioni, F S. Samani, G Bertacchi, and F Pellicano. Dynamic optimization of spur gears. *Mechanism and Machine Theory*, 46(4):544 – 557, 2011.

[23] G Litak and M I Friswell. Dynamics of a gear system with faults in meshing stiffness. *Nonlinear Dynamics*, 41(4):415–421, 2005.

[24] A Kahraman and R Singh. Non-linear dynamics of a geared rotor-bearing system with multiple clearances. *Journal of Sound and Vibration*, 144(3):469 – 506, 1991.

[25] V Skrickij and M Bogdevičius. Vehicle gearbox dynamics: Centre distance influence on mesh stiffness and spur gear dynamics. *Transport*, 25(3):278–286, 2010.

[26] W Kim, H Yoo, and J Chung. Dynamic analysis for a pair of spur gears with translational motion due to bearing deformation. *Journal of Sound and Vibration*, 329(21):4409 – 4421, 2010.

[27] C Siyu, T Jinyuan, L Caiwang, and W Qibo. Nonlinear dynamic characteristics of geared rotor bearing systems with dynamic backlash and friction. *Mechanism and Machine Theory*, 46(4):466 – 478, 2011.

[28] S He, R Gunda, and R Singh. Effect of sliding friction on the dynamics of spur gear pair with realistic time-varying stiffness. *Journal of Sound and Vibration*, 301(3–5):927–949, 2007.

[29] S He, S Cho, and R Singh. Prediction of dynamic friction forces in spur gears using alternate sliding friction formulations. *Journal of Sound and Vibration*, 309(3–5):843–851, 2008.

[30] G Liu and R G Parker. Impact of tooth friction and its bending effect on gear dynamics. *Journal of Sound and Vibration*, 320(4-5):1039–1063, 2009.

[31] I Howard, S Jia, and J Wang. The dynamic modelling of a spur gear in mesh including friction and a crack. *Mechanical Systems and Signal Processing*, 15 (5):831–853, 2001.

[32] S Jia, I Howard, and J Wang. The dynamic modeling of multiple pairs of spur gears in mesh, including friction and geometrical errors. *International Journal of Rotating Machinery*, 9(6):437–442, 2003.

[33] N Sawalhi and R B Randall. Simulating gear and bearing interactions in the presence of faults: Part i. the combined gear bearing dynamic model and the simulation of localised bearing faults. *Mechanical Systems and Signal Processing*, 22(8):1924 – 1951, 2008.

[34] N Sawalhi and R B Randall. Simulating gear and bearing interactions in the presence of faults: Part ii: Simulation of the vibrations produced by extended bearing faults. *Mechanical Systems and Signal Processing*, 22(8):1952 – 1966, 2008.

[35] G W Blankenship and R Singh. A new gear mesh interface dynamic model to predict multi-dimensional force coupling and excitation. *Mechanism and Machine Theory*, 30(1):43 – 57, 1995.

[36] P Velex and M Maatar. A mathematical model for analyzing the influence of shape deviations and mounting errors on gear dynamic behaviour. *Journal of Sound and Vibration*, 191(5):629–660, 1996.

[37] P Velex and V Cahouet. Experimental and numerical investigations on the influence of tooth friction in spur and helical gear dynamics. *Journal of Mechanical Design*, 122:515–522, 2000.

[38] T Eritenel and R G Parker. Computational nonlinear vibration analysis of gear pairs using a three-dimensional model. *ASME Conference Proceedings*, 2009(49033):149–165, 2009.

[39] P J Sweeney and R B Randall. Gear transmission error measurement using phase demodulation. In *Proceedings of the Institute of Mechanical Engineers - Part C: Journal of Mechanical Engineering Science*, volume 210, pages 201–214, 1996.

[40] S Baud and P Velex. Static and dynamic tooth loading in spur and helical geared systems - experiments and model validation. *American Society of Mechanical Engineers Journal of Mechanical Design*, 124:334–346, 2002.

[41] S L Harris. Dynamic load on the teeth of spur gears. In *Proceedings of the Institute of Mechanical Engineers*, volume 172, pages 87–112, 1958.

[42] M S Tavakoli and D R Houser. Optimum profile modification for the minimization of static transmission errors of spur gears. *Journal of Mechanisms, Transmissions, and Automation in Design, Transactions of the American Society of Mechanical Engineers*, 108:86–95, 1986.

[43] S Du, R B Randall, and D W Kelly. Modelling of spur gear mesh stiffness and static transmission error. In *Proceedings of the Institute of Mechanical Engineers - Part C: Journal of Mechanical Engineering Science*, volume 212, pages 287–297, 1998.

[44] T F Conry and A Seireg. A mathematical programming technique for the evaluation of load distribution and optimal modifications for gear systems. *American Society of Mechanical Engineers Journal of Engineering for Industry, Series B*, 95:1115–1122, 1973.

[45] D C H Yang and Z S Sun. A rotary model for spur gear dynamics. *American Society of Mechanical Engineers*, 107:529–535, 1985.

[46] D C H Yang and J Y Lin. Hertzian damping, tooth friction and bending elasticity in gear impact dynamics. *Journal of Mechanisms, Transmissions, and Automation in Design, Transactions of the American Society of Mechanical Engineers*, 109(2):189–196, 1987.

[47] X H Tian. Dynamic simulation for system response of gearbox including localized gear faults. Master's thesis, University of Alberta, Edmonton, Alberta, Canada, 2004.

[48] J H Kuang and Y T Yang. An estimate of mesh stiffness and load sharing ratio of a spur gear pair. In *Proceedings of the ASME 12th International Power Transmission and Gearing Conference*, pages 1–10, Scottsdale,AZ,DE-43, 1992.

[49] M Vaishya and D R Houser. Modelling and analysis of sliding friction in gear dynamics. In *Proceedings of the Eighth ASME International Power Transmission and Gearing Conference*, pages 601–610, Baltimore, MD, 2000.

[50] B Rebbechi, F B Oswald, and D P Townsend. Measurement of gear tooth dynamic friction. In *Proceedings of the Seventh ASME international Power Transmission and Gearing Conference*, pages 355–363, San Diego, CA, 1996.

[51] H N Ozguven and D R Houser. Dynamic analysis of high speed gears by using loaded static transmission error. *Journal of Sound and Vibration*, 125 (1):71–83, 1988.

[52] H N Ozguven. Further work on dytem computer code. Technical report, The Ohio State University, Columbus, Ohio, 1989.

[53] R Maliha, C U Drogruer, and H N Ozguven. Nonlinear dynamic modelling od gear-shaft-disk-bearing systems using finite elements and describing functions. *American Society of Engineers Journal of Mechanical Design*, 126:534–541, 2004.

[54] Y H Guan, M Li, T C Lim, and W S Shepard. Comparative analysis of actuator concepts for active gear pair vibration control. *Journal of Sound and Vibration*, 269:273–294, 2004.

[55] M Kubur, A Kahraman, D M Zini, and K Kienzle. Dynamic analysis of a multi-shaft helical gear transmission by finite elements: Model and experiment. *Journal of Vibration and Acoustics, Transactions of the American Society of Mechanical Engineers*, 126:398–406, 2004.

[56] J J Coy and C H Chao. A method of selecting grid size to account for hertzian deformation in finite element analysis of spur gears. *American Society of Mechanical Engineers Journal of Mechanical Design*, 104:759–766, 1982.

[57] R Muthukumar and M R Raghavan. Estimation of gear tooth deflection by the finite element method. *Mechanism and Machine Theory*, 22(2):177 – 181, 1987.

[58] M N Bettaieb, P Velex, and M Ajmi. A static and dynamic model of geared transmissions by combining substructures and elastic foundations - applications to thin-rimmed gears. *Transactions of the American Society of Mechanical Engineers*, 129:184–194, 2007.

[59] F Chaari, T Fakhfakh, and M Haddar. Analytical modelling of spur gear tooth crack and influence on gearmesh stiffness. *European Journal of Mechanics A/Solids*, 28(3):461–468, 2009.

[60] C B Tsay and Z H Fong. Computer simulation and stress analysis of helical gears with pinion circular arc teeth and gear involute teeth. *Mechanism and Machine Theory*, 26(2):145 – 154, 1991.

[61] J J Zhang, I I Esat, and Y H Shi. Load analysis with varying mesh stiffness. *Computers and Structures*, 70(3):273–280, 1999.

[62] H A Ameen. Effect of shaft misalignment on the stresses distribution of spur gears. *Engineering and Technology Journal*, 28(7):1321–1339, 2010.

[63] V Simon. Fem stress analysis in hypoid gears. *Mechanism and Machine Theory*, 35(9):1197–1220, 2000.

[64] J Wang and I Howard. The torsional stiffness of involute spur gears. *Proceedings of the Institution of Mechanical Engineers, Part C: Journal of Mechanical Engineering Science*, 218(1):131–142, 2004.

[65] J Wang and I Howard. Finite element analysis of high contact ratio spur gears in mesh. *Journal of Tribology*, 127:469–483, 2005.

[66] J D Wang and I M Howard. Error analysis on finite element modeling of involute spur gears. *Journal of Mechanical Design*, 128(1):90–97, 2006.

[67] K Mao. An approach for powertrain gear transmission error prediction using the non-linear finite element method. *Proceedings of the Institution of Mechanical Engineers - Part D: Journal of Automobile Engineering*, 220(10): 1455–1463, 2006.

[68] K Mao. Gear tooth contact analysis and its application in the reduction of fatigue wear. *Wear*, 262(11-12):1281–1288, 2007.

[69] W Li, A Wood, R Weidig, and K Mao. An investigation on the wear behaviour of dissimilar polymer gear engagements. *Wear*, 271(9-10):2176–2183, 2011.

[70] A R Hassan. Contact stress analysis of spur gear teeth pair. *World Academy of Science, Engineering and Technology*, 58:611–616, 2009.

[71] F L Litvin, A Fuentes, J M Hawkins, and R F Handschuh. *Design, generation and tooth contact analysis (TCA) of asymmetric face gear drive with modified geometry.* NASA/TM-2001-210614, 2001.

[72] F L Litvin, A Fuentes, Q Fan, and R F Handschuh. Computerized design, simulation of meshing, and contact and stress analysis of face-milled formate generated spiral bevel gears. *Mechanism and Machine Theory*, 37(5):441–459, 2002.

[73] Y C Chen and M L Gu. Contact stress of modified curvilinear gears. In *AIP Conference Proceedings*, volume 1285, pages 546–560, 2010.

[74] Y C Chen and M L Gu. A study on the contact stress of modified curvilinear gears. In *Proceedings of the International MultiConference of Engineers and Computer Scientists 2010, IMECS 2010*, pages 2203–2208, 2010.

[75] Y C Chen and M L Gu. Tooth contact analysis of a curvilinear gear set with modified pinion tooth geometry. *Proceedings of the Institution of Mechanical Engineers, Part C: Journal of Mechanical Engineering Science*, 225(4):975–986, 2011.

[76] J I Pedrero, M Pleguezuelos, M Artes, and J A Antona. Load distribution model along the line of contact for involute external gears. *Mechanism and Machine Theory*, 45(5):780–794, 2010.

[77] R Tharmakulasingham, G Alfano, and M A Atherton. Reduction of gear pair transmission error with tooth profile modification. In *23rd International Conference on Noise and Vibration Engineering 2008*, pages 1141–1152, Leuven, Belgium, September 2009.

[78] Z Wei. Stresses and deformations in involute spur gears by finite element method. Master's thesis, University of Saskatchewan, Canada, 2004.

[79] H Ding and A Kahraman. Interactions between nonlinear spur gear dynamics and surface wear. *Journal of Sound and Vibration*, 307(3-5):662–679, 2007.

[80] R G Parker, S M Vijayakar, and T Imajo. Non-linear dynamic response of a spur gear pair: Modelling and experimental comparisons. *Journal of Sound and Vibration*, 237(3):435–455, 2000.

[81] V K Ambarisha and R G Parker. Nonlinear dynamics of planetary gears using analytical and finite element models. *Journal of Sound and Vibration*, 302: 577–595, 2007.

[82] S Li. Finite element analyses for contact strength and bending strength of a pair of spur gears with machining errors, assembly errors and tooth modifications. *Mechanism and Machine Theory*, 42(1):88 – 114, 2007.

[83] S Li. Effects of machining errors, assembly errors and tooth modifications on loading capacity, load-sharing ratio and transmission error of a pair of spur gears. *Mechanism and Machine Theory*, 42(6):698 – 726, 2007.

[84] S Li. Effect of addendum on contact strength, bending strength and basic performance parameters of a pair of spur gears. *Mechanism and Machine Theory*, 43(12):1557–1584, 2008.

[85] R G Munro, L Morrish, and D Palmer. Gear transmission error outside the normal path of contact due to corner and top contact. In *Proceedings of the Institute of Mechanical Engineers - Part C: Journal of Mechanical Engineering Science*, volume 213, pages 389–400, 1999.

[86] J L Li and S T Chiou. Surface design and tooth contact analysis of an innovative modified spur gear with crowned teeth. In *Proceedings of the Institute of Mechanical Engineers - Part C: Journal of Mechanical Engineering Science*, volume 219, pages 193–207, 2005.

[87] V. Simon. Influence of tooth errors and misalignments on tooth contact in spiral bevel gears. *Mechanism and Machine Theory*, 43(10):1253–1267, 2008.

[88] G H Benedict and B W Kelley. Instantaneous coefficients of gear tooth friction. *Transactions of the American Society of Lubrication Engineers*, 4:59–70, 1961.

[89] H Xu, A Kahraman, N E Anderson, and D G Maddock. Prediction of mechanical efficiency of parallel-axis gear pairs. *American Society of Mechanical Engineers Journal of Mechanical Design*, 129(1):58–68, 2007.

[90] H Xu. *Development of a generalized mechanical efficiency prediction methodology*. PhD thesis, The Ohio State University, 2005.

[91] B W Kelley and A J Lemanski. Lubrication of involute gearing. *Proceedings of the Institute of Mechanical Engineers*, 182(3A):173–184, 1967.

[92] G Davis, P Brooks, and M Findlay. Recent advances in automotive gear pair dynamic behaviour measurement and prediction - a review. In *Proceedings JSME International Conference Motion and Power Transmissions*, 2001.

[93] V Simon. The influence of misalignments on mesh performances of hypoid gears. *Mechanism and Machine Theory*, 33(8):1277 – 1291, 1998.

[94] V.V. Simon. Influence of tooth errors and shaft misalignments on loaded tooth contact in cylindrical worm gears. *Mechanism and Machine Theory*, 41 (6):707–724, 2006.

[95] V. Simon. Computer simulation of tooth contact analysis of mismatched spiral bevel gears. *Mechanism and Machine Theory*, 42(3):365–381, 2007.

[96] V.V. Simon. Loaded tooth contact analysis and stresses in spiral bevel gears. *Proceedings of the ASME Design Engineering Technical Conference*, 6:271–279, 2009.

[97] B Hefeng, M Savage, and R J Knorr. Computer modelling of rack-generated spur gears. *Mechanism and Machine Theory*, 20(4):351–360, 1985.

[98] C Salamoun and M Suchy. Computation of helical or spur gear fillets. *Mechanism and Machine Theory*, 8(3):305–323, 1973.

[99] Dassault Systemes. *ABAQUS Analysis User Manual*. 2010.

[100] J H Kuang and A D Lin. The effect of tooth wear on the vibration spectrum of a spur gear pair. *Journal of Vibration and Acoustics: Transactions of the American Society of Mechanical Engineers*, 123(3):311–317, 2001.

[101] Q Han, J Wang, and Q Li. Analysis of parametric stability for a spur gear pair system considering the effect of extended tooth contact. *Proceedings of the Institution of Mechanical Engineers, Part C: Journal of Mechanical Engineering Science*, 223(8):1787–1797, 2009.

[102] R G Munro, L Morrish, and D Palmer. Gear transmission error outside the normal path of contact due to corner and top contact. *Proceedings of the Institution of Mechanical Engineers, Part C: Journal of Mechanical Engineering Science*, 213(4):389–400, 1999.

[103] R G Munro, D Palmer, and L Morrish. An experimental method to measure gear tooth stiffness throughout and beyond the path of contact. *Proceedings of the Institution of Mechanical Engineers, Part C: Journal of Mechanical Engineering Science*, 215(7):793–803, 2001.

[104] C H Wink and A L Serpa. Investigation of tooth contact deviations from the plane of action and their effects on gear transmission error. *Proceedings of the Institution of Mechanical Engineers, Part C: Journal of Mechanical Engineering Science*, 219(5):501–509, 2005.

[105] H Walker. Gear tooth deflection and profile modification. *The Engineer*, 166: 410 and 435, 1938.

[106] H Walker. Gear tooth deflection and profile modification. *The Engineer*, 170: 102, 1938.

[107] M Amabili and A Rivola. Dynamic analysis of spur gear pairs: steady-state response and stability of the sdof model with time-varying meshing damping. *Mechanical Systems and Signal Processing*, 11(3):264–289, 1997.

[108] F Chaari, W Baccar, M S Abbes, and M Haddar. Effect of spalling or tooth breakage on gearmesh stiffness and dynamic response of a one-stage spur gear transmission. *European Journal of Mechanics - A/Solids*, 27(4):691 – 705, 2008.

[109] N Sawalhi and R B Randall. Simulating gear and bearing interactions in the presence of faults: Part i. the combined gear bearing dynamic model and the simulation of localised bearing faults. *Mechanical Systems and Signal Processing*, 22(8):1924 – 1951, 2008.

[110] L Vedmar and A Andersson. A method to determine dynamic loads on spur gear teeth and on bearings. *Journal of Sound and Vibration*, 267(5):1065 – 1084, 2003.

[111] F Chaari, R Zimroz, W Bartelmus, T Fakhfakh, and M Haddar. Model based explanation of properties of signal generated by plaentary gearbox with local damage in non-stationary operations. In *Seventh International Conference on Condition Monitoring and Machinery Failure Prevention Technologies*, Stratford-upon-Avon, UK, June 2010.

[112] J S Przemieniecki. *Theory of matrix structural analysis*. McGraw-Hill, 1968.

[113] P N Saavedra and D E Ramírez. Vibration analysis of rotors for the identification of shaft misalignment part 1: Theoretical analysis. *Proceedings of the Institution of Mechanical Engineers, Part C: Journal of Mechanical Engineering Science*, 218(9):971–985, 2004.

[114] D E Ramírez. Analysis of the vibratory behaviour of rotating machines. Master's thesis, Universidad de Concepción, Chile, 2003.

[115] T C Lim and R Singh. Vibration transmission through rolling element bearings, part i: Bearing stiffness formulation. *Journal of Sound and Vibration*, 139(2):179 – 199, 1990.

[116] T C Lim and R Singh. Vibration transmission through rolling element bearings, part ii: System studies. *Journal of Sound and Vibration*, 139(2):201 – 225, 1990.

[117] T C Lim and R Singh. Vibration transmission through rolling element bearings. part iii: Geared rotor system studies. *Journal of Sound and Vibration*, 151(1):31 – 54, 1991.

[118] T C Lim and R Singh. Vibration transmission through rolling element bearings, part iv: statistical energy analysis. *Journal of Sound and Vibration*, 153 (1):37 – 50, 1992.

[119] H V Liew and T C Lim. Analysis of time-varying rolling element bearing characteristics. *Journal of Sound and Vibration*, 283(3-5):1163 – 1179, 2005.

[120] P Eschmann, L Hasbargen, and K Weigand. *Ball and Roller Bearings: Theory, Design and Application*. John Wiley & Sons, 2nd edition, 1985.

[121] B Rebbechi, F Oswald, and D Townsend. Dynamic measurements of gear tooth friction and load. *NASA Technical Memorandum 103281*, 1991.

[122] A Palmgren. *Ball and Roller Bearing Engineering*. SKF Industries, 2nd edition, 1945.

[123] J A Greenwood. Analysis of elliptical hertzian contacts. *Tribology International*, 30(3):235–237, 1997.

[124] R J Guyan. Reduction of stiffness and mass matrices. *American Institute of Aeronautics and Astronautics Journal*, 3(2):380, 1965.

[125] R R Craig and M C C Bampton. Coupling of substructures for dynamic analysis. *American Institute of Aeronautics and Astronautics Journal*, 6(7): 1313–1319, 1968.

Appendix A

ABAQUS Gear Generation Python Script

A.1 Unmodified Spur Gears

```
from abaqus import *
import testUtils
testUtils.setBackwardCompatibility()
from abaqusConstants import *
import sketch
import part
import assembly
import regionToolset
import interaction
import mesh
import job

# Create a new model
M1 = mdb.Model(name='Mod')

# Create the three analysis steps, to initiate contact,
    apply the correct load and rotate the gear through a
    single contact cycle
M1.StaticStep(name='Contact', previous='Initial')
M1.steps['Contact'].setValues(nlgeom=ON, maxNumInc=1000000,
    initialInc=0.5, minInc=(1.E-6), maxInc=0.5)

M1.StaticStep(name='Force', previous='Contact')
M1.steps['Force'].setValues(nlgeom=ON, maxNumInc=1000000,
    initialInc=0.5, minInc=(1.E-6), maxInc=0.5)
```

```
M1.StaticStep(name='Rotate', previous='Force')
M1.steps['Rotate'].setValues(nlgeom=ON, maxNumInc=1000000,
    initialInc=0.02, minInc=(1.E-6), maxInc=0.02)

# set the name of the first gear
N='Gear_0'
N1='Gear_0'

# create the constant TWOPI and set the total rotation of
    the gear in the rotation step to TWOPI divided by the
    number of teeth on the second gear.
TWOPI = 2*pi
ROTATION = TWOPI/24

# create a sketch for the flank of the first gear
S1 = M1.ConstrainedSketch(name='Involute_0', sheetSize=125)

# set the coordinates of the first gear flank
xyCoords = ((7.04999438799211,55.8064519489394)
    ,(6.91562216476228,55.8232628039086)
    ,(6.78120985947602,55.8397501144279)
    ,(6.64675825116976,55.8559137849387)
    ,(6.5122681191077,55.8717537217587)
    ,(6.2486410067766,55.9222241407822)
    ,(5.99195346072761,56.0117587447713)
    ,(5.74442845996328,56.1414814566159)
    ,(5.50785983535851,56.3143521720439)
    ,(5.2833610596126,56.5370783697555)
    ,(5.07120191662635,56.8246306411043)
    ,(4.87130428825683,57.2120900753764)
    ,(4.68785888866165,57.7914173585898)
    ,(4.56389283188061,58.8586003179893)
    ,(4.55784673089054,59.0224453060259)
    ,(4.5456603636109,59.2211349169919)
    ,(4.52562771090325,59.4544459213459)
    ,(4.49605050954882,59.7220925413951)
    ,(4.4552402896375,60.0237267095749)
    ,(4.40152040365953,60.3589383889283)
    ,(4.33322804547704,60.7272559555231)
    ,(4.24871625736125,61.1281466424999)
    ,(4.14635592328973,61.5610170453841)
    ,(4.02453774670956,62.0252136882532)
    ,(3.88167421098372,62.5200236502897)
    ,(3.71620152075245,63.0446752522077)
    ,(3.52658152245549,63.5983388019858)
    ,(3.31130360227838,64.18012739929)
    ,(3.0688865598032,64.7890977979229)
```

```
    ,(2.79788045566366,65.4242513255835)
    ,(2.49686843152492,66.0845348601762)
    ,(2.16446850073047,66.7688418618578)
    ,(1.79933530798157,67.4760134599655))

# create a constant for all the geometry in the sketch
E = S1.geometry

# create a spline which passes through all the flank
    coordinates in the sketch
E1 = S1.Spline(xyCoords)

# set x-y values for points at the top and bottom of the
    gear flank
bOFs_X = 7.04999438799211
bOFs_Y = 55.8064519489394
tOFs_X = 1.79933530798157
tOFs_Y = 67.4760134599655

# create a vertical construction line which passes through
    the origin
E3 = S1.ConstructionLine(point1 = (0,0), point2 = (0,tOFs_Y)
    )

# Mirror-copy the spline through the construction line
S1.copyMirror(mirrorLine = E3, objectList = (E1,))

# create a line which joins the tops of the two gear tooth
    flanks (top land)
E2 = S1.Line(point1 = (tOFs_X,tOFs_Y), point2 = (-tOFs_X,
    tOFs_Y))

# create an empty list and append all the geometry in the
    sketch to it
ALL = []
for key in E.keys() : ALL.append(E[key])

# radially pattern the geometry in ALL about the origin.
    The number of objects is equal to the number of tteth on
    the gear.
S1.radialPattern(number = 25, totalAngle = 360, centerPoint
    = (0,0), geomList = ALL)

# create a circular hole in the centre of the sketch to
    represent the shaft hole of the gear
ShaftD = 12.5
S1.CircleByCenterPerimeter(center=(0,0), point1=(ShaftD,0))
```

```
# create a three dimensional deformable part
P1 = M1.Part(name='Gear_0', dimensionality=THREE_D, type=
    DEFORMABLE_BODY)

# within the part create two datum planes, one which is
    equal to the original xy plane and another which is
    offset by the facewidth of the gears
P1.DatumPlaneByPrincipalPlane(principalPlane=XYPLANE, offset
    =15)
P1.DatumPlaneByPrincipalPlane(principalPlane=XYPLANE, offset
    =0)

# create a datum axis which is equal to the gloabl y axis
P1.DatumAxisByPrincipalAxis(YAXIS)

# within the part create a body by extruding the gear sketch
    by the facewidth
P1.BaseSolidExtrude(sketch=S1, depth=15)

# create two sketches on the two new datum planes, using the
    newly created y-axis as the vertical axis of the
    sketches. Within the sketches create circles to define
    the web portion of the gears
S2 = M1.ConstrainedSketch(name='Rim', sheetSize=125,
    transform=P1.MakeSketchTransform(sketchPlane=P1.datums
    [1], sketchPlaneSide=SIDE1, sketchUpEdge=P1.datums[3],
    sketchOrientation=RIGHT, origin=(0.0, 0.0, 0.0)))
S2.CircleByCenterPerimeter(center=(0,0), point1=(49.375,0))
S3 = M1.ConstrainedSketch(name='Rim2', sheetSize=125,
    transform=P1.MakeSketchTransform(sketchPlane=P1.datums
    [2], sketchPlaneSide=SIDE1, sketchUpEdge=P1.datums[3],
    sketchOrientation=RIGHT, origin=(0.0, 0.0, 0.0)))
S3.CircleByCenterPerimeter(center=(0,0), point1=(49.375,0))

# cut extrude the rim sketches to create the gear web
P1.CutExtrude(sketchPlane=P1.datums[1], sketchPlaneSide=
    SIDE1, sketchUpEdge=P1.datums[3], sketchOrientation=RIGHT
    , sketch=S2, depth=2.5)
P1.CutExtrude(sketchPlane=P1.datums[2], sketchPlaneSide=
    SIDE1, sketchUpEdge=P1.datums[3], sketchOrientation=RIGHT
    , sketch=S3, depth=2.5, flipExtrudeDirection=ON)

# create fillets at the rim edges
e = P1.edges
P1.Round(radius=1.25, edgeList=(e.findAt(coordinates
    =(49.375,0,0)),))
P1.Round(radius=1.25, edgeList=(e.findAt(coordinates
    =(49.375,0,15)),))
```

```
P1.Round(radius=1.25, edgeList=(e.findAt(coordinates
    =(49.375,0,2.5)),))
P1.Round(radius=1.25, edgeList=(e.findAt(coordinates
    =(49.375,0,12.5)),))

# Set up reference point to couple with inner surface of
    gear.  This point is where loads and boundary conditions
    are applied.
R = P1.ReferencePoint((0,0,0))
REG = regionToolset.Region(referencePoints=(P1.
    referencePoints[11],))
SET = P1.Set(name='ControlPoint', region=REG)

# Create surface for coupling
side1Faces = P1.faces.findAt(((ShaftD,0,7.5),))
P1.Surface(side1Faces=side1Faces, name='CoupleSurf')

# create the elastic material properties
Mat = M1.Material(name='Low Carbon Steel 0')
Mat.Elastic(table=((210.E3, 0.3),))

# create the part section properties, assign material
    properties to the section and apply to the model
M1.HomogeneousSolidSection(name='Gear_0_Section', material='
    Low Carbon Steel 0')
F = P1.faces
SET = P1.Set(name='AllFaces', faces=F)
P1.SectionAssignment(region=SET, sectionName=N+'_Section')

# create an assembly and instance the gear part to the
    assembly
A = M1.rootAssembly
I = A.Instance(name='Gear_0', part=P1, dependent=ON)

# Create a kinematic coupling between the central reference
    point and the inner surface of the gear created above
M1.Coupling(name='Gear_0_Couple', surface=A.instances['
    Gear_0'].surfaces['CoupleSurf'], controlPoint=A.instances
    ['Gear_0'].sets['ControlPoint'], influenceRadius=
    WHOLE_SURFACE, couplingType=KINEMATIC)

# Create History Output to monitor the rotational positions
    of the gear in the rotate step
M1.HistoryOutputRequest(name='Position_'+N, createStepName='
    Rotate', region=I.sets['ControlPoint'], variables=('UR3'
    ,), timeInterval=0.002)
```

```
# rotate the gear about the z-axis in the assembly to ensure
    alignment of the contacting teeth
A.rotate(('Gear-0',), (0,0,0), (0,0,1), 10.8)


# set the name of the second gear
N='Pinion-1'
N2='Pinion-1'

# create a sketch for the flank of the second gear
S1 = M1.ConstrainedSketch(name='Involute-1', sheetSize=120)

# set the coordinates of the second gear flank
xyCoords = ((7.01578283182777,53.2901612988423)
    ,(6.88212127770995,53.3075877030549)
    ,(6.7484164424637,53.3246788599714)
    ,(6.61466916694838,53.3414346621069)
    ,(6.48088029229026,53.3578550040854)
    ,(6.21485660888778,53.4101790639167)
    ,(5.95598022058057,53.5020766434319)
    ,(5.70643874655896,53.6347608935526)
    ,(5.46799997624746,53.8113836332906)
    ,(5.24177540817208,54.0390290631116)
    ,(5.02810903046053,54.3334212822912)
    ,(4.82725850509788,54.7312673169679)
    ,(4.64477632325869,55.3285217639093)
    ,(4.53021492078854,56.433201690318)
    ,(4.52666333003503,56.5817300429065)
    ,(4.51756644168542,56.7664535482544)
    ,(4.50108453202724,56.9871629108889)
    ,(4.47538552610754,57.2435787729154)
    ,(4.43864736858575,57.5353519826149)
    ,(4.38906038549454,57.8620639382353)
    ,(4.32482963461932,58.2232270066811)
    ,(4.24417724221718,58.6182850167322)
    ,(4.14534472380709,59.0466138263606)
    ,(4.02659528677677,59.5075219636438)
    ,(3.88621611256712,60.0002513407078)
    ,(3.72252061621229,60.5239780400656)
    ,(3.53385068103284,61.0778131726534)
    ,(3.31857886630045,61.6608038067994)
    ,(3.07511058571572,62.2719339672962)
    ,(2.80188625456557,62.9101257036856)
    ,(2.49738340345337,63.5742402267987)
    ,(2.16011875652354,64.2630791125349)
    ,(1.78865027213272,64.9753855717994))

# create a constant for all the geometry in the sketch
```

```
E = S1.geometry

# create a spline which passes through all the flank
    coordinates in the sketch
E1 = S1.Spline(xyCoords)

# set x-y values for points at the top and bottom of the
    gear flank
bOFs_X = 7.01578283182777
bOFs_Y = 53.2901612988423
tOFs_X = 1.78865027213272
tOFs_Y = 64.9753855717994

# create a vertical construction line which passes through
    the origin
E3 = S1.ConstructionLine(point1 = (0,0), point2 = (0,tOFs_Y)
    )

# Mirror-copy the spline through the construction line
S1.copyMirror(mirrorLine = E3, objectList = (E1,))

# create a line which joins the tops of the two gear tooth
    flanks (top land)
E2 = S1.Line(point1 = (tOFs_X,tOFs_Y), point2 = (-tOFs_X,
    tOFs_Y))

# create an empty list and append all the geometry in the
    sketch to it
ALL = []
for key in E.keys() : ALL.append(E[key])

# radially pattern the geometry in ALL about the origin.
    The number of objects is equal to the number of tteth on
    the gear.
S1.radialPattern(number = 24, totalAngle = 360, centerPoint
    = (0,0), geomList = ALL)

# create a circular hole in the centre of the sketch to
    represent the shaft hole of the gear
ShaftD = 12.5
S1.CircleByCenterPerimeter(center=(0,0), point1=(ShaftD,0))

# create a three dimensional deformable part
P1 = M1.Part(name='Pinion_1', dimensionality=THREE_D, type=
    DEFORMABLE_BODY)

# within the part create two datum planes, one which is
    equal to the original xy plane and another which is
```

```
    offset by the facewidth of the gears
P1.DatumPlaneByPrincipalPlane(principalPlane=XYPLANE, offset
    =15)
P1.DatumPlaneByPrincipalPlane(principalPlane=XYPLANE, offset
    =0)

# create a datum axis which is equal to the gloabl y axis
P1.DatumAxisByPrincipalAxis(YAXIS)

# within the part create a body by extruding the gear sketch
     by the facewidth
P1.BaseSolidExtrude(sketch=S1, depth=15)

# create two sketches on the two new datum planes, using the
     newly created y-axis as the vertical axis of the
    sketches. Within the sketches create circles to define
    the web portion of the gears
S2 = M1.ConstrainedSketch(name='Rim', sheetSize=125,
    transform=P1.MakeSketchTransform(sketchPlane=P1.datums
    [1], sketchPlaneSide=SIDE1, sketchUpEdge=P1.datums[3],
    sketchOrientation=RIGHT, origin=(0.0, 0.0, 0.0)))
S2.CircleByCenterPerimeter(center=(0,0), point1=(49.375,0))
S3 = M1.ConstrainedSketch(name='Rim2', sheetSize=125,
    transform=P1.MakeSketchTransform(sketchPlane=P1.datums
    [2], sketchPlaneSide=SIDE1, sketchUpEdge=P1.datums[3],
    sketchOrientation=RIGHT, origin=(0.0, 0.0, 0.0)))
S3.CircleByCenterPerimeter(center=(0,0), point1=(49.375,0))

# cut extrude the rim sketches to create the gear web
P1.CutExtrude(sketchPlane=P1.datums[1], sketchPlaneSide=
    SIDE1, sketchUpEdge=P1.datums[3], sketchOrientation=RIGHT
    , sketch=S2, depth=2.5)
P1.CutExtrude(sketchPlane=P1.datums[2], sketchPlaneSide=
    SIDE1, sketchUpEdge=P1.datums[3], sketchOrientation=RIGHT
    , sketch=S3, depth=2.5, flipExtrudeDirection=ON)

# create fillets at the rim edges
e = P1.edges
P1.Round(radius=1.25, edgeList=(e.findAt(coordinates
    =(49.375,0,0)),))
P1.Round(radius=1.25, edgeList=(e.findAt(coordinates
    =(49.375,0,15)),))
P1.Round(radius=1.25, edgeList=(e.findAt(coordinates
    =(49.375,0,2.5)),))
P1.Round(radius=1.25, edgeList=(e.findAt(coordinates
    =(49.375,0,12.5)),))
```

```
# Set up reference point to couple with inner surface of
    gear.  This point is where loads and boundary conditions
    are applied.
R = P1.ReferencePoint((0,0,0))
REG = regionToolset.Region(referencePoints=(P1.
    referencePoints[11],))
SET = P1.Set(name='ControlPoint', region=REG)

# Create surface for coupling
side1Faces  = P1.faces.findAt(((ShaftD,0,7.5),))
P1.Surface(side1Faces=side1Faces, name='CoupleSurf')

# create the elastic material properties
Mat = M1.Material(name='Low Carbon Steel 1')
Mat.Elastic(table=((210.E3, 0.3),))

# create the part section properties, assign material
    properties to the section and apply to the model
M1.HomogeneousSolidSection(name='Pinion 1 Section', material
    ='Low Carbon Steel 1')
F = P1.faces
SET = P1.Set(name='AllFaces', faces=F)
P1.SectionAssignment(region=SET, sectionName=N+'_Section')

# instance the gear part to the root assembly
A = M1.rootAssembly
I = A.Instance(name='Pinion_1', part=P1, dependent=ON)

# Create a kinematic coupling between the central reference
    point and the inner surface of the gear created above
M1.Coupling(name='Pinion_1_Couple', surface=A.instances['
    Pinion_1'].surfaces['CoupleSurf'], controlPoint=A.
    instances['Pinion_1'].sets['ControlPoint'],
    influenceRadius=WHOLE_SURFACE, couplingType=KINEMATIC)

# Create History Output to monitor the rotational positions
    of the gear in the rotate step
M1.HistoryOutputRequest(name='Position_'+N, createStepName='
    Rotate', region=I.sets['ControlPoint'], variables=('UR3'
    ,), timeInterval=0.002)

# translate the gear in the assembly by the ideal centre
    distance
A.translate(('Pinion_1',), (122.5,0,0))

# rotate the gear about the z-axis in the assembly to ensure
     alignment of the contacting teeth
A.rotate(('Pinion_1',), (122.5,0,0), (0,0,1), 7.5)
```

```
# set the model contact properties, for hard frictionless
    contact using the penaly method (these are the default
    properties)
M1.ContactProperty(name='Cont_Prop')

# assign contact to the model.  This is set as general
    contact meaning that all areas of the gears can contact
    each other.  The interation property 'Cont_Prop' is used
    thoughout contact.
M1.ContactStd(name='Tooth_Contact', createStepName='Initial'
    )
M1.interactions['Tooth_Contact'].contactPropertyAssignments.
    appendInStep(stepName='Initial',assignments=((GLOBAL,SELF
    ,'Cont_Prop'),))

# Set up boundary conditions
# Contact step - Gear 1 is held in position, gear two is
    rotated by a small amount about the z-axis
M1.VelocityBC(name=N1+'_BC', createStepName='Contact',
    region=A.instances[N1].sets['ControlPoint'], v1=0, v2=0,
    v3=0, vr1=0, vr2=0, vr3=0)
M1.VelocityBC(name=N2+'_BC', createStepName='Contact',
    region=A.instances[N2].sets['ControlPoint'], v1=0, v2=0,
    v3=0, vr1=0, vr2=0, vr3=0.005)
# Force Step - Gear 1 is freed in the z-axis, Gear 2 is
    rotated back to the zero position
M1.boundaryConditions[N1+'_BC'].setValuesInStep(stepName='
    Force', v1=UNCHANGED, v2=UNCHANGED, v3=UNCHANGED, vr1=
    UNCHANGED, vr2=UNCHANGED, vr3=FREED)
M1.boundaryConditions[N2+'_BC'].setValuesInStep(stepName='
    Force', v1=UNCHANGED, v2=UNCHANGED, v3=UNCHANGED, vr1=
    UNCHANGED, vr2=UNCHANGED, vr3=0)
# Rotate Step - Gear 1 is still freed, the pitch rotation '
    ROTATION' defined ear;ier is applied to Gear 2
M1.boundaryConditions[N2+'_BC'].setValuesInStep(stepName='
    Rotate', v1=UNCHANGED, v2=UNCHANGED, v3=UNCHANGED, vr1=
    UNCHANGED, vr2=UNCHANGED, vr3=ROTATION)

# set the system forces - the set load is applied to gear 1
    during the load step.  This is propagated into the
    rotation step.
M1.Moment(name='Load', createStepName='Force', region=A.
    instances[N1].sets['ControlPoint'], cm3=100000)

# create a new analysis job based on the new model
J = mdb.Job(name='Analysis_Job', model=M1, description='TE_
    extraction_from_gear_pair')
```

A.2 Crowned Spur Gears

```
from abaqus import *
import testUtils
testUtils.setBackwardCompatibility()
from abaqusConstants import *
import sketch
import part
import assembly
import regionToolset
import interaction
import mesh
import job


# Create a new model
M1 = mdb.Model(name='Model')

# Create the three analysis steps, to initiate contact,
    apply the correct load and rotate the gear through a
    single contact cycle
M1.StaticStep(name='Contact', previous='Initial')
M1.steps['Contact'].setValues(nlgeom=ON, maxNumInc=1000000,
    initialInc=0.5, minInc=(1.E-6), maxInc=0.5)

M1.StaticStep(name='Force', previous='Contact')
M1.steps['Force'].setValues(nlgeom=ON, maxNumInc=1000000,
    initialInc=0.5, minInc=(1.E-6), maxInc=0.5)

M1.StaticStep(name='Rotate', previous='Force')
M1.steps['Rotate'].setValues(nlgeom=ON, maxNumInc=1000000,
    initialInc=0.02, minInc=(1.E-6), maxInc=0.02)

# set the name of the first gear
N='Gear1_0'
N1='Gear1_0'

# create the constant TWOPI and set the total rotation of
    the gear in the rotation step to TWOPI divided by the
    number of teeth on the second gear.
TWOPI = 2*pi
ROTATION = TWOPI/24

# create a sketch for the flank of the first gear
S1 = M1.ConstrainedSketch(name='Involute_0', sheetSize=120)
```

```
# set the coordinates of the first gear flank
xyCoords = ((7.01578283182777,53.2901612988423)
    ,(6.88212127770995,53.3075877030549)
    ,(6.74841644246369,53.3246788599714)
    ,(6.61466916694838,53.3414346621069)
    ,(6.48088029229026,53.3578550040854)
    ,(6.21485660888778,53.4101790639167)
    ,(5.95598022058057,53.5020766434319)
    ,(5.70643874655896,53.6347608935526)
    ,(5.46799997624746,53.8113836332906)
    ,(5.24177540817208,54.0390290631116)
    ,(5.02810903046053,54.3334212822912)
    ,(4.82725850509788,54.7312673169679)
    ,(4.64477632325869,55.3285217639093)
    ,(4.53021492078854,56.433201690318)
    ,(4.52842107851541,56.5264162233729)
    ,(4.52451970921253,56.6351929837349)
    ,(4.51799252312136,56.7594833217718)
    ,(4.50832233787978,56.8992256510463)
    ,(4.49499336548733,57.0543454728953)
    ,(4.47749149873935,57.2247554069763)
    ,(4.45530459701058,57.4103552277687)
    ,(4.42792277126975,57.6110319070186)
    ,(4.39483866820615,57.8266596621083)
    ,(4.35554775335031,58.0571000103355)
    ,(4.30954859307057,58.3022018290788)
    ,(4.25634313532827,58.5618014218295)
    ,(4.19543698907435,58.835722590063)
    ,(4.12633970217091,59.1237767109227)
    ,(4.04856503772163,59.4257628206877)
    ,(3.96163124869567,59.7414677039918)
    ,(3.86506135073022,60.0706659887602)
    ,(3.75838339299754,60.4131202468273)
    ,(3.64113072702301,60.7685811001977)
    ,(3.5128422733415,61.1367873329088)
    ,(3.37306278588029,61.5174660084535)
    ,(3.22134311395718,61.910332592717)
    ,(3.05724046178392,62.3150910823804)
    ,(2.88031864536536,62.7314341387433)
    ,(2.69014834668625,63.1590432269113)
    ,(2.48630736507817,63.5975887602981)
    ,(2.26838086566037,64.0467302503842)
    ,(2.03596162474932,64.506116461675)
    ,(1.78865027213272,64.9753855717994))

# create a spline which passes through all the flank
    coordinates in the sketch
S1.Spline(xyCoords)
```

```
# set x-y values for points at the top and bottom of the
    gear flank
bOFs_X = 7.01578283182777
bOFs_Y = 53.2901612988423
tOFs_X = 1.78865027213272
tOFs_Y = 64.9753855717994

# Enlose the profile for sweep

# Facewidth and crowning values
FW = 7.5
c = 0.1

# if statement to allow 2 routines to enclose the profile
if c != 0 :
        pointneeded = sqrt(pow(bOFs_X,2)+pow(bOFs_Y,2)-pow((
            bOFs_X+(1.5*c)),2));
        # create a horizontal line between the top of the
            tooth flank to the centre of the top land
        S1.Line(point1=(tOFs_X,tOFs_Y), point2=(0,tOFs_Y));
        # create a line from the centre of the top land to
            the origin
        S1.Line(point1=(0,tOFs_Y), point2=(0,0));
        # create an arc to extend the bottom land
        S1.ArcByCenterEnds(center=(0,0), point2=(bOFs_X,
            bOFs_Y), point1=((bOFs_X+(1.5*c)),pointneeded));
        # create a line from the end of the bottom land to
            the origin
        S1.Line(point1=(0,0), point2=((bOFs_X+(1.5*c)),
            pointneeded))
else :
        # create a horizontal line between the top of the
            tooth flank to the centre of the top land
        S1.Line(point1=(tOFs_X,tOFs_Y), point2=(0,tOFs_Y));
        # create a line from the centre of the top land to
            the origin
        S1.Line(point1=(0,tOFs_Y), point2=(0,0));
        # create a line from the end of the bottom land to
            the origin
        S1.Line(point1=(0,0), point2=(bOFs_X,bOFs_Y))


# create a sketch for the sweep path
S2 = M1.ConstrainedSketch(name='Path_0', sheetSize=FW)

# if statement to determine if crowning is specified.  If
    crowning is not present the sweep path is a straight line
```

```
    , else it is a curve
if c == 0 : S2.Line(point1=(0,0), point2=(0,FW))
else :
        # calculate the centre of the crowning
        pheta = atan2(FW,c);
        len_x = sqrt(pow(c,2)+pow(FW,2));
        radius = sin(pheta)*(len_x/(sin((pi-(2*pheta)))));
        # create the sweep path
        S2.ArcByCenterEnds(center=(-radius,0), point1=(0,0),
            point2=(-c,FW))

# Create the tooth quarter part and sweep
P1 = M1.Part(name='Gear11_0', dimensionality=THREE_D, type=
    DEFORMABLE_BODY)
P1.BaseSolidSweep(sketch=S1, path=S2)

# Create a new plane for trimming the gear quarter
P1.DatumPlaneByPrincipalPlane(principalPlane=XZPLANE, offset
    =(FW+10))
P1.DatumAxisByPrincipalAxis(ZAXIS)

# create a rectangle to be cut from the side of the gear
    tooth
S3 = M1.ConstrainedSketch(name='Cut_0', sheetSize=120,
    transform=P1.MakeSketchTransform(sketchPlane=P1.datums
    [2], sketchPlaneSide=SIDE1, sketchUpEdge=P1.datums[3],
    sketchOrientation=RIGHT, origin=(0.0, 0.0, 0.0)))
S3.rectangle(point1=(tOFs_Y*1.1,tOFs_Y*1.1), point2=(-tOFs_Y
    *1.1,-tOFs_Y*1.1))
P1.CutExtrude(sketchPlane=P1.datums[2], sketchUpEdge=P1.
    datums[3], sketchPlaneSide=SIDE1, sketchOrientation=RIGHT
    , sketch=S3, depth=10)

# Cut through parts of the tooth section which protrude into
     the negative x-axis region (result of the sweep extrude
    technique)
S4 = M1.ConstrainedSketch(name='Cut2_0', sheetSize=120,
    transform=P1.MakeSketchTransform(sketchPlane=P1.datums
    [2], sketchPlaneSide=SIDE2, sketchUpEdge=P1.datums[3],
    sketchOrientation=BOTTOM, origin=(0,0,0)))
if c > 0 : S4.rectangle(point1=(0,0), point2=(tOFs_Y*1.1,c
    *2))
else : S4.rectangle(point1=(0,0), point2=(tOFs_Y*1.1,1))
P1.CutExtrude(sketchPlane=P1.datums[2], sketchUpEdge=P1.
    datums[3], sketchPlaneSide=SIDE2, sketchOrientation=
    BOTTOM, sketch=S4,flipExtrudeDirection=ON)

# create mirrored parts for tooth section
```

```
P2 = M1.Part(name='Gear12_0', objectToCopy=P1, mirrorPlane=
    XZPLANE)
P3 = M1.Part(name='Gear13_0', objectToCopy=P1, mirrorPlane=
    YZPLANE)
P4 = M1.Part(name='Gear14_0', objectToCopy=P3, mirrorPlane=
    XZPLANE)

# Instance mirrored parts into Assembly
I1 = M1.rootAssembly.Instance(name='Q1', part=P1)
I2 = M1.rootAssembly.Instance(name='Q2', part=P2)
I3 = M1.rootAssembly.Instance(name='Q3', part=P3)
I4 = M1.rootAssembly.Instance(name='Q4', part=P4)

# Merge parts to form gear tooth, rotate tooth into correct
    plane, radial pattern to achieve complete gear and merge
    gear teeth into complete gear.
i = M1.rootAssembly.instances
I4 = M1.rootAssembly.InstanceFromBooleanMerge(name='
    Gear1_T_0', instances=(I1, I2, I3, I4), originalInstances
    =DELETE)
M1.rootAssembly.rotate(instanceList=('Gear1_T_0-1',),
    axisPoint=(0,0,0), axisDirection=(1,0,0), angle=270)
M1.rootAssembly.RadialInstancePattern(instanceList=('
    Gear1_T_0-1',), number=24, totalAngle=360)
I5 = M1.rootAssembly.InstanceFromBooleanMerge(name='
    Gear1_C_0', instances=(i['Gear1_T_0-1'], i['Gear1_T_0-1-
    rad-2'], i['Gear1_T_0-1-rad-3'], i['Gear1_T_0-1-rad-4'], i['
    Gear1_T_0-1-rad-5'], i['Gear1_T_0-1-rad-6'], i['Gear1_T_0
    -1-rad-7'], i['Gear1_T_0-1-rad-8'], i['Gear1_T_0-1-rad-9'],
    i['Gear1_T_0-1-rad-10'], i['Gear1_T_0-1-rad-11'], i['
    Gear1_T_0-1-rad-12'], i['Gear1_T_0-1-rad-13'], i['Gear1_T_0
    -1-rad-14'], i['Gear1_T_0-1-rad-15'], i['Gear1_T_0-1-rad-16
    '], i['Gear1_T_0-1-rad-17'], i['Gear1_T_0-1-rad-18'], i['
    Gear1_T_0-1-rad-19'], i['Gear1_T_0-1-rad-20'], i['Gear1_T_0
    -1-rad-21'], i['Gear1_T_0-1-rad-22'], i['Gear1_T_0-1-rad-23
    '], i['Gear1_T_0-1-rad-24']), originalInstances=DELETE)
P5 = M1.parts['Gear1_C_0']

# Create datums on part to fill in gaps created in the
    centre of gear during generation. This will also be used
     to cut into the face of the gear for various rim
    thicknesses.
P5.DatumAxisByPrincipalAxis(YAXIS)
P5.DatumPlaneByPrincipalPlane(principalPlane=XYPLANE, offset
    =FW)
P5.DatumPlaneByPrincipalPlane(principalPlane=XYPLANE, offset
    =-FW)
```

```
# Create fill section for gear centre
S5 = M1.ConstrainedSketch(name='Fill_0', sheetSize=120,
    transform=P5.MakeSketchTransform(sketchPlane=P5.datums
    [3], sketchPlaneSide=SIDE2, sketchUpEdge=P5.datums[2],
    sketchOrientation=RIGHT, origin=(0.0, 0.0, 0.0)))
S5.CircleByCenterPerimeter(center=(0,0), point1=(bOFs_Y
    *0.9,0))
P5.SolidExtrude(sketchPlane=P5.datums[3], sketchUpEdge=P5.
    datums[2], sketchPlaneSide=SIDE2, sketch=S5, depth=(2*FW)
    )

# cut shaft hole
shaft_perim =  12.5
S6 = M1.ConstrainedSketch(name='Shaft_0', sheetSize=120,
    transform=P5.MakeSketchTransform(sketchPlane=P5.datums
    [3], sketchPlaneSide=SIDE1, sketchUpEdge=P5.datums[2],
    sketchOrientation=RIGHT, origin=(0.0, 0.0, 0.0)))
S6.CircleByCenterPerimeter(center=(0,0), point1=(0,
    shaft_perim))
P5.CutExtrude(sketchPlane=P5.datums[3], sketchUpEdge=P5.
    datums[2], sketchPlaneSide=SIDE1, sketchOrientation=RIGHT
    , sketch=S6)

# cut into gear body to produce web
body_perim1 = 50
body_perim2 = 50
body_depth1 = 2.5
body_depth2 = 2.5

# web on right hand side
S7 = M1.ConstrainedSketch(name='BCut_RHS_0', sheetSize=120,
    transform=P5.MakeSketchTransform(sketchPlane=P5.datums
    [3], sketchPlaneSide=SIDE1, sketchUpEdge=P5.datums[2],
    sketchOrientation=RIGHT, origin=(0.0, 0.0, 0.0)))
S7.CircleByCenterPerimeter(center=(0,0), point1=(body_perim1
    ,0))
P5.CutExtrude(sketchPlane=P5.datums[3], sketchUpEdge=P5.
    datums[2], sketchPlaneSide=SIDE1, sketchOrientation=RIGHT
    , sketch=S7, depth=body_depth1)

# web on left hand side
S8 = M1.ConstrainedSketch(name='BCut_LHS_0', sheetSize=120,
    transform=P5.MakeSketchTransform(sketchPlane=P5.datums
    [4], sketchPlaneSide=SIDE2, sketchUpEdge=P5.datums[2],
    sketchOrientation=RIGHT, origin=(0.0, 0.0, 0.0)))
S8.CircleByCenterPerimeter(center=(0,0), point1=(body_perim2
    ,0))
```

```
P5.CutExtrude(sketchPlane=P5.datums[4], sketchUpEdge=P5.
    datums[2], sketchPlaneSide=SIDE2, sketchOrientation=RIGHT
    , sketch=S8, depth=body_depth2)

# create fillets at the rim edges
e = P5.edges
P5.Round(radius=0.5, edgeList=(e.findAt(coordinates=(
    body_perim1,0,FW)),))
P5.Round(radius=0.5, edgeList=(e.findAt(coordinates=(
    body_perim1,0,(FW-body_depth1)),),))
P5.Round(radius=0.5, edgeList=(e.findAt(coordinates=(
    body_perim2,0,-FW)),))
P5.Round(radius=0.5, edgeList=(e.findAt(coordinates=(
    body_perim2,0,-(FW-body_depth2)),),))

# rotate the gear about the z-axis in the assembly to ensure
    alignment of the contacting teeth
M1.rootAssembly.rotate(('Gear1_C_0-1',), (0,0,0), (0,0,1),
    0)

# repair any small faces that are created through the
    merging process
P5.RepairSmallFaces(faceList=P5.faces)

# create the elastic material properties
Mat = M1.Material(name='Low_Carbon_Steel_0')
Mat.Elastic(table=((210.E3, 0.3),))

# create the part section properties, assign material
    properties to the section and apply to the model
M1.HomogeneousSolidSection(name='Gear1_0_Section', material=
    'Low_Carbon_Steel_0', thickness=0)
F = P5.faces
SET = P5.Set(name='AllFaces', faces=F)
P5.SectionAssignment(region=SET, sectionName=N+'_Section')

# Set up reference point to couple with inner surface of
    gear.  This point is where loads and boundary conditions
    are applied.
R = P5.ReferencePoint((0,0,0))
REG = regionToolset.Region(referencePoints=(P5.
    referencePoints[15],))
SET = P5.Set(name='ControlPoint', region=REG)

# create surface for coupling
side1Faces = P5.faces.findAt(((shaft_perim,0,0),))
P5.Surface(side1Faces=side1Faces, name='CoupleSurf')
```

```
# Create a kinematic coupling between the central reference
    point and the inner surface of the gear created above
M1.Coupling(name=N+'_Couple', surface=I5.surfaces['
    CoupleSurf'], controlPoint=I5.sets['ControlPoint'],
    influenceRadius=WHOLE_SURFACE, couplingType=KINEMATIC)

# Create History Output to monitor the rotational positions
    of the gear in the rotate step
M1.HistoryOutputRequest(name='Position_'+N, createStepName='
    Rotate', region=I5.sets['ControlPoint'], variables=('UR3'
    ,), timeInterval=0.01)


# set the name of the second gear
N='Gear2_1'
N2='Gear2_1'

# create a sketch for the flank of the second gear
S1 = M1.ConstrainedSketch(name='Involute_1', sheetSize=125)

# set the coordinates of the second gear flank
xyCoords = ((7.04999438799211,55.8064519489394)
    ,(6.91562216476228,55.8232628039086)
    ,(6.78120985947602,55.8397501144279)
    ,(6.64675825116976,55.8559137849387)
    ,(6.5122681191077,55.8717537217587)
    ,(6.2486410067766,55.9222241407822)
    ,(5.99195346072761,56.0117587447713)
    ,(5.74442845996328,56.1414814566159)
    ,(5.50785983535852,56.3143521720439)
    ,(5.2833610596126,56.5370783697555)
    ,(5.07120191662635,56.8246306411043)
    ,(4.87130428825683,57.2120900753764)
    ,(4.68785888866166,57.7914173585898)
    ,(4.56389283188061,58.8586003179893)
    ,(4.5605386240983,58.9620015162797)
    ,(4.55480173309953,59.0803878827649)
    ,(4.54620142558588,59.2137057558986)
    ,(4.53425813781484,59.3618899220226)
    ,(4.51849372226536,59.5248636400558)
    ,(4.49843169379677,59.7025386711197)
    ,(4.47359747520614,59.8948153130906)
    ,(4.44351864208948,60.1015824400664)
    ,(4.40772516691239,60.3227175467348)
    ,(4.365749662196,60.5580867976267)
    ,(4.31712762272425,60.8075450812383)
    ,(4.26139766667923,61.0709360690025)
    ,(4.19810177561106,61.3480922790891)
```

```
    ,(4.12678553314996,61.638835145011)
    ,(4.04699836236775,61.942975089013)
    ,(3.95829376169722,62.2603116002163)
    ,(3.86022953931774,62.5906333174917)
    ,(3.75236804591642,62.9337181170326)
    ,(3.63427640573425,63.289333204595)
    ,(3.50552674580771,63.6572352123743)
    ,(3.36569642331656,64.0371703004823)
    ,(3.21436825094932,64.4288742629898)
    ,(3.05113072019871,64.8320726384965)
    ,(2.87557822249979,65.2464808251883)
    ,(2.6873112681245,65.6718042003425)
    ,(2.48593670274701,66.1077382442372)
    ,(2.27106792159488,66.5539686684204)
    ,(2.04232508110222,67.010171548294)
    ,(1.79933530798157,67.4760134599655))

# create a spline which passes through all the flank
    coordinates in the sketch
S1.Spline(xyCoords)

# set x-y values for points at the top and bottom of the
    gear flank
bOFs_X = 7.04999438799211
bOFs_Y = 55.8064519489394
tOFs_X = 1.79933530798157
tOFs_Y = 67.4760134599655

# Enlose the profile for sweep

# Facewidth and crowning values
FW = 7.5
c = 0.1

# if statement to allow 2 routines to enclose the profile
if c != 0 :
        pointneeded = sqrt(pow(bOFs_X,2)+pow(bOFs_Y,2)-pow((
            bOFs_X+(1.5*c)),2));
        # create a horizontal line between the top of the
            tooth flank to the centre of the top land
        S1.Line(point1=(tOFs_X,tOFs_Y), point2=(0,tOFs_Y));
        # create a line from the centre of the top land to
            the origin
        S1.Line(point1=(0,tOFs_Y), point2=(0,0));
        # create an arc to extend the bottom land
        S1.ArcByCenterEnds(center=(0,0), point2=(bOFs_X,
            bOFs_Y), point1=((bOFs_X+(1.5*c)),pointneeded));
```

```
        # create a line from the end of the bottom land to
            the origin
        S1.Line(point1=(0,0), point2=((bOFs_X+(1.5*c)),
            pointneeded))
else :
        # create a horizontal line between the top of the
            tooth flank to the centre of the top land
        S1.Line(point1=(tOFs_X,tOFs_Y), point2=(0,tOFs_Y));
        # create a line from the centre of the top land to
            the origin
        S1.Line(point1=(0,tOFs_Y), point2=(0,0));
        # create a line from the end of the bottom land to
            the origin
        S1.Line(point1=(0,0), point2=(bOFs_X,bOFs_Y))


# create a sketch for the sweep path
S2 = M1.ConstrainedSketch(name='Path_1', sheetSize=FW)

# if statement to determine if crowning is specified.  If
    crowning is not present the sweep path is a straight line
    , else it is a curve
if c == 0 : S2.Line(point1=(0,0), point2=(0,FW))
else :
        # calculate the centre of the crowning
        pheta = atan2(FW,c);
        len_x = sqrt(pow(c,2)+pow(FW,2));
        radius = sin(pheta)*(len_x/(sin((pi-(2*pheta)))));
        # create the sweep path
        S2.ArcByCenterEnds(center=(-radius,0), point1=(0,0),
            point2=(-c,FW))

# Create the tooth quarter part and sweep S1 along S2
P1 = M1.Part(name='Gear21_1', dimensionality=THREE_D, type=
    DEFORMABLE_BODY)
P1.BaseSolidSweep(sketch=S1, path=S2)

# Create a new plane for trimming the gear quarter
P1.DatumPlaneByPrincipalPlane(principalPlane=XZPLANE, offset
    =(FW+10))
P1.DatumAxisByPrincipalAxis(ZAXIS)

# create a rectangle to be cut from the side of the gear
    tooth
S3 = M1.ConstrainedSketch(name='Cut_1', sheetSize=125,
    transform=P1.MakeSketchTransform(sketchPlane=P1.datums
    [2], sketchPlaneSide=SIDE1, sketchUpEdge=P1.datums[3],
    sketchOrientation=RIGHT, origin=(0.0, 0.0, 0.0)))
```

```
S3.rectangle(point1=(tOFs_Y*1.1,tOFs_Y*1.1), point2=(-tOFs_Y
    *1.1,-tOFs_Y*1.1))
P1.CutExtrude(sketchPlane=P1.datums[2], sketchUpEdge=P1.
    datums[3], sketchPlaneSide=SIDE1, sketchOrientation=RIGHT
    , sketch=S3, depth=10)

# Cut through parts of the tooth section which protrude into
     the negative x-axis region (result of the sweep extrude
    technique)
S4 = M1.ConstrainedSketch(name='Cut2_1', sheetSize=125,
    transform=P1.MakeSketchTransform(sketchPlane=P1.datums
    [2], sketchPlaneSide=SIDE2, sketchUpEdge=P1.datums[3],
    sketchOrientation=BOTTOM, origin=(0,0,0)))
if c > 0 : S4.rectangle(point1=(0,0), point2=(tOFs_Y*1.1,c
    *2))
else : S4.rectangle(point1=(0,0), point2=(tOFs_Y*1.1,1))
P1.CutExtrude(sketchPlane=P1.datums[2], sketchUpEdge=P1.
    datums[3], sketchPlaneSide=SIDE2, sketchOrientation=
    BOTTOM, sketch=S4,flipExtrudeDirection=ON)

# create mirrored parts for tooth section
P2 = M1.Part(name='Gear22_1', objectToCopy=P1, mirrorPlane=
    XZPLANE)
P3 = M1.Part(name='Gear23_1', objectToCopy=P1, mirrorPlane=
    YZPLANE)
P4 = M1.Part(name='Gear24_1', objectToCopy=P3, mirrorPlane=
    XZPLANE)

# Instance mirrored parts into Assembly
I1 = M1.rootAssembly.Instance(name='Q1', part=P1)
I2 = M1.rootAssembly.Instance(name='Q2', part=P2)
I3 = M1.rootAssembly.Instance(name='Q3', part=P3)
I4 = M1.rootAssembly.Instance(name='Q4', part=P4)

# Merge parts to form gear tooth, rotate tooth into correct
    plane, radial pattern to achieve complete gear and merge
    gear teeth into complete gear.
i = M1.rootAssembly.instances
I4 = M1.rootAssembly.InstanceFromBooleanMerge(name='
    Gear2_T_1', instances=(I1, I2, I3, I4), originalInstances
    =DELETE)
M1.rootAssembly.rotate(instanceList=('Gear2_T_1-1',),
    axisPoint=(0,0,0), axisDirection=(1,0,0), angle=270)
M1.rootAssembly.RadialInstancePattern(instanceList=('
    Gear2_T_1-1',), number=25, totalAngle=360)
I5 = M1.rootAssembly.InstanceFromBooleanMerge(name='
    Gear2_C_1', instances=(i['Gear2_T_1-1'],i['Gear2_T_1-1-
    rad-2'],i['Gear2_T_1-1-rad-3'],i['Gear2_T_1-1-rad-4'],i['
```

```
    Gear2_T_1-1-rad-5'], i['Gear2_T_1-1-rad-6'], i['Gear2_T_1
    -1-rad-7'], i['Gear2_T_1-1-rad-8'], i['Gear2_T_1-1-rad-9'],
    i['Gear2_T_1-1-rad-10'], i['Gear2_T_1-1-rad-11'], i['
    Gear2_T_1-1-rad-12'], i['Gear2_T_1-1-rad-13'], i['Gear2_T_1
    -1-rad-14'], i['Gear2_T_1-1-rad-15'], i['Gear2_T_1-1-rad-16
    '], i['Gear2_T_1-1-rad-17'], i['Gear2_T_1-1-rad-18'], i['
    Gear2_T_1-1-rad-19'], i['Gear2_T_1-1-rad-20'], i['Gear2_T_1
    -1-rad-21'], i['Gear2_T_1-1-rad-22'], i['Gear2_T_1-1-rad-23
    '], i['Gear2_T_1-1-rad-24'], i['Gear2_T_1-1-rad-25']),
    originalInstances=DELETE)
P5 = M1.parts['Gear2_C_1']

# Create datums on part to fill in gaps created in the
    centre of gear during generation. This will also be used
     to cut into the face of the gear for various rim
    thicknesses.
P5.DatumAxisByPrincipalAxis(YAXIS)
P5.DatumPlaneByPrincipalPlane(principalPlane=XYPLANE, offset
    =FW)
P5.DatumPlaneByPrincipalPlane(principalPlane=XYPLANE, offset
    =-FW)

# Create fill section for gear centre
S5 = M1.ConstrainedSketch(name='Fill_1', sheetSize=125,
    transform=P5.MakeSketchTransform(sketchPlane=P5.datums
    [3], sketchPlaneSide=SIDE2, sketchUpEdge=P5.datums[2],
    sketchOrientation=RIGHT, origin=(0.0, 0.0, 0.0)))
S5.CircleByCenterPerimeter(center=(0,0), point1=(bOFs_Y
    *0.9,0))
P5.SolidExtrude(sketchPlane=P5.datums[3], sketchUpEdge=P5.
    datums[2], sketchPlaneSide=SIDE2, sketch=S5, depth=(2*FW)
    )

# cut shaft hole
shaft_perim = 12.5
S6 = M1.ConstrainedSketch(name='Shaft_1', sheetSize=125,
    transform=P5.MakeSketchTransform(sketchPlane=P5.datums
    [3], sketchPlaneSide=SIDE1, sketchUpEdge=P5.datums[2],
    sketchOrientation=RIGHT, origin=(0.0, 0.0, 0.0)))
S6.CircleByCenterPerimeter(center=(0,0), point1=(0,
    shaft_perim))
P5.CutExtrude(sketchPlane=P5.datums[3], sketchUpEdge=P5.
    datums[2], sketchPlaneSide=SIDE1, sketchOrientation=RIGHT
    , sketch=S6)

# cut into gear body to produce web
body_perim1 = 50
body_perim2 = 50
```

```
body_depth1 = 2.5
body_depth2 = 2.5

# web on right hand side
S7 = M1.ConstrainedSketch(name='BCut_RHS_1', sheetSize=125,
    transform=P5.MakeSketchTransform(sketchPlane=P5.datums
    [3], sketchPlaneSide=SIDE1, sketchUpEdge=P5.datums[2],
    sketchOrientation=RIGHT, origin=(0.0, 0.0, 0.0)))
S7.CircleByCenterPerimeter(center=(0,0), point1=(body_perim1
    ,0))
P5.CutExtrude(sketchPlane=P5.datums[3], sketchUpEdge=P5.
    datums[2], sketchPlaneSide=SIDE1, sketchOrientation=RIGHT
    , sketch=S7, depth=body_depth1)

# web on left hand side
S8 = M1.ConstrainedSketch(name='BCut_LHS_1', sheetSize=125,
    transform=P5.MakeSketchTransform(sketchPlane=P5.datums
    [4], sketchPlaneSide=SIDE2, sketchUpEdge=P5.datums[2],
    sketchOrientation=RIGHT, origin=(0.0, 0.0, 0.0)))
S8.CircleByCenterPerimeter(center=(0,0), point1=(body_perim2
    ,0))
P5.CutExtrude(sketchPlane=P5.datums[4], sketchUpEdge=P5.
    datums[2], sketchPlaneSide=SIDE2, sketchOrientation=RIGHT
    , sketch=S8, depth=body_depth2)

# create fillets at the rim edges
e = P5.edges
P5.Round(radius=0.5, edgeList=(e.findAt(coordinates=(
    body_perim1,0,FW)),))
P5.Round(radius=0.5, edgeList=(e.findAt(coordinates=(
    body_perim1,0,(FW-body_depth1)),),))
P5.Round(radius=0.5, edgeList=(e.findAt(coordinates=(
    body_perim2,0,-FW)),))
P5.Round(radius=0.5, edgeList=(e.findAt(coordinates=(
    body_perim2,0,-(FW-body_depth2)),),))

# translate the gear in the assembly by the ideal centre
    distance
M1.rootAssembly.translate(('Gear2_C_1-1',), (122.5,0,0))

# rotate the gear about the z-axis in the assembly to ensure
     alignment of the contacting teeth
M1.rootAssembly.rotate(('Gear2_C_1-1',), (122.5,0,0),
    (0,0,1), 10.8)

# repair any small faces that are created through the
    merging process
P5.RepairSmallFaces(faceList=P5.faces)
```

```
# create the elastic material properties
Mat = M1.Material(name='Low Carbon Steel 1')
Mat.Elastic(table=((210.E3, 0.3),))

# create the part section properties, assign material
    properties to the section and apply to the model
M1.HomogeneousSolidSection(name='Gear2_1_Section', material=
    'Low Carbon Steel 1', thickness=0)
F = P5.faces
SET = P5.Set(name='AllFaces', faces=F)
P5.SectionAssignment(region=SET, sectionName=N+'_Section')

# Set up reference point to couple with inner surface of
    gear. This point is where loads and boundary conditions
    are applied.
R = P5.ReferencePoint((0,0,0))
REG = regionToolset.Region(referencePoints=(P5.
    referencePoints[15],))
SET = P5.Set(name='ControlPoint', region=REG)

# create surface for coupling
side1Faces = P5.faces.findAt(((shaft_perim,0,0),))
P5.Surface(side1Faces=side1Faces, name='CoupleSurf')

# Create a kinematic coupling between the central reference
    point and the inner surface of the gear created above
M1.Coupling(name=N+'_Couple', surface=I5.surfaces['
    CoupleSurf'], controlPoint=I5.sets['ControlPoint'],
    influenceRadius=WHOLE_SURFACE, couplingType=KINEMATIC)

# Create History Output to monitor the rotational positions
    of the gear in the rotate step
M1.HistoryOutputRequest(name='Position_'+N, createStepName='
    Rotate', region=I5.sets['ControlPoint'], variables=('UR3'
    ,), timeInterval=0.01)

# set the model contact properties, for hard frictionless
    contact using the penaly method (these are the default
    properties)
M1.ContactProperty(name='Cont_Prop')

# assign contact to the model. This is set as general
    contact meaning that all areas of the gears can contact
    each other. The interation property 'Cont_Prop' is used
    thoughout contact.
M1.ContactStd(name='Tooth_Contact', createStepName='Initial'
    )
```

```
M1.interactions['Tooth_Contact'].contactPropertyAssignments.
    appendInStep(stepName='Initial',assignments=((GLOBAL,SELF
    ,'Cont_Prop'),))

# Set up boundary conditions
# Contact step - Gear 1 is held in position, gear two is
    rotated by a small amount about the z-axis
M1.VelocityBC(name=N1+'_BC', createStepName='Contact',
    region=A.instances[N1].sets['ControlPoint'], v1=0, v2=0,
    v3=0, vr1=0, vr2=0, vr3=0)
M1.VelocityBC(name=N2+'_BC', createStepName='Contact',
    region=A.instances[N2].sets['ControlPoint'], v1=0, v2=0,
    v3=0, vr1=0, vr2=0, vr3=0.005)
# Force Step - Gear 1 is freed in the z-axis, Gear 2 is
    rotated back to the zero position
M1.boundaryConditions[N1+'_BC'].setValuesInStep(stepName='
    Force', v1=UNCHANGED, v2=UNCHANGED, v3=UNCHANGED, vr1=
    UNCHANGED, vr2=UNCHANGED, vr3=FREED)
M1.boundaryConditions[N2+'_BC'].setValuesInStep(stepName='
    Force', v1=UNCHANGED, v2=UNCHANGED, v3=UNCHANGED, vr1=
    UNCHANGED, vr2=UNCHANGED, vr3=0)
# Rotate Step - Gear 1 is still freed, the pitch rotation '
    ROTATION' defined ear;ier is applied to Gear 2
M1.boundaryConditions[N2+'_BC'].setValuesInStep(stepName='
    Rotate', v1=UNCHANGED, v2=UNCHANGED, v3=UNCHANGED, vr1=
    UNCHANGED, vr2=UNCHANGED, vr3=ROTATION)

# set the system forces - the set load is applied to gear 1
    during the load step.  This is propagated into the
    rotation step.
M1.Moment(name='Load', createStepName='Force', region=A.
    instances[N1].sets['ControlPoint'], cm3=100000)

# create new analysis job using the new model
J = mdb.Job(name='Analysis_Job', model=M1, description='TE_
    extraction_from_gear_pair')
```

Appendix B

ABAQUS Misalignment Parameter Study Files

B.1 Parameter Study Control File

```
# create a new parameter study with 5 variables, axial,
    radial, pitch and yaw misalignment and load. The
    parameter study uses the name ParameterStudy when
    generating files.
pStudy = ParStudy(par=('a_align','r_align','p_align','
    y_align','force'), name='ParameterStudy')

# discrete domains are attributed to the various variables.
     In this instance the pitch misalignments are studied
    with an inherent radial misalignment of 0.1 mm and load
    of 100,000 Nmm
pStudy.define(DISCRETE, par='a_align', domain=(0),reference
    =0)
pStudy.define(DISCRETE, par='r_align', domain=(0.1),
    reference=0)
pStudy.define(DISCRETE, par='p_align', domain=(0,0.01,0.1),
    reference=0)
pStudy.define(DISCRETE, par='y_align', domain=(0),reference
    =0)
pStudy.define(DISCRETE, par='force', domain=(100000),
    reference=0)

# the domains are sampled. In this instance each value in
    the discrete domains is studied
pStudy.sample(INTERVAL, par='a_align', interval=1)
```

```
pStudy.sample(INTERVAL, par='r_align', interval=1)
pStudy.sample(INTERVAL, par='p_align', interval=1)
pStudy.sample(INTERVAL, par='y_align', interval=1)
pStudy.sample(INTERVAL, par='force', interval=1)

# the variables are combined into a full factorial study
pStudy.combine(MESH)

# ABAQUS input files are generated based on the Misalignment
    template file
pStudy.generate(template='Misalignment2')

# the input files are executed. The INTERACTIVE keyword
   allows user control of the runs in the command window.
pStudy.execute(INTERACTIVE)
```

B.2 Modified ABAQUS Input File Template

```
*Heading
** Job name: Pitch_Misalignment Model name: Mod
** Generated by: Abaqus/CAE 6.10-1
*Preprint, echo=NO, model=NO, history=NO, contact=NO
*PARAMETER
** radial misalignment
r_align = 0
** axial misalignment
a_align = 0
** pitch misalignment
p_align = 0
** yaw misalignment
y_align = 0
** Mesh torque
force = 100000
** entered gear parameters (pressure angle (degrees and
   radians), number of teeth, module (mm))
PA = 20.
PAr = (PA/360)*2*pi
N1 = 25.
N2 = 24.
m = 5.
** calculated gear parameters (aligned pitch radii, aligned
   centre distance, misaligned centre distance, gear base
   radii, misaligned pressure angle,
** misaligned pitch radii, circular backlash, angular
   backlash)
rp1 = (N1*m)/2
rp2 = (N2*m)/2
CD = rp1 + rp2
CD_new = CD + r_align
rb1 = rp1*cos(PAr)
rb2 = rp2*cos(PAr)
PAr_new = acos((rb1+rb2)/(CD_new))
rp1_new = (rp1*cos(PAr))/(cos(PAr_new))
rp2_new = CD_new - rp1_new
b_circular = r_align*(tan(PAr_new))
b_angular = b_circular/rp1_new
** calculate the rotation of the pinion to bring the teeth
   into the assmebly position
pitch_rotation = (2*pi)/(2*N2)
** calculate the sine and cosine of the rotation to be used
   in the rotation of the local coordinate system in
   applying boundary conditions
```

```
COS_PR = cos(pitch_rotation)
SIN_PR = sin(pitch_rotation)
** convert the pitch and yaw misalignment values into
   radians
p_alignR = (p_align/360)*2*pi
y_alignR = (y_align/360)*2*pi
** calculate sines and cosines of the angular misalignments
COS_p_align = cos(p_alignR)
SIN_p_align = sin(p_alignR)
COS_y_align = cos(y_alignR)
SIN_y_align = sin(y_alignR)
** calculate the sine and cosine of the new pressure angle
cPA = cos(PAr_new)
sPA = sin(PAr_new)
** calculate the unit vectors for the angular misalignment
   about an axis paralell to the LOA
LOA_e1 = sPA
LOA_e2 = cPA
LOA_e3 = 0
** calculate the unit vectors for the angular misalignment
   about an axis perpendicular to the LOA
OLOA_e1 = -cPA
OLOA_e2 = sPA
OLOA_e3 = 0
** calculate terms in the LOA rodrigues rotation matrix
LOA11 = COS_y_align + ((LOA_e1*LOA_e1)*(1-COS_y_align))
LOA12 = (LOA_e1*LOA_e2*(1-COS_y_align)) - (LOA_e3*
   SIN_y_align)
LOA13 = (LOA_e2*SIN_y_align) + (LOA_e1*LOA_e3*(1-COS_y_align
   ))
LOA21 = (LOA_e1*LOA_e2*(1-COS_y_align)) + (LOA_e3*
   SIN_y_align)
LOA22 = COS_y_align + ((LOA_e2*LOA_e2)*(1-COS_y_align))
LOA23 = (LOA_e2*LOA_e3*(1-COS_y_align)) - (LOA_e1*
   SIN_y_align)
LOA31 = (-LOA_e2*SIN_y_align) + (LOA_e1*LOA_e3*(1-
   COS_y_align))
LOA32 = (LOA_e2*LOA_e3*(1-COS_y_align)) + (LOA_e1*
   SIN_y_align)
LOA33 = COS_y_align + ((LOA_e3*LOA_e3)*(1-COS_y_align))
** calculate terms in the OLOA rodrigues rotation matrix
OLOA11 = COS_p_align + ((OLOA_e1*OLOA_e1)*(1-COS_p_align))
OLOA12 = (OLOA_e1*OLOA_e2*(1-COS_p_align)) - (OLOA_e3*
   SIN_p_align)
OLOA13 = (OLOA_e2*SIN_p_align) + (OLOA_e1*OLOA_e3*(1-
   COS_p_align))
OLOA21 = (OLOA_e1*OLOA_e2*(1-COS_p_align)) + (OLOA_e3*
   SIN_p_align)
```

```
OLOA22 = COS_p_align + ((OLOA_e2*OLOA_e2)*(1-COS_p_align))
OLOA23 = (OLOA_e2*OLOA_e3*(1-COS_p_align)) - (OLOA_e1*
    SIN_p_align)
OLOA31 = (-OLOA_e2*SIN_p_align) + (OLOA_e1*OLOA_e3*(1-
    COS_p_align))
OLOA32 = (OLOA_e2*OLOA_e3*(1-COS_p_align)) + (OLOA_e1*
    SIN_p_align)
OLOA33 = COS_p_align + ((OLOA_e3*OLOA_e3)*(1-COS_p_align))
** rotation about the z-axis (shaft rotation)
Z11 = COS_PR
Z12 = -SIN_PR
Z13 = 0
Z21 = SIN_PR
Z22 = COS_PR
Z23 = 0
Z31 = 0
Z32 = 0
Z33 = 1
** calculate total rotation (order of rotation is about z
    then x then y - matrix multiplication order yxz)
** Y*X
YX11 = (OLOA11*LOA11) + (OLOA12*LOA21) + (OLOA13*LOA31)
YX12 = (OLOA11*LOA12) + (OLOA12*LOA22) + (OLOA13*LOA32)
YX13 = (OLOA11*LOA13) + (OLOA12*LOA23) + (OLOA13*LOA33)
YX21 = (OLOA21*LOA11) + (OLOA22*LOA21) + (OLOA23*LOA31)
YX22 = (OLOA21*LOA12) + (OLOA22*LOA22) + (OLOA23*LOA32)
YX23 = (OLOA21*LOA13) + (OLOA22*LOA23) + (OLOA23*LOA33)
YX31 = (OLOA31*LOA11) + (OLOA32*LOA21) + (OLOA33*LOA31)
YX32 = (OLOA31*LOA12) + (OLOA32*LOA22) + (OLOA33*LOA32)
YX33 = (OLOA31*LOA13) + (OLOA32*LOA23) + (OLOA33*LOA33)
** YX*Z
YXZ11 = (YX11*Z11) + (YX12*Z21) + (YX13*Z31)
YXZ12 = (YX11*Z12) + (YX12*Z22) + (YX13*Z32)
YXZ13 = (YX11*Z13) + (YX12*Z23) + (YX13*Z33)
YXZ21 = (YX21*Z11) + (YX22*Z21) + (YX23*Z31)
YXZ22 = (YX21*Z12) + (YX22*Z22) + (YX23*Z32)
YXZ23 = (YX21*Z13) + (YX22*Z23) + (YX23*Z33)
YXZ31 = (YX31*Z11) + (YX32*Z21) + (YX33*Z31)
YXZ32 = (YX31*Z12) + (YX32*Z22) + (YX33*Z32)
YXZ33 = (YX31*Z13) + (YX32*Z23) + (YX33*Z33)
** calculate total rotation
theta = acos((YXZ11+YXZ22+YXZ33-1)/2)
** calculate rotational axis vector terms
e1 = (YXZ32-YXZ23)/(2*sin(theta))
e2 = (YXZ13-YXZ31)/(2*sin(theta))
e3 = (YXZ21-YXZ12)/(2*sin(theta))
** calculate translational positions of pinion (YAW ONLY
    NEEDS CHANGING FOR PITCH)
```

```
**
** Calculate the positions (can be performed for either yaw
   or pitch misalignment - comment out as appropriate)
** Yaw Misalignment
**trans_x = (LOA11*rp2_new) + (LOA12*0) + (LOA13*-7.5) +
   rp1_new
**trans_y = (LOA21*rp2_new) + (LOA22*0) + (LOA23*-7.5)
**trans_z = (LOA31*rp2_new) + (LOA32*0) + (LOA33*-7.5) + 7.5
    + a_align
**
** Pitch Misalignment
trans_x = (OLOA11*rp2_new) + (OLOA12*0) + (OLOA13*-7.5) +
   rp1_new
trans_y = (OLOA21*rp2_new) + (OLOA22*0) + (OLOA23*-7.5)
trans_z = (OLOA31*rp2_new) + (OLOA32*0) + (OLOA33*-7.5) +
   7.5 + a_align
** calculate centre distances
CenterDis = trans_x
CenterDis2 = CenterDis + e1
trans_y2 = trans_y + e2
trans_z2 = trans_z + e3
** convert theta from radians to degrees
theta2 = (theta*360)/(2*pi)
** set rotations to bring the gears into contact and to
   rotate through a mesh cycle.
rotation = 0.001+b_angular
mesh_angle = (2*pi)/24
**
** PARTS
**
*Part, name=Gear_0
*Node
      1,           0.,       48.125,          2.5
      2,           0.,         12.5,          2.5
      3,           0.,         12.5,         12.5

*Element, type=C3D8R
  1,   177,   176,  3691,  3696,  4040,  4041, 35235, 35240
  2,   194,   193,  3704,  3700,  3776,  3775, 35248, 35244
  3,   186,  3692,  3701,   187,  3768, 35236, 35245,  3769
  4,   184,     5,  3692,  3702,  3750,   208, 35236, 35246

*Node
 144925,           0.,           0.,          7.5
*Nset, nset=Gear_0-RefPt_, internal
144925,
*Nset, nset=AllFaces
     1,     2,     3,     4,     5,     6,     7,     8,
```

```
     9,    10,    11,    12,    13,    14,    15,    16
    17,    18,    19,    20,    21,    22,    23,    24,

*Elset, elset=AllFaces
      1,      4,      5,      6,      8,     10,     11,
     12,     13,     14,     23,     24,     26,     27,
     29,     36,     38,     41,     42,     43,     45,

*Nset, nset=ContactTeeth
    38,    39,    40,    41,    42,    43,    44,    45,
    46,    47,   155,   156,   157,   158,   159,   160.
   161,   162,   163,   164,   519,   520,   521,   522,

*Elset, elset=ContactTeeth
   1352,   1353,   1354,   1355,   1356,   1358,   1359,
   1360,   1361,   1362,   1363,   1365,   1366,   1367,
   1368,   1379,   1380,   1381,   1382,   1383,   1385,

*Nset, nset=_PickedSet17, internal, generate
      1,  144924,       1
*Elset, elset=_PickedSet17, internal, generate
      1,  126987,       1
*Nset, nset=ControlPoint
 144925,
*Elset, elset=_CoupleSurf_S6, internal, generate
   13,  1308,    37
*Surface, type=ELEMENT, name=CoupleSurf
_CoupleSurf_S6, S6
*Elset, elset=_ContactSurf_S6, internal
   1352,   1359,   1391,   1393,   1522,   1524,   1528,
   1534,   1538,   1539,   1542,   1571,   1774,   1775,
   1782,   1794,   1810,   1814,   1816,   1817,   1822,
*Elset, elset=_ContactSurf_S4, internal
   1353,   1358,   1360,   1379,   1380,   1381,   1389,
   1390,   1392,   1525,   1530,   1535,   1536,   1537,
   1540,   1543,   1546,   1548,   1549,   1553,   1554,

*Elset, elset=_ContactSurf_S3, internal
   1354,   1368,   1382,   1383,   1386,   1387,   1388,
   1395,   1396,   1403,   1404,   1410,   1544,   1545,
   1572,   1580,   1593,   1599,   1600,   1601,   1602,

*Elset, elset=_ContactSurf_S5, internal
   1355,   1356,   1361,   1362,   1363,   1365,   1366,
   1367,   1385,   1394,   1399,   1400,   1401,   1402,
   1406,   1407,   1408,   1409,   1522,   1531,   1532,

*Surface, type=ELEMENT, name=ContactSurf
```

```
_ContactSurf_S6, S6
_ContactSurf_S4, S4
_ContactSurf_S3, S3
_ContactSurf_S5, S5
** Section: Gear_0_Section
*Solid Section, elset=_PickedSet17, material="Low Carbon
   Steel_0"
,
*End Part
**
*Part, name=Pinion_1
*Node
      1,           0.,       48.125,          2.5
      2,           0.,         12.5,          2.5
      3,           0.,         12.5,         12.5
      4,           0.,       48.125,         12.5

*Element, type=C3D8R
   1,  3748,  3759,  3753,  3745, 39782, 39793, 39787, 39779
   2,   193,   192,  3755,  3764,  3853,  3852, 39789, 39798
   3,  3756,  3767,  3761,  3769, 39790, 39801, 39795, 39803
   4,     6,   184,     5,   185,   258,  3821,   212,  3845

*Node
 177877,           0.,           0.,          7.5
*Nset, nset=Pinion_1-RefPt_, internal
177877,
*Nset, nset=AllFaces
     1,     2,     3,     4,     5,     6,     7,     8,
     9,    10,    11,    12,    13,    14,    15,    16,
    17,    18,    19,    20,    21,    22,    23,    24,

*Elset, elset=AllFaces
      4,      5,      7,      8,      9,     10,     11,
     12,     13,     14,     15,     16,     17,     18,
     24,     26,     27,     30,     31,     32,     39,

*Nset, nset=ContactTeeth
    76,    77,    78,    79,    80,    81,    82,    83,
    84,    85,   111,   112,   113,   114,   115,   116,
   117,   118,   119,   120,   745,   746,   747,   748,

*Elset, elset=ContactTeeth
   2410,   2412,   2415,   2416,   2417,   2419,   2420,
   2421,   2423,   2424,   2425,   2426,   2427,   2428,
   2429,   2431,   2432,   2433,   2434,   2436,   2437,

*Nset, nset=_PickedSet17, internal, generate
```

```
      1,  177876,       1
*Elset, elset=_PickedSet17, internal, generate
      1,  157770,       1
*Nset, nset=ControlPoint
 177877,
*Elset, elset=_CoupleSurf_S5, internal, generate
   14,  2219,    45
*Elset, elset=_CoupleSurf_S6, internal, generate
   15,  2220,    45
*Surface, type=ELEMENT, name=CoupleSurf
_CoupleSurf_S5, S5
_CoupleSurf_S6, S6
*Elset, elset=_ContactSurf_S6, internal
   2410,   2412,   2427,   2429,   2432,   2434,   2506,
   2511,   2516,   2517,   2524,   2674,   2675,   2681,
   2693,   2694,   2700,   2705,   2708,   2710,   2715,

*Elset, elset=_ContactSurf_S5, internal
   2415,   2417,   2431,   2440,   2441,   2443,   2446,
   2447,   2449,   2450,   2451,   2452,   2455,   2456,
   2458,   2462,   2465,   2494,   2500,   2502,   2507,

*Elset, elset=_ContactSurf_S4, internal
   2416,   2419,   2420,   2425,   2433,   2436,   2460,
   2514,   2523,   2532,   2672,   2680,   2682,   2690,
   2699,   2704,   2706,   2707,   2714,   2728,   2733,

*Elset, elset=_ContactSurf_S3, internal
   2421,   2423,   2424,   2426,   2428,   2437,   2445,
   2454,   2499,   2509,   2512,   2513,   2519,   2521,
   2525,   2539,   2546,   2548,   2549,   2553,   2555,

*Surface, type=ELEMENT, name=ContactSurf
_ContactSurf_S6, S6
_ContactSurf_S5, S5
_ContactSurf_S4, S4
_ContactSurf_S3, S3
** Section: Pinion_1_Section
*Solid Section, elset=_PickedSet17, material="Low Carbon
   Steel_1"
,
*End Part
**
**
** ASSEMBLY
**
*Assembly, name=Assembly
**
```

```
*Instance, name=Gear_0, part=Gear_0
        0.,      0.,      0.
        0.,      0.,      0.,      0.,      0.,      1., 10.8
*End Instance
**
*Instance, name=Pinion_1, part=Pinion_1
        <CenterDis>,    <trans_y>,      <trans_z>
        <CenterDis>,    <trans_y>,      <trans_z>,      <
            CenterDis2>,   <trans_y2>,     <trans_z2>, <
            theta2>
*End Instance
**
*Nset, nset=Tooth1_G, instance=Gear_0
    46,     47,    155,    156,   1174,   1175,   1176,   1177,
  1178,   1179,   1180,   1181,   1182,   1183,   1184,   1185,
  1186,   1187,   1188,   1189,   1190,   1191,   1192,   1193,

*Elset, elset=Tooth1_G, instance=Gear_0
   1394,    1395,    1396,    1403,    1404,    1406,    1407,
   1408,    1409,    1410,    2051,    2070,    2073,    2074,
   2075,    2076,    2077,    2078,    2080,    2081,    2082,

*Nset, nset=Tooth2_G, instance=Gear_0
    43,     44,    158,    159,    861,    862,    863,    864,
   865,    866,    867,    868,    869,    870,    871,    872,
   873,    874,    875,    876,    877,    878,    879,    880,

*Elset, elset=Tooth2_G, instance=Gear_0
   1385,    1386,    1387,    1388,    1389,    1399,    1400,
   1401,    1402,    1809,    1810,    1811,    1813,    1814,
   1815,    1816,    1817,    1818,    1819,    1821,    1822,

*Nset, nset=Tooth3_G, instance=Gear_0
    40,     41,    161,    162,    548,    549,    550,    551,
   552,    553,    554,    555,    556,    557,    558,    559,
   560,    561,    562,    563,    564,    565,    566,    567,

*Elset, elset=Tooth3_G, instance=Gear_0
   1358,    1359,    1360,    1361,    1362,    1363,    1365,
   1366,    1367,    1368,    1542,    1543,    1544,    1545,
   1546,    1547,    1548,    1549,    1550,    1553,    1554,

*Nset, nset=Tooth1_P, instance=Pinion_1
    76,     77,    119,    120,    745,    746,    747,    748,
   749,    750,    751,    752,    753,    754,    755,    756,
   757,    758,    759,    760,    761,    762,    763,    764,

*Elset, elset=Tooth1_P, instance=Pinion_1
```

```
   2410,   2412,   2415,   2416,   2417,   2437,   2440,
   2441,   2500,   2502,   2506,   2507,   2508,   2509,
   2510,   2511,   2512,   2513,   2514,   2516,   2517,

*Nset, nset=Tooth2_P, instance=Pinion_1
    79,    80,   116,   117,  1013,  1014,  1015,  1016,
  1017,  1018,  1019,  1020,  1021,  1022,  1023,  1024,
  1025,  1026,  1027,  1028,  1029,  1030,  1031,  1032,

*Elset, elset=Tooth2_P, instance=Pinion_1
   2424,   2425,   2443,   2445,   2446,   2447,   2449,
   2450,   2451,   2710,   2711,   2713,   2714,   2715,
   2716,   2718,   2722,   2724,   2725,   2726,   2727,

*Nset, nset=Tooth3_P, instance=Pinion_1
    82,    83,   113,   114,  1327,  1328,  1329,  1330,
  1331,  1332,  1333,  1334,  1335,  1336,  1337,  1338,
  1339,  1340,  1341,  1342,  1343,  1344,  1345,  1346,

*Elset, elset=Tooth3_P, instance=Pinion_1
   2429,   2431,   2432,   2433,   2434,   2455,   2456,
   2458,   2460,   2499,   2943,   2959,   2960,   2961,
   2962,   2963,   2964,   2965,   2966,   2968,   2970,

*Nset, nset=_PickedSet12, internal, instance=Pinion_1
 177877,
*Nset, nset=_T-Pinion_1-Pinion-CoordinateSys, internal
Pinion_1.ControlPoint,
*Transform, nset=_T-Pinion_1-Pinion-CoordinateSys
<YXZ11>, <YXZ21>, <YXZ31>, <YXZ12>, <YXZ22>, <YXZ32>
** Constraint: Gear_0_Couple
*Coupling, constraint name=Gear_0_Couple, ref node=Gear_0.
   ControlPoint, surface=Gear_0.CoupleSurf
*Kinematic
** Constraint: Pinion_1_Couple
*Coupling, constraint name=Pinion_1_Couple, ref node=
   Pinion_1.ControlPoint, surface=Pinion_1.CoupleSurf
*Kinematic
*End Assembly
**
** MATERIALS
**
*Material, name="Low Carbon Steel_0"
*Elastic
210000., 0.3
*Material, name="Low Carbon Steel_1"
*Elastic
210000., 0.3
```

```
**
** INTERACTION PROPERTIES
**
*Surface Interaction, name=Cont_Prop
1.,
*Surface Behavior, pressure-overclosure=HARD
**
** INTERACTIONS
**
** Interaction: Tooth_Contact
*Contact Pair, interaction=Cont_Prop, type=SURFACE TO
   SURFACE, no thickness
Pinion_1.ContactSurf, Gear_0.ContactSurf
** ----------------------------------------------------
**
** STEP: Contact
**
*Step, name=Contact, nlgeom=YES, inc=1000000
*Static
0.5, 1., 1e-06, 0.5
**
** BOUNDARY CONDITIONS
**
** Name: Gear_vBC Type: Velocity/Angular velocity
*Boundary, type=VELOCITY
Gear_0.ControlPoint, 1, 1
Gear_0.ControlPoint, 2, 2
Gear_0.ControlPoint, 3, 3
Gear_0.ControlPoint, 4, 4
Gear_0.ControlPoint, 5, 5
Gear_0.ControlPoint, 6, 6
** Name: Pinion_1_BC Type: Displacement/Rotation
*Boundary
Pinion_1.ControlPoint, 1, 1
Pinion_1.ControlPoint, 2, 2
Pinion_1.ControlPoint, 3, 3
Pinion_1.ControlPoint, 4, 4
Pinion_1.ControlPoint, 5, 5
Pinion_1.ControlPoint, 6, 6, <rotation>
**
** OUTPUT REQUESTS
**
*Restart, write, frequency=0
**
** FIELD OUTPUT: F-Output-1
**
*Output, field, time interval=0.5
*Node Output
```

```
U, CF
*Element Output, directions=YES
LE, S
*Contact Output
CDISP, CFORCE, CNAREA, CSTATUS, CSTRESS
**
** HISTORY OUTPUT: Position_Gear_0
**
*Output, history, time interval=0.5
*Node Output, nset=Gear_0.ControlPoint
RF1, RF2, RF3, RM1, RM2, RM3, UR1, UR2, UR3
**
** HISTORY OUTPUT: Position_Pinion_1
**
*Node Output, nset=Pinion_1.ControlPoint
RF1, RF2, RF3, RM1, RM2, RM3, UR1, UR2, UR3
*End Step
** ----------------------------------------------------------------
**
** STEP: Force
**
*Step, name=Force, nlgeom=YES, inc=1000000
*Static
0.5, 1., 1e-06, 0.5
**
** BOUNDARY CONDITIONS
**
** Name: Gear_vBC Type: Velocity/Angular velocity
*Boundary, op=NEW, type=VELOCITY
Gear_0.ControlPoint, 1, 1
Gear_0.ControlPoint, 2, 2
Gear_0.ControlPoint, 3, 3
Gear_0.ControlPoint, 4, 4
Gear_0.ControlPoint, 5, 5
** Name: Pinion_1_BC Type: Displacement/Rotation
*Boundary, op=NEW
Pinion_1.ControlPoint, 1, 1
Pinion_1.ControlPoint, 2, 2
Pinion_1.ControlPoint, 3, 3
Pinion_1.ControlPoint, 4, 4
Pinion_1.ControlPoint, 5, 5
Pinion_1.ControlPoint, 6, 6
**
** LOADS
**
** Name: Load    Type: Moment
*Cload
Gear_0.ControlPoint, 6, <force>
```

```
**
** OUTPUT REQUESTS
**
*Restart, write, frequency=0
**
** FIELD OUTPUT: F-Output-1
**
*Output, field, time interval=0.5
*Node Output
U, CF
*Element Output, directions=YES
LE, S
*Contact Output
CDISP, CFORCE, CNAREA, CSTATUS, CSTRESS
**
** HISTORY OUTPUT: Position_Gear_0
**
*Output, history, time interval=0.5
*Node Output, nset=Gear_0.ControlPoint
RF1, RF2, RF3, RM1, RM2, RM3, UR1, UR2, UR3
**
** HISTORY OUTPUT: Position_Pinion_1
**
*Node Output, nset=Pinion_1.ControlPoint
RF1, RF2, RF3, RM1, RM2, RM3, UR1, UR2, UR3
*End Step
** ----------------------------------------------------------------
**
** STEP: Rotate
**
*Step, name=Rotate, nlgeom=YES, inc=1000000
*Static
0.02, 1., 1e-06, 0.02
**
** BOUNDARY CONDITIONS
**
** Name: Pinion_1_BC Type: Displacement/Rotation
*Boundary
Pinion_1.ControlPoint, 3, 3
Pinion_1.ControlPoint, 4, 4
Pinion_1.ControlPoint, 5, 5
Pinion_1.ControlPoint, 6, 6, <mesh_angle>
**
** OUTPUT REQUESTS
**
*Restart, write, frequency=0
**
** FIELD OUTPUT: F-Output-1
```

```
**
*Output, field, time interval=0.05
*Node Output
U, CF
*Element Output, directions=YES
LE, S
*Contact Output
CDISP, CFORCE, CNAREA, CSTATUS, CSTRESS
**
** HISTORY OUTPUT: T1_G
**
*Output, history, time interval=0.02
*Contact Output, nset=Tooth1_G
CFN1, CFN2, CFN3, CFNM, XN1, XN2, XN3
**
** HISTORY OUTPUT: T1_P
**
*Contact Output, nset=Tooth1_P
CFN1, CFN2, CFN3, CFNM, XN1, XN2, XN3
**
** HISTORY OUTPUT: T2_G
**
*Contact Output, nset=Tooth2_G
CFN1, CFN2, CFN3, CFNM, XN1, XN2, XN3
**
** HISTORY OUTPUT: T2_P
**
*Contact Output, nset=Tooth2_P
CFN1, CFN2, CFN3, CFNM, XN1, XN2, XN3
**
** HISTORY OUTPUT: T3_G
**
*Contact Output, nset=Tooth3_G
CFN1, CFN2, CFN3, CFNM, XN1, XN2, XN3
**
** HISTORY OUTPUT: T3_P
**
*Contact Output, nset=Tooth3_P
CFN1, CFN2, CFN3, CFNM, XN1, XN2, XN3
**
** HISTORY OUTPUT: Position_Gear_0
**
*Output, history, time interval=0.02
*Node Output, nset=Gear_0.ControlPoint
RF1, RF2, RF3, RM1, RM2, RM3, UR1, UR2, UR3
**
** HISTORY OUTPUT: Position_Pinion_1
**
```

```
*Node Output, nset=Pinion_1.ControlPoint
RF1, RF2, RF3, RM1, RM2, RM3, UR1, UR2, UR3
*End Step
```

Appendix C

Rig Component Drawings

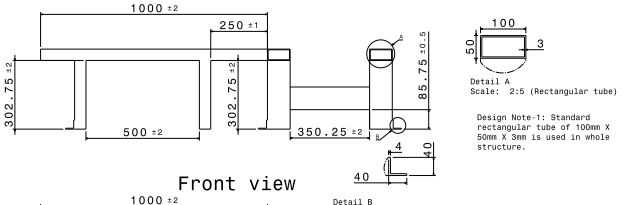

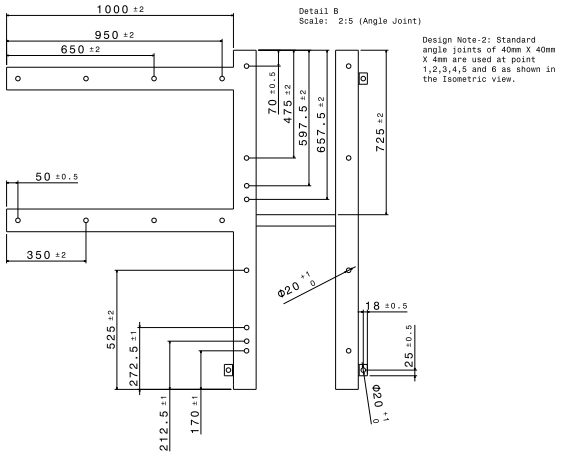

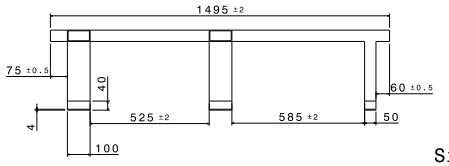

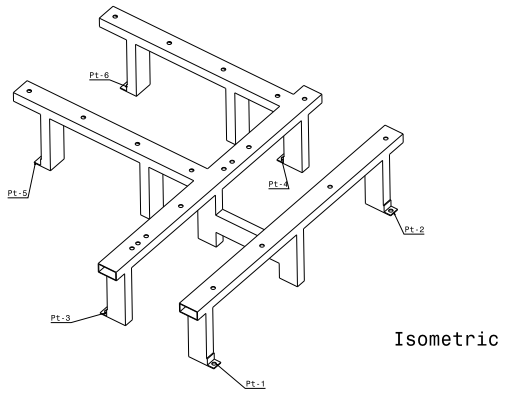

Note: All dimensions are in mm.

GEAR TEST RIG PROJECT
PART NAME: FOUNDATION FRAME
PART NUMBER: STA-008
SCALE: 1:5
SHEET SIZE: A0
MATERIAL: STEEL(Carbon steel)
Version: 8.1
Dated: 29th October 2009

Figure C.1: Foundation frame

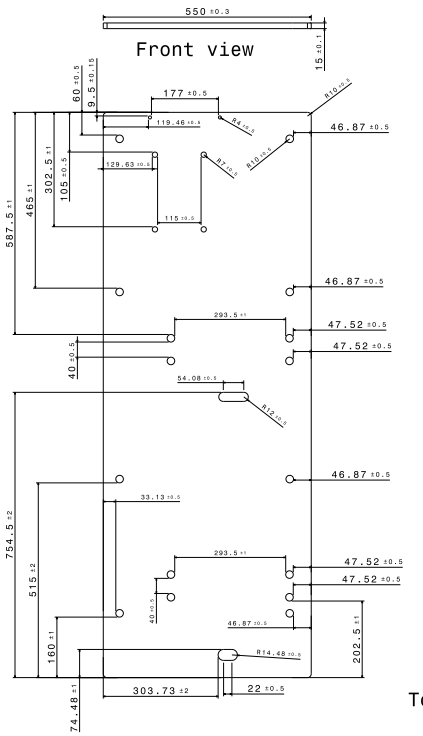

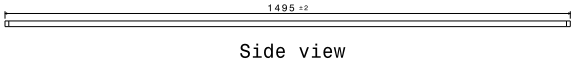

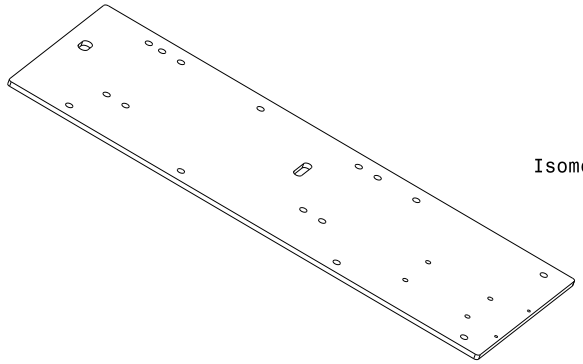

Note: All dimensions are in mm.

GEAR TEST RIG PROJECT
PART NAME: SPUR FOUNDATION PLATE
PART NUMBER: STA-006
SCALE: 1:3
SHEET SIZE: A0
MATERIAL: STEEL(Carbon steel)
Version: 6.1
Dated: 29th October 2009

Figure C.2: Spur foundation plate

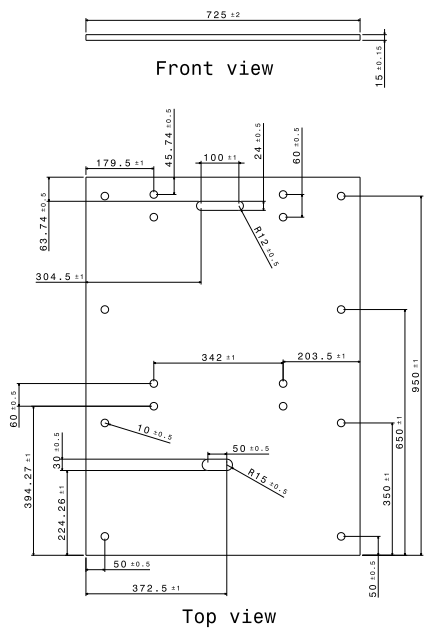

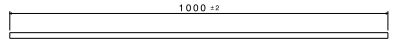

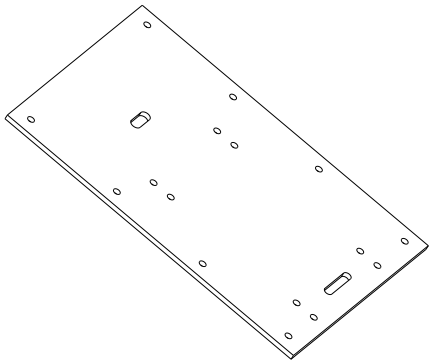

Isometric

Note: All dimensions are in mm.

GEAR TEST RIG PROJECT
PART NAME: BEVEL FOUNDATION PLATE
PART NUMBER: STA-005
SCALE: 1:3
SHEET SIZE: A0
MATERIAL: STEEL(Carbon steel)
Version: 5.1
Dated: 29th October 2009

Figure C.3: Bevel foundation plate

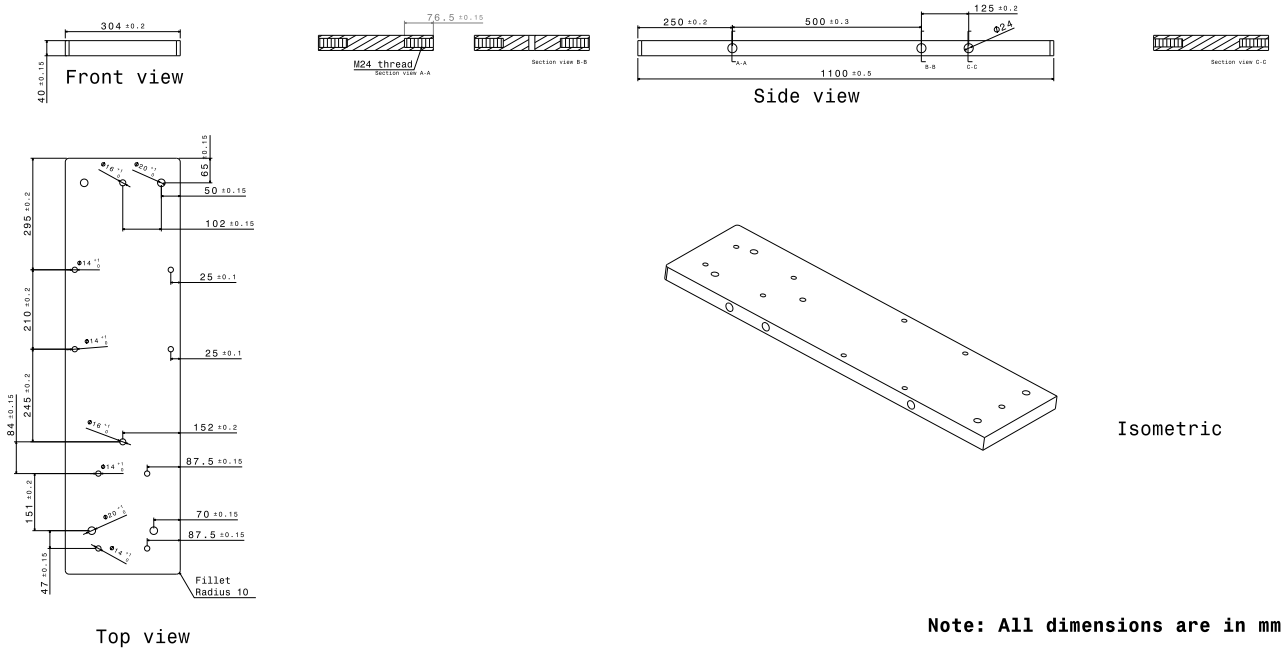

Note: All dimensions are in mm.

GEAR TEST RIG PROJECT
PART NAME: MOVING PLATE
PART NUMBER: DYN-004
SCALE: 1:3
SHEET SIZE: A0
MATERIAL: STEEL(Carbon steel)
Version: 4.1
Dated: 29th October 2009

Figure C.4: Floating platform

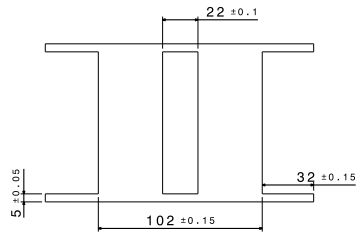

Front view

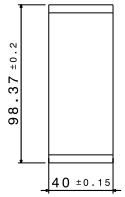

Side view

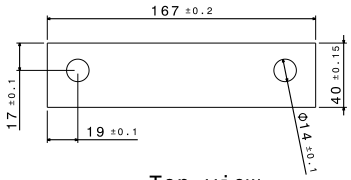

Top view

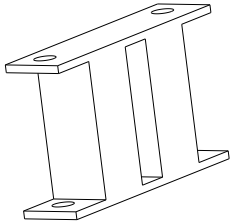

Isometric view

Material Note: Frame can be made by using two standard flat rectangular plates with two standard square tubes. Sizes of plates and tubes are 40mm x 5mm and 40mm x 40mm respectively.

Note: All dimensions are in mm.

GEAR TEST RIG PROJECT
PART NAME: BEARING BASE FRAME
PART NUMBER: DYN-001
SCALE: 1:1
SHEET SIZE: A1
MATERIAL: STEEL (Carbon steel)
Version: 1.1
Dated: 29th October 2009

Figure C.5: Small bearing support frame

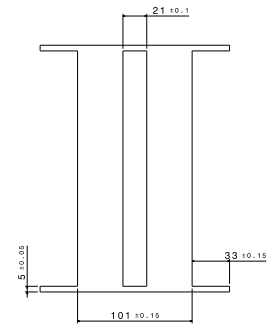

Front view

Side view

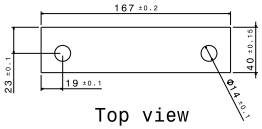

Top view

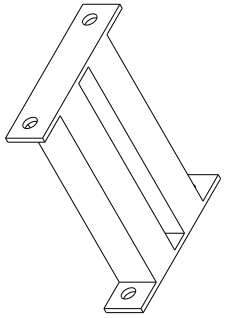

Isometric

Material Note: Frame can be made by using two standard flat rectangular plates with two standard square tubes. Sizes of plates and tubes are 40mm x 5mm and 40mm x 40mm respectively.

Note: All dimensions are in mm.

GEAR TEST RIG PROJECT
PART NAME: BEARING BASE FRAME
PART NUMBER: STA-004
SCALE: 1:1
SHEET SIZE: A0
MATERIAL: STEEL(Carbon steel)
Version: 4.1
Dated: 29th October 2009

Figure C.6: Large bearing support frame

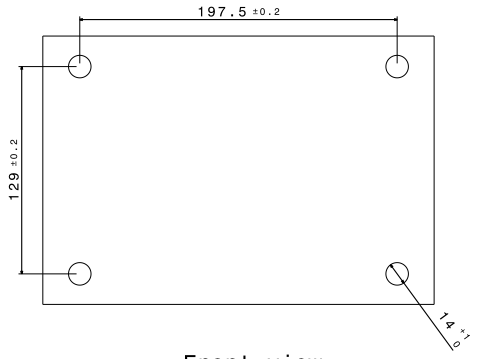

Front view

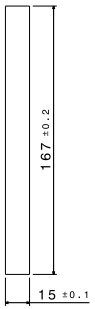

Side view

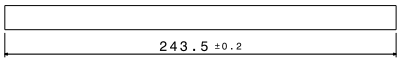

Top view

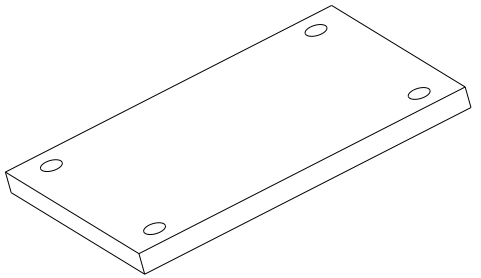

Isometric view

Note: All dimensions are in mm.

GEAR TEST RIG PROJECT
PART NAME: BEARING BASE PLATE
PART NUMBER: STA-003
SCALE: 1:1
SHEET SIZE: A1
MATERIAL: STEEL(carbon steel)
Version: 3.1
Dated: 29th October 2009

Figure C.7: Bearing base plate

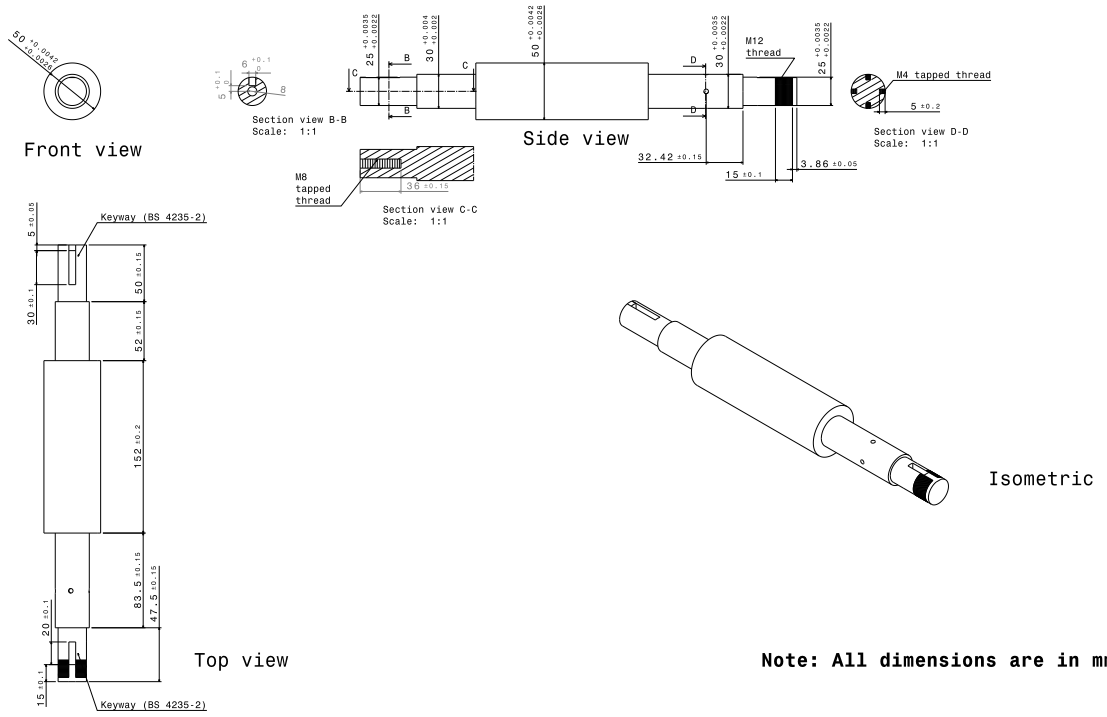

Note: All dimensions are in mm.

GEAR TEST RIG PROJECT
PART NAME: MOTOR SHAFT
PART NUMBER: DYN-003
SCALE: 1:1
SHEET SIZE: A0
MATERIAL: STEEL(EN19 OR EN36)
Version: 3.1
Dated: 29th October 2009

Figure C.8: Shaft

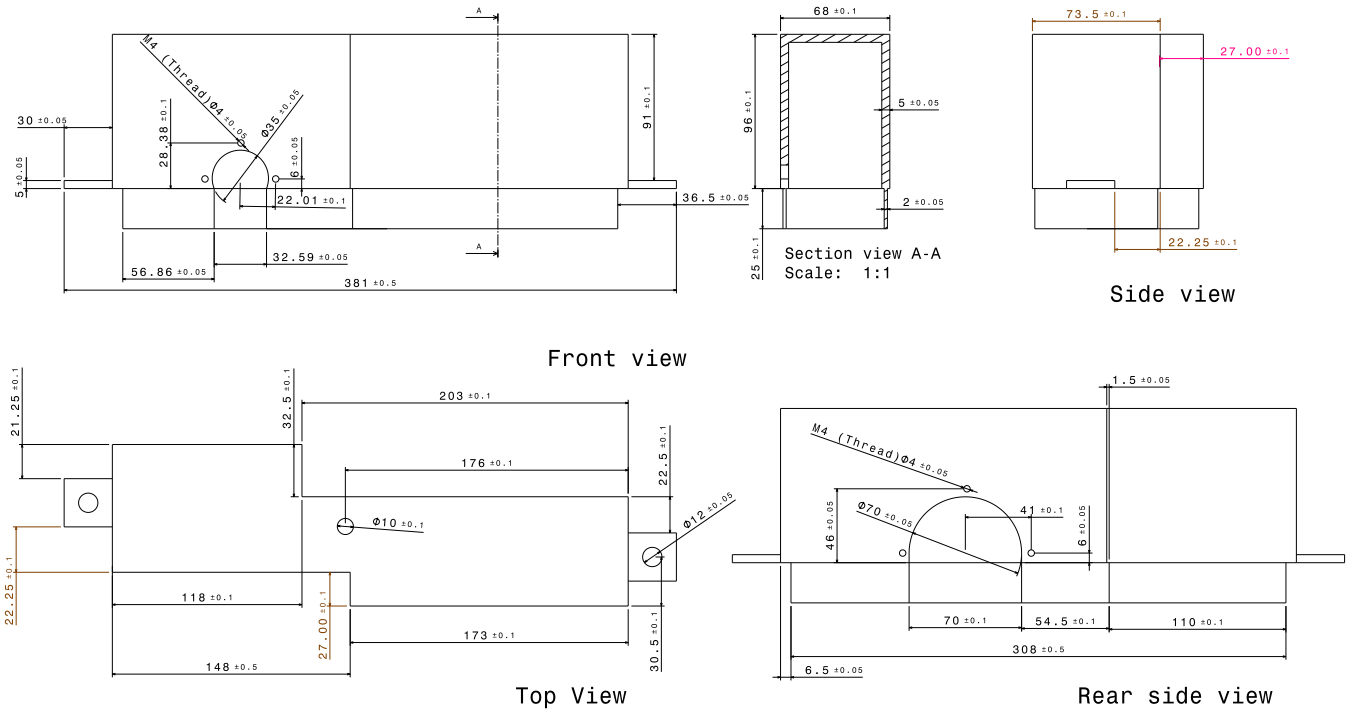

Note: All dimensions are in mm.

GEAR TEST RIG PROJECT
PART NAME: Lubrication box part-1
PART NUMBER: STA-010
SCALE: 1:1
SHEET SIZE: A1
MATERIAL: Aluminium
Version: 1.2
Dated: 1st March 2010

Figure C.9: Top of lubrication box

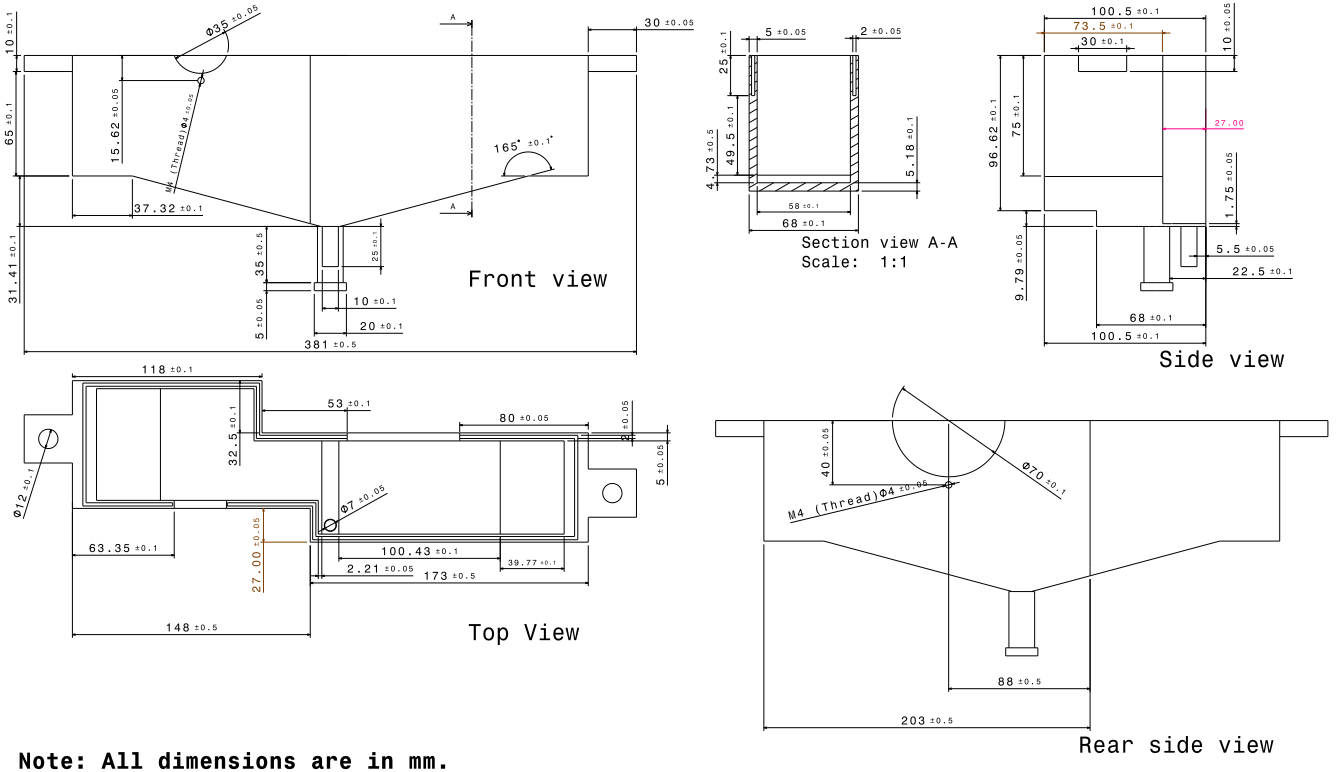

Note: All dimensions are in mm.

GEAR TEST RIG PROJECT
PART NAME: Lubrication box part-2
PART NUMBER: STA-011
SCALE: 1:1
SHEET SIZE: A1
MATERIAL: Aluminium
Version: 1.2
Dated: 1st March 2010

Figure C.10: Bottom of lubrication box

Appendix D

Bearing Hertzian Contact Stiffness

This appendix derives the contact stiffness between two bodies with an elliptical contact.

Palmgren [122] and Lim and Singh [115–118] state the Hertzian contact force deflection relationship for deep grove ball bearings can be given as

$$F_h = K_h \delta_h^{3/2} \tag{D.1}$$

Where F_h is the applied force, K_h is the Hertzian contact stiffness and δ_h is the Hertzian deflection, which can be approximated as

$$\delta_h = \frac{\pi a p_0}{2E^*} \tag{D.2}$$

where a is the contact radius, p_0 is the maximum contact pressure and E^* is the effective Young's modulus of contact, given as:

$$\frac{1}{E^*} = \frac{1-\nu_1^2}{E_1} + \frac{1-\nu_2^2}{E_2} \tag{D.3}$$

Where E_i and ν_i are the Young's modulus and Poisson's ratio of the two contacting surfaces. Shilgley [8] states that the contact ellipse radius for spherical

convex-concave contact can be given as

$$a = \sqrt[3]{\frac{3F_h}{8}\frac{\left[\left(1-\nu_1^2\right)/E_1\right]+\left[\left(1-\nu_2^2\right)/E_2\right]}{(1/d_1)-(1/d_2)}} \tag{D.4}$$

where d_i is the radius of the contacting surfaces and the maximum contact pressure p_0 is given as

$$p_0 = \frac{3F_h}{2\pi a^2} \tag{D.5}$$

Combining Equations (D.2) - (D.4) yields an equation for determining the Hertzian contact stiffness for circular contact in the form of Equation (D.1); however in bearings the contact area is not circular but elliptical due to varying curvatures in the two principle directions, resulting in two axes lengths to consider. To generate a relationship between the force and deflection in the form of Equation (D.1) Greenwood [123] approximated the geometric mean contact radius ($c_e = \sqrt{a_e b_e}$ where a_e and b_e are the major and minor axes) using equations for circular contact and an effective radius (R_e)

$$c_e = \left(\frac{3}{4}\frac{F_h R_e}{E^*}\right)^{1/3} \tag{D.6}$$

$$R_e = \left[A.B.\left(\frac{A+B}{2}\right)\right]^{-1/3} \tag{D.7}$$

Equation (D.6) is identical in form to Equation (D.4) however the effective radius (R_e) is taken as a compromise between the arithmetic and geometric mean of the curvatures in the two directions as shown in Equation (D.7), where A and B are the curvatures in the two directions.

$$A = \frac{1}{R_{1I}} + \frac{1}{R_{2I}} \tag{D.8a}$$

$$B = \frac{1}{R_{1II}} + \frac{1}{R_{2II}} \tag{D.8b}$$

where R is the radius of the surfaces, subscript 1,2 indicate the contacting

body and subscripts I, II indicate the direction of curvature. With knowledge of the mean contact radius (c_e) the minor and major semi-axis lengths can be approximated using the simple equation

$$\left(\frac{b}{a}\right) \sim \left(\frac{A}{B}\right)^{2/3} \tag{D.9}$$

and with the mean contact radius, which is equal to $\sqrt{ab}$, the contact radii can be found as

$$a = c\left(\frac{A}{B}\right)^{-1/3} \tag{D.10a}$$

$$b = c\left(\frac{A}{B}\right)^{1/3} \tag{D.10b}$$

Using the Hetzian deflection equation shown in Equation (D.2) with a equal to the arithmetic mean of the two radii ($(a_e + b_e)/2$), and the maximum pressure as given in Equation (D.5) using the mean contact radius (c_e) rather than the circular radius (a) and combining, results in the following expression for the deflection

$$\delta_h = \frac{3}{8}\frac{F_h \lambda}{E^* c_e} \tag{D.11a}$$

where λ is a constant, which appears during the averaging of the contact radii

$$\left(\frac{a_e + b_e}{2}\right) = \frac{c_e}{2}\left(\frac{1}{(A/B)^{1/3}} + \left(\frac{A}{B}\right)^{1/3}\right) = \frac{c_e}{2}\lambda$$

$$\therefore \lambda = \left(\frac{1}{(A/B)^{1/3}} + \left(\frac{A}{B}\right)^{1/3}\right) \tag{D.11b}$$

Through substituting Equation (D.6) into Equation (D.11a) and rearranging the deflection becomes

$$\delta_h^{3/2} = \frac{3\sqrt{3}}{8\sqrt{6}}\frac{\lambda^{3/2}}{E^*\sqrt{R_e}}F_h \tag{D.11c}$$

Finally Equation (D.11c) can be rearranged into the form of Equation (D.1) and

the Hertzian stiffness can be extracted to give

$$K_h = \frac{8\sqrt{6}}{3\sqrt{3}} \frac{E^* \sqrt{R_e}}{\lambda^{3/2}} \tag{D.11d}$$

Appendix E

Component Mode Synthesis Theory

Taking a simple static problem of the type $\mathbf{Ku} = \mathbf{F}$ and partitioning the matrices into the retained or master DOF ($\mathbf{u}_m$) and the eliminated or slave DOF ($\mathbf{u}_s$), the system of equations becomes.

$$\begin{bmatrix} \mathbf{K}_{mm} & \mathbf{K}_{ms} \\ \mathbf{K}_{sm} & \mathbf{K}_{ss} \end{bmatrix} \begin{Bmatrix} \mathbf{u}_m \\ \mathbf{u}_s \end{Bmatrix} = \begin{Bmatrix} \mathbf{F}_m \\ \mathbf{F}_s \end{Bmatrix} \tag{E.1}$$

which when expanded equates to

$$\mathbf{K}_{mm}\mathbf{u}_m + \mathbf{K}_{ms}\mathbf{u}_s = \mathbf{F}_m \tag{E.2a}$$

$$\mathbf{K}_{sm}\mathbf{u}_m + \mathbf{K}_{ss}\mathbf{u}_s = \mathbf{F}_s \tag{E.2b}$$

Rearranging Equation (E.2b) in terms of the slave DOF results in.

$$\mathbf{u}_s = \mathbf{K}_{ss}^{-1}\mathbf{F}_s - \mathbf{K}_{ss}^{-1}\mathbf{K}_{sm}\mathbf{u}_m \tag{E.3}$$

And by substituting Equation (E.3) into Equation (E.2a) the response of the substructure can be determined from the motions of the master DOF.

$$[\mathbf{K}_{mm} - \mathbf{K}_{ms}\mathbf{K}_{ss}^{-1}\mathbf{K}_{sm}]\mathbf{u}_m = \mathbf{F}_m - \mathbf{K}_{ms}\mathbf{K}_{ss}^{-1}\mathbf{F}_s \tag{E.4a}$$

From which the reduced stiffness matrix ($\mathbf{K}_r$) can be determined.

$$\mathbf{K}_r = \mathbf{K}_{mm} - \mathbf{K}_{ms}\mathbf{K}_{ss}^{-1}\mathbf{K}_{sm} \tag{E.4b}$$

This leads to a transformation matrix ($\mathbf{J}$) and when applied to the global stiffness matrix ($\mathbf{K}$) generates the reduced stiffness matrix ($\mathbf{K}_r$).

$$\mathbf{J} = \begin{bmatrix} \mathbf{I} \\ -\mathbf{K}_{ss}^{-1}\mathbf{K}_{sm} \end{bmatrix} \tag{E.5a}$$

$$\mathbf{K}_r = \mathbf{J}^T\mathbf{K}\mathbf{J} \tag{E.5b}$$

Where $\mathbf{I}$ is an identity matrix.

This technique is known as Guyan reduction [124], which can be applied to the dynamic problem $\mathbf{M}\ddot{\mathbf{u}} + \mathbf{C}\dot{\mathbf{u}} + \mathbf{K}\mathbf{u} = \mathbf{F}$ by applying the same transformation matrix ($\mathbf{J}$) to the mass matrix, as performed in Equation (E.5b), and by applying Rayleigh proportional damping to the system of equations.

Although the stiffness matrix is exact, Guyan reduction assumes that for lower frequency modes, the inertia forces of the slave nodes are much less important than the elastic forces between the master DOF and therefore the slave DOF are assumed to move in a quasi-static sense, with the mass apportioned to the master DOF. This means that errors are inherent in the reduction technique, however these can be reduced with appropriate selection of the master DOF.

An alternative dynamic reduction technique based on Craig-Bampton CMS [125] is also available, which uses a combination of the master DOF and generalized DOF ($\mathbf{q}$) associated with the natural modes of the substructure, assuming the master DOF are fixed. This leads to a generalized system of equations based on the master DOF and the natural modes of the substructure.

$$\mathbf{J}^T\mathbf{M}\mathbf{J}\begin{Bmatrix}\ddot{\mathbf{u}}\\ \ddot{\mathbf{q}}\end{Bmatrix}+\mathbf{J}^T\mathbf{C}\mathbf{J}\begin{Bmatrix}\dot{\mathbf{u}}\\ \dot{\mathbf{q}}\end{Bmatrix}+\mathbf{J}^T\mathbf{K}\mathbf{J}\begin{Bmatrix}\mathbf{u}\\ \mathbf{q}\end{Bmatrix}=\mathbf{J}^T\mathbf{P} \tag{E.6a}$$

Where the transfer matrix ($\mathbf{J}$) is constructed of the static transfer matrix and the matrix of eigenvectors ($\boldsymbol{\phi}_E$)

$$\mathbf{J}=\begin{bmatrix}\mathbf{I} & \mathbf{0}\\ -\mathbf{K}_{ss}^{-1}\mathbf{K}_{sm} & (\boldsymbol{\phi}_E)\end{bmatrix} \tag{E.6b}$$

The inclusion of the natural modes of the structure enables the setting of a frequency range of interest, however no information is gained on the accuracy of the procedure. To assess the appropriate number of eigenvalues to include in the reduced matrix a simple model is developed, where the reduced mass, spring and damper are periodically forced at the master DOF based on the gear contact frequency, which at a speed of around 1500 rpm and with 24 contact cycles per revolution leads to a frequency of 600 Hz. Looking purely at the small bearing support described in Chapter 5, the displacement in the direction of loading with 1, 5, 10 and 30 natural modes are investigated and shown in Figure E.1.

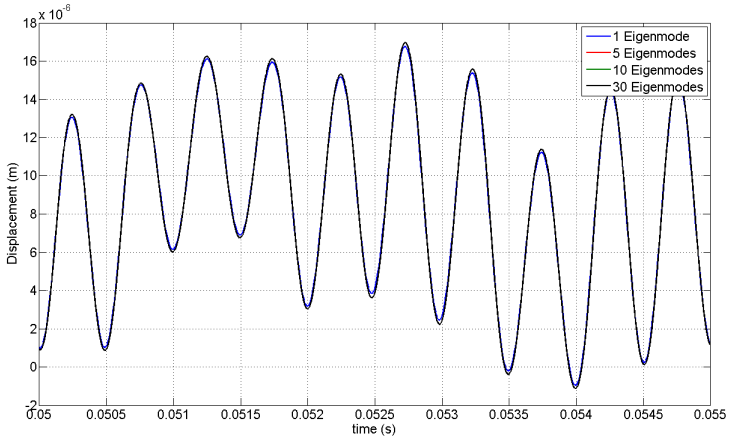

Figure E.1: Small support response data using Craig-Bampton Component Mode Synthesis with various included eigenmodes

This shows that the number of included eigenmodes has little effect on the dynamic response of the supports under the primary meshing frequency; however it

is noted that under increased loading frequency this may not hold true. Therefore initially the Guyan reduction technique, which does not contain the system eigenmodes, is used as an approximation of the supporting structure stiffness. This is calculated within ABAQUS from the full finite element model of the supporting structure with two reference points placed in the middle of the top and bottom surfaces acting as the master DOF, as shown in Figure E.2 for the smaller support, where the master DOF are coupled to their respective surfaces.

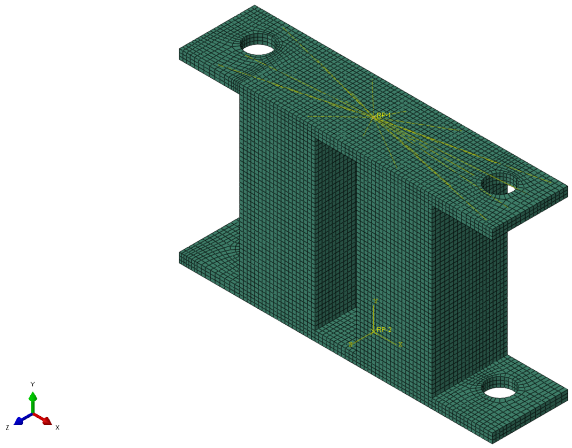

Figure E.2: Model Order Reduction model of small support

Appendix F

Support Matrices

F.1 Small Support

$$\mathbf{K} = \begin{bmatrix}
1.55E+08 & -4.33E+02 & -2.20E+04 & -1.17E+03 & -4.50E+02 & -7.60E+06 & -1.55E+08 & 4.33E+02 & 2.20E+04 & -1.00E+03 & 4.50E+02 & -7.60E+06 \\
-4.33E+02 & 1.37E+09 & -1.03E+03 & -9.91E+01 & 1.57E+02 & -2.31E+02 & 4.33E+02 & -1.37E+09 & 1.03E+03 & -2.25E+00 & -1.57E+02 & 2.74E+02 \\
-2.20E+04 & -1.03E+03 & 1.57E+08 & 7.71E+06 & -1.60E+03 & 1.05E+03 & 2.20E+04 & 1.03E+03 & -1.57E+08 & 7.71E+06 & 1.60E+03 & 1.12E+03 \\
-1.17E+03 & -9.91E+01 & 7.71E+06 & 2.02E+06 & -7.95E+01 & 7.52E+01 & 1.17E+03 & 9.91E+01 & -7.71E+06 & -1.27E+06 & 7.95E+01 & 3.96E+01 \\
-4.50E+02 & 1.57E+02 & -1.60E+03 & -7.95E+01 & 3.46E+05 & 2.30E+01 & 4.50E+02 & -1.57E+02 & 1.60E+03 & -7.77E+01 & -3.46E+05 & 2.13E+01 \\
-7.60E+06 & -2.31E+02 & 1.05E+03 & 7.52E+01 & 2.30E+01 & 7.01E+05 & 7.60E+06 & 2.31E+02 & -1.05E+03 & 2.84E+01 & -2.30E+01 & 4.74E+04 \\
-1.55E+08 & 4.33E+02 & 2.20E+04 & 1.17E+03 & 4.50E+02 & 7.60E+06 & 1.55E+08 & -4.33E+02 & -2.20E+04 & 1.00E+03 & -4.50E+02 & 7.60E+06 \\
4.33E+02 & -1.37E+09 & 1.03E+03 & 9.91E+01 & -1.57E+02 & 2.31E+02 & -4.33E+02 & 1.37E+09 & -1.03E+03 & 2.25E+00 & 1.57E+02 & -2.74E+02 \\
2.20E+04 & 1.03E+03 & -1.57E+08 & -7.71E+06 & 1.60E+03 & -1.05E+03 & -2.20E+04 & -1.03E+03 & 1.57E+08 & -7.71E+06 & -1.60E+03 & -1.12E+03 \\
-1.00E+03 & -2.25E+00 & 7.71E+06 & -1.27E+06 & -7.77E+01 & 2.84E+01 & 1.00E+03 & 2.25E+00 & -7.71E+06 & 2.02E+06 & 7.77E+01 & 7.01E+01 \\
4.50E+02 & -1.57E+02 & 1.60E+03 & 7.95E+01 & -3.46E+05 & -2.30E+01 & -4.50E+02 & 1.57E+02 & -1.60E+03 & 7.77E+01 & 3.46E+05 & -2.13E+01 \\
-7.60E+06 & 2.74E+02 & 1.12E+03 & 3.96E+01 & 2.13E+01 & 4.74E+04 & 7.60E+06 & -2.74E+02 & -1.12E+03 & 7.01E+01 & -2.13E+01 & 7.01E+05
\end{bmatrix}$$

$$\mathbf{M} = \begin{bmatrix} 3.93E-01 & 4.52E-05 & -1.60E-05 & -2.64E-06 & 7.64E-07 & -2.55E-03 & 6.67E-02 & -4.37E-05 & -1.76E-04 & 6.44E-06 & -1.29E-06 & 1.70E-03 \\ 4.52E-05 & 3.87E-01 & -9.66E-06 & -1.46E-07 & 2.79E-06 & -3.70E-05 & 4.50E-05 & 7.24E-02 & 3.18E-05 & -1.03E-06 & 2.71E-06 & 4.47E-07 \\ -1.60E-05 & -9.66E-06 & 3.95E-01 & 2.76E-03 & 3.58E-05 & 6.23E-07 & 5.37E-05 & 9.94E-06 & 6.44E-02 & -1.77E-03 & 1.84E-06 & 3.56E-06 \\ -2.64E-06 & -1.46E-07 & 2.76E-03 & 7.45E-04 & 1.13E-07 & 3.67E-08 & -1.10E-06 & -2.73E-07 & 1.77E-03 & 3.49E-05 & -2.08E-08 & 8.94E-08 \\ 7.64E-07 & 2.79E-06 & 3.58E-05 & 1.13E-07 & 7.89E-04 & -2.02E-08 & -5.41E-07 & -2.68E-06 & -2.67E-06 & 1.37E-07 & 9.97E-05 & 8.26E-09 \\ -2.55E-03 & -3.70E-05 & 6.23E-07 & 3.67E-08 & -2.02E-08 & 9.13E-05 & -1.70E-03 & 9.98E-07 & 1.02E-06 & -7.15E-08 & 1.01E-08 & -3.14E-05 \\ 6.67E-02 & 4.50E-05 & 5.37E-05 & -1.10E-06 & -5.41E-07 & -1.70E-03 & 3.93E-01 & -4.65E-05 & 1.38E-04 & 1.01E-06 & 1.72E-06 & 2.55E-03 \\ -4.37E-05 & 7.24E-02 & 9.94E-06 & -2.73E-07 & -2.68E-06 & 9.98E-07 & -4.65E-05 & 3.87E-01 & -3.21E-05 & 8.21E-07 & -2.82E-06 & -3.64E-05 \\ -1.76E-04 & 3.18E-05 & 6.44E-02 & 1.77E-03 & -2.67E-06 & 1.02E-06 & 1.38E-04 & -3.21E-05 & 3.95E-01 & -2.75E-03 & 3.68E-05 & 1.37E-05 \\ 6.44E-06 & -1.03E-06 & -1.77E-03 & 3.49E-05 & 1.37E-07 & -7.15E-08 & 1.01E-06 & 8.21E-07 & -2.75E-03 & 7.45E-04 & -5.31E-08 & -1.74E-07 \\ -1.29E-06 & 2.71E-06 & 1.84E-06 & -2.08E-08 & 9.97E-05 & 1.01E-08 & 1.72E-06 & -2.82E-06 & 3.68E-05 & -5.31E-08 & 7.89E-04 & 9.28E-08 \\ 1.70E-03 & 4.47E-07 & 3.56E-06 & 8.94E-08 & 8.26E-09 & -3.14E-05 & 2.55E-03 & -3.64E-05 & 1.37E-05 & -1.74E-07 & 9.28E-08 & 9.13E-05 \end{bmatrix}$$

F.2 Large Support

$$\mathbf{K} = \begin{bmatrix}
2.78E+07 & 6.28E+01 & 4.52E+01 & 1.16E+01 & 1.52E+00 & -3.02E+06 & -2.78E+07 & -6.28E+01 & -4.52E+01 & -1.76E+00 & -1.52E+00 & -3.02E+06 \\
6.28E+01 & 6.01E+08 & 2.44E+02 & -4.02E+00 & -8.37E+00 & -3.31E+01 & -6.28E+01 & -6.01E+08 & -2.44E+02 & 5.71E+01 & 8.37E+00 & 1.94E+01 \\
4.52E+01 & 2.44E+02 & 2.82E+07 & 3.07E+06 & -4.53E+00 & -6.24E+00 & -4.52E+01 & -2.44E+02 & -2.82E+07 & 3.07E+06 & 4.53E+00 & -3.60E+00 \\
1.16E+01 & -4.02E+00 & 3.07E+06 & 1.04E+06 & -4.05E-01 & -1.75E+00 & -1.16E+01 & 4.02E+00 & -3.07E+06 & -3.71E+05 & 4.05E-01 & -7.68E-01 \\
1.52E+00 & -8.37E+00 & -4.53E+00 & -4.05E-01 & 1.13E+05 & -1.67E-01 & -1.52E+00 & 8.37E+00 & 4.53E+00 & -5.81E-01 & -1.13E+05 & -1.64E-01 \\
-3.02E+06 & -3.31E+01 & -6.24E+00 & -1.75E+00 & -1.67E-01 & 4.73E+05 & 3.02E+06 & 3.31E+01 & 6.24E+00 & 3.97E-01 & 1.67E-01 & 1.84E+05 \\
-2.78E+07 & -6.28E+01 & -4.52E+01 & -1.16E+01 & -1.52E+00 & 3.02E+06 & 2.78E+07 & 6.28E+01 & 4.52E+01 & 1.76E+00 & 1.52E+00 & 3.02E+06 \\
-6.28E+01 & -6.01E+08 & -2.44E+02 & 4.02E+00 & 8.37E+00 & 3.31E+01 & 6.28E+01 & 6.01E+08 & 2.44E+02 & -5.71E+01 & -8.37E+00 & -1.94E+01 \\
-4.52E+01 & -2.44E+02 & -2.82E+07 & -3.07E+06 & 4.53E+00 & 6.24E+00 & 4.52E+01 & 2.44E+02 & 2.82E+07 & -3.07E+06 & -4.53E+00 & 3.60E+00 \\
-1.76E+00 & 5.71E+01 & 3.07E+06 & -3.71E+05 & -5.81E-01 & 3.97E-01 & 1.76E+00 & -5.71E+01 & -3.07E+06 & 1.04E+06 & 5.81E-01 & -1.49E-02 \\
-1.52E+00 & 8.37E+00 & 4.53E+00 & 4.05E-01 & -1.13E+05 & 1.67E-01 & 1.52E+00 & -8.37E+00 & -4.53E+00 & 5.81E-01 & 1.13E+05 & 1.64E-01 \\
-3.02E+06 & 1.94E+01 & -3.60E+00 & -7.68E-01 & -1.64E-01 & 1.84E+05 & 3.02E+06 & -1.94E+01 & 3.60E+00 & -1.49E-02 & 1.64E-01 & 4.73E+05
\end{bmatrix}$$

$$\mathbf{M} = \begin{bmatrix} 6.05E-01 & 1.29E-06 & 3.73E-07 & 7.15E-08 & -3.37E-09 & -1.17E-02 & 1.40E-01 & -8.21E-07 & -4.43E-07 & 1.07E-08 & 1.71E-09 & 7.73E-03 \\ 1.29E-06 & 5.77E-01 & -8.71E-07 & -2.83E-08 & -1.61E-08 & -3.56E-05 & 5.52E-07 & 1.68E-01 & -1.30E-06 & 4.17E-08 & 3.31E-08 & 3.32E-08 \\ 3.73E-07 & -8.71E-07 & 6.07E-01 & 1.20E-02 & 3.55E-05 & -2.19E-08 & 4.29E-07 & 6.44E-07 & 1.38E-01 & -7.72E-03 & -1.56E-08 & 1.86E-08 \\ 7.15E-08 & -2.83E-08 & 1.20E-02 & 1.36E-03 & 8.84E-08 & -3.88E-09 & 1.93E-08 & 3.70E-08 & 7.72E-03 & -2.39E-04 & -2.07E-09 & 1.51E-09 \\ -3.37E-09 & -1.61E-08 & 3.55E-05 & 8.84E-08 & 1.08E-03 & 3.47E-10 & -2.14E-09 & 1.64E-08 & -8.84E-11 & 1.56E-09 & 2.12E-04 & 7.98E-11 \\ -1.17E-02 & -3.56E-05 & -2.19E-08 & -3.88E-09 & 3.47E-10 & 5.15E-04 & -7.73E-03 & 3.83E-08 & 3.72E-09 & -2.04E-10 & -1.41E-10 & -3.90E-04 \\ 1.40E-01 & 5.52E-07 & 4.29E-07 & 1.93E-08 & -2.14E-09 & -7.73E-03 & 6.05E-01 & -1.02E-06 & -3.59E-07 & 7.29E-08 & 3.78E-09 & 1.17E-02 \\ -8.21E-07 & 1.68E-01 & 6.44E-07 & 3.70E-08 & 1.64E-08 & 3.83E-08 & -1.02E-06 & 5.77E-01 & 1.53E-06 & -9.96E-08 & -3.35E-08 & -3.56E-05 \\ -4.43E-07 & -1.30E-06 & 1.38E-01 & 7.72E-03 & -8.84E-11 & 3.72E-09 & -3.59E-07 & 1.53E-06 & 6.07E-01 & -1.20E-02 & 3.55E-05 & 1.47E-08 \\ 1.07E-08 & 4.17E-08 & -7.72E-03 & -2.39E-04 & 1.56E-09 & -2.04E-10 & 7.29E-08 & -9.96E-08 & -1.20E-02 & 1.36E-03 & -8.87E-08 & 5.25E-10 \\ 1.71E-09 & 3.31E-08 & -1.56E-08 & -2.07E-09 & 2.12E-04 & -1.41E-10 & 3.78E-09 & -3.35E-08 & 3.55E-05 & -8.87E-08 & 1.08E-03 & 7.45E-11 \\ 7.73E-03 & 3.32E-08 & 1.86E-08 & 1.51E-09 & 7.98E-11 & -3.90E-04 & 1.17E-02 & -3.56E-05 & 1.47E-08 & 5.25E-10 & 7.45E-11 & 5.15E-04 \end{bmatrix}$$

F.3 Base Plate

$$\mathbf{K} = \begin{bmatrix}
1.91E+09 & -1.01E-05 & 2.27E+04 & 3.23E-06 & -3.00E+03 & -2.86E-01 & -1.91E+09 & 9.49E-06 & -2.27E+04 & -3.40E-06 & -1.48E+03 & 2.86E-01 \\
-1.01E-05 & 1.23E+07 & 6.30E-06 & 3.70E+00 & -1.13E-07 & 1.22E+06 & 6.86E-06 & -1.23E+07 & 8.06E-07 & -3.70E+00 & 2.40E-07 & 1.22E+06 \\
2.27E+04 & 6.30E-06 & 5.61E+08 & 8.41E-02 & -5.54E+07 & -3.32E-06 & -2.27E+04 & 2.98E-07 & -5.61E+08 & -8.41E-02 & -5.54E+07 & 3.38E-06 \\
3.23E-06 & 3.70E+00 & 8.41E-02 & 1.21E+05 & -8.30E-03 & 2.31E-01 & -3.44E-06 & -3.70E+00 & -8.41E-02 & -1.21E+05 & -8.30E-03 & 4.99E-01 \\
-3.00E+03 & -1.13E-07 & -5.54E+07 & -8.30E-03 & 1.14E+07 & 4.31E-07 & 3.00E+03 & 1.15E-07 & 5.54E+07 & 8.30E-03 & -4.53E+05 & -4.60E-07 \\
-2.86E-01 & 1.22E+06 & -3.32E-06 & 2.31E-01 & 4.31E-07 & 1.66E+05 & 2.86E-01 & -1.22E+06 & 3.42E-06 & -2.31E-01 & 2.37E-07 & 7.46E+04 \\
-1.91E+09 & 6.86E-06 & -2.27E+04 & -3.44E-06 & 3.00E+03 & 2.86E-01 & 1.91E+09 & -4.61E-06 & 2.27E+04 & 3.18E-06 & 1.48E+03 & -2.86E-01 \\
9.49E-06 & -1.23E+07 & 2.98E-07 & -3.70E+00 & 1.15E-07 & -1.22E+06 & -4.61E-06 & 1.23E+07 & 4.74E-06 & 3.70E+00 & -3.67E-08 & -1.22E+06 \\
-2.27E+04 & 8.06E-07 & -5.61E+08 & -8.41E-02 & 5.54E+07 & 3.42E-06 & 2.27E+04 & 4.74E-06 & 5.61E+08 & 8.41E-02 & 5.54E+07 & -3.30E-06 \\
-3.40E-06 & -3.70E+00 & -8.41E-02 & -1.21E+05 & 8.30E-03 & -2.31E-01 & 3.18E-06 & 3.70E+00 & 8.41E-02 & 1.21E+05 & 8.30E-03 & -4.99E-01 \\
-1.48E+03 & 2.40E-07 & -5.54E+07 & -8.30E-03 & -4.53E+05 & 2.37E-07 & 1.48E+03 & -3.67E-08 & 5.54E+07 & 8.30E-03 & 1.14E+07 & -2.13E-07 \\
2.86E-01 & 1.22E+06 & 3.38E-06 & 4.99E-01 & -4.60E-07 & 7.46E+04 & -2.86E-01 & -1.22E+06 & -3.30E-06 & -4.99E-01 & -2.13E-07 & 1.66E+05
\end{bmatrix}$$

$$\mathbf{M} = \begin{bmatrix} 1.45E+00 & -2.69E-12 & 3.33E-05 & 6.14E-15 & -2.13E-06 & -2.17E-10 & 9.13E-01 & -2.50E-12 & 9.90E-07 & 8.83E-16 & 1.05E-07 & -1.37E-10 \\ -2.69E-12 & 1.84E+00 & -1.10E-14 & 7.83E-07 & -4.49E-15 & 3.11E-02 & 2.56E-12 & 5.19E-01 & -1.07E-14 & -4.66E-07 & 2.43E-15 & -2.29E-02 \\ 3.33E-05 & -1.10E-14 & 1.73E+00 & 2.60E-10 & -2.21E-02 & -5.75E-15 & -1.79E-05 & -1.64E-16 & 6.24E-01 & 9.35E-11 & 3.70E-02 & 2.87E-15 \\ 6.14E-15 & 7.83E-07 & 2.60E-10 & 4.25E-03 & -3.31E-12 & 3.67E-08 & -3.69E-15 & -2.02E-07 & 9.35E-11 & 1.21E-03 & 5.55E-12 & -3.85E-09 \\ -2.13E-06 & -4.49E-15 & -2.21E-02 & -3.31E-12 & 3.89E-03 & 2.37E-16 & -1.32E-07 & -1.94E-15 & -3.70E-02 & -5.55E-12 & -7.68E-04 & 8.18E-17 \\ -2.17E-10 & 3.11E-02 & -5.75E-15 & 3.67E-08 & 2.37E-16 & 1.24E-03 & -1.37E-10 & 2.29E-02 & -3.09E-16 & -5.47E-09 & 2.95E-17 & -9.56E-04 \\ 9.13E-01 & 2.56E-12 & -1.79E-05 & -3.69E-15 & -1.32E-07 & -1.37E-10 & 1.45E+00 & 2.59E-12 & -1.63E-05 & -3.10E-15 & -8.69E-07 & -2.17E-10 \\ -2.50E-12 & 5.19E-01 & -1.64E-16 & -2.02E-07 & -1.94E-15 & 2.29E-02 & 2.59E-12 & 1.84E+00 & -1.05E-14 & -1.14E-07 & -5.79E-17 & -3.11E-02 \\ 9.90E-07 & -1.07E-14 & 6.24E-01 & 9.35E-11 & -3.70E-02 & -3.09E-16 & -1.63E-05 & -1.05E-14 & 1.73E+00 & 2.60E-10 & 2.21E-02 & 2.28E-15 \\ 8.83E-16 & -4.66E-07 & 9.35E-11 & 1.21E-03 & -5.55E-12 & -5.47E-09 & -3.10E-15 & -1.14E-07 & 2.60E-10 & 4.25E-03 & 3.31E-12 & 2.10E-09 \\ 1.05E-07 & 2.43E-15 & 3.70E-02 & 5.55E-12 & -7.68E-04 & 2.95E-17 & -8.69E-07 & -5.79E-17 & 2.21E-02 & 3.31E-12 & 3.89E-03 & 1.00E-16 \\ -1.37E-10 & -2.29E-02 & 2.87E-15 & -3.85E-09 & 8.18E-17 & -9.56E-04 & -2.17E-10 & -3.11E-02 & 2.28E-15 & 2.10E-09 & 1.00E-16 & 1.24E-03 \end{bmatrix}$$

Appendix G

Matrix Multiplication Error

Using the matrix convention for the rotations about the vertical and horizontal axes as shown in Equations (6.48a),(6.48b) and (G.1a), the complete multiplication matrices for $\mathbf{R} = \mathbf{R_y R_z}$ and $\mathbf{R} = \mathbf{R_z R_y}$ will be obtained along with the variation between the two rotational conventions.

G.1 $\mathbf{R} = \mathbf{R}_y\mathbf{R}_z$

$$
\begin{aligned}
R_{11} =& R_{y11}R_{z11} + R_{y12}R_{z21} + R_{y13}R_{z31} \\
=& \left(\cos\beta + \cos^2\phi\,(1-\cos\beta)\right)\left(\cos\gamma + \sin^2\phi\,(1-\cos\gamma)\right) + \\
& (\cos\phi\sin\phi\,(1-\cos\beta))\,(-\cos\phi\sin\phi\,(1-\cos\gamma)) + \\
& (\sin\phi\sin\beta)\,(-\cos\phi\sin\gamma) \\
=& \cos\beta\cos\gamma + \cos\beta\sin^2\phi\,(1-\cos\gamma) + \cos\gamma\cos^2\phi\,(1-\cos\beta) + \\
& \cos^2\phi\sin^2\phi\,(1-\cos\beta)\,(1-\cos\gamma) - \\
& \cos^2\phi\sin^2\phi\,(1-cos\beta)\,(1-\cos\gamma) - \sin\phi\cos\phi\sin\beta\sin\gamma \\
=& \cos\beta\cos\gamma + \cos\beta\sin^2\phi - \cos\beta\cos\gamma\sin^2\phi + \cos\gamma\cos^2\phi - \\
& \cos\beta\cos\gamma\cos^2\phi - \sin\phi\cos\phi\sin\beta\sin\gamma \\
=& \cos\beta\cos\gamma + \cos\beta\sin^2\phi - \cos\beta\cos\gamma\left(\sin^2\phi + \cos^2\phi\right) + \\
& \cos\gamma\cos^2\phi - \sin\phi\cos\phi\sin\beta\sin\gamma
\end{aligned}
$$

$$
\begin{aligned}
&\textit{Since } \sin^2\phi + \cos^2\phi = 1 \\
&\quad = \cos\beta \sin^2\phi + \cos\gamma \cos^2\phi - \sin\phi \cos\phi \sin\beta \sin\gamma \\
R_{12} =& R_{y11}R_{z12} + R_{y12}R_{z22} + R_{y13}R_{z32} \\
&\quad = \left(\cos\beta + \cos^2\phi\,(1-\cos\beta)\right)(-\cos\phi\sin\phi\,(1-\cos\gamma)) + \\
&\qquad (\cos\phi\sin\phi\,(1-\cos\beta))\left(\cos\gamma + \cos^2\phi\,(1-\cos\gamma)\right) + \\
&\qquad (\sin\phi\sin\beta)\,(-\sin\phi\sin\gamma) \\
&\quad = -\cos\phi\sin\phi\cos\beta\,(1-\cos\gamma) - \cos^3\phi\sin\phi\,(1-\cos\beta)\,(1-\cos\gamma) + \\
&\qquad \cos\phi\sin\phi\cos\gamma\,(1-\cos\beta) + \cos^3\phi\sin\phi\,(1-\cos\beta)\,(1-\cos\gamma) - \\
&\qquad \sin^2\phi\sin\beta\sin\gamma \\
&\quad = -\cos\phi\sin\phi\cos\beta + \cos\phi\sin\phi\cos\beta\cos\gamma + \cos\phi\sin\phi\cos\gamma - \\
&\qquad \cos\phi\sin\phi\cos\beta\cos\gamma - \sin^2\phi\sin\beta\sin\gamma \\
&\quad = \cos\phi\sin\phi\cos\gamma - \cos\phi\sin\phi\cos\beta - \sin^2\phi\sin\beta\sin\gamma \\
&\quad = \cos\phi\sin\phi\,(\cos\gamma - \cos\beta - \tan\phi\sin\beta\sin\gamma) \\
R_{13} =& R_{y11}R_{z13} + R_{y12}R_{z23} + R_{y13}R_{z33} \\
&\quad = \left(\cos\beta + \cos^2\phi\,(1-\cos\beta)\right)(\cos\phi\sin\gamma) + \\
&\qquad (\cos\phi\sin\phi\,(1-\cos\beta))\,(\sin\phi\sin\gamma) + (\sin\phi\sin\beta)\,(\cos\gamma)) \\
&\quad = \cos\phi\cos\beta\sin\gamma + \cos\phi\sin\gamma\,(1-\cos\beta)\cos^2\phi + \\
&\qquad \cos\phi\sin\gamma\,(1-\cos\beta)\sin^2\phi + \sin\phi\sin\beta\cos\gamma \\
&\quad = \cos\phi\cos\beta\sin\gamma + \cos\phi\sin\gamma\,(1-\cos\beta)\left(\cos^2\phi + \sin^2\phi\right) + \\
&\qquad \sin\phi\sin\beta\cos\gamma \\
&\quad = \cos\phi\cos\beta\sin\gamma + \cos\phi\sin\gamma - \cos\phi\cos\beta\sin\gamma + \sin\phi\sin\beta\cos\gamma \\
&\quad = \cos\phi\sin\gamma + \sin\phi\sin\beta\cos\gamma \\
R_{21} =& R_{y21}R_{z11} + R_{y22}R_{z21} + R_{y23}R_{z31} \\
&\quad = (\cos\phi\sin\phi\,(1-\cos\beta))\left(\cos\gamma + \sin^2\phi\,(1-\cos\gamma)\right) + \\
&\qquad \left(\cos\beta + \sin^2\phi\,(1-\cos\beta)\right)(-\cos\phi\sin\phi\,(1-\cos\gamma)) + \\
&\qquad (-\cos\phi\sin\beta)\,(-\cos\phi\sin\gamma)
\end{aligned}
$$

$$
\begin{aligned}
&= \cos\phi \sin\phi \cos\gamma \left(1 - \cos\beta\right) + \cos\phi \sin^3\phi \left(1 - \cos\beta\right)\left(1 - \cos\gamma\right) - \\
&\quad \cos\phi \sin\phi \cos\beta \left(1 - \cos\gamma\right) + \cos\phi \sin^3\phi \left(1 - \cos\beta\right)\left(1 - \cos\gamma\right) + \\
&\quad \cos^2\phi \sin\beta \sin\gamma \\
&= \cos\phi \sin\phi \left(\cos\gamma \left(1 - \cos\beta\right) - \cos\beta \left(1 - \cos\gamma\right) + \left(\sin\beta \sin\gamma / \tan\phi\right)\right) \\
&= \cos\phi \sin\phi \left(\cos\gamma - \cos\beta + \left(\sin\beta \sin\gamma / \tan\phi\right)\right) \\
R_{22} &= R_{y21}R_{z12} + R_{y22}R_{z22} + R_{y23}R_{z32} \\
&= \left(\cos\phi \sin\phi \left(1 - \cos\beta\right)\right)\left(-\cos\phi \sin\phi \left(1 - \cos\gamma\right)\right) + \\
&\quad \left(\cos\beta + \sin^2\phi \left(1 - \cos\beta\right)\right)\left(\cos\gamma + \cos^2\phi \left(1 - \cos\gamma\right)\right) + \\
&\quad \left(-\cos\phi \sin\beta\right)\left(-\sin\phi \sin\gamma\right) \\
&= -\cos^2\phi \sin^2\phi \left(1 - \cos\beta\right)\left(1 - \cos\gamma\right) + \cos\beta \cos\gamma + \\
&\quad \cos\beta \cos^2\phi \left(1 - \cos\gamma\right) + \cos\gamma \sin^2\phi \left(1 - \cos\beta\right) + \\
&\quad \cos^2\phi \sin^2\phi \left(1 - \cos\beta\right)\left(1 - \cos\gamma\right) + \sin\phi \cos\phi \sin\beta \sin\gamma \\
&= \cos\beta \cos\gamma + \cos\beta \cos^2\phi - \cos\beta \cos\gamma \cos^2\phi + \cos\gamma \sin^2\phi - \\
&\quad \cos\beta \cos\gamma \sin^2\phi + \sin\phi \cos\phi \sin\beta \sin\gamma \\
&= \cos\beta \cos\gamma + \cos\beta \cos^2\phi - \cos\beta \cos\gamma \left(\cos^2\phi + \sin^2\phi\right) + \\
&\quad \cos\gamma \sin^2\phi + \sin\phi \cos\phi \sin\beta \sin\gamma \\
&= \cos\beta \cos^2\phi + \cos\gamma \sin^2\phi + \sin\phi \cos\phi \sin\beta \sin\gamma \\
R_{23} &= R_{y21}R_{z13} + R_{y22}R_{z23} + R_{y23}R_{z33} \\
&= \left(\cos\phi \sin\phi \left(1 - \cos\beta\right)\right)\left(\cos\phi \sin\gamma\right) + \\
&\quad \left(\cos\beta + \sin^2\phi \left(1 - \cos\beta\right)\right)\left(\sin\phi \sin\gamma\right) + \left(-\cos\phi \sin\beta\right)\left(\cos\gamma\right) \\
&= \cos^2\phi \sin\phi \sin\gamma \left(1 - \cos\beta\right) + \sin\phi \cos\beta \sin\gamma + \\
&\quad \sin^2\phi \sin\phi \sin\gamma \left(1 - \cos\beta\right) - \cos\phi \sin\beta \cos\gamma \\
&= \sin\phi \sin\gamma \left(1 - \cos\beta\right)\left(\cos^2\phi + \sin^2\phi\right) + \\
&\quad \sin\phi \cos\beta \sin\gamma - \cos\phi \sin\beta \cos\gamma \\
&= \sin\phi \sin\gamma - \sin\phi \cos\beta \sin\gamma \ + \sin\phi \cos\beta \sin\gamma - \cos\phi \sin\beta \cos\gamma \\
&= \sin\phi \sin\gamma - \cos\phi \sin\beta \cos\gamma
\end{aligned}
$$

$$
\begin{aligned}
R_{31} =& R_{y31}R_{z11} + R_{y32}R_{z21} + R_{y33}R_{z31} \\
=& (-\sin\phi\sin\beta)\left(\cos\gamma + \sin^2\phi\,(1-\cos\gamma)\right) + \\
& (\cos\phi\sin\beta)\left(-\cos\phi\sin\phi\,(1-\cos\gamma)\right) + (\cos\beta)\left(-\cos\phi\sin\gamma\right) \\
=& -\sin\phi\sin\beta\sin\gamma - \sin^2\phi\sin\phi\sin\beta\,(1-\cos\gamma) - \\
& \cos^2\phi\sin\phi\sin\beta\,(1-\cos\gamma) - \cos\phi\cos\beta\sin\gamma \\
=& -\sin\phi\sin\beta\sin\gamma - \left(sin^2\phi\ + \cos^2\phi\right)\sin\phi\sin\beta\,(1-\cos\gamma) - \\
& \cos\phi\cos\beta\sin\gamma \\
=& -\sin\phi\sin\beta\sin\gamma - \sin\phi\sin\beta + \sin\phi\sin\beta\cos\gamma - \cos\phi\cos\beta\sin\gamma \\
=& -\sin\phi\sin\beta - \cos\phi\cos\beta\sin\gamma \\
R_{32} =& R_{y31}R_{z12} + R_{y32}R_{z22} + R_{y33}R_{z32} \\
=& (-\sin\phi\sin\beta)\left(-\cos\phi\sin\phi\,(1-\cos\gamma)\right) + \\
& (\cos\phi\sin\beta)\left(\cos\gamma + \cos^2\phi\,(1-\cos\gamma)\right) + (\cos\beta)\left(-\sin\phi\sin\gamma\right) \\
=& \cos\phi\sin\beta\,(1-\cos\gamma)\sin^2\phi + \cos\phi\sin\beta\cos\gamma + \\
& \cos\phi\sin\beta\,(1-\cos\gamma)\cos^2\phi - \sin\phi\cos\beta\sin\gamma \\
=& \cos\phi\sin\beta\,(1-\cos\gamma)\left(\sin^2\phi + \cos^2\phi\right) + \\
& \cos\phi\sin\beta\cos\gamma - \sin\phi\cos\beta\sin\gamma \\
=& \cos\phi\sin\beta - \cos\phi\sin\beta\cos\gamma + \cos\phi\sin\beta\cos\gamma - \sin\phi\cos\beta\sin\gamma \\
=& \cos\phi\sin\beta - \sin\phi\cos\beta\sin\gamma \\
R_{33} =& R_{y31}R_{z13} + R_{y32}R_{z23} + R_{y33}R_{z33} \\
=& (-\sin\phi\sin\beta)\left(\cos\phi\sin\gamma\right) + \\
& (\cos\phi\sin\beta)\left(\sin\phi\sin\gamma\right) + (\cos\beta)\left(\cos\gamma\right)) \\
=& -\cos\phi\sin\phi\sin\beta\sin\gamma + \cos\phi\sin\phi\sin\beta\sin\gamma + \cos\beta\cos\gamma \\
=& \cos\beta\cos\gamma
\end{aligned}
$$

G.2 $\mathbf{R} = \mathbf{R}_z\mathbf{R}_y$

$$
\begin{aligned}
R_{11} =& R_{z11}R_{y11} + R_{z12}R_{y21} + R_{z13}R_{y31} \\
=& \left(\cos\gamma + \sin^2\phi\,(1-\cos\gamma)\right)\left(\cos\beta + \cos^2\phi\,(1-\cos\beta)\right) + \\
& (-\cos\phi\sin\phi\,(1-\cos\gamma))\,(\cos\phi\sin\phi\,(1-\cos\beta)) + \\
& (\cos\phi\sin\gamma)\,(-\sin\phi\sin\beta) \\
=& \cos\beta\cos\gamma + \cos\beta\sin^2\phi\,(1-\cos\gamma) + \cos\gamma\cos^2\phi\,(1-\cos\beta) + \\
& \cos^2\phi\sin^2\phi\,(1-\cos\beta)\,(1-\cos\gamma) - \\
& \cos^2\phi\sin^2\phi\,(1-cos\beta)\,(1-\cos\gamma) - \sin\phi\cos\phi\sin\beta\sin\gamma \\
=& \cos\beta\cos\gamma + \cos\beta\sin^2\phi - \cos\beta\cos\gamma\sin^2\phi + \cos\gamma\cos^2\phi - \\
& \cos\beta\cos\gamma\cos^2\phi - \sin\phi\cos\phi\sin\beta\sin\gamma \\
=& \cos\beta\cos\gamma + \cos\beta\sin^2\phi - \cos\beta\cos\gamma\left(\sin^2\phi + \cos^2\phi\right) + \\
& \cos\gamma\cos^2\phi - \sin\phi\cos\phi\sin\beta\sin\gamma \\
\textit{Since}\ & \sin^2\phi + \cos^2\phi = 1 \\
=& \cos\beta\sin^2\phi + \cos\gamma\cos^2\phi - \sin\phi\cos\phi\sin\beta\sin\gamma \\
R_{12} =& R_{z11}R_{y12} + R_{z12}R_{y22} + R_{z13}R_{y32} \\
=& \left(\cos\gamma + \sin^2\phi\,(1-\cos\gamma)\right)(\cos\phi\sin\phi\,(1-\cos\beta)) + \\
& (-\cos\phi\sin\phi\,(1-\cos\gamma))\left(\cos\beta + \sin^2\phi\,(1-\cos\beta)\right) + \\
& (\cos\phi\sin\gamma)\,(\cos\phi\sin\beta) \\
=& \cos\phi\sin\phi\cos\gamma\,(1-\cos\beta) + \sin^3\phi\sin\phi\,(1-\cos\beta)\,(1-\cos\gamma) - \\
& \cos\phi\sin\phi\cos\beta\,(1-\cos\gamma) + \sin^3\phi\sin\phi\,(1-\cos\beta)\,(1-\cos\gamma) + \\
& \cos^2\phi\sin\beta\sin\gamma \\
=& \cos\phi\sin\phi\,(\cos\gamma\,(1-\cos\beta) - \cos\beta\,(1-\cos\gamma) + ((\sin\beta\sin\gamma)\,/\,\tan\phi)) \\
=& \cos\phi\sin\phi\,(\cos\gamma - \cos\beta + ((\sin\beta\sin\gamma)\,/\,\tan\phi)) \\
R_{13} =& R_{z11}R_{y13} + R_{z12}R_{y23} + R_{z13}R_{y33}
\end{aligned}
$$

$$
\begin{aligned}
&= \left(\cos\gamma + \sin^2\phi\,(1-\cos\gamma)\right)(\sin\phi\sin\beta) + \\
&\quad (-\cos\phi\sin\phi\,(1-\cos\gamma))\,(-\cos\phi\sin\beta) + (\cos\phi\sin\gamma)\,(\cos\beta)) \\
&= \sin\phi\sin\beta\cos\gamma + \sin\phi\sin\beta\,(1-\cos\gamma)\sin^2\phi + \\
&\quad \sin\phi\sin\beta\,(1-\cos\gamma)\cos^2\phi + \cos\phi\cos\beta\sin\gamma \\
&= \sin\phi\sin\beta\cos\gamma + \sin\phi\sin\beta\,(1-\cos\gamma)\left(\sin^2\phi + \cos^2\phi\right) + \\
&\quad \cos\phi\cos\beta\sin\gamma \\
&= \sin\phi\sin\beta\cos\gamma + \sin\phi\sin\beta - \sin\phi\sin\beta\cos\gamma + \cos\phi\cos\beta\sin\gamma \\
&= \sin\phi\sin\beta + \cos\phi\cos\beta\sin\gamma \\
R_{21} =& R_{z21}R_{y11} + R_{z22}R_{y21} + R_{z23}R_{y31} \\
&= (-\cos\phi\sin\phi\,(1-\cos\gamma))\left(\cos\beta + \cos^2\phi\,(1-\cos\beta)\right) + \\
&\quad \left(\cos\gamma + \cos^2\phi\,(1-\cos\gamma)\right)(\cos\phi\sin\phi\,(1-\cos\beta)) + \\
&\quad (\sin\phi\sin\gamma)\,(-\sin\phi\sin\beta) \\
&= -\cos\phi\sin\phi\cos\beta\,(1-\cos\gamma) - \sin\phi\cos^3\phi\,(1-\cos\beta)\,(1-\cos\gamma) + \\
&\quad \cos\phi\sin\phi\cos\gamma\,(1-\cos\beta) + \sin\phi\cos^3\phi\,(1-\cos\beta)\,(1-\cos\gamma) - \\
&\quad \sin^2\phi\sin\beta\sin\gamma \\
&= \cos\phi\sin\phi\,(\cos\gamma\,(1-\cos\beta) - \cos\beta\,(1-\cos\gamma) - \tan\phi\sin\beta\sin\gamma) \\
&= \cos\phi\sin\phi\,(\cos\gamma - \cos\beta - \tan\phi\sin\beta\sin\gamma) \\
R_{22} =& R_{z21}R_{y12} + R_{z22}R_{y22} + R_{z23}R_{y32} \\
&= (-\cos\phi\sin\phi\,(1-\cos\gamma))\,(\cos\phi\sin\phi\,(1-\cos\beta)) + \\
&\quad \left(\cos\gamma + \cos^2\phi\,(1-\cos\gamma)\right)\left(\cos\beta + \sin^2\phi\,(1-\cos\beta)\right) + \\
&\quad (\sin\phi\sin\gamma)\,(\cos\phi\sin\beta) \\
&= -\cos^2\phi\sin^2\phi\,(1-\cos\beta)\,(1-\cos\gamma) + \cos\beta\cos\gamma + \\
&\quad \cos\beta\cos^2\phi\,(1-\cos\gamma) + \cos\gamma\sin^2\phi\,(1-\cos\beta) + \\
&\quad \cos^2\phi\sin^2\phi\,(1-\cos\beta)\,(1-\cos\gamma) + \sin\phi\cos\phi\sin\beta\sin\gamma \\
&= \cos\beta\cos\gamma + \cos\beta\cos^2\phi - \cos\beta\cos\gamma\cos^2\phi + \cos\gamma\sin^2\phi - \\
&\quad \cos\beta\cos\gamma\sin^2\phi + \sin\phi\cos\phi\sin\beta\sin\gamma
\end{aligned}
$$

$$
\begin{aligned}
&= \cos\beta\cos\gamma + \cos\beta\cos^2\phi - \cos\beta\cos\gamma\left(\cos^2\phi + \sin^2\phi\right) + \\
&\quad \cos\gamma\sin^2\phi + \sin\phi\cos\phi\sin\beta\sin\gamma \\
&= \cos\beta\cos^2\phi + \cos\gamma\sin^2\phi + \sin\phi\cos\phi\sin\beta\sin\gamma \\
R_{23} =& R_{z21}R_{y13} + R_{z22}R_{y23} + R_{z23}R_{y33} \\
&= \left(-\cos\phi\sin\phi\left(1-\cos\gamma\right)\right)\left(\sin\phi\sin\beta\right) + \\
&\quad \left(\cos\gamma + \cos^2\phi\left(1-\cos\gamma\right)\right)\left(-\cos\phi\sin\beta\right) + \left(\sin\phi\sin\gamma\right)\left(\cos\beta\right) \\
&= -\sin^2\phi\cos\phi\sin\beta\left(1-\cos\gamma\right) - \cos\phi\sin\beta\cos\gamma - \\
&\quad \cos^2\phi\cos\phi\sin\beta\left(1-\cos\gamma\right) + \sin\phi\sin\beta\cos\gamma \\
&= -\cos\phi\sin\beta\left(1-\cos\gamma\right)\left(\cos^2\phi + \sin^2\phi\right) - \\
&\quad \cos\phi\sin\beta\cos\gamma + \sin\phi\cos\beta\sin\gamma \\
&= -\cos\phi\sin\beta + \cos\phi\sin\beta\cos\gamma \;\; - \cos\phi\sin\beta\cos\gamma + \sin\phi\cos\beta\sin\gamma \\
&= \sin\phi\cos\beta\sin\gamma - \cos\phi\sin\beta \\
R_{31} =& R_{z31}R_{y11} + R_{z32}R_{y21} + R_{z33}R_{y31} \\
&= \left(-\cos\phi\sin\gamma\right)\left(\cos\beta + \cos^2\phi\left(1-\cos\beta\right)\right) + \\
&\quad \left(-\sin\phi\sin\gamma\right)\left(\cos\phi\sin\phi\left(1-\cos\beta\right)\right) + \left(\cos\gamma\right)\left(-\sin\phi\sin\beta\right) \\
&= -\cos\phi\cos\beta\sin\gamma - \cos^2\phi\cos\phi\sin\gamma\left(1-\cos\beta\right) - \\
&\quad \sin^2\phi\cos\phi\sin\gamma\left(1-\cos\beta\right) - \sin\phi\sin\beta\cos\gamma \\
&= -\cos\phi\cos\beta\sin\gamma - \left(sin^2\phi \;\; + \cos^2\phi\right)\cos\phi\sin\gamma\left(1-\cos\beta\right) - \\
&\quad \sin\phi\sin\beta\cos\gamma \\
&= -\cos\phi\cos\beta\sin\gamma - \cos\phi\sin\gamma + \cos\phi\cos\beta\sin\gamma - \sin\phi\sin\beta\cos\gamma \\
&= -\cos\phi\sin\gamma - \sin\phi\sin\beta\cos\gamma \\
R_{32} =& R_{z31}R_{y12} + R_{z32}R_{y22} + R_{z33}R_{y32} \\
&= \left(-\cos\phi\sin\gamma\right)\left(\cos\phi\sin\phi\left(1-\cos\beta\right)\right) + \\
&\quad \left(-\sin\phi\sin\gamma\right)\left(\cos\beta + \sin^2\phi\left(1-\cos\beta\right)\right) + \left(\cos\gamma\right)\left(\cos\phi\sin\beta\right) \\
&= -\sin\phi\sin\gamma\left(1-\cos\beta\right)\cos^2\phi - \sin\phi\cos\beta\sin\gamma - \\
&\quad \sin\phi\sin\gamma\left(1-\cos\beta\right)\sin^2\phi + \cos\phi\sin\beta\cos\gamma
\end{aligned}
$$

$$
\begin{aligned}
&= -\sin\phi\sin\gamma\,(1-\cos\beta)\left(\sin^2\phi+\cos^2\phi\right)+\\
&\quad -\sin\phi\cos\beta\sin\gamma+\cos\phi\sin\beta\cos\gamma\\
&= -\sin\phi\sin\gamma+\sin\phi\cos\beta\sin\gamma+\cos\phi\sin\beta\cos\gamma-\sin\phi\cos\beta\sin\gamma\\
&= \cos\phi\sin\beta\cos\gamma-\sin\phi\sin\gamma\\
R_{33} &= R_{z31}R_{y13}+R_{z32}R_{y23}+R_{z33}R_{y33}\\
&= (-\cos\phi\sin\gamma)\,(\sin\phi\sin\beta)+\\
&\quad (-\sin\phi\sin\gamma)\,(-\cos\phi\sin\beta)+(\cos\beta)\,(\cos\gamma))\\
&= -\cos\phi\sin\phi\sin\beta\sin\gamma+\cos\phi\sin\phi\sin\beta\sin\gamma+\cos\beta\cos\gamma\\
&= \cos\beta\cos\gamma
\end{aligned}
$$

G.3 Order of Multiplication Error

The error, or variation, caused through the chosen order of multiplication can be found by subtracting the two rotational matrices, which leads to

$$
\begin{aligned}
R_{11} &= 0\\
R_{12} &= -\cos\phi\sin\phi\sin\beta\sin\gamma\,(\tan\phi-1/\tan\phi)\\
R_{13} &= \cos\phi\sin\gamma\,(1-\cos\beta)-\sin\phi\sin\beta\,(\cos\gamma-1)\\
R_{21} &= \cos\phi\sin\phi\sin\beta\sin\gamma\,(\tan\phi-1/\tan\phi)\\
R_{22} &= 0\\
R_{23} &= \sin\phi\sin\gamma\,(1-\cos\beta)-\cos\phi\sin\beta\,(\cos\gamma-1)\\
R_{31} &= -\sin\phi\sin\beta\,(1-\cos\gamma)-\cos\phi\sin\gamma\,(\cos\beta-1)\\
R_{32} &= \cos\phi\sin\beta\,(1-\cos\gamma)-\sin\phi\sin\gamma\,(\cos\beta-1)\\
R_{33} &= 0
\end{aligned}
$$

From this it is apparent that as the rotation angle tend to zero so does the variation caused through the order of multiplication, which is the assumption utilised in determining the applied yaw and pitch misalignment.

G.4 Calculation of Misalignments Through $\mathbf{R} = \mathbf{R}_z\mathbf{R}_y$

From section G.2 the rotation matrix is given as:

$$\left(\mathbf{R_z R_y}\right)_j(t) = \begin{bmatrix} R_{11,j}(t) & R_{12,j}(t) & R_{13,j}(t) \\ R_{21,j}(t) & R_{22,j}(t) & R_{23,j}(t) \\ R_{31,j}(t) & R_{32,j}(t) & R_{33,j}(t) \end{bmatrix} \tag{G.1a}$$

where

$$\begin{aligned} R_{11,j}(t) &= \cos\gamma_j(t)\cos^2\phi'(t) + \cos\beta_j(t)\sin^2\phi'(t) - \dots \\ &\quad \cos\phi'(t)\sin\phi'(t)\sin\gamma_j(t)\sin\beta_j(t) && \text{(G.1b)} \\ R_{12,j}(t) &= \cos\phi'(t)\sin\phi'(t)\left(\cos\gamma_j(t) - \cos\beta_j(t) + \dots\right. \\ &\quad \left.\left(\sin\gamma_j(t)\sin\beta_j(t)\tan\phi'(t)\right)\right) && \text{(G.1c)} \\ R_{13,j}(t) &= \cos\phi'(t)\sin\gamma_j(t)\cos\beta_j(t) + \sin\phi'(t)\sin\beta_j(t) && \text{(G.1d)} \\ R_{21,j}(t) &= \cos\phi'(t)\sin\phi'(t)\left(\cos\gamma_j(t) - \cos\beta_j(t) - \dots\right. \\ &\quad \left.\tan\phi'(t)\sin\gamma_j(t)\sin\beta_j(t)\right) && \text{(G.1e)} \\ R_{22,j}(t) &= \cos\gamma_j(t)\sin^2\phi'(t) + \cos\beta_j(t)\cos^2\phi'(t) + \dots \\ &\quad \cos\phi'(t)\sin\phi'(t)\sin\gamma_j(t)\sin\beta_j(t) && \text{(G.1f)} \\ R_{23,j}(t) &= \sin\phi'(t)\sin\gamma_j(t)\cos\beta_j(t) - \cos\phi'(t)\sin\beta_j(t) && \text{(G.1g)} \\ R_{31,j}(t) &= -\cos\phi'(t)\sin\gamma_j(t) - \sin\phi'(t)\cos\gamma_j(t)\sin\beta_j(t) && \text{(G.1h)} \\ R_{32,j}(t) &= \cos\phi'(t)\cos\gamma_j(t)\sin\beta_j(t) - \sin\phi'(t)\sin\gamma_j(t) && \text{(G.1i)} \\ R_{33,j}(t) &= \cos\gamma_j(t)\cos\beta_j(t) && \text{(G.1j)} \end{aligned}$$

This matrix can now be compared against the rotational matrix constructed through the combination of the local orthogonal coordinate system rotations, which are aligned with the local coordinate system. These are about the LOA (θ_{yaw}), OLOA (θ_{pitch}) and the z (θ_z) axes, where each individual rotation matrix is shown below

$$\mathbf{R_{yaw,j}}(t) = \begin{bmatrix} 1 & 0 & 0 \\ 0 & \cos\theta_{yaw,j}(t) & -\sin\theta_{yaw,j}(t) \\ 0 & \sin\theta_{yaw,j}(t) & \cos\theta_{yaw,j}(t) \end{bmatrix} \tag{G.2a}$$

$$\mathbf{R_{pitch,j}}(t) = \begin{bmatrix} \cos\theta_{pitch,j}(t) & 0 & \sin\theta_{pitch,j}(t) \\ 0 & 1 & 0 \\ -\sin\theta_{pitch,j}(t) & 0 & \cos\theta_{pitch,j}(t) \end{bmatrix} \tag{G.2b}$$

$$\mathbf{R_{z,j}}(t) = \begin{bmatrix} \cos\theta_{z,j}(t) & -\sin\theta_{z,j}(t) & 0 \\ \sin\theta_{z,j}(t) & \cos\theta_{z,j}(t) & 0 \\ 0 & 0 & 1 \end{bmatrix} \tag{G.2c}$$

These are combined by applying yaw misalignment, then pitch and finally rotating about the line of contact, i.e. ($\mathbf{R_z R_{pitch} R_{yaw}}$), which results in the complete rotation matrix

$$R_{11,j}(t) = \cos\theta_{pitch,j}(t)\cos\theta_{z,j}(t) \tag{G.3a}$$

$$R_{12,j}(t) = -\cos\theta_{yaw,j}(t)\sin\theta_{z,j}(t) + \ldots$$
$$\sin\theta_{yaw,j}(t)\sin\theta_{pitch,j}(t)\cos\theta_{z,j}(t) \tag{G.3b}$$

$$R_{13,j}(t) = \sin_{yaw,j}(t)\sin\theta_{z,j}(t) + \cos\theta_{yaw,j}(t)\sin\theta_{pitch,j}(t)\cos\theta_{z,j}(t) \tag{G.3c}$$

$$R_{21,j}(t) = \cos\theta_{pitch,j}(t)\sin\theta_{z,j}(t) \tag{G.3d}$$

$$R_{22,j}(t) = \cos\theta_{yaw,j}(t)\cos\theta_{z,j}(t) + \ldots$$
$$\sin\theta_{yaw,j}(t)\sin\theta_{pitch,j}(t)\sin\theta_{z,j}(t) \tag{G.3e}$$

$$R_{23,j}(t) = -\sin\theta_{yaw,j}(t)\cos\theta_{z,j}(t) + \ldots$$
$$\cos\theta_{yaw,j}(t)\sin\theta_{pitch,j}(t)\sin\theta_{z,j}(t) \tag{G.3f}$$

$$R_{31,j}(t) = -\sin\theta_{pitch,j}(t) \tag{G.3g}$$

$$R_{32,j}(t) = \sin\theta_{yaw,j}(t)\cos\theta_{pitch,j}(t) \tag{G.3h}$$

$$R_{33,j}(t) = \cos\theta_{yaw,j}(t)\cos\theta_{pitch,j}(t) \tag{G.3i}$$

By comparing the two rotational matrices described by Equations (G.1) and (G.3) the various angular misalignments can be determined, where the pitch misalignment can be obtained through comparing matrix elements $R_{31,j}$.

$$-\sin\theta_{pitch,j}(t) = -\cos\phi'(t)\sin\gamma_j(t) - \sin\phi'(t)\cos\gamma_j(t)\sin\beta_j(t)$$

$$\theta_{pitch,j}(t) = \sin^{-1}\left(\cos\phi'(t)\sin\gamma_j(t) + \sin\phi'(t)\cos\gamma_j(t)\sin\beta_j(t)\right) \tag{G.4a}$$

The yaw misalignment can be found through the division of matrix element $R_{32,j}$ by $R_{33,j}$ which results in.

$$\begin{aligned}
\frac{R_{32,j}(t)}{R_{33,j}(t)} &= \frac{\sin\theta_{yaw,j}(t)(t)\cos\theta_{pitch,j}(t)}{\cos\theta_{yaw,j}(t)\cos\theta_{pitch,j}(t)} = \tan\theta_{yaw,j}(t) \\
\tan\theta_{yaw,j}(t) &= \frac{\cos\phi'(t)\cos\gamma_j(t)\sin\beta_j(t) - \sin\phi'(t)\sin\gamma_j(t)}{\cos\gamma_j(t)\cos\beta_j(t)} \\
\theta_{yaw,j}(t) &= \tan^{-1}\left(\cos\phi'(t)\tan\beta_j(t) - \frac{\sin\phi'(t)\tan\gamma_j(t)}{\cos\beta_j(t)}\right)
\end{aligned} \tag{G.4b}$$

Finally the rotation about the global axial direction can be obtained in a similar fashion by dividing element $R_{21,j}$ by $R_{11,j}$, which gives.

$$\frac{R_{21,j}(t)}{R_{11,j}(t)} = \frac{\cos\theta_{pitch,j}(t)\sin\theta_{z,j}(t)}{\cos\theta_{pitch,j}(t)\cos\theta_{z,j}(t)} = \tan\theta_{z,j}(t)$$

$$\tan\theta_{z,j}(t) = \frac{\cos\phi'(t)\sin\phi'(t)(\cos\gamma_j(t) - \cos\beta_j(t) - \tan\phi'(t)\sin\gamma_j(t)\sin\beta_j(t))}{\cos\gamma_j(t)\cos^2\phi'(t) + \cos\beta_j(t)\sin^2\phi'(t) - \cos\phi'(t)\sin\phi'(t)\sin\gamma_j(t)\sin\beta_j(t)}$$

$$\theta_{z,j}(t) = \tan^{-1}\left(\frac{\cos\gamma_j(t) - \cos\beta_j(t) - \tan\phi'(t)\sin\gamma_j(t)\sin\beta_j(t)}{(\cos\gamma_j(t)(1/\tan\phi'(t))) + \cos\beta_j(t)\tan\phi'(t) - \sin\gamma_j(t)\sin\beta_j(t)}\right) \tag{G.4c}$$